SWELLING AND CREEP DAMAGE ACCUMULATION IN HOT-PRESSED ALUMINA

by

A. GORDON ROBERTSON

A thesis

submitted to the School of Graduate Studies

in partial fulfillment of the requirements

for the degree

Doctor of Philosophy

McMaster University

February 1989

SWELLING AND CREEP DAMAGE ACCUMULATION IN HOT-PRESSED ALUMINA

DOCTOR OF PHILOSOPHY — McMASTER UNIVERSITY

(Materials Science and Engineering) — Hamilton, Ontario

TITLE: Swelling and creep damage accumulation in hot-pressed alumina.

AUTHOR: A. Gordon Robertson

SUPERVISOR: D.S. Wilkinson

NUMBER OF PAGES: xvii,514

ABSTRACT

This thesis consists of two parts. The first describes work on swelling — the second, on creep damage accumulation.

The first part develops a model for pressure-driven diffusional dedensification (or swelling) in a polycrystal containing isolated pores. The model is sufficiently general to be directly applicable also to pressure sintering. It is tested against experimental data for hot-pressed alumina (HPA) which swells during high-temperature, pressureless anneals in air.

The model includes two independent, coupled, pore growth rate components: (1) diffusional (de)densification, driven by gas pressures in closed pores, and (2) coalescence of pores attached to grain boundaries, driven by grain growth against pore drag. Internal pore pressures may be due to inert trapped gas or to gas generated by chemical reactions.

In a polycrystal with *inert* trapped gas, the trapped gas drives early swelling, but is self-dissipating. Pore coalescence, by progressively releasing capillarity constraint, becomes the dominant cause of swelling at longer times.

The model predicts what magnitudes of chemically-generated pore

pressures will increase swelling rates beyond those arising from inert trapped gas alone. And, for research on creep damage accumulation, it predicts what precreep anneals are required to dissipate an initial trapped-gas pore pressure, and the range of distinct, *pre*damaged porous microstructures available.

The second part of the thesis presents experimental data from flexural and uniaxial tensile creep tests. The data demonstrate that HPA's cavitation damage tolerance and failure strains are high enough that creep fracture tests should be done in uniaxial tension, rather than in bending. A high temperature tensile test system, with optical extensometry, was designed, built and tested. The uniaxial tensile data suggest design improvements for testing ductile ceramics.

The combined mechanical and microstructural data indicate that, at 1250 C, failures at high stress are controlled by slow crack growth from microstructural heterogeneities. An abrupt transition at about 200 MPa separates rapid failures from failures at strains on the order of 0.1. At about 50 MPa, a more gradual transition occurs, to fracture at higher strains, controlled by strain-driven damage. The internal microstructural data show internal creep damage at levels at which cavity coalescence generates macrocracks in HPA.

TABLE OF CONTENTS

Appendices

Figures

B — Creep and creep damage accumulation

Appendices

Tables

Acknowledgments

Many people contributed with skill and care to this project. Warm thanks to Li Shujie, for generating immersion and damage data on swelled and crept specimens; Marg Chadwick, for preparing foils for and operating the TEM; Ed McCaffery, for designing, building and maintaining test and computer components and systems; Tom Bryner, for rock-solid photographic work; Frank Zok, for guidance on immersion density systems; and members of Engineering and Instrument Machine Shops — in particular Michael Roberts, Gino Innocente and Grant McCabe.

This report was written entirely in 'ChiWriter' from Horstmann Software Design, San Jose CA, (408)298-0828. Plots were generated on a DEC PDP-11/VT240, using 'DrawGraph', a custom package written by Ed McCaffery.

Part A

Swelling in hot-pressed alumina

1 Introduction

This introduction first sketches the origins and results of the swelling work. It then briefly reviews the literature for sintering and swelling, and ends by listing the research objectives.

1.1 Overview: origins and results

In this report, we develop a general model for pressure-driven densification or *de*densification in final-stage polycrystals,[1] and test the model against experimental data for swelling in hot-pressed alumina (HPA). The problem arose while we were studying creep cavitation and creep fracture, using HPA as a model structural ceramic (Robertson and Wilkinson, 1986). During creep tests in air, *unstressed* controls swelled uniformly.[2] The swelling had several implications for creep fracture research —

[1] That is, polycrystals with discontinuous (closed) intergranular pores.

[2] Internal porosities in the center of a given sample were comparable to those near its external surfaces.

some positive, some negative. No existing swelling model could explain why, when swelling kinetics were examined in more detail in subsequent experimental work, swelling was linear in grain size. Accordingly, we sought to develop a model capable of giving general answers to three related issues:

1) How to distinguish, experimentally, two types of swelling: that driven by high-pressure *inert* gas, which had been trapped in intergranular pores during hot-pressing, from that due to ongoing, gas-generating chemical reactions. This was important to the two subsequent issues:

Using pre-creep heat treatments:

2) How to reduce internal pore pressures, which might otherwise bias *stress*-driven cavitation in creep fracture tests, and

3) How to generate a range of distinct *pre*damaged microstructures.

Given the predamage/creep fracture context for the work, the swelling model currently applies only to a final-stage

microstructure.[3] However, it is sufficiently general that it also can describe final-stage *pressure sintering*, and so it makes it possible to add grain growth-driven pore coalescence to pressure sintering (HIP) maps (Helle et al., 1985). For severe swelling, the model could be extended to include pore channel development and gas release. It could also be extended to *intermediate* stage pressure sintering, which would permit adding an intermediate stage, with grain growth-driven coalescence, to HIP maps.

Because our swelling data showed that pore growth and grain growth are closely linked, we include grain growth-driven pore coalescence quantitatively in the model. This coalescence affects the diffusional pore growth rate via the capillarity component of pore pressure. We used the pressure*less*, final-stage *sintering* model of Yan, Cannon and Chowdry (1980) as a framework for our pressure swelling model, because their approach is both physically satisfying and readily tested experimentally, and has been used in a number of recent sintering studies (Yan et al., 1983; Occhionero, 1984; Handwerker et al., 1984; Berry and Harmer, 1986; Zhao and Harmer, 1988a). We replaced their pressure*less* diffusional pore growth model with a pressure-driven model (Wilkinson, 1978), which we extended to permit pore gas mixtures to consist of inert gases, as well as gases generated by

---

[3] That is, to *early* swelling in polycrystals which have been pressure sintered nearly to theoretical density.

ongoing chemical reactions.

Our experimental data demonstrated that the pore coalescence rate modeled by Yan, Cannon and Chowdry (1980) is a limiting case for one of three possible limiting microstructural paths — two of which bracketed our swelling data.[4] Our model extends their approach by dealing explicitly with all three limiting paths. We couple grain growth to coalescence via phenomenological pore drag, and express the drag directly in terms of the three microstructural trajectories, and a general grain boundary mobility which can be determined directly from grain growth data. We extend phenomenological equations for pore separation, expressing them in terms of the two bounding microstructural trajectories. Finally, we suggest how *non*-phenomenological[5] pore

---

[4] These paths are defined in terms of coalescence rates for intergranular pores, with respect to grain size. That is, they describe how rapidly the number of pores which are attached to grain boundaries decreases with grain growth. The three limiting coalescence rates are: constant number of pores (1) per unit volume, (2) per unit area grain boundary and (3) per grain. The current swelling data fell between the last two limiting paths.

[5] 'Phenomenological' pore drag/separation models are reviewed by Hsueh et al. (1982) and Handwerker et al. (1984). By '*non*-phenomenological' we refer to Hsueh et al.'s (1982) model, and to similar models by Spears and Evans (1982) and Hsueh and Evans (1983), which include mutual pore/grain boundary

separation predictions can be used within a phenomenological framework.

Given the creep fracture context within which we developed the swelling model, we generated experimental data at rather low temperatures and long times, relative to previous swelling work on hot-pressed aluminas (Table 1-1). The annealing schedules were chosen from preliminary swelling data to permit generating controlled, uniform creep predamage. The temperature range spanned 200 C above a lower limit at which minimal microstructural change occurred (1250 C).

1.2 Literature review

At the time the problem arose of HPA's swelling during creep, sintering models were better developed than swelling models. Accordingly, this review surveys three areas: sintering models (including pore drag and separation), swelling models and data, and cavitation creep fracture.

Variables are listed in section 1.4.

---

distortion (see Apps. 11,12).

1.2.1 Sintering and swelling: general

Sintering and swelling have many physical similarities. An evolving, porous polycrystal may progress smoothly from one to the other (Francois and Kingery, 1967; Gupta and Coble, 1968; Solomon and Hsu, 1980a). Closed pores may contain gases under pressure, either trapped by pore closure (ice: Wilkinson, 1978, Fig. 3-26) or generated internally after closure (Table 1-1). The pore pressures can inhibit final stage densification in sintering, and can cause swelling (Coble, 1962; Solomon and Hsu, 1980a). The pressure and stress driving forces for pore growth can be written in the form:[6]

$$DF = P_{int} - P_{cap}\{r(\psi), \gamma_s\} - g\{P_{app}\} \qquad (1)$$

in which the internal pressure, P_{int}, arises from the gas trapped in a pore, P_{cap} is the capillarity component due to pore surface curvature, and the applied external stress or pressure, P_{app}, often is modified by some function of the porosity (Coble, 1970; Vieira and Brook, 1984).

A closed pore may be out of equilibrium, and so may experience a

---

[6] Equations for driving force which include applied stress are given in section 1.2.5.1. In the third term on the RHS of Eq. (1), '$g\{x\}$' denotes a function of x.

net driving force for growth or shrinkage, as a result of (Gupta, 1971; Solomon and Hsu, 1980b; Haroun and El-Masry, 1981; Howlett and Brook, 1984):

1. Temperature changes, which alter pore pressure, gas solubility or surface adsorption equilibria (Rice, 1969).
2. Temperature or atmosphere changes which affect internal gas-generating reactions, such as O_2 attack on dissolved C or S impurities (Raj, 1982; Shewmon et al., 1983; Bennison and Harmer, 1985a).
3. Changes in external stress or pressure (e.g. a pressureless anneal after HP or HIP; Solomon and Hsu, 1980b).
4. Gas release to the exterior, after extensive swelling (Solomon and Hsu, 1980b; Rest, 1986; Gruber, 1986).
5. Ostwald ripening[7] of pores by lattice, pipe or boundary diffusion (Greenwood and Boltax, 1962; Masuda and Watanabe, 1980; Kuczynski, 1982; Randle et al., 1986, Kingery and Francois, 1967).

---

[7] While Ostwald ripening occasionally has been called 'coalescence' (Table 1-1), in this work we refer to it only as 'ripening' or 'coarsening'.

6. Pore coalescence:[8]

6.1. For pores in a crystal lattice, distant from dislocations and grain boundaries, coalescence due to:

a) pore growth without motion (Greenwood and Boltax, 1962).

b) pore motion (by surface, lattice and vapor diffusion; Nichols, 1972a).

i) Unbiased, random 'Brownian' pore migration (Gruber, 1967).

ii) pore migration biased by, for example, thermal gradients (Gruber, 1967).

6.2. For pores attached to dislocations or grain boundaries, coalescence due to:

a) pore growth without motion (Gruber, 1986).

b) dislocation motion (Barnes, 1964).

c) grain boundary motion (e.g. Brook, 1976).

7. Nuclear radiation, generating excess vacancies and interstitials (e.g. fission, decay, implantation; Solomon and Hsu, 1980b; Hsu and Solomon, 1983).

Save perhaps for monodisperse powder compacts — which lack the

---

[8] Outside of the current list, we reserve the term 'coalescence' for the collision and fusion of intergranular pores, driven by grain growth.

grain size dispersion which drives grain growth (Wong and Pask, 1979) — grain growth tends to occur during both intermediate- and final-stage sintering, and during swelling. When pores attached to sweeping grain boundaries coalesce, the coalescence affects (de)densification through (a) changes in P_{cap}, and so in the net driving force for pore growth, at each coalescence event (Nichols, 1969), and (b) pore drag, which is sensitive to pore size, and which couples pore coalescence rates to grain growth rates (section 1.2.4, below). In addition, pores which separate from grain boundaries grow more slowly than those which remain attached to boundaries (section 1.2.4). Consequently, grain growth with pore coalescence, and pore drag and separation are key components in sintering and swelling models.

1.2.2 Pore coalescence in sintering

Grain growth-driven pore coalescence has been modeled more thoroughly for intermediate- and final-stage sintering than for swelling. Sintering coalescence has been reviewed by Beeré (1976), Exner and Petzow (1980: 'EP'), Yan, Cannon and Chowdry (1980: 'YCC') and Occhionero (1984). Here, we briefly summarize and extend their conclusions.

Early models either do not include grain growth, or do not couple grain to pore growth. Coble (1961), Eadie and Weatherly (1975)

and Beeré (1975b) use cubic grain growth relations which are independent of diffusional pressure*less* densification, but do not explicitly include pore coalescence. Coble (1970) includes no grain growth in his pressure sintering model. Johnson's (1970) stereologically-based model includes no porosity in its time-dependent microstructural evolution equations, so cannot be integrated (EP).

Later models have been criticized for different reasons. Rosolowski and Greskovitch (1975) base their model on a partial, rather than a total derivative of pore size (YCC). Ikegami et al. (1978) assume too simple a {pore surface area/density} relation, which fixed the {grain size/ density} relation (YCC). Kuczynski's (1982) statistical sintering theory includes pore growth in intermediate and final stages, and could be integrated with a phenomenological grain growth relation (Occhionero and Halloran, 1984); however, Occhionero (1984) questions one of its key assumptions.

Wilkinson's (1978) pressure sintering model includes no coalescence.[9] Recent HIP maps are based in part on his work, and

---

[9] Wilkinson (1978) notes Nichols' (see Nichols, 1972a,b) and Brook's (1969) phenomenological models for pore drag, but, because of uncertain matrix boundary mobility and global boundary driving pressure, includes no grain growth in

include neither grain growth-driven coalescence nor an intermediate stage (Arzt et al., 1983; Helle et al., 1985).

The most successful of recent pressureless sintering models describes a final stage microstructure with a simple geometric model, and, by simple physical arguments, generates equations describing simultaneous pore and grain growth. Yan, Cannon and Chowdry 's (1980) original final stage model has been applied by Berry and Harmer (1986) to sintering in $MgO-Al_2O_3$. It has been modified for both boundary mobility controlled by solute drag, and grain size distributions by Yan et al. (1983) and Handwerker et al. (1984). It has been extended to handle pore size distributions by Zhao and Harmer (1988a). Occhionero (1984) modified the original model to intermediate-stage sintering.

1.2.3 Swelling models and data

As suggested by section 1.2.1, many different factors can cause materials to swell. In Table 1-1, we summarize the work most relevant to swelling in HPA.

Solomon and Hsu (1980b), Haroun and El-Masry (1981), Howlett and

---

pressure sintering models and maps. He develops only a final-stage model for diffusional pore growth.

Brook (1984) and Bennison and Harmer (1985a) surveyed swelling data and models, with Solomon and Hsu (1980b) showing clearly the similarities between models for pore growth in sintering, swelling, and cavity growth in creep fracture.

Swelling in a hot-pressed polycrystal likely is driven by pressurized pore gas, and often occurs at sufficiently high temperatures that grain growth occurs at the same time. However, no swelling models include grain growth-driven coalescence.[10] That is, neither those models reported prior to Yan (1981) referring to Yan et al.'s (1980) *un*published sintering analysis, nor more recent ones (e.g. Hsu and Solomon, 1983; Howlett and Brook, 1984; Bennison and Harmer, 1985a) describe simultaneous growth of grains and intergranular pores. (And, as noted above, recent pressure *sintering* models do not include coalescence.)

In developing the current swelling model, we began by replacing the diffusional pore growth component of Yan et al.'s (1980) pressure*less* sintering model with Wilkinson's (1978) final stage, pressure-driven pore growth model. This foundation then was

---

[10] Rest's (1986) model for swelling in nuclear fuels contains *intra- and inter*granular pore coalescence. It was not used in the current work, because Yan et al. (1980) offered a simpler framework for developing a swelling model, and one which was more directly related to the pressure sintering by which the HPAs had been fabricated.

extended in directions suggested by the experimental swelling data.

Table 1-1: Survey of swelling in ceramics.

Material	T [C]	Atmosphere	Mechanism	Ref.*
Al_2O_3	1900	H_2, O_2	• Trapped gas (N_2?) • Ostwald coarsening?	1
Al_2O_3	1090-1315	air(HP)	• trapped H_2O, CO, H_2S	2
Al_2O_3	1600	air, vacuum	• O_2 attack on dissolved C, S impurities	3
Al_2O_3	1250-1450	air	• trapped HP gas • coalescence	This work.
CaO	970-1205	air(HP)	• trapped H_2O, CO_x	2
CoO-(In_2O_3)	1250	air	• trapped HP gas • C residue oxidation?	4
Fe_2O_3	1000-1200	air	• trapped HP gas • Ostwald coarsening?	5
MgO	1450-1650	air	• trapped N_2 • Cl, OH residues • coalescence?	6
MgO	970-1315	air(HP)	• trapped H_2O, CO_x	7
Ni	1100	He	• trapped inert HP gas	8
ThO_2 (CaO)-ThO_2	1800	air, vac.	• C, S oxidation • coalescence?	9

UO_2	1700	H_2/H_2O	• C oxidation	10
UO_2	16-1800	H_2	• binder decomposition	11
ZnO	1350, 1400	air, O_2	• trapped, inert gas • organics decomposition • Ostwald coarsening?	12
ZnO	920-1120	Ar	• trapped inert HIP gas	13

Notes:

- In some cases, Ostwald ripening was called 'coalescence'.
- Modified from Table 1 in Bennison and Harmer (1985a).
- Excludes nuclear fuel swelling due to radiation effects (see section 1.2.1).
- Exclusively ceramic materials, except Ni (Ref. 8).
- Includes density loss in final-stage sintering.
- Question marks denote a postulated mechanism, or one in which the supporting analysis is incomplete.

* References in Table 1-1

1 Warman and Budworth (1967)

2 Rice (1969)

3 Bennison and Harmer (1983b, 1985a)

4 Howlett and Brook (1984)

5 Crouch and Pascoe (1972)

6 Gupta (1971)

7 Haroun and El-Masry (1981)

8 Hsu and Solomon (1983)

9 Morgan et al. (1976)

10 Francois and Kingery (1967)

11 Amato and Columbo (1964)

12 Gupta and Coble (1968)

13 Solomon and Hsu (1980a)

1.2.4 Grain growth with pore drag and separation

The simplest useful relation expresses *normal* grain growth rates in a *pore-free* polycrystal as a function only of mean grain size, and the mean energy and mobility of the boundary (Yan et al., 1977).[11] Such a relation requires a global proportionality constant (Wilkinson, 1978) related to the dispersion in grain size. Approximate values for this constant are available, but no satisfying derivation has been reported (Yan et al., 1977; Zhao and Harmer, 1988a,b).[12] Also, it requires a value for the

[11] Recent reviews of grain growth are given by Abbruzzese and Lucke (1986) and Randle et al. (1986).

[12] Explicitly *excluding* the grain size distribution and texture from such a grain growth relation implies that these parameters have 'typical' values for normal grain growth (Wong and Pask, 1979; Abbruzzese and Lucke, 1986; Yan et al., 1983).

intrinsic boundary mobility, for which, typically, few data are available (Yan et al., 1977).[13]

Pores are energetically favored to remain attached to sweeping boundaries during grain growth (Hsueh et al., 1982). While they remain attached, pores and their local grain boundary regions distort interactively (Hsueh et al., 1982). The boundary distortion reduces the mean boundary curvature and driving pressure, and the reduced grain growth rate is described as 'pore drag'.

Pores separate from two-grain-facet boundaries when the boundary maintains a sweep velocity greater than the maximum sustainable by the pore, for a long enough time (Hsueh et al., 1982). Once separated, such pores grow or shrink slowly, as rapid boundary diffusion is replaced by slower lattice diffusion, and diffusion distances increase.[14]

---

[13] Despite this, detailed physical forms for M_B have been used in sintering models (Yan et al., 1983; Handwerker et al., 1984). When grain growth occurs with pore drag, the lack of M_B data may be made less important by assuming *pore* drag control, Yan et al., 1980; Zhao and Harmer, 1988a.

[14] In principle, Ostwald ripening and various forms of intragranular coalescence also are possible for such pores (see Section 1.2.1).

*'Non*phenomenological' drag/separation models which include mutual pore/boundary distortion have been developed by Hsueh et al. (1982), Spears and Evans (1982), and Hsueh and Evans (1983). However, these apply to a small number of specific local pore/grain geometries (Handwerker et al., 1984).

Only phenomenological drag/separation models currently are applicable to *arbitrary* microstructures. These are derived from Zener drag calculations for *solid* second phase particles (e.g. Brook, 1976, Carpay, 1977). As noted by Hsueh et al. (1982), the approach assumes a fixed number of rigid, average spherical pores on an *isolated*[15] two-grain facet. Because it is rigid, the pore has a unique, temperature-dependent mobility (Hsueh et al., 1982),[16] which reflects several potential controlling mechanisms — surface diffusion, lattice diffusion or vapor diffusion/evaporation-condensation. The force exerted on the average pore by the sweeping boundary equals the drag force exerted by that pore on the boundary. The total drag from all the pores subtracts from the pore-free driving pressure on the unit area boundary to give a reduced, effective pressure (e.g. Carpay,

---

[15] The representative boundary area is considered in isolation from the network which defines the polycrystal's grain structure.

[16] Defined as mean pore velocity divided by mean boundary driving pressure (or force) per pore.

1977).[17]

In phenomenological models, grain boundary distortion is included only as a force-dependent boundary contact circle on the pore surface. The models do not distinguish between the three pore site types (two-grain facet, three-grain edge and four-grain junction). Pore coalescence is included as simple limiting cases[18] which have not been derived from experimental data.

Because of uncertainties and simplifications in models for matrix grain growth and phenomenological drag, the limited stereological data available for porous polycrystals, and the complicated geometry of polycrystals — porous or pore-free — it will be difficult to improve on the phenomenological models for either drag or separation.

---

[17] This is expressed as the product of an unmodified global driving pressure and a reduced, effective boundary mobility (Ch. 3).

[18] Constant number of pores per unit volume polycrystal or per grain (Brook, 1976; Carpay, 1977).

1.2.5 Internal pore pressures in cavitation creep fracture

Cavity growth in creep fracture can be enhanced by internal pore pressures. In this section, we survey models for such a bias, referring extensively to the single best review, Riedel (1987).[19]

Variables are listed in section 1.4.

1.2.5.1 General

Models for cavitation creep fracture in polycrystals describe either (1) cavities growing to coalescence on an oriented, representative two-grain facet (*growth/coalescence* models), or (2) damaged facets increasing in number density, and perhaps interacting mechanically, to form larger cracks capable of propagating by local tip cavitation (*damage accumulation* models). Cavity growth models are better supported by data than damage accumulation models. (We review damage accumulation in Ch. 9.)

Cavity growth models can be separated according to three issues: (1) cavity shape (equilibrium or crack-like), (2) cavity configuration (arrays or single cavities) and (3) constraint.

---

[19] Ashby and Brown (1983), Evans (1984) and Riedel (1987) are key references in creep fracture. Ashby and Dyson (1984) survey a wider range of high temperature damage mechanisms.

Array cavitation is typical of diffusional creep in structural metals (Riedel, 1987, Chs. 11,12; Cocks and Ashby, 1982). On the other hand, single-cavity models are more appropriate to the only structural ceramic for which detailed cavitation data have been generated: hot-pressed alumina (HPA; e.g. Porter et al., 1981).

Unconstrained cavity growth models include both bicrystal models and the high strain rate limit for *constrained* growth. *Constrained* polycrystal/cage models describe the low strain rate limit for spatially *in*homogeneous cavitating facets.

1.2.5.2 Unconstrained creep cavity growth

For unconstrained cavity growth on two-grain facets, there are two limiting-case growth modes: quasi-equilibrium (*QE*) and crack-like (*CL*). Typically, growth models assume that cavities occur in a regular *array* across a representative facet; however, the same models have been used for the single/lateral growth mode discussed below (see section 1.2.5.4).[20]

Davanas and Solomon (1986) summarize how an internal pore pressure, P_{int}, would bias unconstrained cavity growth rates. Given a net applied stress normal to a two-grain facet, σ_{∞}^{net}, the

---

[20] Most models assume *regular* cavity arrays; recent work permits non-regular arrays (clustered or random; Wilkinson, 1988; Fairborz et al., 1985).

driving force for cavity growth is:

$$\underline{QE}: \quad DF \propto \left(\sigma_{\infty}^{net} + P_{int} - g\{P_{cap}\} \right) \qquad (2a,b)$$

$\underline{CL}$:

$$DF \propto \left\{ \left[1 + g\{P_{cap}, f\} \left(\sigma_{\infty}^{net} + P_{int} - g\{P_{cap}\} \right) \right]^{1/2} - 1 \right\}^{3}$$

The form of the full equations (e.g. the function for capillarity constraint, $g\{P_{cap}\}$) varies depending on whether a cylindrical or an axisymmetric cavity is being modelled.[21]

Riedel (1987, p.169-70, 182-5) summarizes experimental results for creep fracture in structural metals, in which test specimens were *pre*damaged (with H_2O bubbles or by prestraining) in order to eliminate continuous cavity nucleation. Experiments with precavitated *model* metals (Cu, Ag or Ag-(MgO)) were consistent with unconstrained diffusional growth models, whereas experiments with precavitated *commercial* metals (Nimonic 80A, Inconel X-750,

---

[21] Boundary and surface *diffusion* controlled cavity growth is sensitive largely to the component of applied stress which is *normal* to the cavitating representative facet. Grain boundary sliding makes diffusion-controlled cavity growth somewhat sensitive to transverse stress components (Cocks and Ashby, 1982, pp.31ff). For *dislocation* creep controlled cavity growth, however, the *effective* stress is important (Cocks and Ashby, 1982, p.13, 40).

α-brass) were consistent with constrained diffusional models.[22]

1.2.5.3 Constrained cavity growth

When only *some* of the available oriented facets in a polycrystal are cavitated, the deforming, damage-free polycrystalline 'cage' surrounding a cavitating facet (or multi-facet damage zone) may constrain cavity growth rates, on that facet, to be proportional to the macroscopic creep rate in the cage (Riedel, 1987, Ch.12). Such constraint develops at *low* macroscopic strain rates — at sufficiently high remote strain rates, cavity growth in such a system is *un*constrained. The transition is predicted in models by requiring the local strain rate within the damage zone[23] to be compatible with that in its creep-viscous cage. Under constraint, the average normal stress on the facet or zone is less than the far-field stress, while the cage sustains a stress higher than the remote stress.

Constrained cavity growth has been modeled for several simple damage distributions: (1) homogeneously distributed single facets, of arbitrary number density, each damaging via an array of growing cavities (Cocks and Ashby, 1982, pp.47ff);

---

[22] Experiments tested the dependence of failure times on stress or cavity separation.

[23] The grain pair above and below the cavitating facet, for single-facet cases.

(2) *isolated* single facets, each damaging via a similar array of cavities (Riedel, 1987, pp.172ff); and (3) isolated, *multi*-facet damage zones, on each facet of which a *single* cylindrical cavity grows laterally from a three grain edge, and the zone spreads laterally by cavitation in the stress-enhanced region at its periphery (Hsueh and Evans, 1981). Riedel (1987, p.185-97) reviews other studies in which facet-facet interactions were estimated. Such interaction increases constrained cavity growth rates, particularly if grain boundaries slide.

Such models build from standard *un*constrained cavity growth models, which can be expected to be of the form of Eq. (2). However, no general analysis has been presented for the effect of a P_{int} in constrained cavity growth.[6]

A constrained cavitating facet behaves mechanically like a low-traction microcrack, from an early stage in cavitation (Riedel, 1987, p.181-2). So, although data for failure times in precavitated commercial metals fit this growth model, coalescence on such an unloaded facet is likely to be of less physical significance in creep fracture than is facet-facet interaction

---

[6] While an internal pressure remains high, the driving force for cavity growth will be increased, while that for creep will not be. The transition to constrained cavitation will be shifted to lower remote stress levels.

and microcrack linking, or continuous cavity nucleation on undamaged facets (Riedel, 1987, p.181-2). This implies that damage accumulation, and not cavity coalescence, controls lifetimes.

In creeping alumina, cavities do *not* grow in arrays. Instead, individual four-grain junction pores nucleate on loading, propagate rapidly down three-grain edges to become cylindrical, and then grow more slowly across oriented two-grain facets (e.g. Porter et al., 1981). In Hsueh and Evans' (1981) model for cavity growth in HPA, in constrained, multi-facet damage zones, load-shedding from a damage zone causes enhanced cavity growth in the highly stressed peripheral region, and so the zone spreads laterally. Macroscopic failure is not addressed.

Because Hsueh and Evans (1981) base their model on standard growth equations for cylindrical cavities in arrays, a P_{int} should bias such a model by adding linearly into the driving force for pore growth (Eq. 2). However, as noted above, no general analysis currently is available for internal pore pressures in constrained damage zones.

1.2.5.4 Continuous nucleation

Continuous nucleation of *QE* or *CL*[25] cavities is brought into models for *un*constrained array cavity growth as a decreasing mean cavity spacing. Either experimental nucleation rates ($J^{\bullet} \propto \dot{\varepsilon}_{\infty}$) or theoretical vacancy condensation models are used (Riedel, 1987, Ch.16). For vacancy condensation, assuming that an equilibrium gas pressure is established within subcritical vacancy clusters, an internal pore pressure affects nucleation as a tensile stress does, and ($\sigma + P_{int}$) replaces σ in nucleation equations (Riedel, 1987, p.131).

It is more difficult to incorporate cavity nucleation into *constrained* array growth models. The time to constrained cavity coalescence should not be a strong function of nucleation kinetics (Riedel, 1987, p.246). However, it is physically unlikely that nucleation would continue on an *already*-cavitating facet, as such a facet is subject to low tractions (Riedel, 1987, p.231). The alternative — that cavities nucleate on *new* facets — is noted by Riedel (1987, p.194-7), but he presents no data. This is a closer to a damage accumulation than a cavity growth approach.

*Pre*damage experiments aim to eliminate continuous nucleation from

---

[25] *CL from nucleation;* i.e. no *QE*-to-*CL* transition is modeled.

subsequent creep cavitation, and so to permit cavity *growth* models to be tested directly. In metals, H_2O bubbles and strain predamage on grain boundaries have been used (e.g. Riedel, 1987, p.169-70,182-5). It is possible that residual porosity from sintering, or porosity generated by swelling in HPA, could be used in a similar way for creep fracture studies in ceramics.

1.3 Objectives of the current work

1. To develop a general model for swelling due to gas trapped at high pressures in pores, in a final-stage, pressure-sintered polycrystal, in which grain growth is occuring.

2. To test the model with swelling data for two HPAs which swelled at very different rates.

3. Based on numerical solutions to the swelling model, to consider how to distinguish, using experimental data, (1) swelling driven by pore pressures maintained by internal gas-generating reactions from (2) swelling driven by a constant number of moles of (inert) trapped gas.

4. To determine the magnitudes of chemically maintained pore pressures which, in numerical swelling simulations, (1) will *just* enhance swelling rates above those for 'inert' gas, and

(2) will cause rapid, 'runaway' swelling. To compare these pressures with equilibrium thermochemical pore pressures for carbon or sulfur oxidation, when the pore oxygen involved (1) is liberated by dissociation of the doped aluminas at high temperature, or (2) is at the partial pressure of the external furnace atmosphere.

5. To determine the range of unique predamaged microstructures which could be generated by swelling, for purposes of testing creep damage accumulation models in creep fracture studies (in which the predamage is intended to eliminate continuous creep cavity nucleation).

6. To determine the rate at which trapped gas pore pressures could be dissipated at high temperature, in order not to enhance cavity growth in either creep service or creep fracture studies.

1.4 Variables

DF driving force for cavity growth; [N/m^2]

$\dot{\varepsilon}_e^{\infty}$ macroscopic, equivalent strain rate; [s^{-1}]

f the area fraction of oriented two-grain facet that is cavitated; [-]

$g(x)$ function of x

γ_s pore surface energy; [J/m^2]

J^* nucleation rate on two-grain facets; [s^{-1}]

P_{app} applied, external hydrostatic pressure; [N/m^2]

P_{cap} sintering stress for a two-grain facet cavity; [N/m^2]

P_{int} internal pore pressure due to trapped gas; [N/m^2]

ψ pore dihedral angle; [deg] or [rad]

r pore radius; [m]

σ_∞^{net} net far-field applied stress; [N/m^2]

σ_e^∞ applied equivalent stress; [N/m^2]

σ_b average normal stress on a cavitating model two-grain facet; [N/m^2]

σ_I^∞ applied stress component, normal to cavitating facet; [N/m^2]

2 Experimental: Swelling

This section describes the materials and experimental methods for the swelling tests.

2.1 Materials

Two commercial, hot-pressed aluminas were studied (Table 2-1a). The as-received materials were analyzed for dopants and impurities by combustion and X-ray fluorescence (Table 2-1b).

2.2 Annealing tests

Specimens about 5 x 5 x 10 mm were sawn from billet stock away from the 'rind'[1] (Table 2-2 and section 2.2.1, below). They were neither ground nor lapped before being annealed.

Sets of 5-6 specimens were annealed in static air in a 99.8%

[1] By 'rind' we mean the surface layer of the billet which was altered by contact with or proximity to the graphite hot-pressing die and punches.

alumina (McDanel 'AD998') tube furnace, following schedules given in Table 2-3. High-quality alumina ceramics were used with the control thermocouple; the thermocouple wire was replaced frequently (Bently, 1981; Froschauer and Schmidt, 1977).[2] The specimens were stood on end on a 99+% Al_2O_3 shim, which was supported by a high-alumina fiber carrier block (Zircar 'SALI'). The temperature range over the 30-40 mm length of a specimen set was on the order of 3-5 C.[3] Periodically, a specimen was withdrawn slowly from the hot zone.

Immersion density changes were determined with a precision

---

[2] Frequent prophylactic renewal of the hottest 5-10 cm of a high-T, Pt-based thermocouple can be reasonably economic. A new thermocouple, some 30-100+ cm longer than the minimum length necessary, is installed with the *extra* wire coiled outside the furnace wall. Renewing the hot junction means removing only the hot 5-10 cm (for furnaces similar in size to those used here), and not the entire ≈ 30 cm length of a typical thermocouple.

[3] The furnace's type B *control* thermocouple was outside the alumina tube which held the specimens during an anneal; however, the temperature to which the controller was set (the 'setpoint') was determined by inserting a B thermocouple temporarily into the hot zone, from one end of the tube. This test thermocouple was inserted through a small hole in the radiation plug at one end of the hot zone, when the furnace was at the nominal operating temperature. In this work, setpoint temperatures were 15-25 C higher than the internal tube temperatures. Annealing temperatures given are the internal tube temperatures.

balance (Sartorius R160P; reproducible to $2(10^{-5})$ g and linear to $3(10^{-5})$ g in the weighing range 0-30 g) after Ratcliffe (1965). The absolute density of the immersion liquid — diethyl phthalate (99%; Aldrich D 9,962-5) — was determined by pycnometer, and the temperature dependence of its density by hydrometer (Canlab H 8770-3; ASTM 113H; Sp. Gr. range 1.100-1.150, subdivisions 0.0005). *Relative* uncertainties in calculated density changes were typically less than 0.001.[4]

Specimens were sectioned internally by diamond sawing (Table 2-2). They then were polished through a 20 to 0.25 μm diamond paste sequence (Table 2-4, and section 2.3, below), and were cleaned and thermally etched (Table 2-5, and section 2.4). Etched specimens were mounted for SEM and were coated with gold (section 2.5).

Pore number density, N_A, and grain size, (as mean linear intercept, $\bar{L}_2$), were determined on internal polish planes from a set of about four SEM micrographs per specimen, taken at widely-spaced locations,[5] at magnifications of 2500X for small

---

[4] The relative uncertainty varied inversely with the magnitude of the change in absolute density (see error bars in Fig. 4-2).

[5] Chosen to have typical microstructures.

$\bar{L}_2$, and 1250X for large $\bar{L}_2$.[6] A typical micrograph contained 40 to 50 pores and 200 to 600 grains on the polish plane. Grain boundary intercept counts were made on five traces per micrograph: one on each corner-to-corner diagonal; and three horizontal, parallel to the long dimension of a micrograph, at top, center and bottom of the print.

2.3 Metallography

Metallographic techniques were developed for both swelled and crept specimens. Particularly for the crept specimens, in which near-surface cavitation was of interest, it was important to maintain a flat polish plane right up to the edge of the specimen (i.e. to minimize edge rounding) and to minimize pullouts not only on the polish plane, but also at the sharp edges between this plane and the external surface of a specimen.

The polishing schedule is described in Table 2-4.

Annealed chips were sectioned transversely while hot-waxed to a ceramic plate, which was secured to a wafering saw (Table 2-2). Chips were cleaned in acetone, and were labelled on one face with

---

[6] That is, in specimens annealed for long times at high temperatures.

a 0.3 mm technical pencil.[7]

Internal sections were polished as follows. Up to four at a time were hot-waxed onto the flat ends of 19 - 25 mm diameter x 25 mm long steel cylinders ('plugs') which served as both heat sinks and handles during lapping. Specimens of about the same thickness were mounted on a plug, in order to simplify grinding.

A shallow 'dam' was made around and above the waxed end of each plug, by wrapping around it a length of masking tape. The dam height matched the thickness of the specimens waxed to the plug's end. The plug was heated to somewhat hotter than could be held by hand, and freshly-mixed five-minute epoxy was added around the chips, until the epoxy between the chips bulged somewhat above the chip faces. (In order to simplify cleaning between polishing steps, and so to minimize contaminating cloths with coarse debris from the previous stage, *as few bubbles as possible* were introduced into the epoxy during mixing and while filling the dam.) Once the epoxy had set, the tape was removed from each plug, and the set of plugs was then baked at 50-60 C for 15 m to harden the epoxy. (The harder the epoxy, the fewer potential complications in subsequent polishing.)

---

[7] This face would not be polished, and the pencil label would last until thermal etching.

After plugs were cool, a water-cooled belt sander (with SiC paper) was used, carefully, to bring the level of the epoxy back to the plane of the faces of the embedded Al_2O_3 chips. Also, the circular outer edge of the epoxy pad was beveled rather deeply, to minimize subsequent damage to polishing cloths. (The epoxy bed protected the cloths from the sharp edges of the chips which develop during polishing; the bevel prevented the epoxy from developing a sharp outer edge.) Plugs then were scrubbed gently with a toothbrush and liquid detergent (Liquinox), under flowing water, to remove SiC particles.

Subsequent polishing, through to 0.25 μm diamond, began on a Struers Planopol/Pedemax polisher, and finished on a Buehler polisher.[8] The stage at which the specimens were transferred between polishers varied with the success of the polishing run. For the Struers polisher, a company-recommended schedule was followed (Table 2-4).

While the entire polishing sequence *could* be done by hand, the *flattest* epoxy/ceramic faces were generated by mounting at least three plugs (with embedded specimens) equidistantly in the

---

[8] The Struers unit had a 150/300 rpm polishing head drive, used with adhesive-backed cloths on lift-off wheelheads. The speed and load on its motorized specimen head were variable; the head took a multi-specimen holder.

specimen holder of the Struers Planopol/Pedemax (several dummy plugs, each with an embedded, scrap HPA chip, were kept on hand for cases when only 1 or 2 specimens had to be polished). The set was then polished, as a unit, to 3 μm diamond paste, without removing any specimens from the holder (Table 2-4).

Struers lapping was never carried on to diamond finer than 3 μm. In order to monitor closely the developing polish on the tensile surface, final lapping was done on benchmount wheels (Buehler 'Whirlamet') which were located close to optical microscopes. Throughout these final stages, specimens were held manually by their plugs. The Buehler system had lift-off wheelheads, onto which adhesive-backed cloths were mounted. Fresh cloths were charged with about 0.75 g of diamond paste. A cloth that cut slowly had more paste added to it. Periodically, polishing oil was removed from the polished surface by gentle scrubbing with liquid soap and water, and the surface was examined with a reflected light microscope.[9] Final polishing proceeded from 3, through 1, to 0.25 μm pastes. A longitudinal finish could have been generated, but Blanchard lapping gave a better surface

---

[9] Whenever specimen/plugs were cleaned (ultrasonically between stages, or by brushing only for progress checks), *only* soap and water were used; solvents such as acetone and methanol removed polishing oil, but softened the surface of the epoxy, after which it smeared over specimens in subsequent polishing.

finish. (A Blanchard pattern was generated by moving each specimen, by its plug, slowly around the polishing wheel, by hand, against the direction of motion.)

When all chips on a plug were polished, the plug was heated on a hotplate. In a temperature range just below that where the wax softened, the epoxy became rubbery, and easily could be cut and peeled away from the chips with a fine pair of tweezers. Soon after, as heating continued, the chips could be lifted clear.[10] They then were washed ultrasonically in several changes of glass-distilled acetone, followed by several of HPLC-grade methanol.

Achieving sharp — non-rounded — polished *edges* on a specimen was far from routine. It depended on several factors. It was important to have a hard epoxy bed[11] (with minimal hot-wax

---

[10] Once the chips had been lifted clear of the hot plugs, they were handled with *plastic* tweezers only. Metal tweezers can leave marks on the polished face of a specimen, and easily can chip the sharp polished edge between the tensile face and the internal polish plane, during the many subsequent washing stages. This chipping occurs when a specimen is picked up so that such an edge contacts the arm(s) of a pair of metal tweezers at an angle, and the tweezers are squeezed — even gently. It is surprisingly easy to generate such damage.

[11] Embedding is not yet optimized. Five-minute epoxy seems to harden if left overnight. We have not tried adding alumina

interface, when wax was used as a release agent on a fracture surface). Also, *a rapid* polish cycle seemed necessary, which could be generated by minimizing the area of ceramic to be polished per plug; using fresh, 'hard', *adhesive-backed* cloths; and charging cloths *generously* with diamond paste.A cloth which became contaminated and began to introduce scratches, or which 'wore out' and failed to support *rapid* polishing with a fresh charge of paste, was discarded.

2.4 Thermal etching

The etching schedules are given in Table 2-5. Because the etching furnace was shared with other users, some time typically passed between polishing and etching a specimen. Dirt etched onto a polish plane was difficult to remove; the fail-safe procedure was adopted of washing *all* specimens before etching.[12]

Polished chips were washed ultrasonically in glass-distilled (GD) acetone, and then in HPLC-grade methanol. Polished faces were

---

powder to the epoxy to harden it. Such ceramic powders must not scratch the specimen surface during lapping.

[12] Before procedures were adopted to ensure clean specimens, such 'dirt' typically was detected as a 20-50 μm-wide band at one edge of the polish plane, on a gold-coated specimen, in the SEM. In such a band, grain boundaries and pores were hidden.

checked by optical microscope to ensure that absolutely no dirt was present. If any was found, it was removed with a fine swab consisting of cotton wool wrapped tightly around the tips of a pair of fine tweezers, moistened with HPLC methanol or GD acetone.

Freshly cleaned and inspected specimens were placed, polish planes up, in sets on a 10 x 20 x 40 mm carrier of refractory block insulation (Zircar; e.g. ZAL-15 or -30) from which loose fiber dust had been removed by a jet of compressed air. A lightweight, $MoSi_2$-heated, programmable box furnace (C&M Inc.) was preheated to some 25-40 C higher than the etch temperature, and was allowed to soak for 15 minutes. The furnace temperature was verified from the mV reading of a separate type B thermocouple. The furnace door then was opened for the minimum time necessary to load the carrier with its chips gently into the furnace. During loading, the furnace temperature fell abruptly to near the nominal etch temperature, and, when the door had been closed, the controller set point was adjusted manually, to hold the mV output of the monitoring thermocouple at a value corresponding to the desired etch temperature. Allowance was made for the cold junction (i.e. the voltmeter attached to the monitoring thermocouple's leads) not being at 0 C. The etching atmosphere was air.

When the etch time had elapsed, the furnace power was shut off,

and the carrier was immediately removed from the furnace. This was done carefully if several chips had been etched at one time on one carrier — no identification other than chip shape survived the etch. Chips were cooled, and were stored on a small card, using double-sided tape, in small zip-lock plastic bags.[13]

2.5 SEM

2.5.1 Mounting

A small vee was filed in the rim of each (numbered) SEM pin mount, to permit identifying coated specimens (in a set) in the SEM, and orienting them.[14]

Mounts and specimens were cleaned ultrasonically in GD acetone, and then HPLC methanol.[15] Specimens then were cemented to mounts with minimal, high quality, commercial colloidal silver. Specimen faces were rechecked for cleanliness with a low-power optical microscope, and were reswabbed if required. Once the solvent had evaporated from the cement, pin mounts were coated with Au or

---

[13] Residual tape adhesive was removed by acetone and methanol washes just before mounting for SEM.

[14] This was more important for *crept* specimens than for annealed (Chs. 9-14).

[15] These washes minimized organic contamination of the SEM column.

Au/Pd, and were stored in clean, dust-tight containers.

2.5.2 SEM microscopy

A Philips Model 515 SEM was used. Typical operating parameters were 15-20 kV, with a 50 nm diameter spot. (For magnifications above 5000, the spot size was reduced to 20 nm.) When surface relief was important (for example, on a fracture surface) or when it was necessary to suppress enhanced secondary electron (*se*) emission from cavity rims on the polish plane[16] the positive bias of the *se* detector was reduced.

In some cases, EDS spectra were taken from spots, using standard procedures.

2.6 TEM

HPA slices about 1 x 5 x 5 mm were ground on one side with a 20 μm, resin-bonded diamond plate (Struers 'Planopol' 'Grasi'). Each slice was hot-waxed (Aremco 'Crystalbond'), ground side down, to a standard glass microscope slide, which previously had been abraded with coarse SiC paper to enhance adhesion. The wax was

---

[16] Or, for crept specimens, from crack edges on polish plane or specimen surface (Chs. 9-14).

allowed to 'set' overnight.[17] Then, the mounted slices were thinned to about 80-120 μm using a grinder with a 20 μm cup wheel, and a vacuum chuck with manual micrometer advance (Struers 'Discotom'). During this grinding, the total slide/chip thickness was monitored periodically with a micrometer.

Discs 3 mm diameter were cut ultrasonically (Gatan, Model 601) from the thinned slices. These were dimpled mechanically (Gatan, Model 656) with 15 and 6 μm diamond paste. No metal grids were used: the ceramic discs were self-supporting.

The dimpled disks then were perforated by ion thinning from both sides at a 12° incidence angle, using Ar gas at 4.0 mV and 0.7 mA (Gatan, Model 600). Foils were coated with carbon, and were examined by CTEM (Philips CM 12) at 120 kV with a single axis, ±30° tilting stage.

---

[17] After such setting, there was less chance that the chip would be swept off the slide in the final stages of thinning to 80-120 μm (M. Chadwick, personal communication).

Table 2-1a: Materials

	ARCO	AVCO
Manufacturer	ARCO Silag Operation Greer, SC	AVCO Systems Division Wilmington, MA
Date of manufacture:	mid '86	mid '83
Billet size	115ϕ x 13t+ mm (4.5ϕ x 0.5t+ in)	180ϕ x 30t+ mm (7.0ϕ x 1.0t+ in)
Supplied as	Full billets	Half-billets

Dimensioning abbreviations: ϕ, diameter; t, thick

Table 2-1b: Chemical analysis of as-received materials.

		ARCO	AVCO	Note
C	w/o	0.025	0.014	1
	ppm	250	140	
Fe_2O_3	ppm	90	130	2
K_2O		4	6	2
MgO		200	3000	2
MnO		3	2	2
S		16	17	2
SiO_2		200	140	2
TiO_2		< 5	< 5	2
Y		800	10	2
Zn		19	17	2

- Analyses were performed at McMaster University, by Mr. O. Mudroch.
- Note dopants and impurities reported as *oxides* vs those reported as *elements*.

Notes

(1) by combustion: LECO Carbon Determinator WR 12.

(2) by XRF: Phillips PW 1450 XRF analyzer.

Table 2-2: Sawing

Blade:	Type:	D1A1R, circular (see Note 1)
	Size:	Coarse (billet slicing): 5"ϕ x 0.025" (Note 2)
		Fine (cutting spec'n blanks from slices): 4"ϕ x 0.015"
	Diamond:	220 grit, 100 conc., metal bond
Speeds:	Spindle:	3600 rpm
	Leadscrew:	(Notes 3,4)
Depth of cut:	Slicing billets:	typ., $\leq$ 0.5" (Per pass)
	Cutting specimens from slices:	slice thickness (4-5 mm)
Coolant:	kerosene or commercial, water-based coolant.	

Notes:

1) Clamp saw blade between hub plates of maximum diameter possible for the cut.
2) Blade dimensions are given in the units used by their manufacturer.

3) Leadscrew feed rates were low, and were set by experience. For example, a 5 mm-thick slice was cut into specimens at about 50 mm per 10 min. In general, the saw was advanced at the fastest rate that still gave only minimal sparking from the blade. Advancing a thin blade too rapidly can cause the blade to wander off a straight cut, particularly if small-diameter hubs are used. Not only does this waste both test material and subsequent grinding time and tools, but it fatigues the metal web of the blade at the rim of the hub clamp plates, and so can destroy a blade quickly.
4) The direction of specimen/blade movement was chosen which maximized cooling *at the point at which the blade contacted the specimen.*

Table 2-3: Annealing schedules:

	Anneal times (h)	
T (C)	ARCO	AVCO
1450	5, 10, 21, 50, 100, 300	4, 12, 36, 100, 300
1400	5, 16, 48, 100, 200, 400	5, 16, 48, 100, 200, 400
1350	8, 24, 72, 200, 600	8, 24, 72, 200, 600
1250	10, 30, 100, 300, 600	—

Table 2-4: Polishing on the Struers Planopol/Pedemax[1]

Step	1	2	3	4,5[2]
Diamond	20μm embed.	6μm spray, paste	6μm paste	3, (1μm) paste
Wheel	resin (GRASI)	plastic (P'disc-M)	cloth[3]	cloth[3]
Planopol Speed (rpm)	150	150	150	150
Pressure[4]	3-4	4-5	3-5+	3-5+
Lubricant	blue (alcohol-based; Struers)		diamond-polishing oil	
Time (m)	1-2[5]	(6)	(7)	(7)

Notes:

1) The form of this table follows data sheets supplied by Struers. The information presented combines our polishing experience with their recommendations for Al_2O_3.

2) During stages from 3 to 0.25 μm, the developing polish should be checked frequently, using an optical microscope. See text and note (5) below.

3) Use 'hard' cloths (e.g. Struers 'DP-PLAN' or 'PAN-W'). For the flattest polished surfaces and edges, choose adhesive-backed, rather than oversized cloths which are intended to be clamped to the wheelhead by a metal band. It is unproductive to try to economize by using (and reusing) 'clamp-on' cloths, because (1) such cloths perform poorly in polishing large areas of Al_2O_3 evenly, (2) all cloths become contaminated rapidly during typical use, and subsequently scratch specimens, and (3) cloths gradually lose their ability to support a good polish: even if they are recharged, they wear out. (Of the Struers cloths used here, DP-PLAN seems somewhat more durable than PAN-W).

4) ..."marks", @ 50 N per mark, on the Pedemax head load scale.

5) This stage cut rapidly; care must be taken to check the specimens every 30s.

6) This stage was unpredictable! An HPA surface, roughly-ground with a 20 μm resin-bond plate, was prone to generalized, ongoing pullouts. The HPA surface eroded the surface *without* (or only slowly) developing an initial (6 μm) polish. Progress could be monitored easily, without removing specimens from the holder (and so losing their mutual alignment), by periodically checking by eye (window) light reflected off the tensile face. In cases where polishing progress was slow, recharging the

plastic (Petrodisc-M) wheelface sometimes helped. Otherwise, it was best to move directly to a 6 μm cloth.

7) Progress through intermediate polishing stages, when these were done on sets of specimens mounted on the Struers, could be monitored by removing the *entire* specimen holder from the head, and placing it carefully, on a paper mask, on the table of a low-power metallographic microscope which had optics beneath the table. In contrast, when specimens were polished from 3 μm on the Buehler unit, they were held individually by their plugs, and checks were best made with a metallographic microscope with a table beneath the optics. Before such a check by microscope, the polishing oil was removed from the specimen by scrubbing gently with toothbrush and liquid soap under running water, followed by drying with a moderate air jet or paper towel. Methanol or acetone remove the oil, but soften the embedding epoxy. They should not be used.

When a set of specimens was moved to the next finer diamond, the holder, carriers and specimens were carefully scrubbed with detergent and water to remove residual grit that otherwise would be carried over, contaminating the cloth at the next stage. When available, an ultrasonic bath large enough to permit the specimen holder disc to be submerged was used for such inter-stage cleaning.

Table 2-5: Thermal etching

Material	ARCO	AVCO
T [C]	1300	1600
t [min]	10.	2.75
Atmosphere	static air	static air

- Grain boundary grooving rates were noticeably slower in specimens annealed at high T for long times (Table 2-3).

3 Final-stage polycrystal swelling model: internally pressurized intergranular pores, with concurrent grain growth

3.1 Overview

Pressure-driven diffusional pore growth may cause a barely porous, hot-pressed (HP) polycrystal to swell during stress-free anneals. Such pore growth may result from (1) gas, trapped in intergranular pores during final-stage pressure sintering, now being at high pressure due to densification, (2) internal chemical reactions maintaining high gas pressures in pores over an extended period, and (3) capillarity constraint being released gradually by (a) grain growth sweeping intergranular pores together, or (b) the pore population coarsening by diffusional Ostwald ripening.[1]

In this section we develop a general model for swelling in an HP polycrystal which is nearly fully dense, whose pores are at four-grain junctions. The model includes the first three of the

[1] Additional possible mechanisms were outlined in the literature review.

above factors, in simplified form. We do not include an Ostwald ripening pore growth component.[2]

The following argument extends the pressureless sintering model of Yan et al. (1980) in three ways. First, we generalize pore coalescence to three limiting-case microstructural trajectories — a change called for by our experimental data. In the two of these which include coalescence, we permit pores to occupy an arbitrary and time-variable fraction of the available intergranular sites. (In contrast, Yan et al. (1980) assumed that one pore was present at each four-grain junction, throughout densification.) By excluding coalescence in the third case, we demonstrate clearly how coalescence affects swelling, for contrast with models which include no coalescence. Second, we include the effect of pressure on diffusional densification, allowing us to apply the model to, for example, HIPping. As part of this, we expand the effective pore pressure's internal

---

[2] Ostwald ripening should *not* occur by boundary diffusion between two pores of different size, but with surface curvature of the same sign, because, for sintering [swelling] "the intervening grain boundary has a chemical potential [for atoms] greater [less] than either" pore surface (Francois and Kingery, 1967, p. 487). Consequently, mass transport always occurs "from [to] the boundary toward [from] both large and small pores". Wilkinson's (1978) chemical potential *gradients*, during final-stage diffusional densification, are consistent with this.

pressure component, to permit it to arise from both an inert trapped gas, and a gas-generating chemical reaction. Also, we correct the capillarity pressure component for the pore dihedral angle. Third, we do not assume pore drag control, in order to generate analytic solutions; rather, we permit mixed control of grain growth, and include in the phenomenological drag formulation a general grain boundary mobility.

As well, we extend the phenomenological pore separation analysis to the limiting microstructural paths which bracketed our experimental swelling data, developing equations capable of plotting contours of arbitrary drag intensity and normalized pore velocity — including velocities beyond the separation limit, which are suggested by *non*phenomenological drag analyses.

While we developed the model with the problem of swelling in mind, and tested it with experimental swelling data, it is sufficiently general to apply also to pressure-driven sintering, to relate swelling to specific previous pressure sintering conditions (for example, to describe densification followed by *de*densification within a single HIP cycle).

Variables are listed at the end of this chapter, in section 3.7.

3.2 General

In any porous microstructure in which pores are spherical, the volume fraction porosity can be expressed as:

$$V_v = V_c \cdot N_v = (4\pi/3)\, N_v\, r^3 \qquad (1a,b)$$

from which the mean pore radius can be written as:

$$r\{t\} = r\,\{\, V_v\{t\},\, N_v\{t\}\,\} \qquad (2)$$

The number of pores per unit volume, $N_v\{t\}$, is controlled by grain growth-driven pore coalescence.[3] At this time, we cannot derive, from a detailed understanding of the topological processes occurring during grain growth (Rhines and DeHoff, 1984; DeHoff, 1984; Rhines, 1985) a general coalescence model capable of predicting N_v and r as functions of grain size (and, e.g. temperature). However, by idealizing the porous microstructure, we can include coalescence in swelling for three limiting-case, final stage microstructural trajectories — cases in which the number of pores is constant (1) per unit volume, (2) per unit area grain boundary and (3) per grain.

---

[3] Over the range of V_v studied, and with the pores confined to four-grain junctions, we expect adjacent pores *not* to coalesce without being swept together by grain growth (Greenwood and Boltax, 1962).

In common with previous final-stage sintering analyses, we idealize the grain structure as a space-filling assemblage of identical truncated-octahedra (App. 1; Fig. 3-1a). We set the grain size so that the ideal polycrystal's specific grain boundary area $S_V\{t\}$ is equal to that of the real polycrystal being modeled. Then, if we assume that all pores are at four-grain junctions in both real and ideal microstructures, we can relate $N_V\{t\}$, the number of pores per unit volume, to $f_3\{t\}$, the fraction of the four-grain junctions which are cavitated. We permit f_3 to have any value between zero and one. That is, in the idealized, three-dimensional microstructure (App. 1's Table A1-1):

$$N_V \approx 2.6\ f_3\ \bar{L}_2^{-3} \tag{3}$$

From Eqs. (1) and (3):

$$V_V \approx 10.7\ f_3\ (\bar{L}_2)^{-3}\ r^3 \tag{4}$$

Based on our experimental data (Fig. 4-12), we propose that f_3 is not an independent variable, but is controlled by grain growth-driven pore coalescence. That is:

$$f_3 = f_3\{t\} = f_3\{\ \bar{L}_2\{t\}\ \} \tag{5}$$

Differentiating Eq. (5) with respect to time:

$$\dot{f}_3 = (df_3/ d\bar{L}_2) (d\bar{L}_2/ dt) \quad (6a)$$

$$\equiv f_3' \cdot \dot{\bar{L}}_2 \quad (6b)$$

where $$f_3' \equiv df_3/ d\bar{L}_2 \quad (6c)$$

Then we can rewrite the mean pore radius (Eq. 2) as:

$$r = r\{t\} = r [V_v\{t\} , f_3\{t\} , \bar{L}_2\{t\}] \quad (7a)$$

which, from Eq. (5), is equivalent to:

$$r\{t\} = r [V_v\{t\} , \bar{L}_2\{t\}] \quad (7b)$$

It follows that the pore growth rate can be expressed as a total differential which is the sum of pressure- and coalescence-driven components:

$$\frac{dr}{dt} = \left(\frac{\partial r}{\partial t} \right)_{\bar{L}_2} + \left(\frac{\partial r}{\partial t} \right)_{V_v} \quad (8a)$$

$$\equiv \dot{r}_P + \dot{r}_L \quad (8b)$$

This corresponds to Yan et al.'s (1980) Eq. (4). They held the fraction of four-grain junctions constant at $f_3 = 1$ for final-stage sintering; however, in our experimental swelling data (Fig. 4-12), f_3 varies, and we include this variation in the present model.

3.3 The pressure-driven pore growth rate component

The first term on the right hand side of Eq. (8) is:

$$\dot{r}_P \equiv \left(\frac{\partial r}{\partial t} \right)_{\bar{L}_2} \tag{9}$$

For swelling or final-stage sintering, this represents diffusional (de)densification at constant average grain size. Depending on conditions, the average pore may be growing (early swelling) or shrinking (final stage sintering).

Either lattice or boundary diffusion may control this pore growth rate component. For the test conditions reported here, materials property data (App. 15) predict mixed $D_L/\delta D_B$ control, with δD_B dominant (App. 16). Given this, we adapt Wilkinson's (1978) expression for $\dot{r}_P$, for the present case of pressure-driven, boundary diffusion-controlled *de*-densification. We now outline his argument.

In a representative spherical material element of radius *b*, a planar diametral grain boundary disc intersects a central spherical pore of radius r (Fig. 3-1b). The material element has the same volume fraction porosity as the bulk polycrystal:

$$r/b = V_v^{1/3} \tag{10}$$

Differentiating (by time) the equation for the volume of the average spherical pore, the pressure-driven diffusional pore growth rate is:

$$\dot{r}_p = \dot{V}_{CP} / 4\pi r^2 \tag{11}$$

The diffusional atom flux leaving the pore's surface along the grain boundary of width δ, $J\{r\}$, represents a volumetric pore growth rate of:

$$\dot{V}_{CP} = \Omega \cdot J\{r\} \cdot 2\pi\delta r \tag{12}$$

For grain boundary diffusion controlled pore growth, the magnitude of this flux is (Herring, 1950):

$$J\{r\} = - \frac{\delta D_B}{\Omega k T} \nabla\mu\{r\} \tag{13}$$

in which $\nabla\mu$ is the chemical potential gradient for atoms in the isotropic, planar grain boundary disc, on which $\nabla^2\mu$ is constant. The pressure-dependent chemical potential gradient, at the pore surface, is calculated from potentials at the pore and shell surfaces, and from mechanical equilibrium on the grain boundary:[4]

---

[4] The P_{eff} defined here for swelling is the *negative* of that defined by Wilkinson (1978, p.21) for sintering.

$$\nabla\mu(r) \quad = \quad - B_3\{V_v\}\cdot\Omega\cdot P_{eff} \tag{14}$$

where $$B_3\{V_v\} = \left(\frac{2\pi(1-V_v^{2/3})}{(1+V_v^{2/3})\ ln(V_v^{-1/3}) - (1-V_v^{2/3})} \right) \tag{15}$$

A pore at a four-grain junction is intersected by six two-grain facets. Consequently, more grain boundary area is available to such a pore in a real polycrystal, and in its equi-V_v/equi-S_v idealization, than in the representative spherical shell. (For the range of porosities studied here, this boundary area ratio (β) is about two; Fig. 4-16; App. 6-2).

The pressure-driven, volumetric pore growth rate is:

$$\dot{V}_{CP} \quad \equiv \quad B\{T, V_v\}\cdot P_{eff} \tag{16a}$$

$$= \quad \beta\cdot\frac{\delta D_B \Omega}{kT}\cdot B_3\{V_v\}\cdot P_{eff} \tag{16b}$$

which, from Eq. (11), corresponds to a radial growth rate of:

$$\dot{r}_P \quad = \quad \beta\cdot\frac{\delta D_B \Omega}{4\pi r^2 kT}\cdot B_3\{V_v\}\cdot P_{eff} \tag{17}$$

To complete the analysis of the $\dot{r}_P$ term, we now extend Wilkinson's (1978) argument, by expanding the internal pressure component, and correcting the capillarity component for dihedral

angle.

The net driving pressure for diffusional pore growth is:[5]

$$P_{eff} = P_{int} - P_{cap} - P_{app} \qquad (18)$$

For polycrystal swelling driven by inert trapped gas — and perhaps also by an ongoing, gas-generating reaction — we assume a simple form for the internal pore pressure component (App. 4):

$$P_{int}(t) = \frac{(P_i V_v)_o}{V_v(t)} + P^G_{int} \qquad (19a)$$

$$\equiv P^I_{int} + P^G_{int} \qquad (19b)$$

The first term on the right hand side, P^I_{int}, represents any gas component(s) for which the number of moles trapped is constant in swelling. This may be an inert gas with low boundary and lattice diffusion coefficients (e.g. N_2 or Ar). It also may be a reaction product generated in final-stage pressure sintering (e.g. CO)

---

[5] Coble (1970) suggests that the P_{app} term should be $P_{app} / (1-V_v)$; however, for the small V_v for the current data, the difference is not important (see also Vieira and Brook, 1984). For swelling to larger V_v, this and other changes will be required in both the model and the data analysis — to handle cylindrical pores, continuous pore channels, and gas release.

when diffusion or reaction kinetics permit no significant reaction response to a change in pore pressure.

The second term, P^{G}_{int}, represents the total internal partial pressure for pore gases generated by internal chemical reactions *during* swelling. As a limiting case, it will have a thermochemically determined constant value throughout swelling. (Potential reactions are discussed in App. 5).

Capillarity constraint is a potentially important component of the chemical potential gradients driving diffusional pore growth *throughout* dedensification, particularly when an inert trapped gas dissipates its initial internal pressure during swelling. Whereas pores trapped within grains may be spherical, pores attached to grain boundaries typically will *not* be (Fig. 4-13). Rather, they will be lens-shaped spherical caps, cylinders or lenses with a spherical-triangular cross section, or spherical tetrahedra, depending on whether they are located on two-grain facets, along three-grain edges or at four-grain junctions, respectively (Beeré, 1975b; Raj and Ashby, 1975). When dihedral angles are low in pores attached to grain boundaries, the capillarity pressure must be corrected for dihedral angle-dependent surface curvature:[6]

---

[6] Wilkinson's (1978) original model was developed for *spherical* pores on grain boundaries.

$$P_{cap} = \frac{2\,\gamma_s}{r} \cdot g(\psi) \qquad (20)$$

We discuss the form of $g(\psi)$ and its importance in swelling in App. 3.

In the current tests, the external pressure is 1 atmosphere.[7]

$$P_{app} = 0.1 \text{ MPa} \qquad (21)$$

Substituting Eqs. (18)-(21) into Eq. (17) generates the final equation for $\dot{r}_p$. We now turn to the second pore growth term — coalescence, driven by grain growth.

3.4 The coalescence pore growth rate component

The second pore growth rate component on the right hand side of Eq. (8) is due to grain growth-driven coalescence:

$$\dot{r}_L = \left(\frac{\partial r}{\partial t} \right)_{V_v} \qquad (22)$$

We develop this term in two steps. First, in this section, we

---

[7] Were this model applied to final-stage pressure sintering (e.g. HIPping), P_{app} would be much higher (Arzt et al.'s (1983) Tables IV, V: for Al_2O_3, $P_{app} \approx 100$ - 200 MPa).

generate expressions for the *pore* growth rate as a function of the grain growth rate, for three different microstructural trajectories. Then, in the following section, we develop an expression for the grain growth rate, which includes pore drag.

We develop a general expression for pore coalescence as a function of the grain growth rate by differentiating Eq. (4) with respect to time, substituting Eq. (6b) into the result, and then holding V_v constant.[8] In this, as noted previously, we extend Yan et al. (1980) to *general* final-stage microstructural trajectories:

$$\frac{\dot{V}_v}{10.7} = \left(3 f_3 (\bar{L}_2)^{-3} r^2 \dot{r} \right) - \left(3 f_3 r^3 (\bar{L}_2)^{-4} \dot{\bar{L}}_2 \right) + \left((\bar{L}_2)^{-3} r^3 \dot{f}_3 \right) \tag{23a}$$

$$= (r/\bar{L}_2)^3 \left\{ (3f_3/r)\dot{r} + \left[(-3f_3/\bar{L}_2) + f_3' \right] \dot{\bar{L}}_2 \right\} \tag{23b}$$

Setting $\dot{V}_v$ equal to zero in (23b):

---

[8] We treat a pore coalescence event as occurring rapidly, at constant total volume ($\dot{V}_v = 0$). The effect on swelling follows more slowly, via pressure-driven diffusional pore growth, by the release of capillarity constraint (Eq. 18).

$$\dot{r}_L = \left[(r/\bar{L}_2) - (r/3f_3)\, f_3' \right] \dot{\bar{L}}_2\Big|_{V_V} \qquad (24)$$

(Recall from section 3.2 that f_3 is the fraction of four-grain junctions at which a pore is located.)

Eq. (24) extends to variable f_3 Yan et al.'s (1980) Eq. (5). The first term in the square brackets relates to pore coalescence at constant f_3; the second to pore coalescence arising from a change in f_3 during grain growth.

The pore growth rate component due to coalescence, Eq. (24), can be simplified for the three limiting porous-microstructural trajectories of constant-N_V, -N and -f_3 (see Apps. 1,2).

3.4.1 Case 1: Constant $N_V = N_V^*$

For this case no coalescence occurs, and $\dot{r}_L$ should equal zero. While this would hold in microstructures which swell *without* grain growth, in microstructures with values of f_3 well above zero, and extensive grain growth, it is hypothetical. Even for such cases, however, the following calculation provides a check on the expressions developed in previous sections.

If N_V is constant and equal to (say) $N_V^\bullet$, then (App. 2's Eq. 13):

$$f_3 = (N_V^\bullet / c_1)\, \bar{L}_2^{\,3} \tag{25a}$$

so that $$f_3' = (3\, N_V^\bullet / c_1)\, \bar{L}_2^{\,2} = 3 f_3 / \bar{L}_2 \tag{25b}$$

Substituting Eq. (25b) into (24):

$$\dot{r}_L = \left[(r/\bar{L}_2) - (r/\bar{L}_2)\right]\left(\frac{\partial \bar{L}_2}{\partial t}\right)_{V_V} \tag{26a}$$

$$= 0 \tag{26b}$$

At constant N_V, no coalescence is permitted. This case gives *upper* bounds to N_V, N and f_3 trajectories with respect to time or grain size (App. 2), but a *lower* bound to $\dot{r}_L$.

3.4.2 Case 2: Constant $N = N^\bullet$

If N, the number of pores per unit grain boundary area, is constant and equal to $N^\bullet$, then (App. 2's Eq. 15):

$$f_3 = (2\, N^\bullet / c_1)\, \bar{L}_2^{\,2} \tag{27a}$$

so $$f_3' = (4\, N^\bullet / c_1)\, \bar{L}_2 \tag{27b}$$

$$= 2\, f_3\, \bar{L}_2^{\,-1} \tag{27c}$$

Substituting Eq. (27c) into (24):

$$\dot{r}_L = \left[(r/\bar{L}_2) - (2r/3\bar{L}_2)\right]\left(\frac{\partial \bar{L}_2}{\partial t}\right)_{V_V} \tag{28a}$$

$$= \left(\frac{r}{3\bar{L}_2}\right)\left(\frac{\partial \bar{L}_2}{\partial t}\right)_{V_V} \tag{28b}$$

This case gives *intermediate* N_V, N, and f_3 trajectories with respect to time or grain size (App. 2), and *intermediate* values for $\dot{r}_L$.

3.4.3 Case 3: Constant $f_3 = f_3^*$

On a constant-f_3 microstructural trajectory, the fraction of four-grain junctions with pores remains constant while the mean grain and pore sizes increase. Since, for this case:

$$f_3' = 0 \tag{29}$$

then

$$\dot{r}_L = \left(\frac{r}{\bar{L}_2}\right)\left(\frac{\partial \bar{L}_2}{\partial t}\right)_{V_V} \tag{30}$$

This case gives physically reasonable *lower* bounds to N_V, N, and f_3 trajectories with respect to time or grain size (App. 2), but an *upper* bound to $\dot{r}_L$.

The results for the three limiting cases can be summarized as follows:

$$\dot{r}_L = x_1 \left(\frac{r}{\bar{L}_2}\right)\left(\frac{\partial \bar{L}_2}{\partial t}\right)_{V_V} \qquad (31)$$

Case (i)	Parameter held constant	x_1
1	N_V	0
2	N	1/3
3	f_3	1

This completes the first step in handling final-stage pore coalescence: coalescence rate as a function of grain growth rate. Now, we develop a general expression for the grain growth rate at a given pore volume fraction, which includes drag due to the pores.

3.5 Grain growth rate, with phenomenological pore drag

We will formulate a simple model for *normal* grain growth with attached pores, use Ashby's (1980) nomenclature (Fig. 3-1c), and the phenomenological pore drag analysis of Brook (1976); Yan et al. (1977); Carpay (1977) and Yan (1981), referring also to

Hillert (1965).[9,10] We extend this analysis by including in it a boundary mobility which permits using experimental grain growth data directly in a numerical solution to the swelling model.[11]

The time rate of increase of the mean linear intercept grain size ($\bar{L}_2$) is proportional to the mean boundary sweep velocity ($\bar{v}_B$):[12]

$$\dot{\bar{L}}_2 = a_2 \cdot \bar{v}_B \qquad (32)$$

In the phenomenological model of pore drag, the mean boundary velocity is expressed as the product of a global boundary driving

---

[9] In contrast to models which refer to a boundary driving *force* [N], and bring in separately the boundary area [m^2] on which this force acts (e.g. Heuer, 1979; Bannister, 1980), we will use a boundary driving *pressure* [N/m^2] (Ashby, 1980).

[10] In current models for grain growth and phenomenological drag, it is difficult to separate local and global parameters rigorously. This ambiguity is evident in Yan et al.'s (1977) Eqs. (30-32).

[11] Often only limited M_B data are available. However, choosing a reasonable value permits determining the sensitivity of the model to its value, and so yields information on the experimental accuracy needed in this parameter.

[12] The values which a, a_1 and a_2 take on depend on whether the grain size is the mean linear intercept, $\bar{L}_2$, or its spherical equivalent, $\bar{G} \equiv 1.5\,\bar{L}_2$ (see App. 9). In this model, we use $\bar{L}_2$. However, to keep equations compact in this section, we will omit the subscript 'L' used explicitly in that appendix.

pressure, $\bar{P}_B$, and a reduced, effective grain boundary mobility, M_B^{eff} (see, for example, Brook, 1976):

$$\bar{v}_B = \bar{P}_B \cdot M_B^{eff} \tag{33}$$

In its simplest form, the global driving pressure is proportional to the mean boundary energy divided by the grain size (App. 10):

$$\bar{P}_B = a_1 \gamma_B / \bar{L}_2 \tag{34}$$

The effective *boundary* mobility depends on the 'intrinsic'[13] boundary mobility for the pore-free matrix, M_B, the number of pores per unit area boundary, N, and the effective *pore* mobility, M_P^{eff}:

$$M_B^{eff} = \frac{M_P^{eff}}{N + M_P^{eff} / M_B} \tag{35}$$

The effective *pore* mobility, M_P^{eff}, sums three mass transport mechanisms which operate in parallel: (1) lattice diffusion around the pore, (2) diffusion on the surface of the pore, and (3) vapor transport through the pore. Vapor transport may be controlled by either (a) evaporation/condensation at the pore/vapor interface or (b) vapor diffusion within the pore.[14] The

---

[13] Here, 'intrinsic' refers not to the pure material, but to the *pore-free* system, which, in general, will be impure and doped.

[14] These two vapor transport mechanisms act in *series*.

effective pore mobility, in which superscripts ℓ, s, ec and vd denote the above mechanisms, then is (Yan et al., 1980; Ashby, 1980):

$$M_p^{eff} = M_p^{\ell} + M_p^{s} + \frac{M_p^{ec}\, M_p^{vd}}{M_p^{ec} + M_p^{vd}} \qquad (36)$$

In cases when *one* of these mechanisms controls (for example, surface diffusion) then M_p^{eff} is simply (see section 3.4.2, below, and Ashby's (1980) Table 2):

$$M_p^{\ell} = K_{\ell} / r^{n_{\ell}} \qquad (37)$$

For surface diffusion-controlled pore mobility, for example (Ashby, 1980):

$$K_s = \frac{\omega D_S \Omega}{\pi k T}, \quad \text{and} \quad n_s = 4 \qquad (38)$$

The intrinsic *boundary* mobility, for the *pore-free* polycrystal matrix, is given by (Yan et al., 1977; see also App. 9):

$$M_{BL}(m,T) \equiv \frac{K_L(m,T)}{a\, m\, \gamma_B\, \bar{L}_2^{m-2}} \qquad (39)$$

in which, from Eqs. (32) and (34):

$$a = a_1 \cdot a_2 \qquad (40)$$

Parameters a_1 and a_2 convert local model parameters to global

stereological parameters, and have a product value, a, on the order of 0.3 for normal grain growth, when $\bar{L}_2$ is the grain size basis (Apps. 9 and 10).[15]

In Eq. (39), $K_L\{m\}$ is an experimentally-determined rate constant for grain growth. It is the slope of the differential $\{\Delta_L^m\text{-}t\}$ grain growth data, for the exponent value, m, which generates the most linear plot from a given set of raw {grain size-time} data. Typically, the exponent is a small integer (Yan et al., 1977; Brook, 1976; App. 9):

$$\Delta_L^m\{t,T\} \equiv \bar{L}_2\{t,T\}^m - \bar{L}_2^{o\,m} \tag{41a}$$

$$\equiv K_L\{m,T\}\cdot t \tag{41b}$$

We assume that $K_L\{m,T\}$ has the form:

$$K_L\{m,T\} \equiv K_L^o\{m\}\cdot \exp\{-Q_K/RT\} \tag{42}$$

Both the exponent, m, and the activation energy, Q_K, depend on the mechanism controlling boundary mobility (Yan et al., 1977;

---

[15] The a_1 parameter no doubt is sensitive to, for instance, the width of the grain size distribution, as well as anisotropy in grain boundary energies with crystal orientation and sample texture (Wong and Pask, 1979; Abbruzzese and Lucke, 1986; see App. 10).

App. 9).

Eqs. (32)-(34) and (40) give:

$$\dot{\bar{L}}_2 = (a \gamma_B / \bar{L}_2) \; M_B^{eff} \qquad (43)$$

Consistent with our experimental data, we assume that pores remain *attached* to sweeping grain boundaries. For grain growth occurring against drag due to such pores, there are two limiting cases: boundary mobility control, and pore drag control.[16]

3.5.1 Case: Boundary mobility control.

In Eq. (35), when:

$$M_P^{eff} / M_B \gg N \qquad (44a)$$

then

$$M_B^{eff} \approx M_B \qquad (44b)$$

and pore drag is *un*important in controlling the grain growth rate. Instead, the intrinsic boundary mobility controls. In this limiting case, the grain growth rate is:

---

[16] In cases with *mixed* control, M_B^{eff} are *smaller* then either M_B or (M_P/N).

$$\dot{\bar{L}}_2 = \frac{a\,\gamma_B}{\bar{L}_2}\, M_B\{\bar{L}_2^{\,2-m}\} \qquad (45)$$

Boundary mobility, M_B, is *in*dependent of grain size only when the exponent *m* has the value two (Eq. 39).

When — as will often be the case — too few data are available for grain growth in a pore-free material, we will treat M_B as an adjustable parameter. In such cases, possible values for M_B will be bounded by experimental data (e.g. Yan et al.'s (1977) *normalized* Fig. 8; see also Apps. 9 and 15). On the other hand, from Eq. (47), when pore drag control can be assumed, the scarcity of M_B data is less important (e.g. Yan et al., 1980).

3.5.2 Case: Pore drag control.

In Eq. (35), when:

$$M_P^{eff} / M_B \ll N \qquad (46a)$$

then the effective boundary mobility is controlled by pore drag:

$$M_B^{eff} \approx M_P^{eff} / N \qquad (46b)$$

in which the effective *pore* mobility is given by Eq. (36). In this case, the grain growth rate is:

$$\dot{\bar{L}}_2 = \frac{a\,\gamma_B}{\bar{L}_2}\,\frac{M_P^{eff}}{N} \qquad (47)$$

For the limiting case of *one* controlling pore migration mechanism, the effective pore mobility is equal to a mobility defined for either surface (s) or lattice (l) diffusion, or vapor diffusion-evaporation/condensation (vd,ec) (see Eq. 36, 37):

$$M_P^{eff} = M_P^{i}, \qquad i = s,\ l,\ vd,\ ec \qquad (48)$$

and so

$$\dot{\bar{L}}_2 = \frac{a\,\gamma_B}{\bar{L}_2}\,\frac{M_P^{i}}{N} \qquad (49)$$

where M_p^i is given by Eq. (37).

3.6 Numerical solution

In this work, we have assumed neither boundary nor pore drag control of grain growth, in order to generate analytic solutions. Instead, we permitted *mixed* control. We have, however, assumed that boundary diffusion controlled swelling, and that surface diffusion controlled the pore mobility. Both of these assumptions are consistent with calculations using typical materials parameters values for aluminas, as well as values determined for AVCO in this study (Apps. 15,16; Ashby, 1980; Ch.5). The two

governing differential equations (Eqs. 8 and 43) then were solved together numerically, for the three limiting cases of constant N_v, N or f_3 microstructural trajectories.

In the following chapter, we present the experimental data — both *raw* values (such as density changes or grain size) and microstructural parameters calculated from them (such as volume fraction porosities or the fraction of four-grain junctions with pores). In the subsequent chapter, we present the numerical results obtained from the model.

3.7 Swelling model: Variables

$a, a_{1,2}$ dimensionless parameters in grain growth model which convert local to global parameters (App. 9); $a = a_1 \cdot a_2$; [-]

b radius of representative spherical shell in diffusional pore growth model; [m]

B overall pore growth rate constant; $[m^3/(s(N \cdot m^{-2})^n)]$;

$$B = B\{T, V_v\} = \beta \cdot f\{\delta D_B\{T\}\} \cdot B_3\{V_v\}$$

β dimensionless ratio of the grain boundary area in polycrystal, per pore, to the area of the single grain boundary plane in the representative spherical shell of radius b; [-]

B_3 dimensionless parameter in pore growth rate constant; [-]

D_B boundary diffusion coefficient; $[m^2/s]$

D_L lattice diffusion coefficient; $[m^2/s]$

D_S surface diffusion coefficient; $[m^2/s]$

δ width for grain boundary diffusion; [m]

Δ_L^m differential grain growth parameter; $[metres^m]$

f_3 fraction of four-grain junctions cavitated in ideal microstructure; [-]

f_3' rate of change of f_3 with $\bar{L}_2$: $(df_3/d\bar{L}_2)$; $[m^{-1}]$

$g\{\psi\}$ dimensionless dihedral angle correction factor for P_{cap}, for a four-grain junction pore; [-]

γ_B mean energy of grain boundaries; $[J/m^2]$

γ_S mean energy of pore surfaces; $[J/m^2]$

$J(r)$ diffusional atom flux leaving pore surface; [atoms/m^2·s]

k Boltzmann's constant; [1.381E-23 J/atom·K]

K_i rate constant for i^{th} pore mobility mechanism; [m/N·s]

K_L rate constant for grain growth; [metres^m/s]

K_L^o pre-exponential in temperature-dependent rate constant for grain growth; [metres^m/s]

K_S rate constant for surface diffusion controlled pore mobility; [m/N·s]

ℓ length of facet edge in ideal, truncated-octahedral grain; [m]

$\bar{L}_2$ grain size: mean linear intercept on a random polish plane in a real microstructure; [m]

$\bar{L}_2^o$ initial mean linear intercept: $\bar{L}_2(t = 0)$; [m]

ln base *e* (natural) logarithm

log base 10 logarithm

m grain size exponent in grain growth equation; [-]

M_B, M_{BL} mobility of pore-free grain boundary (App. 9); [m^3/N·s]

M_B^{eff} effective grain boundary mobility, with drag from attached pores; [(m/s)/(N/m^2)]

M_P^i, i = s, l, vd, ec

pore mobility controlled by lattice, surface or vapor diffusion, or by evaporation/condensation, respectively; [m/N·s]

M_P^{eff} effective pore mobility, combining above M_P^i at current conditions (Eq. 36); [m/N·s]

μ chemical potential; [J]

N number of attached pores per unit area grain boundary; $[m^{-2}]$

N_A number of pores per unit area internal polish plane; $[m^{-2}]$

n_i pore size exponent for i^{th} pore mobility mechanism; [-]

n_s pore size exponent for surface diffusion controlled pore mobility; [-]

N_V number of pores per unit volume solid; $[m^{-3}]$

Ω atomic or molecular volume, or volume of controlling diffusing species (App. 15); $[m^3]$

P_{app} hydrostatic pressure applied externally to the polycrystal and representative spherical material element; $[N/m^2]$

$\bar{P}_B$ global boundary driving pressure; $[N/m^2]$

P_{cap} capillarity pressure in a pore; $[N/m^2]$

P_{eff} effective pressure driving diffusional cavity growth; $[N/m^2]$

P_{int} internal gas pressure in a pore; $[N/m^2]$

P^G_{int} P_{int} component maintained by an internal gas-generating reaction; $[N/m^2]$

P^I_{int} the inert trapped gas component of P_{int}; $[N/m^2]$

$(P_i V_V)_o$ $(P_{int} \cdot V_V)$ product at start of anneal at T_{ann}; $[N/m^2]$

ψ dihedral angle at pore-grain boundary edge; [rad] or [deg]

Q_B activation energy in $\delta D_B\{T\}$; [J/mol]

Q_K activation energy in grain growth rate constant, $K_L\{T\}$; [J/mol]

Q_S activation energy in $\omega D_S\{T\}$; [J/mol]

r radius of average spherical pore; [m]

$\dot{r}_i$, i = P, L pore growth rate components due to P_{eff} and

coalescence, respectively; [m/s]

R gas constant; [8.3144 J/mol·K]

S_V specific grain boundary area; [m^2/m^3]

t time; [s]

T temperature; [K] or [C]

$\bar{v}_B$ global grain boundary velocity; [m/s]

V_C volume of average pore; [m^3]

$\dot{V}_{CP}$ component of volumetric pore growth rate driven by effective pressure; [m^3/s]

V_V volume fraction of pores; [-]

ω width for surface diffusion; [m]

x_1 factor giving values for $\dot{r}_L$ which are specific to different limiting-case microstructural paths; [-]

---

* starred variables are constants in a particular limiting case (Sections 3.3.1, 3.3.2 and 3.3.3).

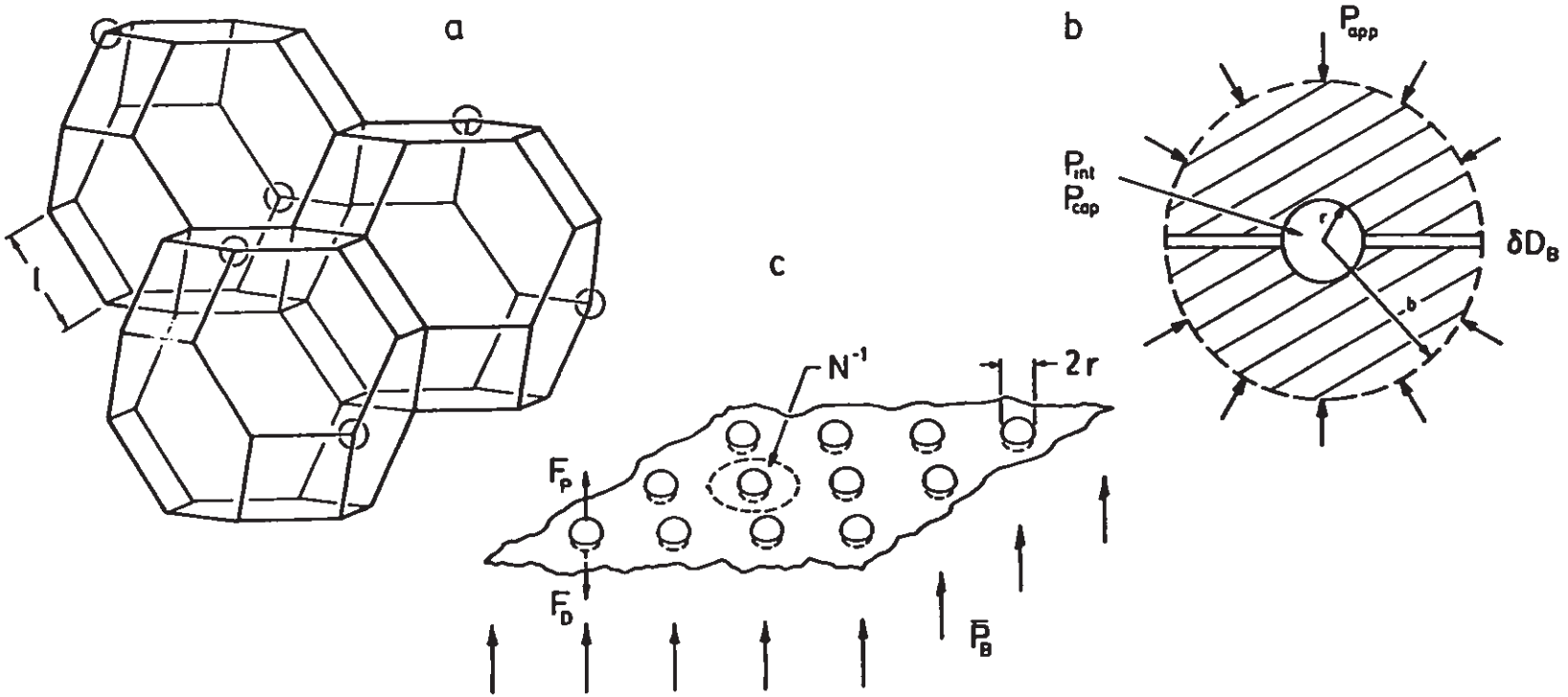

Fig. 3-1a) Ideal final-stage polycrystal, with arbitrary fraction of four-grain junctions cavitated (after Pearce, 1978, p.5).

b) Representative spherical shell, with central pore and single grain boundary disc (after Wilkinson, 1978).

c) Representative isolated grain boundary sheet, sweeping against drag from N pores per m^2 (after Ashby, 1980).

4 Experimental results: swelling

Specimens in both AVCO and ARCO HPAs were annealed in air for up to 600 h at 1250 and 1350 C,[1] up to 400 h at 1400 C, and up to 300 h at 1450 C (Table 2-3). Tables 4-1,-2 give raw experimental data; Tables 4-3,-4 give calculated mean microstructural parameters. Figs. 4-1.1 and 4-1.2 show typical SEM microstructures; Fig. 4-2, typical TEM microstructures. Results are plotted in Figs. 4-4 to 4-16; experimental uncertainties in these plots are discussed in App. 14. Variables are listed in section 4.1, following Table 4-1.

Figs. 4-1.1 and 4-1.2 show typical internal SEM microstructures in AVCO and ARCO, respectively, after thermal etching. Both *as-received* aluminas were close to theoretical density (Figs. 4-1.1*j*,4-1.2*j*). AVCO's pores were intergranular. By SEM, as-received ARCO contained a small number of large pores, either within one grain or as larger flaws on grain boundaries, which spanned several grains. Porosity and grain size increased with time and temperature. Intergranular pores dominated swelling in

[1] Only ARCO was annealed at 1250 C.

both aluminas; such pores had low dihedral angles, and some were elongated (probably extending along three-grain edges, or covering two-grain facets; Figs. 4-1.1a-*i*, 4-1.2a-*i*).

Pore sizes and locations in the *as-received* microstructures were determined from TEM micrographs (Fig. 4-2). The two HPAs were very different. In AVCO (Figs. 4-2a,*b*), almost all as-received pores were individual, intergranular spherical tetrahedra at four-grain junctions. However, as-received pores in ARCO (Figs. 4-2c-*d*) were almost exclusively small intragranular spheres, occurring both as single pores and in clusters. As ARCO swelled, and grain boundaries migrated, the porosity detected by SEM gradually became intergranular (Fig. 4-1.2a-*i*).[2]

For AVCO, as-received pore sizes were estimated directly from TEM micrographs from one foil.[3] From these micrographs, the projected area of each pore was estimated, and was converted into the radius of an equivalent projected sphere. The distribution of

---

[2] This transition is marked on ARCO's data in Table 4-2 (its Note 2), and corresponded to $\tilde{L}_2$ of 1.25 to 1.3, and $\tilde{V}_v$ of 1.34 to 1.6 for that HPA. (Where the current values were normalized by the corresponding initial values; e.g. $\tilde{L}_2 \equiv \bar{L}_2/\bar{L}_2^o$).

[3] The foil ion-thinned with *no* regions of *intermediate* thickness; that is, which were electron transparent, but contained a large number of representative pores. The micrographs were taken from the best available typical regions.

equivalent pore radii is shown in Fig. 4-3a; the mean radius was about 0.12 μm.

Figs. 4-3*b-d* show as-received size distributions for ARCO's *spherical* intragranular pores — both for typical regions, and for one large cluster.[4] Both overall pore size distributions, and size distributions within the large cluster, peaked at pore radii between 10 and 20 nm, and no pores were seen with radii larger than about 80 nm. A small number of intragranular pores were faceted. The few intergranular pores were not spherical, but showed low dihedral angles (Fig. 4-2d).

Immersion density change data (Fig. 4-4) were converted to volume fraction porosities (Fig. 4-5) with formulae developed in App. 7. Both aluminas swelled more rapidly with time and temperature between 1350 and 1450 C; AVCO swelled more rapidly than ARCO. At 1250 C, no measurable swelling occurred in ARCO, over the 600 h time span of the tests.[5]

Fig. 4-6 shows grain growth kinetics. As-received grain sizes (as mean linear intercepts, $\bar{L}_2$) were 1.6 and 1.0 μm for AVCO and ARCO

---

[4] These were calculated from micrographs similar to Figs. 4-2*c,d*. The number of pores in the clusters characterized is given in the caption to Fig. 4-3.

[5] For this reason, no 1250 C data is shown for ARCO.

respectively. At any temperature, grain growth was more rapid in ARCO than in AVCO (as seen by comparing the normalized mean grain sizes at the end of corresponding anneals, in Tables 4-1,4-2). The difference was greater at higher annealing temperatures. Grain growth exponents (m) were between 3 and 4 for both HPAs at all temperatures (save at 1350 in ARCO, for which a value between 2 and 3 seemed more appropriate.)[6]

When plotted against mean grain size, the volume fraction porosity was approximately linear, and was independent of temperature (Fig. 4-7). AVCO's swelling rate (with respect to grain size, $\{dV_v/d\bar{L}_2\}$) was about 5.7 times greater than ARCO's.

Pore number densities on thermally-etched, internal polish planes, N_A, rose steeply at short times, and then decreased more slowly (Fig. 4-8). For ARCO, the rate of *de*crease was higher at higher temperatures; however, in AVCO, this trend was reversed between 1350 and 1400. (While N_A values at short times were low, they were also uncertain; see below.)

In order to calculate the mean pore parameters r, N_v, N and f_3,

---

[6] The exponent values were estimated by plotting differential grain size, $\Delta_L^m\{t,T\}$, against time, for all half-integral values of m over the range two to four (Eq. 3, in App. 9). For a given material and temperature, the m value giving the most linear plot was retained.

we idealized the final-stage polycrystal as consisting of truncated-octahedral grains, with pores located only at four-grain junctions (App. 1; Fig. 3-1a). We held specific grain boundary areas equal in real and ideal microstructures at all times. We treated pores as spheres except when estimating capillarity stress (App. 3).[7] We then were able to convert $\{V_V, N_A, \bar{L}_2\}$ data into average, *three*-dimensional parameters of the ideal porous microstructure which were relevant to the physical swelling model (App. 6). These were: the mean pore radius, r; the number of pores per unit volume, N_V; the number of pores per unit area grain boundary, N; and the fraction of four-grain junctions with a pore, f_3 (six such junctions were available per grain). Figs. 4-9 to 4-14 show how these parameters changed during swelling. In these figures, given the linearity between V_V and $\bar{L}_2$ in Fig. 4-7, the x-axis is not time, but mean linear intercept grain size, $\bar{L}_2$, emphasizing that grain growth was important throughout swelling.

In AVCO, calculated pore sizes were roughly linear in grain size, and were independent of temperature (Fig. 4-9). AVCO's as-received pores were close to but above the 'SEM detection limit'

---

[7] We assumed that a spherical-tetrahedral pore, with a dihedral angle typical of HPA, and a spherical pore of the same volume, have similar stereological properties *in practice* ($\bar{D}_V$; DeHoff and Rhines, 1968, p.131).

of approximately 0.1 μm radius in both SEM and TEM data.[8] This was not an SEM resolution limit, but involved the surface of the ceramic being plastically smeared[9] over small pores cut by the polish plane during polishing, and this layer not being removed from such pores in later thermal etching. The limiting radius was implied by AVCO's 8h/1350C value of N_A being falsely low, given the corresponding bracketed (see below) points in Figs. 4-10 to 4-14. The mean TEM pore size (Figs. 4-2*a,b*; 4-3*a*), 0.12 μm, was consistent with these SEM radii at short times.

In ARCO, Figs. 4-1.2, 4-2 and 4-3 show that pores initially were very small, and evolved, with grain growth, from primarily intragranular to primarily intergranular. In specimens annealed for short times, individual intragranular pores were hidden beneath the plastic layer smeared in polishing, while pores in a cluster which had been cut by the polish plane coalesced, to give a single, larger pore trace. Pores and clusters which reattached to sweeping grain boundaries (Handwerker et al., 1984),[10]

---

[8] Handwerker et al. (1984) report a somewhat smaller detection limit of $r \approx 0.05$ μm, for sintering studies in MgO.

[9] More pores were seen by optical microscope, during routine polishing progress checks, *after* the thicker plastically smeared layer from 3 μm polishing had been thinned by 1 and 0.25 μm diamond pastes.

[10] The fine scale of ARCO's as-received pores suggested they separated from sweeping grain boundaries at an earlier stage of

coalesced to form larger, single intergranular pores. From SEM micrographs, reattachment was largely complete by $\bar{L}_2$ of 1.25 to 1.3, and $\bar{V}_v$ of 1.34 to 1.6 (Table 4-4's Note 2). Assuming linearity *after* reattachment, the overall pore growth rate $(dr/d\bar{L}_2)$ was no more than 1.6 times higher in AVCO than in ARCO.

In ARCO, interpreting the early stages of Figs. 4-9 to 4-16 was complicated both by the SEM artifacts for intragranular pores and pore clusters, and by initially intragranular pores reattaching to sweeping grain boundaries. For example, in Fig. 4-9, we could not simply extrapolate back to short times to estimate pore sizes below the 'SEM detection limit'.

In Figs. 4-10 to 4-16, brackets mark questionable points. Brackets signify *different* uncertainties in the two HPAs. In AVCO, the 8h/1350C data point for N_A appeared to have too low a value (App. 6), and corresponding N_v, N etc. points were bracketed to mark this experimental uncertainty. For ARCO, however, pores reattached and coalesced as they did so, and this was inconsistent with the microstructural evolution modeled. Further, SEM micrographs could not be used to characterize its intragranular porosity. ARCO's brackets denote specimens in which, based on SEM micrographs and trends in Figs. 4-10 to 4-14,

---

sintering. In this case, attachment during swelling is reattachment.

pore reattachment was still underway.

In Figs. 4-10 and 4-11, grain growth-driven coalescence progressively reduced both the volume and boundary area number densities of pores, N_v and N respectively, in both aluminas.[11] At the same time, the fraction of four-grain sites with pores, f_3, increased in all cases except AVCO at 1350 C, for which about one pore per grain was present throughout swelling (Fig. 4-12). As-received AVCO had about one pore per grain; By the time pore reattachment was complete in ARCO, that HPA had about one pore per grain also.

Log-log plots of N and f_3 against $\bar{L}_2$ permit testing experimental coalescence data against slopes for limiting constant-N and constant-f_3 trajectories (Figs. 4-13 and 4-14; App. 2). Both HPAs showed progressive changes in swelling trajectories (paths) with temperature. These distinct, temperature-dependent trajectories were rather *in*sensitive to stereological errors arising from our having treated *non*equiaxed pores on the polish plane as if they were *equiaxed* (Figs. 4-1.1,-1.2; see App. 13).

The path changes, with temperature, occurred in opposite

---

[11] In ARCO, the N_v, N and f_3 — which are parameters for intergranular pores — *increased* at short times, as intragranular pores reattached to sweeping boundaries.

directions in the two materials. AVCO followed a constant-f_3 path at 1350, was intermediate at 1400, and approached constant-N at 1450 C. ARCO, on the other hand, after reattachment, followed a constant-N path at 1350C, was close to this at 1400, and near constant-f_3 at 1450C. That is, at higher temperatures, coalescence was occurring at a a lower rate, relative to grain growth, in AVCO, but at a faster rate in ARCO. In other words, at higher temperatures in AVCO, the polycrystal was losing pores by coalescence less rapidly than it was losing potential pore sites[12] by grain growth. In ARCO, once pores had reattached, the opposite trend held.

For AVCO, all three swelling trajectories extrapolated back to the same N and f_3 origins at the as-received grain size, assuming N_A errors in the few early data points which were inconsistent. No such common origins were evident for ARCO, when both N and f_3 plots were considered.

For AVCO, this common point reinforced the consistency between the TEM micrographs (Figs. 4-2*a,b*), SEM micrographs (Figs. 4-1.1a-*j*) and the porous microstructure modeled, in which pores were at four-grain junctions throughout swelling. It also permitted a self-consistent set of microstructural parameters to

---

[12] Four-grain junctions, the number density of which was linear in the number density of grains (App. 1).

be calculated, which were used as initial conditions in the numerically solving the model (V_V^o, r_o, etc.; Table 5-1). In contrast, for ARCO, the *lack* of a common initial point, and the initial TEM and initial SEM microstructures diverging from that modeled (Figs. 4-2*c,d*; 4-1.2*a-j*) suggested that the model *not* be applied to this HPA at this time.

Dihedral angles for grain-boundary pores in both aluminas were estimated from TEM micrographs (similar to Figs. 4-2) of a small number of carefully selected four-grain junction and three-grain edge pores. Following guidelines outlined in App. 14, the global dihedral angles were determined to be:[13]

	ψ (deg)	
	ARCO	AVCO
Experimental range	90-120	80-100
Value used in calculations	—	90

Further work on the existing foils, preferably with a two-axis stage, would refine these estimates.[14]

---

[13] *Full* dihedral angles, not half-angles.

[14] However, we anticipate a *distribution* of dihedral angles

The ratio (b/ℓ); that is, the ratio of the radius of the solid spherical shell of the average pore, b, to the length of the facet edge of the ideal, equi-S_v grain, ℓ, is given in Fig. 4-15 (Figs. 3-1a,b; Apps. 1,6). The ratio of the grain boundary area in this time-dependent solid shell, *in the ideal microstructure,* to the area of the single, planar boundary disc in the solid shell, β, is shown in Fig. 4-16. The value of β depends on the value of (b/ℓ). From the geometry of an ideal four-grain junction, for (b/ℓ) less than approximately 1.1, β has a constant minimum value of approximately 1.8. For (b/ℓ) greater than approximately 1.1, β is about $1.6 \cdot (b/\ell)$ (App. 6's Eq. 20).

Both parameters decreased as swelling proceeded. Values of (b/ℓ) were between 1.5 and 1, and fell to about 1 for long times and high temperatures.[15] Values of β fell from approximately 2.5 to about 1.5. From geometric arguments (App. 6), β has a minimum value of approximately 1.83, and we accept only experimental values above this floor.

We should be able to calculate β during swelling from an initial N_V^o, along a given path. However, for the present, we simplify the

---

(Handwerker et al., 1984).

[15] Low N_A would give falsely high (b/ℓ) and β.

numerical calculations by assigning β a constant value of 1.8.

The experimental results can be summarized:

- in both HPAs, swelling (as volume fraction porosity) and mean pore radius were linear in grain size and independent of temperature.
- pore coalescence was evident from the decreases in N_A, N_V, and N with increasing grain size, and the simultaneous increase in f_3.
- coalescence rates (with respect to grain size), changed in opposite directions in the two HPAs, with temperature, bounded by constant-f_3 and constant-N limiting microstructural paths. Coalescence was less rapid with increasing temperature in AVCO, but more rapid in ARCO.
- In AVCO, TEM micrographs, and the common origins on N and f_3 plots *vs* grain size, showed the microstructure to have been consistent with that modeled.
- in ARCO, TEM micrographs showed that as-received pores were mostly very small and intragranular. ARCO's microstructural evolution was more complex than that modeled.
- global values of $\beta \approx 1.8$ and $\psi \approx 90^\circ$ were determined for AVCO, along with a consistent set of initial microstructural parameters (V_V°, r_o, etc.; Table 5-1).

Table 4-1: Raw swelling data for AVCO HPA

t [h]	$\bar{L}_2$ [μm]	$\tilde{L}_2^*$ [-]	$10^3(\Delta\rho/\rho_o)$ [-]	$10^{-10}\cdot N_A$ [m^{-2}]
1450 C				
5	1.90±0.17		1.48±0.36	3.2
12	1.99±0.13		3.53±0.41	3.7
36	2.21±0.21		4.68±0.32	4.1
100	3.25±0.45		9.19±0.33	3.5
300	3.85±0.59	2.38±0.47	13.5±0.33	3.0
1400 C				
5	1.54±0.05		0.69±0.22	2.8
16	1.68±0.09		1.95±0.39	3.3
48	1.96±0.18		3.54±0.34	3.9
100	2.13±0.19		5.98±0.20	3.4
200	2.60±0.44		7.85±0.21	3.3
400	3.00±0.18	1.85±0.25	11.3±0.34	3.1
1350 C				
8	1.71±0.11		0.32±0.11	1.2[(1)]
24	1.72±0.12		1.04±0.11	3.2
72	1.92±0.14		2.13±0.12	2.7
200	2.15±0.16		4.02±0.11	2.5
600	2.45±0.24	1.51±0.24	6.24±0.04	2.4
A/R	1.62±0.20	1.00		0.11

* $\tilde{x}$: normalized by the initial value.

ρ_{th} [Mg/m^3] 3.9846(9)±0.0002

ρ_o ["] 3.9818(4)±0.0004

Global *relative* uncertainties for parameter calculations:

We used approximate experimental uncertainties ($\sigma\{x\}$) for $\bar{L}_2$ and N_A, taken for the entire data set for one HPA. The simplest way to handle the time and temperature dependencies was to base the uncertainty on the *normalized* grain size, $\tilde{L}_2$. For N_A, a single representative value was chosen. The global *relative* uncertainties were:

$$\bar{L}_2: \quad \frac{\sigma\{\bar{L}_2\{t\}\}}{\bar{L}_2\{t\}} = -0.004 + 0.064\,\tilde{L}_2\{t\}$$

$$N_A: \quad \frac{\sigma\{N_A\{t\}\}}{N_A\{t\}} \equiv 0.15$$

Table 4-2: raw swelling data for ARCO HPA

t [h]	$\bar{L}_2$ [μm]	$\tilde{L}_2$ [-]	$10^3(\Delta\rho/\rho_o)$ [-]	$10^{-10}\cdot N_A$ [m^{-2}]
1450 C				
5	1.32±0.04		0.75±0.48	2.2(1)
10	1.43±0.07		0.94±0.37	3.3(1)
21	1.92±0.17		0.91±0.27	3.8
50	2.44±0.18		1.82+0.33	2.7
100	2.94±0.41		2.93±0.37	2.3
300	4.08±0.29	4.08±0.41	4.38±0.37	1.7
1400 C				
5	1.03±0.06		0.37±0.14	1.0(1)
16	1.14±0.11		0.66±0.17	2.0(1)
48	1.50±0.14		0.84±0.29	3.2
100	1.69±0.16		1.28±0.20	2.8
200	2.08±0.27		1.53±0.15	2.5
400	2.35±0.47	2.35±0.50	1.66±0.23	2.2
1350 C				
8	1.09±0.08		0.32±0.12	1.3(1)
24	1.13±0.01		0.66±0.15	1.9(1)
72	1.26±0.08		0.43±0.21	2.8
200	1.37±0.09		0.51±0.14	2.6
600	1.99±0.25	1.99±0.29	1.11±0.16	2.3

(2)

1250 C				
10	0.99±0.05		0.03±0.12	0.58[1]
30	0.91±0.03		0.37±0.15	0.64[1]
100	1.00±0.04		0.49±0.18	0.93[1]
				[2]
300.	1.02±0.04		0.10±0.23	0.81[1]
600.	1.00±0.06	1.00±0.09	0.10±0.21	0.87[1]
A/R	1.00±0.07			

ρ_{th} [Mg/m^3] 3.9893(9)±0.0002

ρ_o ["] 3.9844(0)±0.0008

Global *relative* uncertainties for parameter calculations:

(See note at this point in Table 4-1.)

$$\bar{L}_2: \quad \frac{\sigma\{\bar{L}_2(t)\}}{\bar{L}_2(t)} = 0.03 + 0.03\,\tilde{L}_2(t)$$

$$N_A: \quad \frac{\sigma\{N_A(t)\}}{N_A(t)} \cong 0.15$$

Table 4-3: Calculated swelling data for AVCO HPA

t [h]	$10^3 \cdot V_v$ [-]	r [μm]	$10^{-16} \cdot N_v$ [m^{-3}]	$10^{-10} \cdot N$ [m^{-2}]	f_3 [-]	β [-]
1450 C						
4	2.19±0.53	0.18±0.03	8.86±2.27	8.42±2.23	0.24±0.08	1.95±0.22
12	4.24±0.49	0.23±0.02	7.92±1.84	7.88±1.92	0.24±0.08	1.94±0.21
36	5.39±0.37	0.25±0.02	8.19±1.86	9.05±2.19	0.36±0.12	1.72±0.19
100	9.89±0.30	0.37±0.03	4.78±1.08	7.46±1.98	0.64±0.27	1.40±0.20
300	14.2±0.35	0.48±0.04	3.16±0.71	6.07±1.62	0.70±0.34	1.36±0.22
1400 C						
5	1.40±0.45	0.15±0.03	9.07±2.50	6.98±1.97	0.13±0.04	6.13±0.71
16	2.66±0.53	0.20±0.02	8.42±2.07	7.07±1.80	0.16±0.05	4.03±0.43
48	4.25±0.41	0.23±0.02	8.56±1.97	8.34±2.02	0.25±0.08	2.46±0.30
100	6.69±0.22	0.31±0.02	5.55±1.25	5.91±1.41	0.21±0.07	2.41±0.27
200	8.85±0.23	0.35±0.03	4.69±1.06	6.10±1.50	0.32±0.12	2.10±0.25
400	12.0±0.36	0.43±0.03	3.61±0.81	5.41±1.36	0.38±0.15	2.00±0.26
1350 C						
8[3]	1.03±0.35	0.20±0.04	2.97±0.84	2.54±0.74	0.06±0.02	3.13±0.36
24	1.75±0.19	0.16±0.02	9.91±2.29	8.52±2.04	0.20±0.06	2.08±0.21
72	2.84±0.16	0.22±0.02	6.03±1.37	2.79±1.38	0.17±0.05	2.20±0.23
200	4.73±0.13	0.30±0.02	4.16±0.94	4.76±1.07	0.17±0.05	2.22±0.24
600	6.95±0.04	0.37±0.03	3.23±0.73	3.96±0.96	0.19±0.07	2.12±0.25
A/R	0.72±0.11	0.12[4]				

Table 4-4: Calculated swelling data for ARCO HPA

t [h]	$10^3 \cdot V_v$ [-]	r [μm]	$10^{-16} \cdot N_v$ [m^{-3}]	$10^{-10} \cdot N$ [m^{-2}]	f_3 [-]	β [-]
1450 C						
5 [3]	2.00±1.28	0.21±0.07	5.28±2.07	3.49±1.39	0.05±0.02	3.34±0.49
10 [3]	2.19±0.86	0.18±0.04	9.28±2.77	6.59±2.03	0.10±0.04	2.57±0.32
21	2.16±0.64	0.16±0.03	11.5±3.11	11.0±3.12	0.31±0.11	1.78±0.22
50	3.07±0.56	0.23±0.03	5.80±1.41	7.08±1.87	0.33±0.13	1.75±0.23
100	4.18±0.53	0.29±0.03	3.91±0.91	5.74±1.50	0.39±0.17	1.66±0.24
300	5.63±0.48	0.40±0.03	2.14±0.49	4.37±1.20	0.57±0.29	1.46±0.25
1400 C						
5 [3]	1.62±0.61	0.28±0.06	1.80±0.53	6.98±1.97	0.008±.003	6.13±0.71
16 [3]	1.91±0.49	0.21±0.03	4.69±1.22	7.07±1.80	0.03±0.01	4.03±0.43
48 [2]	2.09±0.72	0.18±0.03	9.07±2.57	8.39±2.02	0.12±0.04	2.46±0.30
100	2.53±0.40	0.21±0.02	6.75±1.61	5.91±1.41	0.13±0.04	2.41±0.27
200	2.77±0.27	0.23±0.02	5.43±1.25	6.10±1.50	0.19±0.07	2.10±0.25
400	2.91±0.40	0.25±0.03	4.38±1.03	5.41±1.36	0.22±0.09	2.00±0.26
1350 C						
8 [3]	1.57±0.59	0.24±0.05	2.71±0.79	1.48±0.44	0.014±.005	5.06±0.59
24 [3]	1.91±0.43	0.22±0.03	2.34±1.09	2.45±0.64	0.024±.008	4.17±0.44
72 [2]	1.68±0.82	0.17±0.04	8.28±2.75	5.22±1.77	0.06±0.03	3.01±0.39
200	1.76±0.48	0.18±0.03	7.24±1.91	4.96±1.35	0.07±0.02	2.90±0.33
600	2.36±0.34	0.22±0.02	5.20±1.23	5.17±1.31	0.16±0.06	2.23±0.27
A/R	1.25±0.21	0.01-0.02 [2,4]				

Notes

A/R → as-received

~ → normalized by the initial value.

(1) The microstructural evolution modeled is consistent with that seen by TEM and SEM in AVCO . Figs. 4-10 to 4-14 show this value of N_A to be falsely low.

(2) ARCO's as-received porosity is almost exclusively intragranular (Figs. 4-2*c*,*d*; 4-1.2*j*). Significant intergranular porosity is seen by SEM in ARCO only for $\tilde{L}_2 \geq 1.25\text{-}1.3$ and $\tilde{V}_v \geq 1.34\text{-}1.6$; that is, for data *below* this line (Figs. 4-1.2*a*-*i*)

(3) From Note (1), calculated r, N_v, N and f_3 are unreliable at this temperature and time. App. 6 indicates the directions of the anticipated errors.

(4) From TEM micrographs (Fig. 4-2). As-received pore size distributions are not Gaussian in either HPA (Fig. 4-3). Small pores are dominant. No standard deviations are calculated. For ARCO, modal, not mean radii. For AVCO, mean radii.

4.1 Variables

Variables are as listed in section 3.7, except for:

$\tilde{L}_2$ normalized grain size; i.e. $\bar{L}_2/\bar{L}_2^o$; [-]

ρ absolute density; [g/cm^3]

ρ_o absolute initial density; [g/cm^3]

ρ_{th} absolute theoretical density; [g/cm^3]

$\Delta\rho$ change in absolute density; [g/cm^3]

σ absolute uncertainty in an experimental data point

A/R "as-received"

Fig. 4-1.1 (cont'd on next page)

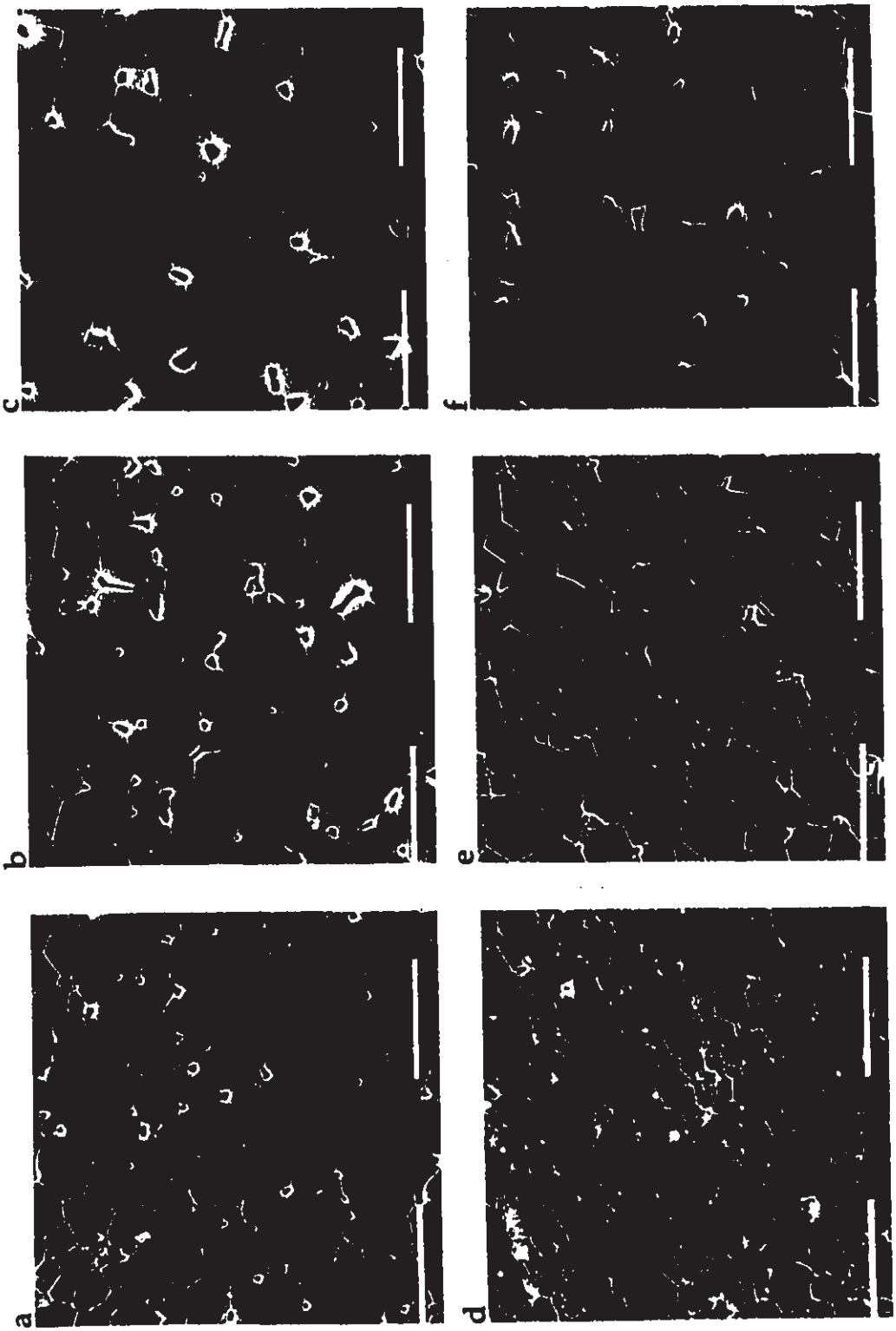

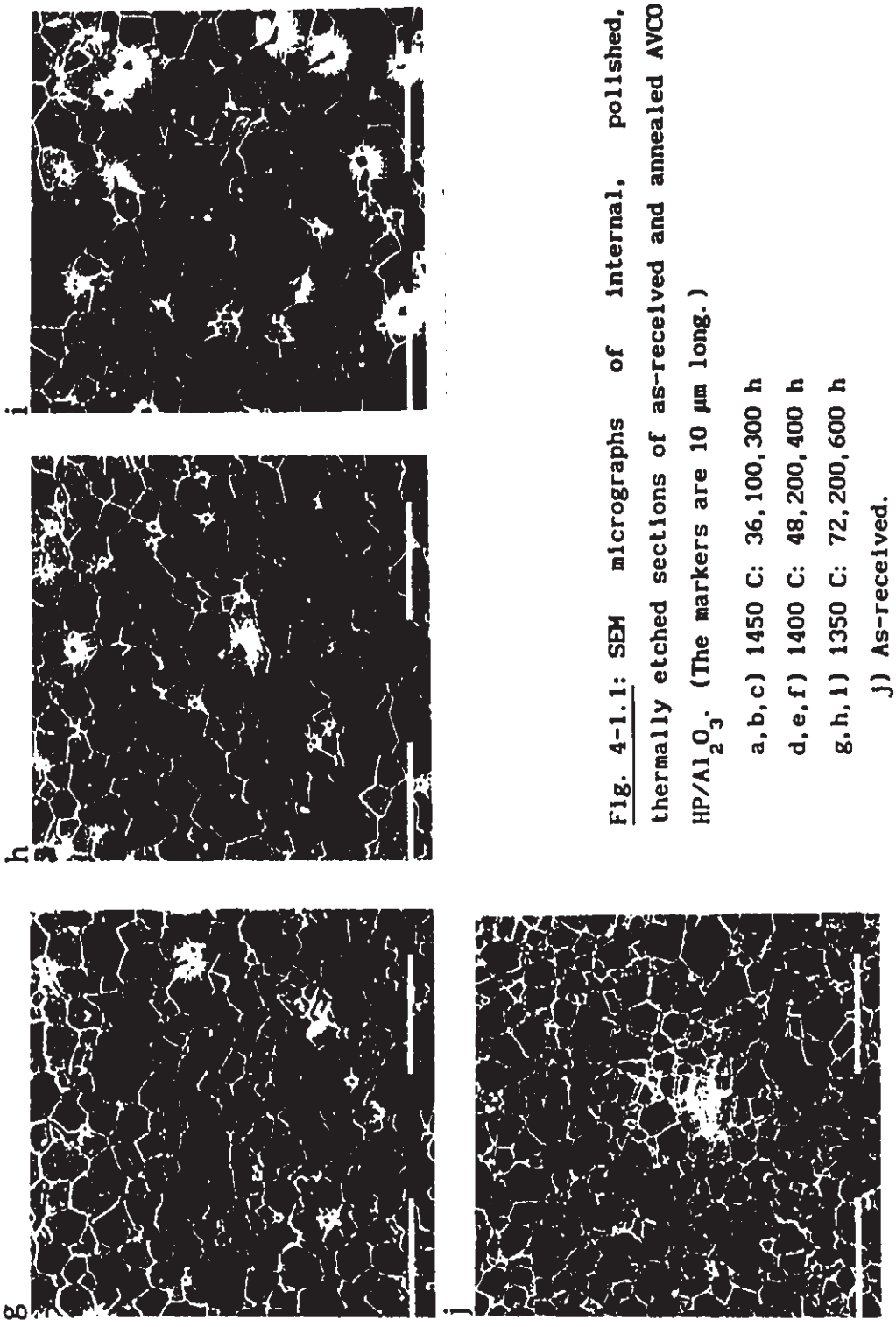

Fig. 4-1.1: SEM micrographs of internal, polished, thermally etched sections of as-received and annealed AVCO HP/Al_2O_3. (The markers are 10 μm long.)

a,b,c) 1450 C: 36,100,300 h

d,e,f) 1400 C: 48,200,400 h

g,h,i) 1350 C: 72,200,600 h

j) As-received.

Fig. 4-1.2 (cont'd on next page)

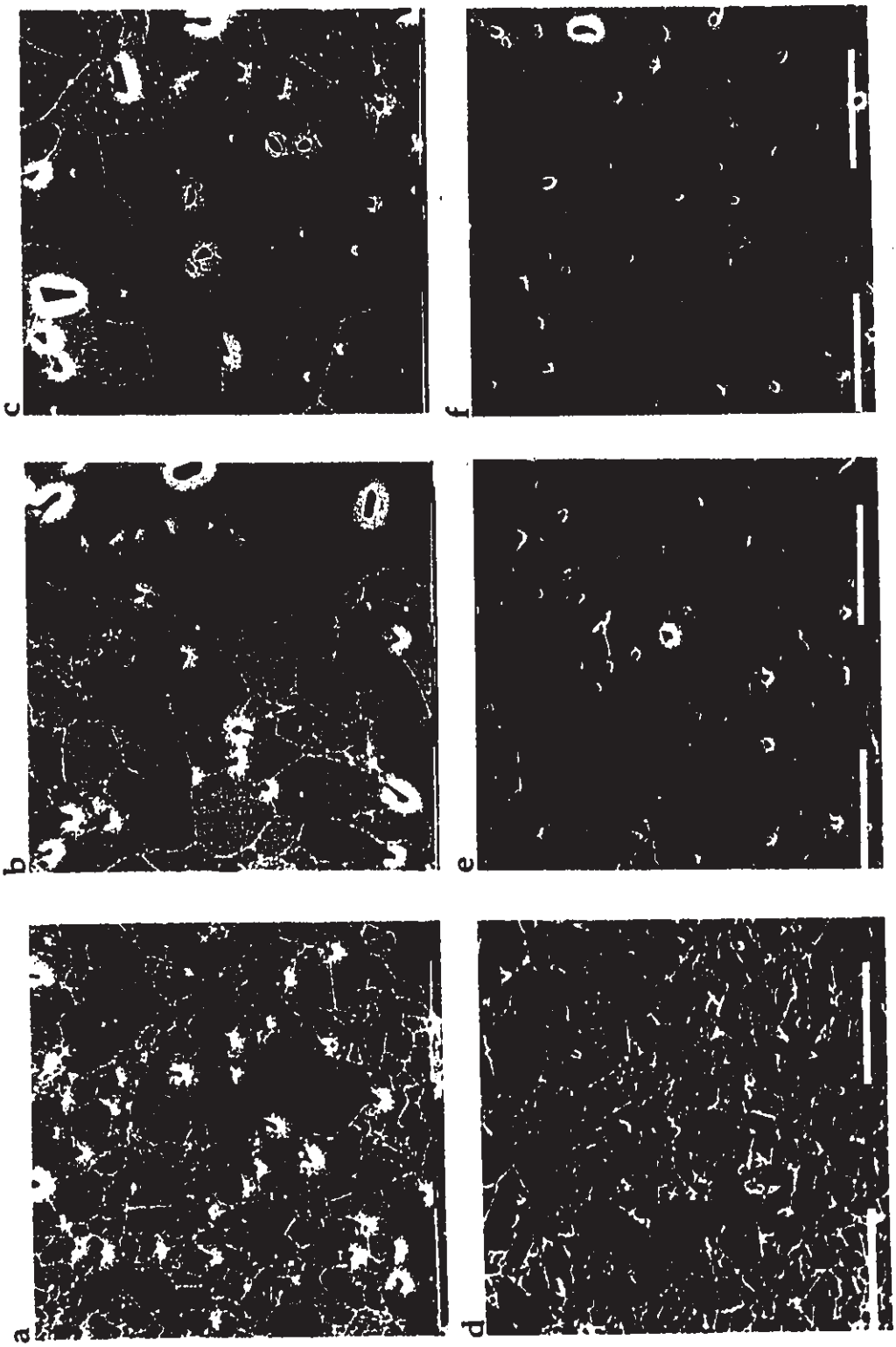

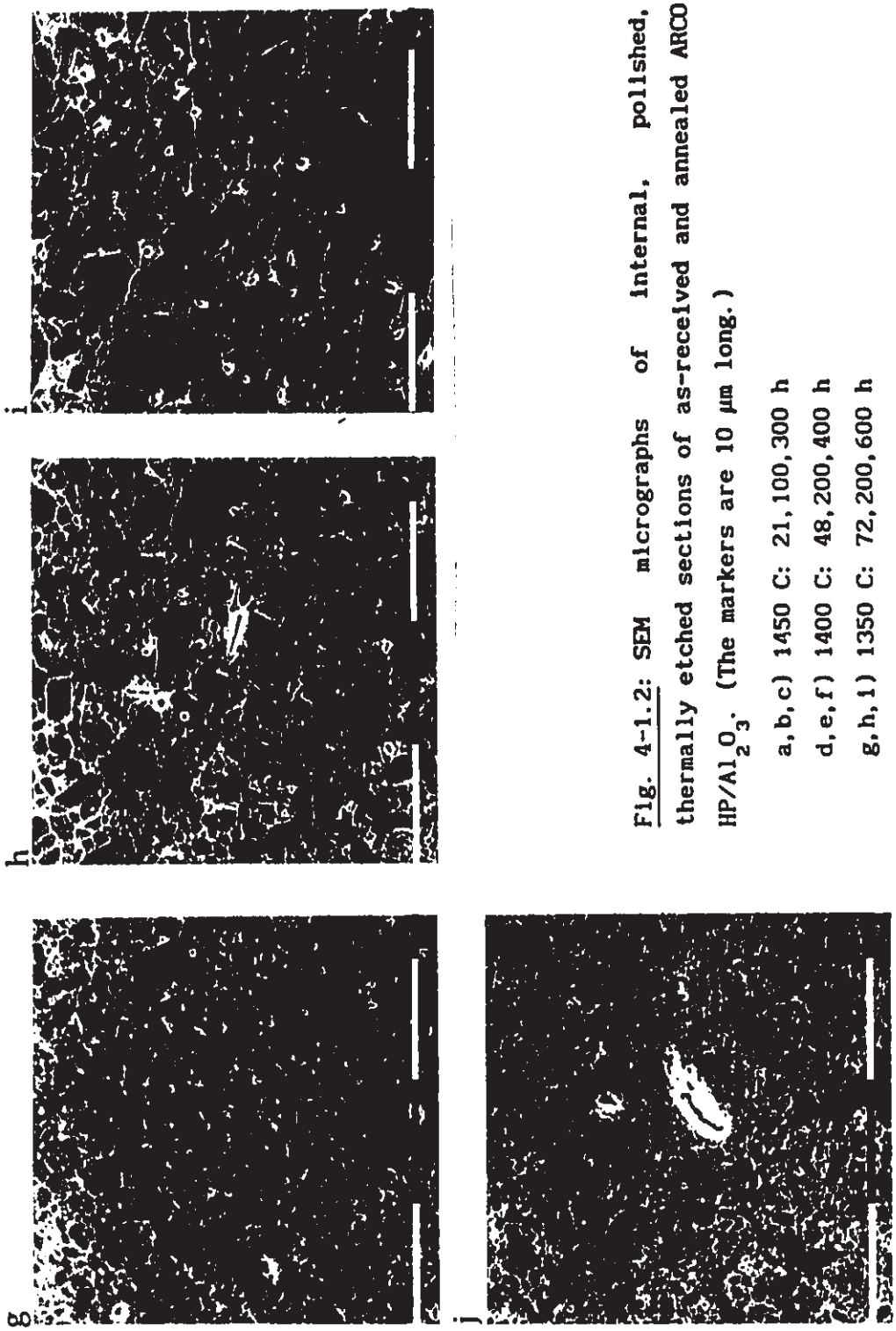

Fig. 4-1.2: SEM micrographs of internal, pollshed, thermally etched sections of as-received and annealed ARCO HP/Al_2O_3. (The markers are 10 μm long.)

a,b,c) 1450 C: 21,100,300 h

d,e,f) 1400 C: 48,200,400 h

g,h,1) 1350 C: 72,200,600 h

j) As-received.

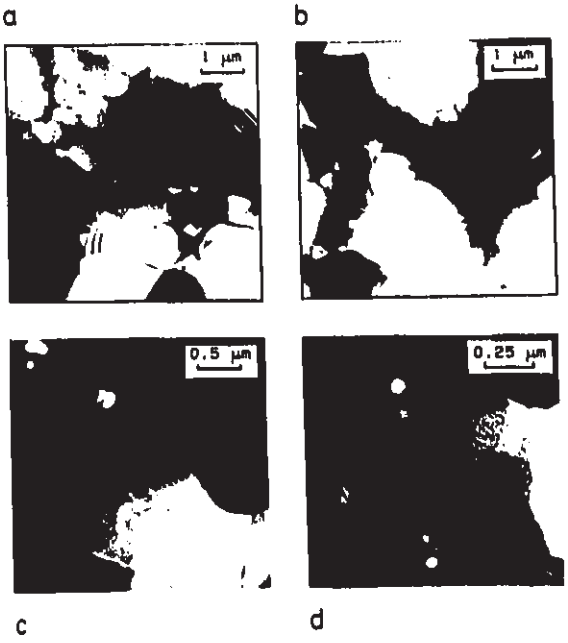

Fig. 4-2: TEM micrographs of as-received HPAs.

a, b) AVCO c, d) ARCO.

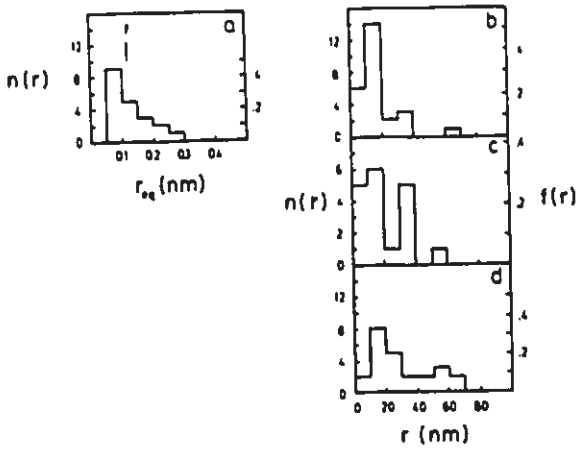

Fig. 4-3: Pore size distributions in as-received HPAs, determined from TEM micrographs.

a) AVCO, typical (20 pores; 2 micrographs).

b) ARCO, from one intRAgranular cluster (27 pores).

c, d) ARCO, typical (19 pores, 24 pores; 2 μgraphs).

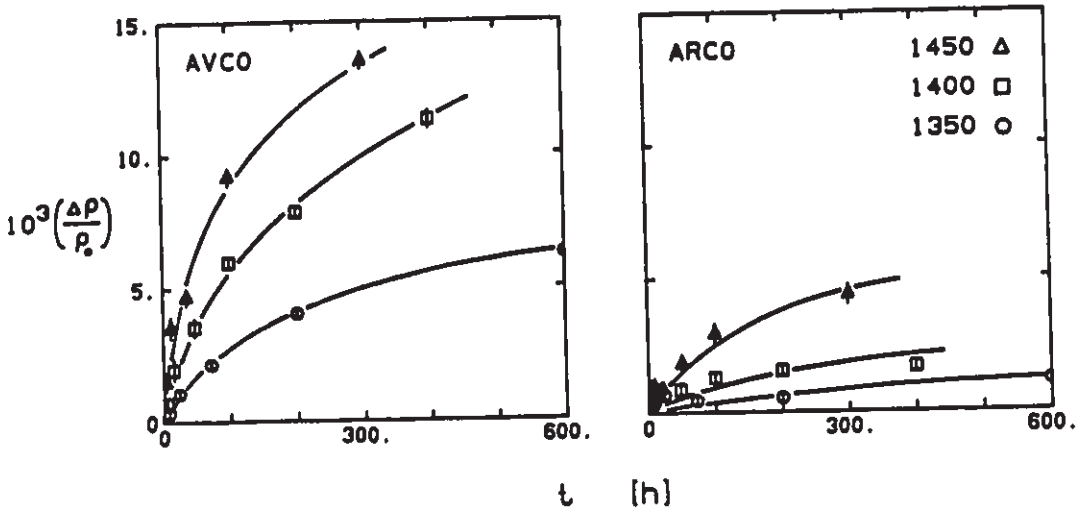

Fig. 4-4: Experimental immersion density changes in annealed ARCO and AVCO HPAs, as a function of annealing time and temperature.

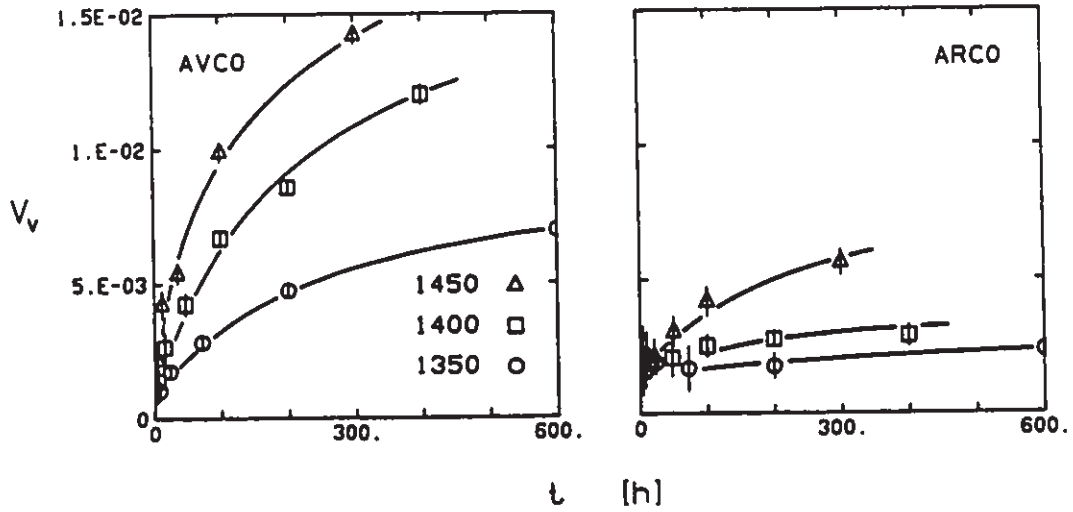

Fig. 4-5: Calculated volume fraction porosity, V_v, in annealed ARCO and AVCO HPA, as a function of annealing time and temperature.

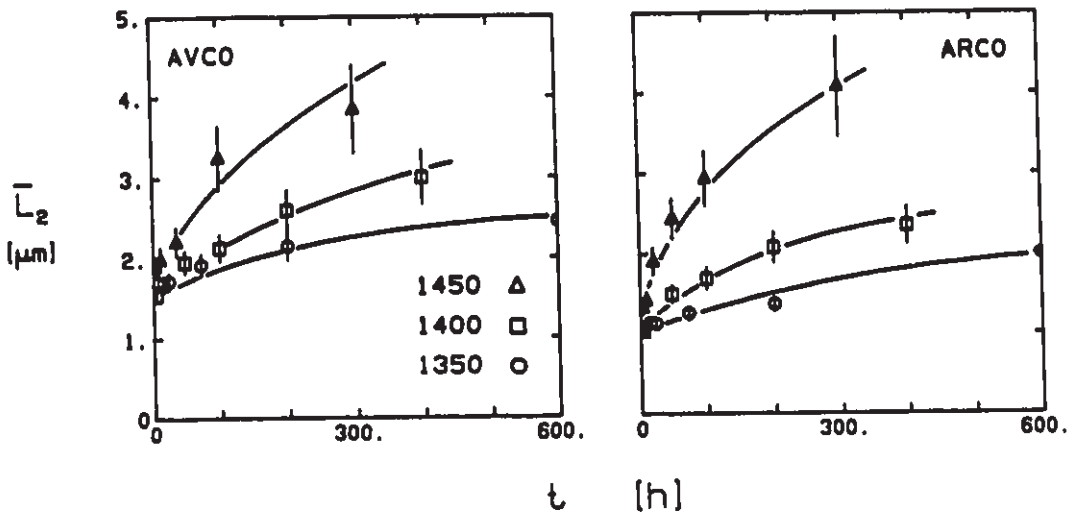

Fig. 4-6: Experimental grain growth in annealed ARCO and AVCO HPAs: mean linear intercept, $\bar{L}_2$, on internal, thermally-etched polish planes, as a function of annealing time and temperature.

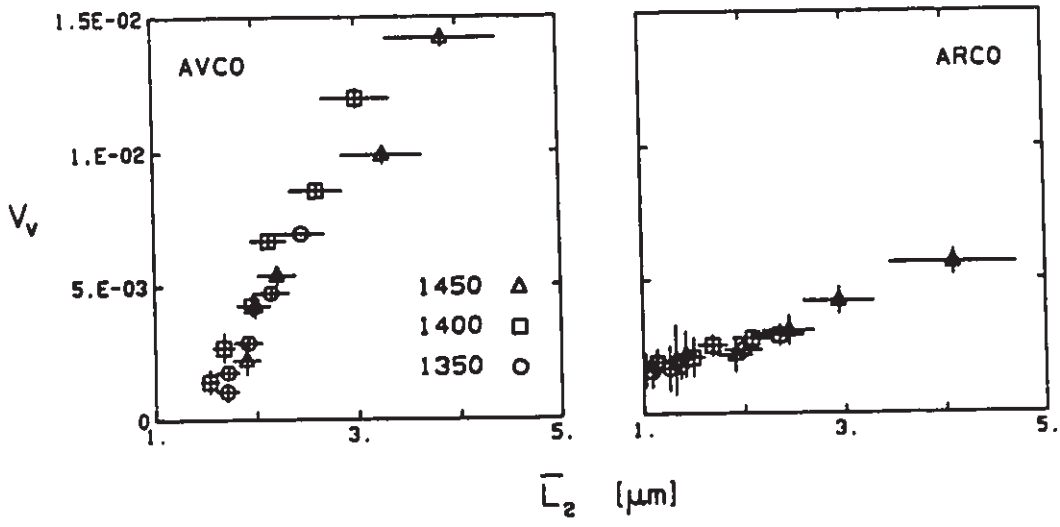

Fig. 4-7: Experimental volume fraction porosity, V_v, as a function of mean grain size, $\bar{L}_2$, in annealed HPAs.

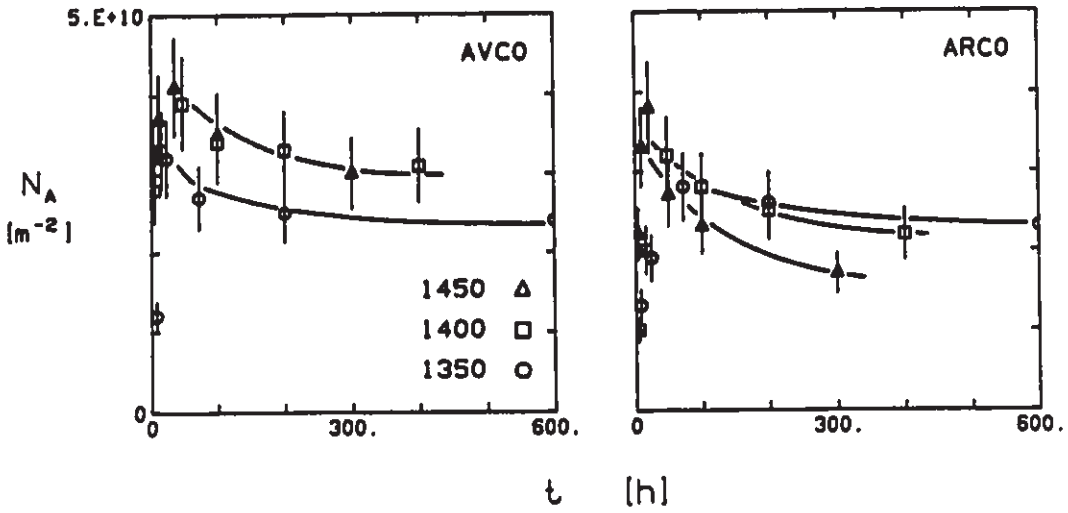

Fig. 4-8: Experimental number of pores per unit area of internal, thermally etched polish plane, N_A, as a function of time.

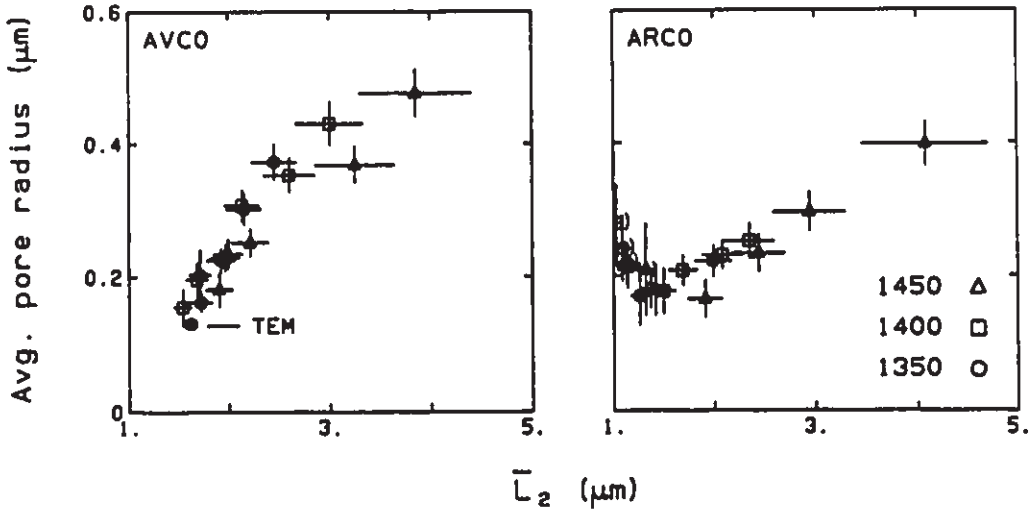

Fig. 4-9: Calculated mean pore size, r, as a function of mean grain size, $\bar{L}_2$, in annealed HPAs. The solid dot is the as-received pore size determined by TEM.

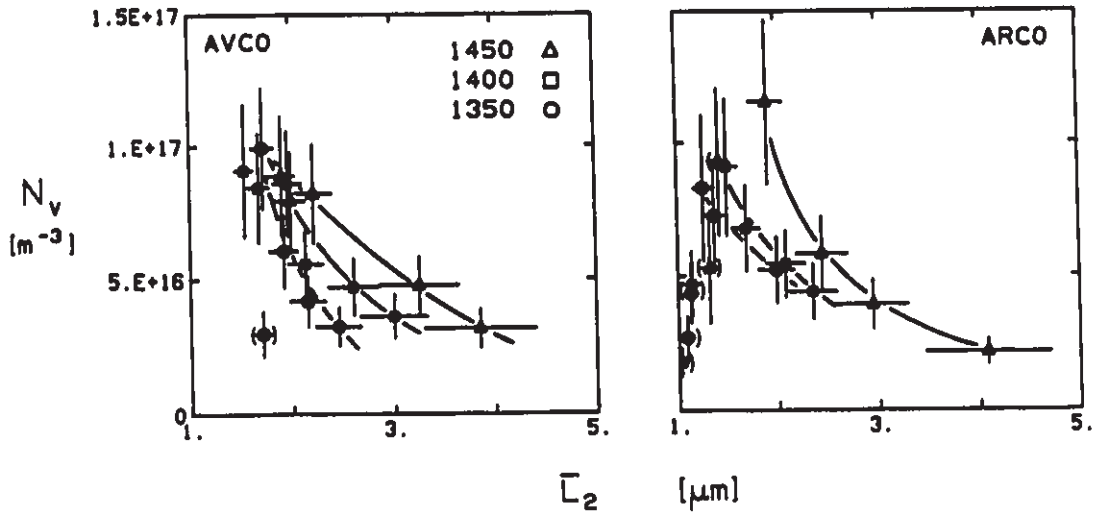

Fig. 4-10: Calculated number of pores per unit volume porous polycrystal, N_v, as a function of mean grain size, $\bar{L}_2$, in annealed HPAs.

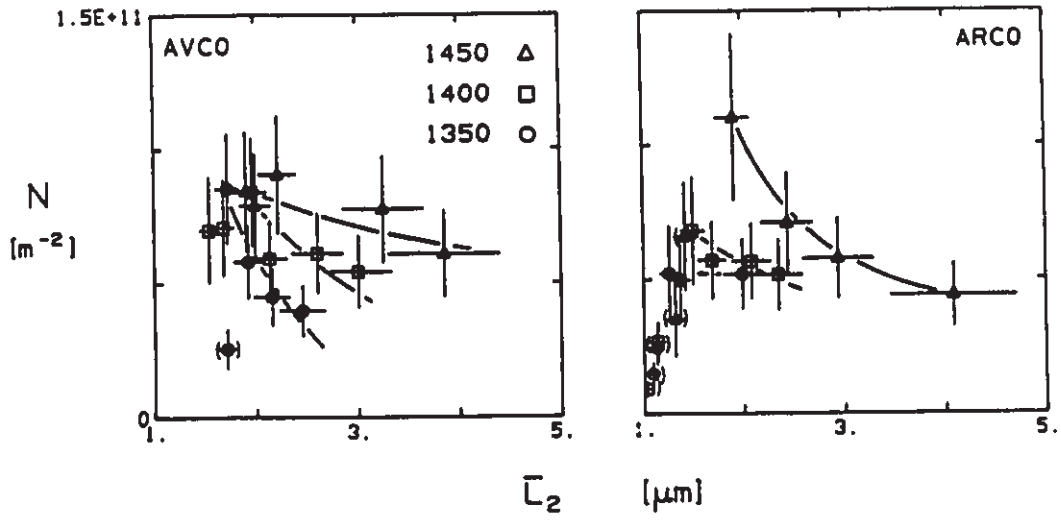

Fig. 4-11: Calculated number of pores per unit area grain boundary, N, as a function of mean grain size.

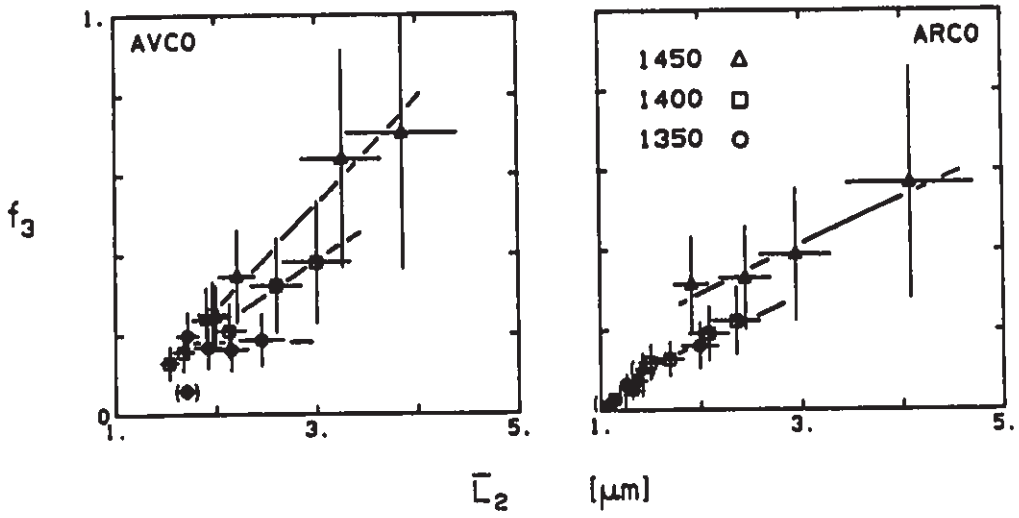

Fig. 4-12: Fraction of four-grain junctions which hold pores, per ideal, equi-S_v, truncated-octahedral grain, f_3, as a function of mean grain size, $\bar{L}_2$.

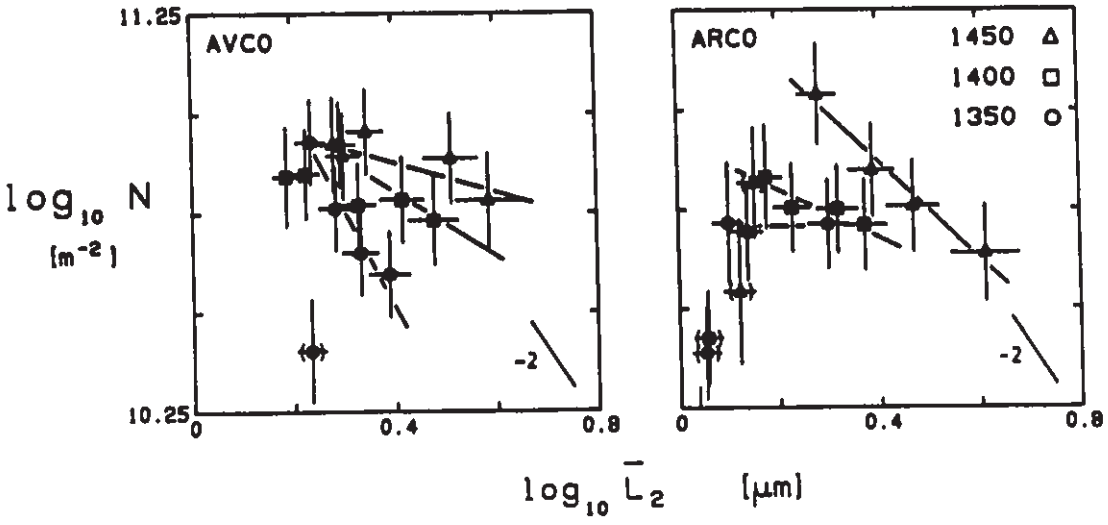

Fig. 4-13: Log-log plot of mean number of pores per unit area grain boundary, N, as a function of mean grain size, $\bar{L}_2$.

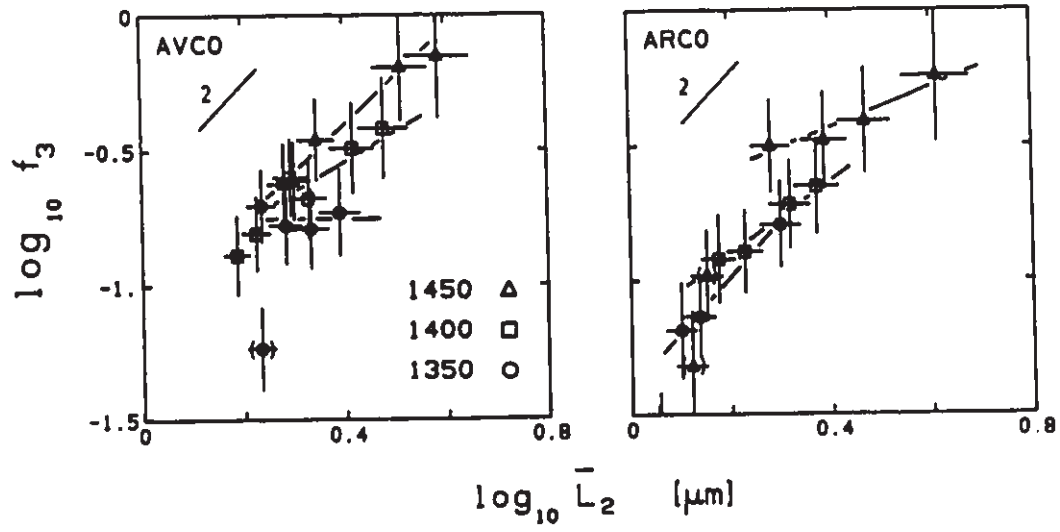

Fig. 4-14: Log-log plot of fraction of available four-grain junctions with pores per ideal grain, f_3, as a function of mean grain size, $\bar{L}_2$.

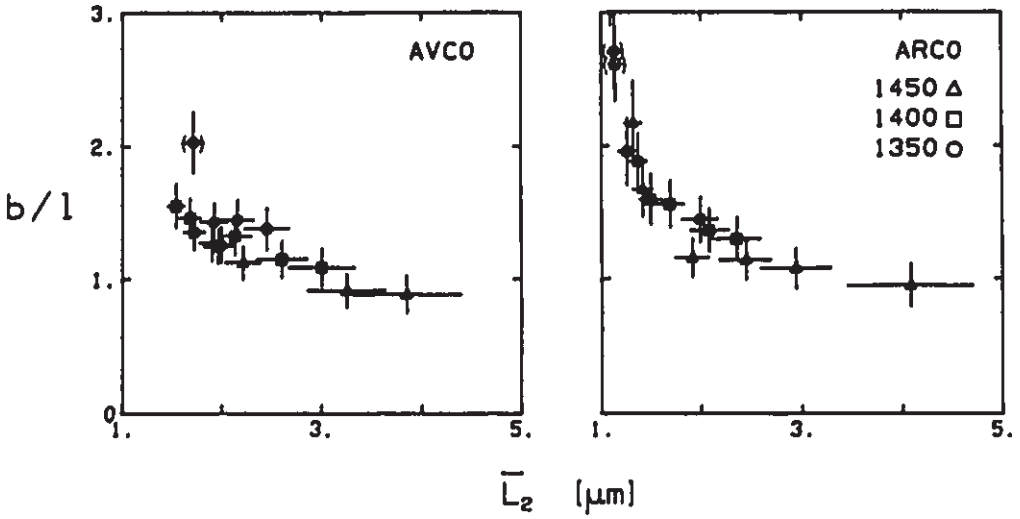

Fig. 4-15: Ratio of the radius of the representative spherical shell, b, to the facet edge length of the equi-S_v ideal grain, ℓ, as a function of grain size.

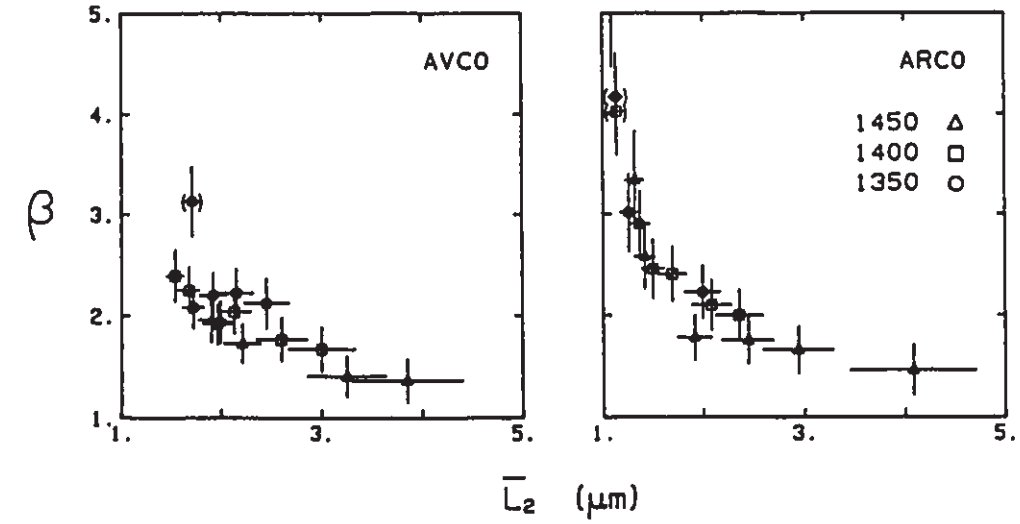

Fig. 4-16: Ratio of grain boundary area in a volume equal to the spherical shell, in the ideal microstructure, to the area of the single boundary disc in the model spherical shell, β, as a function of grain size.

5 Numerical results

In this section, we briefly review the swelling model, describe cases for which numerical solutions were generated, and sketch the dimensions of the computing involved (code size and run times). Then, we present the numerical results. In App. 17, we describe how values were determined for the parameters. Variables are listed in section 5-3.

5.1 Overview

We integrated numerically the coupled differential equations for pore and grain growth rates (Eqs. 8 and 43 in the swelling model), using a fourth-order Runge-Kutta integration algorithm:[1]

[1] DEC RT-11 Scientific Subroutines Package: Subroutine RK2, p. 3-32 in SSP Reference Manual DEC-11-ARSMA-A-D. The Runge-Kutta algorithm was tested against analytic results for the limiting case of drag-free grain growth (Eqs. 43 and 44b in the swelling model). As well, the constraints imposed at each time step in order to generate specific coalescence paths (constant-N_v, -N or -f_3) were tested against theoretical (log N - log $\bar{L}_2$) slopes (see Fig. 4-11 and App. 2).

$$\dot{r} = \dot{r}_P(r, P_{eff}, \ldots) + \dot{r}_L(r, \bar{L}_2, \dot{\bar{L}}_2, \text{path}) \qquad (1)$$

and

$$\dot{\bar{L}}_2 = (a\,\gamma_B/\bar{L}_2) \cdot M_B^{eff}(M_B, M_P(r), N) \qquad (2)$$

As initial conditions, we used experimentally determined mean pore and grain sizes and volume fraction porosity (Table 5-1). We assumed surface diffusion control of pore mobility, but permitted mixed control of grain growth.

In most runs, we assumed that the internal pore pressure (Eq. 19 in the swelling model) included only an *inert* trapped gas term; i.e. that *no* gas was generated internally ($P^G_{int} = 0$). For comparison, in some runs we approximated a gas-generating pore reaction (accompanied by inert trapped gas) by assigning a constant, nonzero value to P^G_{int} (Figs. 5-9, 5-10 only). The two-term P_{int} permitted modeling a range of pore gas mixtures, which could contain inert (e.g. N_2 or Ar) and reactive components (e.g. O_2) or reaction products (CO_x, SO_x; Coble, 1962; Rice, 1969; Bennison and Harmer, 1985b).

In all cases (whether or not we assumed that gas was generated in pores during swelling) we solved the model for three limiting microstructural paths — the two which bounded our experimental data, constant-N and $-f_3$, and, for comparison, constant-N_v, from which coalescence was excluded. Polycrystals swelling with very

little grain growth would follow constant-N_v paths at pore volume fractions low enough to exclude immobile pores touching by pore growth alone. Constant-N_v results show the consequences of neglecting coalescence in the model, by contrast with constant-N and -f_3 results.

All constant-f_3 cases were calculated for an f_3 equivalent to approximately one pore per grain (Table 5-1; Fig. 4-10).[2] For AVCO HPA, f_3 retained this value only in experimental data for 1350 C; however, *variable*-f_3 runs for the other temperatures were *bounded* by constant-N runs (App. 2).

We solved the model to 600 h of swelling, with a fixed time step of 60 s (the results were unchanged for time steps ranging from 1 to 60 s). The program was coded for speed; that is, with only one function (for B_3) and no subroutines. The source file was about 750 lines, or 20 kB. Run in double precision FORTRAN 77 (Lahey LP77), 100 model hours required about 2.5 minutes on a 12 MHz-80286/8 MHz-80287 microcomputer.[3] Adaptive step-size control likely would give faster runs (Press et al., 1986: p.

---

[2] This f_3 value was used in *all* the numerical calculations presented here. Comparable runs for AVCO at different f_3 could *not* be made simply by changing *only* f_3: many key variables were geometrically coupled (e.g. f_3° and V_v°, for constant r_o and $\bar{L}_2^\circ$).

[3] VAX 8650 runtimes, in double precision F77, were about 15 times faster, and gave identical results.

554).

TEM data (Fig. 4-13) showed that AVCO's — but not ARCO's — as-received porosity was intergranular, as we assumed in the model. We therefore fit the numerical results *only to AVCO's* experimental data.

5.2 Numerical results

The numerical results plotted in Figs. 5-1 to 5-8 are for runs with only *inert* gas trapped in pores ($(P_l V_v)_{ehp}$ = 0.02 MPa; P^G_{int} = 0). Figs. 5-9 and 5-10 assumed the same inert trapped gas, but included nonzero values for P^G_{int} as well.

In Fig. 5-1, grain growth was more rapid when coalescence was excluded (constant-N_V), and slowest for rapid coalescence (constant-f_3). This occurred because P_{eff}, and with it, pressure-driven pore growth rates, $\dot{r}_p$, fell rapidly to low values (Figs. 5-2,-7,-8). Subsequently, coalescence-driven pore growth rates and P_{eff} (and so, $\dot{r}_p$) remained higher for constant-f_3 cases than for constant-N (Figs. 5-7,-8), and were higher than when coalescence was excluded. Grain growth was slower in microstructures with drag from larger pores.

Fig. 5-2 shows the ratio of coalescence to pressure-driven pore

growth rate components, $(\dot{r}_L/\dot{r}_P)$. The ratio rose steeply from values of about 0.01, to values in the range 1 to 2, after a time which depended on the trajectory and temperature.[4,5] That is, when coalescence was included, the $\dot{r}_P$ term *never* became negligible, relative to the coalescence component of pore growth rate, $\dot{r}_L$.

The linear relationship between porosity and grain size, observed experimentally, was found only for small, but still reasonable values of the grain boundary diffusion coefficient (Figs. 5-3,-4; Apps. 15,17). (During fitting, smaller δD_B were compensated for by larger $(P_i V_V)_{ehp}$; App. 17.) For such 'linear' values of δD_B, $\dot{r}_P$ remained high for long periods, and, while high, masked the differences in purely coalescence pore growth rate component, $\dot{r}_L$, between different microstructural paths (Figs. 5-3,-4). When coalescence was *excluded* by holding N_V constant, swelling and pore growth ceased by the time the microstructure reached a temperature-*in*dependent grain size of about 2.5 μm. Coalescence permitted swelling to continue.[6]

---

[4] For constant-f_3 paths, though x_i is higher than for constant-N (Ch.3's Eq. 31), P_{eff} remains higher also (Fig. 5-8).

[5] For constant-N_V cases, the ratio $(\dot{r}_L/\dot{r}_P)$ was zero throughout swelling, by definition (Eq. 31 in the swelling model); curves for these cases could not be plotted on this figure.

[6] See the final paragraph in App. 17.

The *area* number density of pores, N_A (Fig. 5-5), depends both on pore size and *volume* number density, N_V (DeHoff and Rhines 1968, p.131). For spherical pores:

$$N_A = N_V \cdot 2r \qquad (3)$$

For constant-N_V trajectories, the numerical N_A curves in Fig. 5-5 rose rapidly at short times, due solely to pressure-driven pore growth (Fig. 5-2). When the trapped gas driving force had dissipated itself, and the effective pressure had decreased to zero (Figs. 5-7,-8) N_A was constant, and the curves were flat. Because the initial P^I_{int} was weakly temperature dependent, at higher annealing temperatures, a slightly higher constant value of N_A was reached. For constant-N and -f_3 cases, however, the curves passed through maxima, as the decreasing, pressure-driven pore growth rate was overtaken by grain growth-driven pore coalescence (Fig. 5-2), which reduced N_V more rapidly than it increased mean pore size.[7] (From Fig. 5-2, at such long t, coalescence-driven $\dot{r}_L$ increased to values of between one and two times $\dot{r}_P$.) For a given path (constant-N or -f_3) the grain growth

---

[7] The fit is more difficult to gauge in this figure than in Figs. 5-1, 5-3, and 5-4, but again is best judged by the overall position of experimental points, for one temperature, within the curved, fan-shaped region which is bounded by constant-N and -f_3 curves for that temperature (see also Figs. 5-11,-12). The fit is good for 1450 and 1400 C points.

rate increased with temperature (Fig. 5-1), and with it the time rate of coalescence, so N_V and N_A fell to lower values. All constant-f_3 curves were below constant-N curves, showing that the higher rate of coalescence is not offset by the higher pore size (Fig. 5-4) and drag (Fig. 5-6). However, a material such as AVCO, in which the pore coalescence rate changes from constant-f_3 to constant-N as the temperature increases, will show a minimal or reversed dependence of N_A *vs* time on temperature (Figs. 4-8,5-5).

Yan et al. (1980) assume pore drag control of grain growth, in order to generate analytic solutions. However, in the current numerical calculations, we retained *mixed* control. Fig. 5-6 compares the mixed, effective boundary mobility, M_B^{eff}, to the values it would have had, had we assumed drag control.

In the phenomenological model for pore drag, the effective boundary mobility takes different values for the two limiting cases. For purely grain boundary mobility control, $M_B^{eff} \rightarrow M_B$, while for pore drag control, $M_B^{eff} \rightarrow (M_P/N)$. For *mixed* control:[8]

$$M_B^{eff} = \frac{M_P}{N + M_P / M_B} \qquad (4)$$

In such cases, M_B^{eff} is smaller than in *either* of the two limiting

---

[8] We assume *one* controlling pore mobility mechanism; i.e. $M_P^{eff} \rightarrow M_P$ (Ch.3's Eq. 36).

cases. Fig. 5-6 shows the ratio of the effective boundary mobility under *mixed* control, to the instantaneous values the mobility would have had in these microstructures, if pore *drag* had been controlling:

$$\tilde{M}_2 = M_B^{eff} / (M_p/N) \qquad (5)$$

An $\tilde{M}_2$ value of one denotes pore drag control; a value of zero denotes no grain growth. Initially, because the pores were small, the systems were under M_B control.[9] However, they evolved rapidly to relatively stable mixed control at $\tilde{M}_2 \approx 0.6$ to 0.8, which was closer to drag control for constant-f_3 than constant-N cases, and at higher T.

Figs. 5-7 and 5-8, showing how the internal, P_{int}, capillarity, P_{cap} and effective pore pressures, P_{eff}, evolved during swelling. In Figs. 5-7a and 5-8a, the magnitudes of all three pressures decreased sharply during the initial, pressure-driven pore growth transient. Figs. 5-7b and 5-8b magnify the y-axis, showing how trajectory and temperature influence these pressure changes.

---

[9] We can define an effective boundary mobility normalized by the boundary mobility of the pore-free matrix:

$$\tilde{M}_1 = M_B^{eff} / M_B \qquad (f1a)$$

$$= 1 - \tilde{M}_2 \qquad (f1b)$$

For low $\tilde{M}_2$, $M_B^{eff} \approx M_B$.

Figs. 5-7c and 5-8c, enlarge the y-axis again, showing only P_{eff}.

The ranges of the *initial* pressure components, P^{o}_{int} and P^{o}_{eff}, were about 1 MPa, on magnitudes of approximately 24 and 18 MPa, respectively.[10] As the initial P^{o}_{cap} were constant, these narrow pressure ranges reflect the small temperature difference between T_{HP} and annealing temperatures, which affected the trapped gas component, P^{I}_{int} (App. 4).[11]

P_{int} decreased rapidly (as r^{-3}), and with it, P_{eff}. The magnitude of P_{cap} decreased more slowly (as r^{-1}; Figs. 5-7a,-8a). In constant-N_V cases, in which coalescence was excluded, P_{eff} decreased to zero at a rate dependent on δD_B and temperature (Figs. 5-7c,-8c). In contrast, when coalescence was included, P_{eff} fell to low, but *non*zero values, remaining some 3 to 10 times larger for constant-f_3 than for constant-N cases, depending on the temperature (Figs. 5-7c,-8c).[12] The higher P_{eff}, in constant-f_3 cases, was primarily due to coalescence reducing the

---

[10] These ranges are given by the pair of braces near the start of the curves, in Figs. 5-7a and 5-8a.

[11] This is the basis for the small temperature sensitivity of long term N_A in Fig. 5-5, for constant-N_V cases .

[12] Linearity in experimental $\{r-\bar{L}_2\}$ and $\{V_V-\bar{L}_2\}$ results set an upper limit to δD_B, and so set maximum rates for pore pressures decreasing, given a fit P^{o}_{eff} value.

magnitude of P_{cap} more rapidly than for constant-N cases, throughout swelling; i.e. after P^{I}_{int} had dissipated itself (Fig. 5-8*b*).

Fig. 5-9 and 5-10 present results for swelling simulations in which chemical reactions were assumed to maintain a constant partial pressure, P^{G}_{int}, in addition to inert trapped gas, P^{I}_{int}. The swelling model was integrated numerically, without changing the other parameter values for the inert trapped-gas case (Table 5-1). Progressively larger values of P^{G}_{int} were assigned in different runs, over the range 0.1 to 10 MPa. In Fig. 5-10, P^{G}_{int} had a value of 1.0 MPa.

In Fig. 5-9, for all three temperatures and all trajectories, a constant reaction pressure, P^{G}_{int}, of 0.1 MPa caused a small increase in the time rate of swelling, relative to inert gas cases. Much larger increases in swelling rates occurred for P^{G}_{int} of 1.0 MPa, and the effect was more extreme at higher temperatures. For pressures somewhat greater than 1 MPa, for constant-N and -f_3 cases, continuous three-grain edge channels likely would develop at 1450 C over the range of swelling times calculated, permitting gas to escape from the sample. For the same P^{G}_{int} and time scale, this would not develop at 1350 C. For a P^{G}_{int} of 10. MPa, swelling was very rapid at all three

temperatures.[13]

For P^G_{int} large enough to alter swelling rates from the inert trapped gas results (> 0.1 MPa) the relative positions of curves for the three trajectories, at any temperature, depended on the value for $\delta D_B\{T\}$. For 'linear' $\delta D_B\{T\}$, pore coalescence made a difference to swelling, in the transitional pressure range (P^G_{int} $\approx$ 1. MPa), only for constant-N cases. In this range, the relative position of constant-f_3 curves was different from inert-gas and higher, nonlinear δD_B cases, being closer to constant-N_v curves. The physical basis for these differences is unclear.

Fig. 5-10 shows P_{eff} against time and grain size, for cases in which the chemically-maintained P^G_{int} was 1 MPa; that is, P^G_{int} was sufficiently large to raise swelling rates significantly from the inert gas case, but was not large enough to cause catastrophic swelling (Fig. 5-9). As expected, for a P^G_{int} of 1 MPa, effective pressures were higher in all cases than for corresponding inert gas cases. (For coalescence cases, the (f_3/N) pressure ratio was approximately two, at any given time.) In constant-N_v cases, P_{eff}

---

[13] The current model applies only to a final stage microstructure, and would require modifications for continuous three-edge pore channels forming, and for gas release, in order to handle such severe swelling. At the maximum V_v values in Figs. 5-9, 0.05, a final stage microstructure should still hold.

did not decrease to zero; P_{eff} for constant-N were about half of the P^{G}_{int} value of 1.0 MPa, but for constant-f_3 cases were approximately equal to P^{G}_{int}. The higher pore drag developing with chemically-maintained pore growth rates, particularly at higher temperatures, is evident when 600 h grain sizes are compared in Figs. 5-10b and 5-8c. In considering how a gas-generating reaction could be distinguished from trapped inert gas, using experimental swelling data, the figure should be compared to Figs. 5-7c and 5-8c, which show corresponding curves for inert pore gas.

For all these cases, for a $\delta D_B\{T\}$ low enough to give *linear* $\{r-\bar{L}_2\}$ and $\{V_v-\bar{L}_2\}$ results, consistent with experimental data, effective pressures declined monotonically. However, other runs (whose results are not given here) used Cannon et al.'s (1980) higher δD_B (App. 15). In these runs, the corresponding results were *not* linear, and, for some paths, and at high T, P_{eff} *did* pass through minima, and then increased, as the driving force component due to inert trapped gas largely dissipated itself, and then the constant, chemically-maintained component continued to drive pore growth, so reducing the magnitude of the capillarity component.

5.3 Variables

Variables are as listed in section 3.7, with the following additions:

$\tilde{M}_1$ effective boundary mobility, normalized by the intrinsic boundary mobility in the same microstructure; [-]

$\tilde{M}_2$ effective boundary mobility, normalized by its value in that microstructure if pore drag controlled; (M_p/N); [-]

$(P_l V_v)_{ehp}$ $P_{int} \cdot V_v$ product at the end of the hot-pressing cycle, at T_{HP}; [N/m^2]

T_{HP} hot-pressing temperature; [C]

Super/subscripts

x^o, x_o For *materials* parameters: pre-exponential.
For *microstructural* parameters, an initial value.

x_L For *diffusion* parameters, denotes 'Lattice'.
For *other* parameters, denotes grain size as $\bar{L}_2$, not $\bar{G}$.

Table 5-1: Values used in numerical integration, for AVCO HPA.

Ω^{Al} = $2.12 \cdot 10^{-29}$	$[m^3]$	App.	15
δD_B^o = $5.5 \cdot 10^{-8}$	$[m^3/s]$	"	15
Q_B = 500.	[kJ/mol]	"	15
ωD_S^o = $7.5 \cdot 10^{-3}$	$[m^3/s]$	"	15
Q_S = 650.	[kJ/mol]	"	15
$g\{\psi = 90^o\}$ = 0.3	[-]	"	3
$\gamma_B = \gamma_S$ = 1.	$[J/m^2]$	"	15
a_L = 0.3	[-]	"	9
β = 1.8	[-]	"	5
K_L^o = $3.8 \cdot 10^{-5}$	$[m^3/N \cdot s]$	"	9, 15
$Q_K = Q_L$ = 577.	[kJ/mol]	"	9, 15
m = 3	[-]	"	9
$(P_l V_V)_{ehp}$ = 0.02	[MPa]	"	4
T_{HP} = 1500	[C]	Dorre and Hubner (1984) p.204	
P_{int}^G = 0.0, 0.1, 1.0, 10.	[MPa]	"	5

Self-consistent initial microstructural parameters (AVCO):

$N_V^* = N_V^o = 1.08 \cdot 10^{17}$	$[m^{-3}]$	$V_V^o = 0.78 \cdot 10^{-3}$	[-]
$N^* = N^o = 8.77 \cdot 10^{10}$	$[m^{-2}]$	$r_o = 0.12$	[μm]
$f_3^* = f_3^o = 0.18$	[-]	$\bar{L}_2^o = 1.62$	[μm]

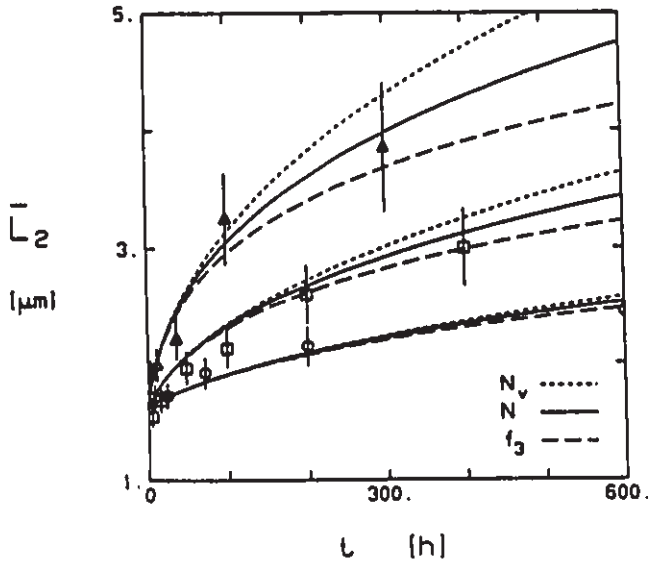

Fig. 5-1: Grain size, $\bar{L}_2$, as a function of time and temperature.

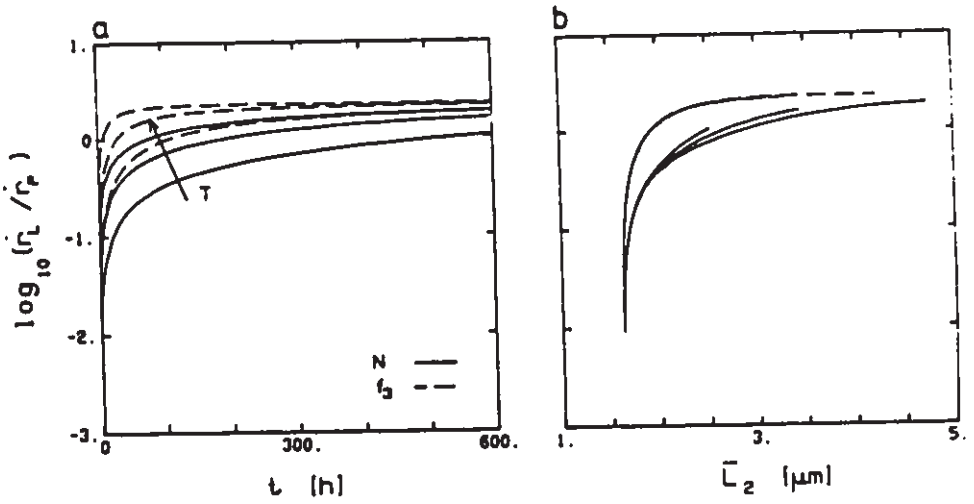

Fig. 5-2: Ratio of the pore growth rate component due to coalescence, $\dot{r}_L$, to the component due to effective pressure, $\dot{r}_P$, as functions of time and of grain size. For constant N_v cases, there is no coalescence component; no curves are drawn.

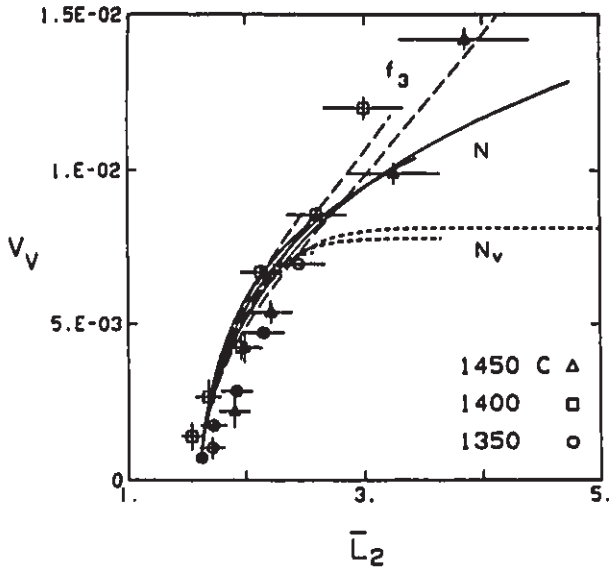

Fig. 5-3: Volume fraction porosity, V_v, as a function of grain size and temperature. The solid dot is the as-received V_v.

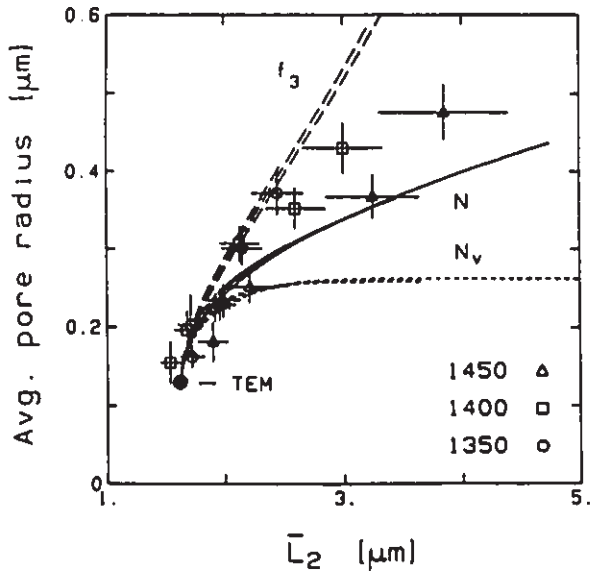

Fig. 5-4: Pore size, r, as a function of time and temperature. The solid dot is the as-received pore size, as determined by TEM.

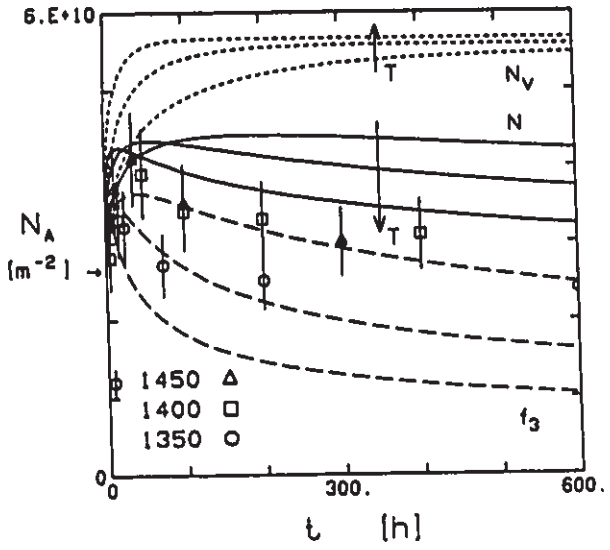

Fig. 5-5: Number of pores per unit area internal polish plane, N_A, as a function of time and temperature. The small arrow shows the common *initial* N_A.

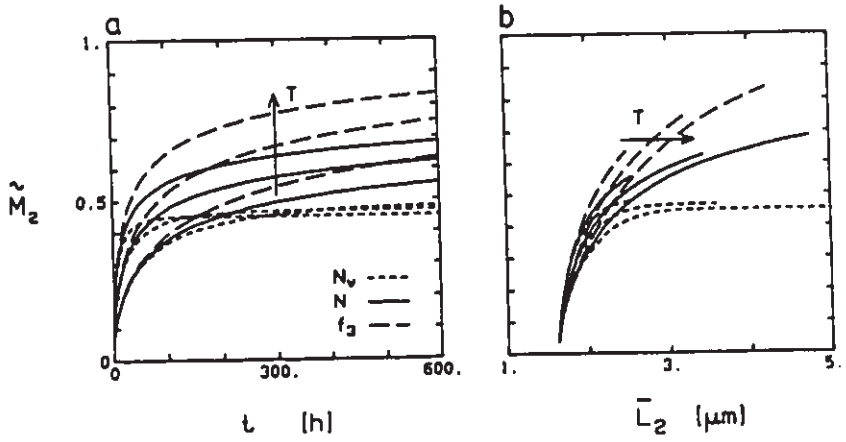

Fig. 5-6: Effective grain boundary mobility, M_B^{eff}, normalized by the boundary mobility for pore drag control, (M_p/N), as a function of (a) time and (b) grain size.

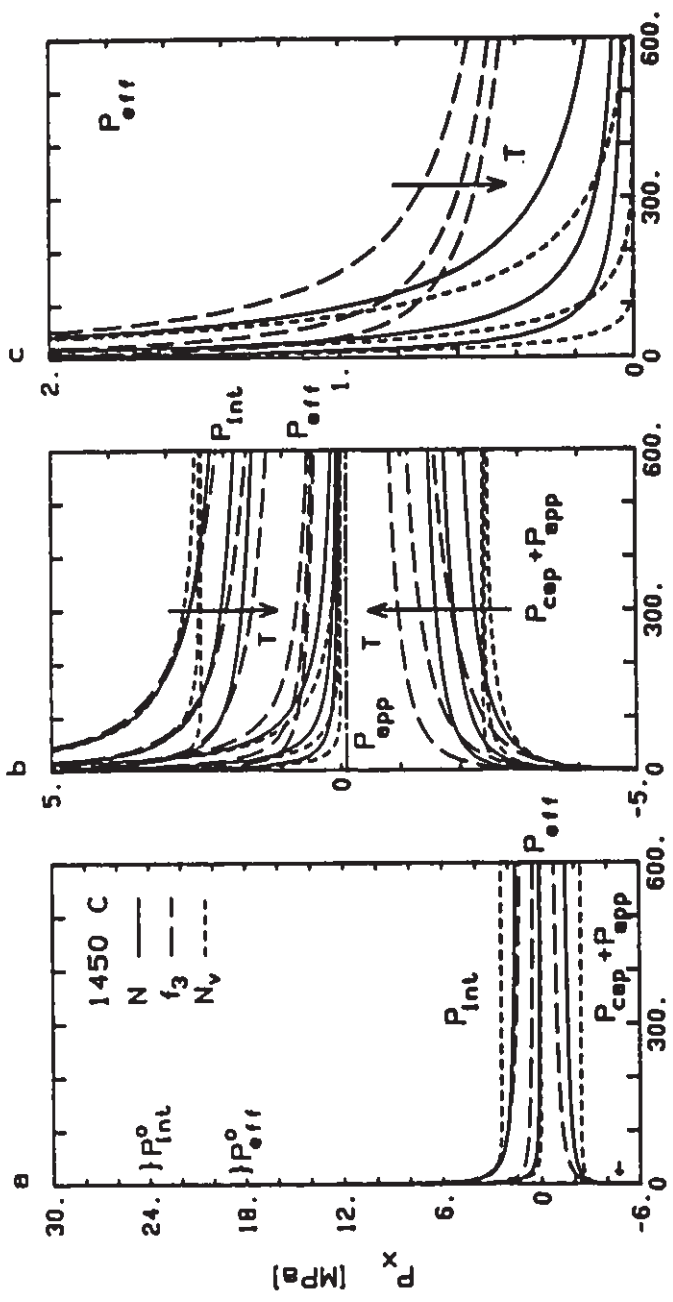

Fig. 5-7: Pore pressure components as functions of time, for swelling in AVCO driven by *inert trapped gas*.

a) Results for 1450 C only. Braces show *initial* internal and effective pressure ranges; the small arrow, the initial capillarity (plus applied) component; (b) all temperatures and pressure components, on an expanded vertical scale; (c) effective pressures, on an expanded vertical scale.

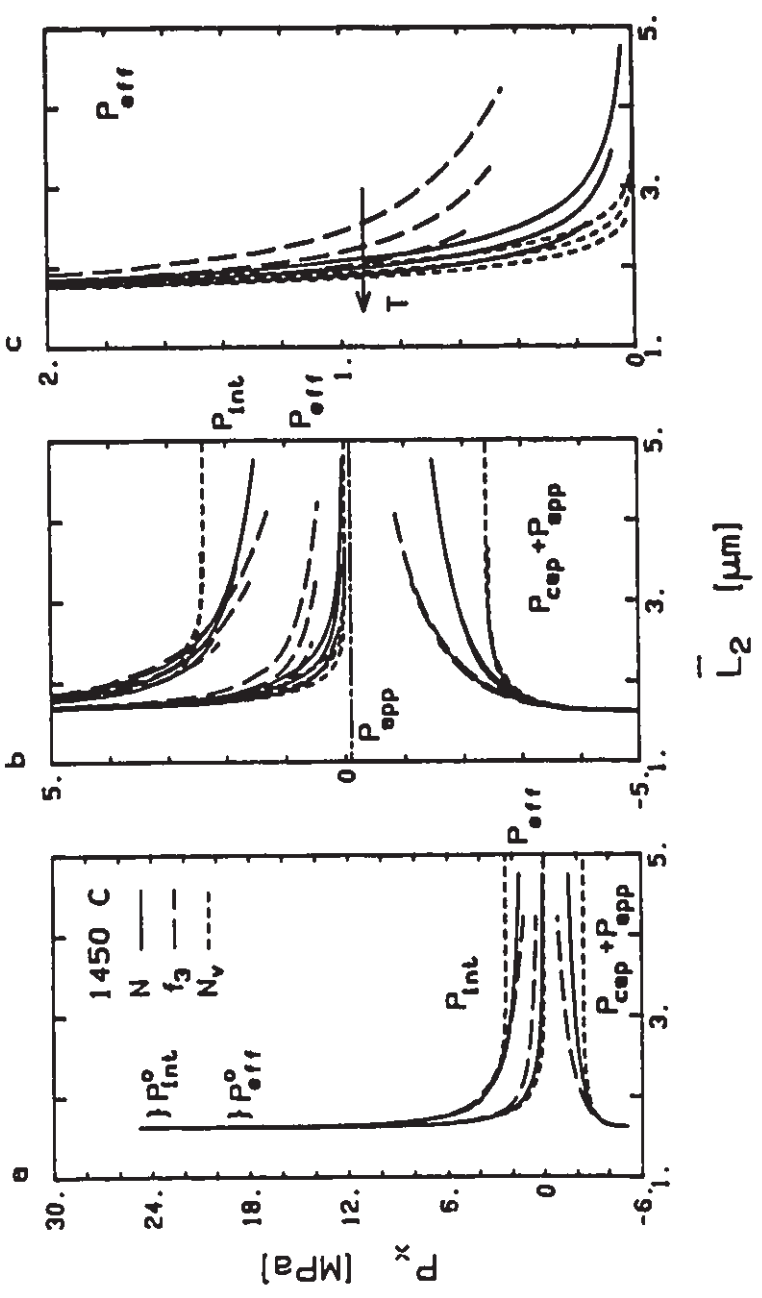

Fig. 5-8: Pore pressure components as functions of grain size, for swelling in AVCO, driven by *inert trapped gas*. Symbols and cases (a,b and c) as in Fig. 5-7.

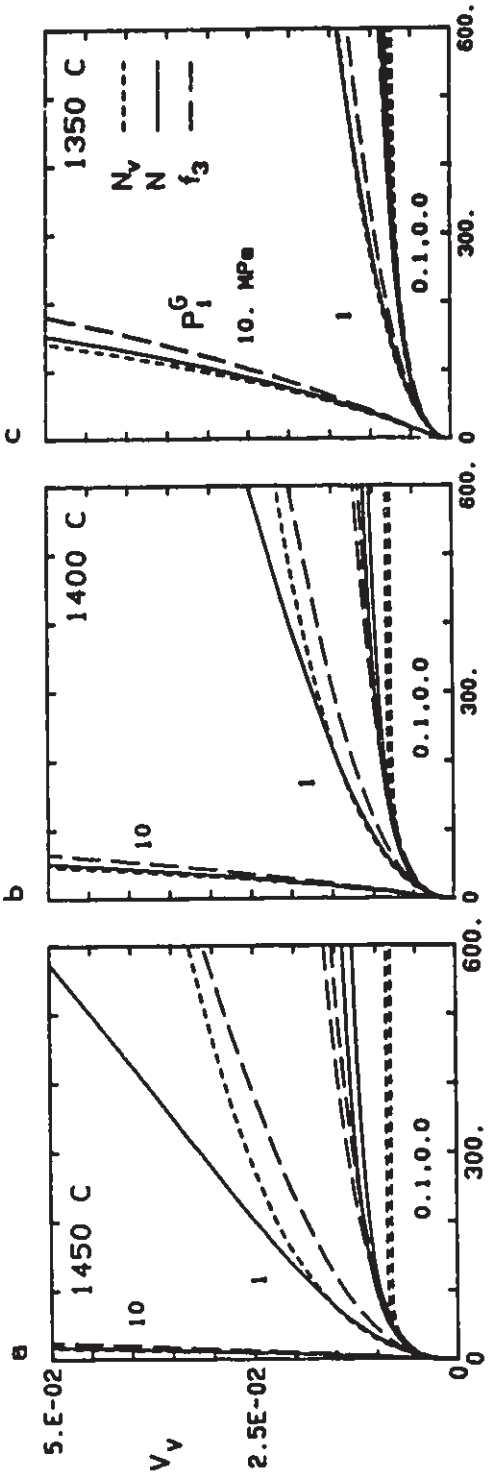

Fig. 5-9: Volume fraction porosity, V_v, as a function of time, when a constant internal pore pressure component, P^G_{int}, is superimposed onto the inert trapped gas results for AVCO. The curves shown are for P^G_{int} values of 0.0, 0.1, 1.0, and 10. MPa.

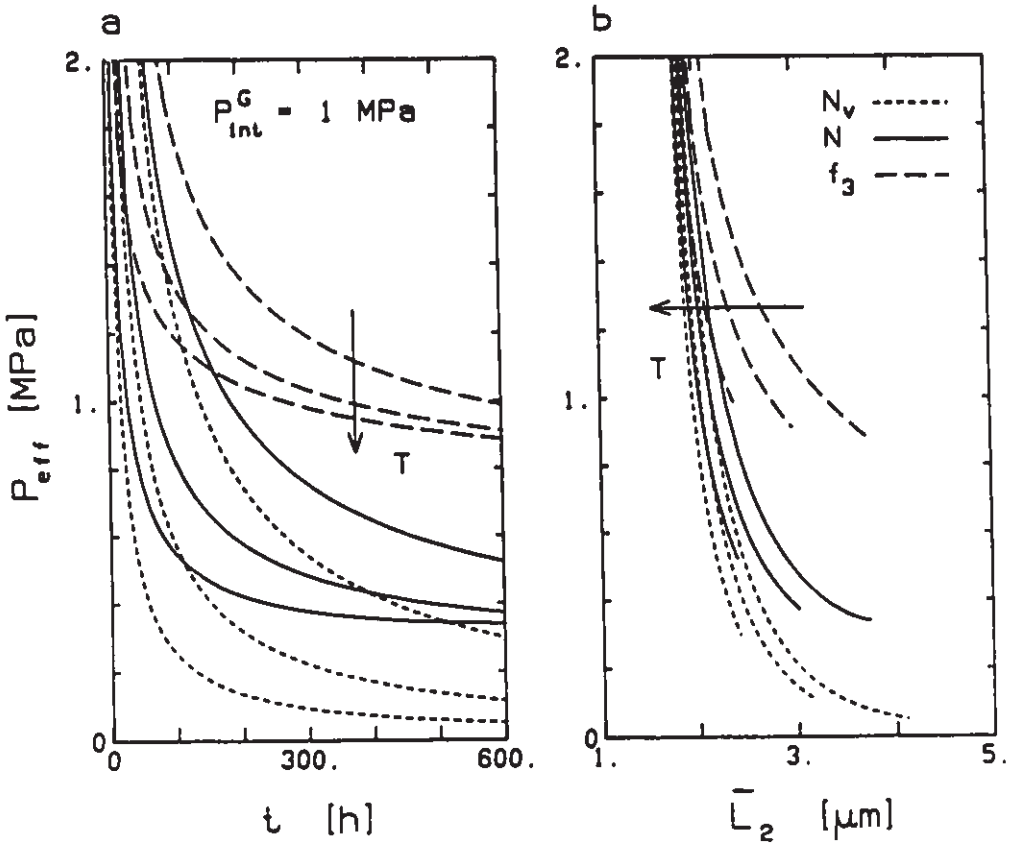

Fig. 5-10: *Effective* pore pressures as a function of (a) time and (b) grain size, when AVCO's internal pressure includes both inert gas and a transitional P^G_{int} value of 1.0 MPa.

6 Discussion

This section is divided into two parts. In the first, 6.1, we review the model, and discuss, for example, detail in the model *vs* parameter uncertainties, paths and coalescence, and the internal pressure term. We also summarize what the numerical simulations have established about the physical processes in swelling with ongoing coalescence. In the second part, 6.2, we discuss the original questions listed in section 1.1, concerning swelling in creep fracture. Variables are listed in section 6.3.

6.1 General

6.1.1 The swelling model

The swelling model developed in Ch.3 includes two pore growth rate components — one diffusional, driven by pore pressures ($\dot{r}_p$), and one from grain growth driven coalescence ($\dot{r}_L$; variables are listed in section 3.7):

$$\dot{r} = \dot{r}_p + \dot{r}_L \qquad (1)$$

The pressure-driven component, which has been included in various forms in previous swelling models (section 1.2.4) is:

$$\dot{r}_p \propto \frac{\delta D_B}{kT} \cdot P_{eff} \qquad (2)$$

in which the effective pore pressure is:

$$P_{eff} = P_{int} - P_{cap} - P_{app} \qquad (3)$$

The internal pressure component, P_{int}, is the sum of a term due to trapped inert gas (P^I_{int}) and a term due to gas generated in pores by a chemical reaction (P^G_{int}; Apps. 4,5):

$$P_{int}\{t\} = P^I_{int} + P^G_{int} \qquad (4a)$$

$$= \frac{(P_i V_v)_o}{V_v\{t\}} + P^G_{int} \qquad (4b)$$

In the current calculations, when P^G_{int} was assigned a nonzero value, it was constant. A pore pressure term with this flexibility has not previously been included in swelling or sintering models.

A pore growth rate component due to grain growth driven coalescence has been included in previous *pressureless sintering* models (section 1.2.2), but only in swelling models for nuclear fuels (Rest, 1986). In the current model, it is:

$$\dot{r}_L = x_1 \left(\frac{r}{\bar{L}_2}\right) \dot{\bar{L}}_2 \qquad (5)$$

in which the value of x_1 depends on the microstructural path (constant-N_v, -N or -f_3; Ch.3, Eq. 31). The grain growth rate, $\dot{\bar{L}}_2$, is:

$$\dot{\bar{L}}_2 = (a_L \gamma_B / \bar{L}_2) \; M_B^{eff} \qquad (6)$$

in which the proportionality factor for normal grain growth, a_L, is on the order of 0.3 to 0.4 (App. 10), and the effective boundary mobility, M_B^{eff}, is (App. 9):

$$M_B^{eff} = \frac{M_P^{eff}}{N + (M_P^{eff} / M_B)} \qquad (7)$$

Surface diffusion control was assumed for the pore mobility, M_P, simplifying M_P^{eff} to M_P in Eq. (7). Mixed M_B/pore drag control was retained; pore drag control was not assumed.

Numerical solutions were generated by integrating together Eq. (1) for the pore growth rate and Eq. (6) for the grain growth rate. Initial conditions were determined from experimental data. The adjustable parameter, $(P_i V_v)_{ehp}$ (approximately equal to $(P_i V_v)_o$, which controlled the initial pore pressure; App. 4) was determined by fitting numerical to experimental swelling data

(App. 17).[1]

While the model was tested only for swelling in hot-pressed alumina in this report, it can be applied to other materials by using suitable values of material, microstructural and process parameters. The current model includes only *diffusional* densification; for swelling, it is unlikely that dislocation creep will contribute to pore growth (Arzt et al., 1983).

However, the model is is sufficiently general to be applied not just to swelling, but also to pressure sintering. While grain growth always results in larger mean grain sizes, pores may either grow or shrink, depending on the effective pressure. Because this flexibility is already included, the current numerical code should be directly applicable in simulating pressure sintering.

While *early* swelling at high relative densities can be modeled with just a final-stage microstructure, a sintering microstructure passes first through initial *and intermediate* stages. Current HIP maps (e.g. Helle et al., 1985) include neither grain growth-driven pore coalescence, nor an intermediate

---

[1] δD_B, while a materials parameter, also was treated as an adjustable parameter. See section 6.1.2, below.

stage.[2] The current swelling model permits including coalescence in the final stage. It also should be extensible to intermediate-stage pressure sintering.

The minimum work which, as a starting point, likely could be modified to generate a pressure-sintering model similar to the current one, but for the intermediate stage, includes:

1) Occhionero's (1984) modification of Yan et al.'s (1980) pressure*less* final-stage model to pressure*less* *intermediate*-stage sintering, and
2) Wilkinson's (1978) final-stage, diffusional pressure-driven model for a *spherical* material element (used here). In modifying this to a *cylindrical* geometry, reference should be made to Tucker's (1981) analysis of pore channel geometries in intermediate microstructures.

For intermediate-stage pressure sintering, that the model currently includes only diffusional densification will have to be checked for different materials. Arzt et al. (1983) claim that it is unlikely that a component being pressure-sintered will *enter* final stage during plastic flow. However, their model includes no

---

[2] For metals which deform by dislocation creep in pressure sintering, omitting the intermediate stage is a reasonable modeling approach. However, it is likely that an intermediate stage will improve maps for materials like ceramics, in which densification is diffusional.

intermediate stage, and it is not clear whether that conclusion holds for a general compact (metallic or nonmetallic).

A HIP instrumented to give continuous shrinkage data during a run, at higher temperatures and relative densities than in, for example, Hsu and Solomon (1983), would permit efficiently testing such a sintering model. However, generating the other microstructural data required (data for pore and grain sizes, and pore geometries, and so internal polish planes, as was done here for swelling) would require many HIP runs — one per specimen. Experimentally, *series* of such samples are generated far more easily from pressureless anneals than from pressure sintering furnaces.

6.1.2 Detail in the model; parameter uncertainties

It is important to consider what level of detail is meaningful in a model in which many parameters are uncertain.

Taken as a whole, the model is more detailed than many previous swelling and sintering models (section 1.2). The detail includes (1) *mixed* control of grain growth (Eq. 7; instead of assuming pore drag control), with (2) a *two-term* internal pore pressure (Eq. 4 and section 6.1.8, below) and (3) *three* limiting microstructural paths (Eq. 5). We now discuss each of these in

turn.

Mixed control of grain growth was included for generality. The model can be applied either to swelling *or* pressure sintering. Including mixed control permits determining how M_B *vs* pore drag control affects microstructural evolution, and permits testing any system for whether pore drag control *can* be assumed.[3] For example, had we assumed drag control in the current numerical simulations, the predicted grain growth rates would have been $\tilde{M}_2^{-1}$ times larger than for the mixed control plotted. That is, from Fig. 5-6, predicted grain growth rates at short times would have been, say, an order of magnitude higher. For swelling, this would have resulted in our fitting a higher boundary mobility activation energy, and lower surface diffusion coefficient, in order to hold down numerical grain growth rates. Were this model applied to pressure sintering, assuming pore drag control would predict similarly high grain growth rates towards the *end* of final-stage densification, during which the microstructures would be similar to those early in swelling.

Retaining mixed control likely did not make a major difference in the current work, due to the rapid dominance of pore drag (Fig. 5-6). However, it is as fast to solve numerically for mixed as

---

[3] Setting M_B^{eff} equal to (M_P/N) in the numerical model will maintain pore drag control.

for pore drag control, and quick to test for the importance of either. Also, from Fig. 5-6, mixed control with a grain size dependent M_B may be important in the pressure anneals suggested below as a way to generate a wider range of predamaged microstructures for creep damage studies (section 6.2.4).

The form chosen for M_B permits using simple experimental grain growth data directly in predicting swelling or sintering behavior (App. 9). Having M_B *dependent* on grain size affects the value of ωD_S fit.[4] Yan et al. (1983) and Handwerker et al. (1984) develop sintering models which use a more complicated form for an M_B controlled by segregated solute drag. However, data for M_B typically are quite limited (Yan et al., 1977). Having a full numerical simulation available permits estimating the experimental accuracy required in M_B data, though this is complicated by M_B's interaction with ωD_S.

The two-term P_{int} (Eq. 4) permits modeling a wide range of possible pore atmospheres, including:

1) inert trapped gas, P^I_{int} (e.g. N_2 or Ar, as industrial furnace atmospheres),

---

[4] For $m = 3$, M_B varies as $\bar{L}_2^{-1}$, so ωD_S can have a higher value (less pore drag need develop at longer times, at given N and r) than would be fit if M_B were independent of grain size.

2) gases generated by chemical reactions (e.g. CO_x, SO_x. As a limiting case, P^G_{int} is assumed to be constant, corresponding to time-independent activities of all reactants at the pore surface.)
3) mixed cases (e.g. trapped air, with the N_2 remaining inert, but the O_2 reacting with dissolved C or S).

As we discuss below (section 6.1.6), although the behavior of pore gas mixtures is more complicated than just sketched, such a P_{int} likely is a reasonable first approximation.

Constant-N and constant-f_3 paths bounded experimental swelling data; constant-N_V is a hypothetical case when grain growth occurs during swelling. Stereological errors due to nonequiaxed pores are anticipated to be small in the current data. That is, the temperature dependence of experimental coalescence rates are not stereological artefacts (App. 13).

It is not clear why these paths should be bounding, and why paths in ARCO and AVCO should vary in opposite directions with temperature. Intergranular coalescence is poorly understood at present. The elementary topological process in grain growth has been described as a polycrystal replacing a triangular boundary facet with a three-grain edge (Rhines and Craig, 1974). In a porous polycrystal with arbitrary numbers of pores per grain and arbitrary internal pore pressures, fusing three, four-grain

junctions, and then dividing the fused junction into two new four-grain junctions has implications for pore coalescence. As the two new junctions gradually separate, what happens to the pore that was at the fused vertex, which may itself have been coalesced from up to three original pores? Whether it remains at one junction only, divides into two, or elongates between the new vertices (retarding their separating, or eventually pinching off by a Raleigh instability) is difficult to predict.

Yan et al. (1983) and Handwerker et al. (1984) include grain size distributions derived from Hillert's (1965) analytic grain growth analysis in sintering models. In the current work, we used a grain growth relation based on *mean* grain size (App. 10), but note that quantitative experimental data on the global boundary pressure which drives grain growth now could be generated directly from polish planes using image analysis. Grain size distributions in powder compacts now can be controlled rather well.

Zhao and Harmer (1988a) include a *pore* size distribution in a sintering model developed from Yan et al. (1980). The *effective* pore drag varies with the width of the distribution, and this affects the microstructural evolution. They give numerical results for f_3 of 0.5 and 1.0, and acknowledge that f_3 may change in real systems. In the current swelling work, we present experimental data showing that f_3 *does* vary. Then, instead of

considering size distributions in assumed equiaxed pores, we acknowledge *none*quiaxed pores and test for stereological errors.

Handwerker et al. (1984) note that dihedral angle effects in initial stage sintering are important, but that dihedral angles seldom are included in sintering models, due to other parameters being uncertain. In the current model, making an approximate correction to the capillarity component of pore pressure was important in determining the effective pressures during swelling. The geometric uncertainties which are so important in modeling initial stage microstructures are far smaller for final-stage microstructures.

In general, then, the level of detail in the current model is comparable to recently published work on pressureless sintering.

The approach adopted here towards parameter uncertainties was to get (and document) the best possible parameter values, and then to test the sensitivity of the model to these parameters, by carrying out a large set of runs with different values. This process identified which parameters were important to the model's overall behavior, how these key parameters interacted, and the physical reasons for such results. The results comment on the accuracy required in materials and adjustable parameters; this is important information in materials/process development based on interactive materials fabrication, characterization and modeling.

A basic assumption was that, given visualisation techniques for working *efficiently* with complicated models for microstructural evolution, significant physical insights can be generated from such models, despite parameter uncertainties.[5]

The parameter values (App. 17; Table 5-1) were determined by :

1) using experimental data where possible (β,ψ,m,K_L^o, initial microstructural parameters), theoretical estimates where necessary (a, trial $(P_i V_v)_{ehp}$) and manufacturing data where available (T_{HP}, limits to $P_{eff}^o \approx P_{app}^{PS}$), and
2) using the materials parameters values (δD_B, ωD_S, γ_S, γ_B, Ω) experienced workers felt were representative, and setting limits on δD_B from the experimental linearity in $(V_v\text{-}\bar{L}_2)$ and $(r\text{-}\bar{L}_2)$ data.

Exploratory runs with the model showed the most important parameters to be M_B, ωD_S, δD_B and $(P_i V_v)_{ehp}$. The sensitivity of the results to variations in these parameters was determined over a large set of numerical runs. Though the results and conclusions presented in Chs.5-7 are influenced by a more detailed sense of model behavior than can be documented here, the overall patterns

---

[5] The current numerical results were generated without the integrated graphics software recommended in Ch.8.

in model sensitivity can be summarized concisely:

1) The four key parameters, M_B, ωD_S, δD_B and $(P_i V_v)_{ehp}$, interacted as two rather independent pairs:
   a) δD_B and $(P_i V_v)_{ehp}$, which together controlled pore growth at short times, via $\dot{r}_p$, and
   b) M_B and ωD_S, which interacted to control grain growth rates, and so pore coalescence, at long times, via $\dot{r}_L$.
2) $(P_i V_v)_{ehp}$ and δD_B were treated as adjustable parameters. $(P_i V_v)_{ehp}$ had a minimum value of 0.005 to 0.01 MPa (App. 4). An upper bound to δD_B was set by experimental V_v and pore size being linear in grain size. $(P_i V_v)_{ehp}$ and δD_B interacted strongly in controlling swelling and pore growth rates. For δD_B values high enough that cases with coalescence diverged from constant-N_v results at *intermediate* times, (i.e. for values between Cannon et al.'s (1980) δD_B and the fit value; Apps. 15,17), the fit value of $(P_i V_v)_{ehp}$ was *independent* of the value of δD_B.
3) High activation energies were necessary for ωD_S and M_B, in order to fit experimental $\{\bar{L}_2\text{-}t\text{-}T\}$ data; however, the model was rather *in*sensitive to these energies. Specifically, given fit values for $(P_i V_v)_{ehp}$ and δD_B, low energies simply gave a somewhat smaller spread of numerical grain growth rates, between 1350 and 1450 C, than the experimental data. For Q_K, this was because

M_B values changed slowly with temperature; for Q_S, this it was because pore growth resulted in pore drag which was temperature insensitive. For reasonable values of all four parameters, values fit for $(P_i V_v)_{ehp}$ and δD_B were relatively independent of changes in M_B and ωD_S.

4) For sufficiently low δD_B (Dynys et al.'s 1980 value; App. 15), coalescence was unnecessary for swelling with V_v and r linear in $\bar{L}_2$.

For simplicity in the current model, a constant minimum value for β of 1.8 was assumed. This was an appropriate value for long times, depending on the temperature (Fig. 4-16). However, at short times, during which $\dot{r}_p$ was dominant (Fig. 5-2), experimental β were between 2.0 and 2.5; that is, were higher than the assumed value by factors of between 1.1 and 1.4. In the current numerical calculations, this difference was compensated for by a somewhat higher δD_B.

6.1.3 Overall results

With the confidence generated by the sensitivity analysis, we can summarize the broadest patterns in the numerical swelling results as follows:

1) At short times, swelling was dominated by pressure-driven, diffusional pore growth ($\dot{r}_p$), which was

controlled interactively by δD_B and the pressure of the trapped gas. Which microstructural path was being followed had little effect on swelling rates during this stage.

2) At longer times, swelling was dominated by the progressive release of P_{cap} constraint, due to pore coalescence driven by grain growth. In this stage, the rate of coalescence (with respect to grain size) varied with the microstructural path, and so the swelling rates were path-sensitive.

3) The *inert* trapped gas driving force was self-dissipating. However, at long times, coalescence maintained P_{eff} at small, but *non*zero values. This occurred because the magnitude of P_{cap} was being reduced by coalescence as well as by pressure-driven pore growth. So, as $\dot{r}_p$ fell to low values, the rate at which it continued to dissipate P_{int} was roughly balanced by the rate at which pore growth (by $\dot{r}_p$ and $\dot{r}_L$) released the opposing capillarity constraint.

4) If pore coalescence was excluded, P_{eff} fell to zero from pressure-driven growth alone. Swelling ceased after a time which depended on temperature.

6.1.4 ARCO *vs* AVCO HPA

ARCO's initial porosity was intragranular, and so did not correspond to the four-grain junction porosity modeled.[6] As well, though its porosity became intergranular with grain growth, data for its microstructural evolution (Figs. 4-13,-14) showed no common origin. For these reasons, we present no swelling analysis for this HPA at this time.

Swelling may occur by oxygen attack on dissolved C or S, which generates large internal pore pressures (Bennison and Harmer, 1985a). In the current work, AVCO had about half the bulk C, and the same S levels as ARCO (Table 2-1b), but swelled more rapidly (Figs. 4-2,-5). Until ARCO's swelling is understood, the reason for this apparent conflict with limiting thermochemical calculations for pressures of gaseous reaction products (App. 5) is unclear. However, clearly C and S levels by themselves may not be reliable guides to an HPA's tendency to swell in high temperature oxidizing atmospheres.

6.1.5 Pore drag and separation

In the current work, *no* pores separated in either HPA, and in

[6] The fine scale of its as-received porosity suggests that it may have arisen from pore separation in sintering.

ARCO, pores which initially were intragranular reattached to sweeping grain boundaries as swelling proceeded.

We discuss phenomenological pore drag and separation in Apps. 11 and 12. In App. 11 we generalize equations for the boundary of the separation field on {pore size/grain size} diagrams (e.g. Carpay, 1977) (1) to give *contours* for arbitrary values of the normalized pore velocity (where a value of one corresponds to the usual separation boundary) and (2) to apply to the bounding coalescence paths modeled here — constant-N and constant-f_3.[7]

In App. 11, we also develop equations for contours of $\tilde{M}_B^{eff}$, an index for the type of control of grain boundary migration. If these contours are drawn with contours for normalized pore velocity, on pore size *vs* grain size diagrams, lines added which show numerical or experimental paths followed by sintering or swelling microstructures can be related rather directly to the phenomenological drag model. (In this report, we developed equations for both contour families, but do not draw such diagrams.)

In App. 12 we consider a theoretical analysis (Hsueh et al.,

---

[7] Constant-N_V requires (de)densification with*out* grain growth; along such a path, grain growth driven pore separation cannot occur, because boundaries do not sweep.

1982) which suggests that the phenomenological drag/separation model gives serious errors in predicting pore separation, for pores with low dihedral angles. We renormalize the results of this analysis on a basis which is sterologically more sound. The new results showed that nonphenomenological separation from a two-grain facet will occur at normalized pore velocities of two to three, and are rather *in*sensitive to dihedral angle. Consequently, we suggest using the phenomenological normalized pore velocity contours of App. 11, but permitting pores to exceed normalized velocities of one without separating, and testing individual materials experimentally for separation velocities (Handwerker et al. (1984) show an efficient way to do such tests).

6.1.6 The two-term internal pressure; AVCO's swelling

The two-term internal pore pressure, P_{int}, is a first approximation. Initially, it was adopted to handle pore gas mixtures which included arbitrary proportions of (1) chemically inert gas (P^{I}_{int}; reflecting hot-press furnaces initially filled with N_2 or Ar) and (2) gases involved in chemical reactions; in particular, O_2 from any of several sources reacting with dissolved impurities such as C and S (P^{C}_{int}; Rice, 1969; Bennison and Harmer, 1985a). As limiting cases, the first term would be inverse in the volume fraction porosity, representing a constant

number of moles of trapped gas; while the second term would be held at a constant value during swelling, representing chemically-maintained partial pressures of reaction products.

However, gas is liberated or generated from the die/punches and within the compact throughout pressure sintering (Rice, 1969; Bennison and Harmer, 1985a), pore gas compositions in HPA are rich in CO_x and SO_x after hot-pressing (Bennison and Harmer, 1985a) and the external furnace atmosphere changes towards CO at high temperatures (T. Vasilos, personal communication). In the general HP case, then, the *local* compact atmosphere (that is, the atmosphere within the compact's porosity) *just before and just after pore closure* likely is controlled not by the initial furnace atmosphere, but by degassing and related chemical reactions in the die, punches and compact. During intermediate stage sintering, gases generated internally will tend to *flush* the compact of gases initially present. Such gases will flow through the continuous pore network of the compact, and then through the narrow annular channels between the punches and die wall, into the external furnace atmosphere.

The local pore atmosphere *just before* pore closure then is sensitive to powder processing (and purity), punch/die materials and furnace schedule (including time/temperature, atmospheres and pressures). The general pore atmosphere is difficult to anticipate, but easily could include CO generated over long

periods by ongoing liberation of low pO_2 from the compact. Also, it will be at a pressure of 0.1 MPa, unless lower pressures are maintained by continuous vacuum pumping (Bennison and Harmer, 1985a).

Similarly, the atmosphere established *just after* pore closure is difficult to predict. During the earliest part of final-stage densification, oxidation reactions (based on the low pO_2 likely available) could establish equilibrium partial pressures of CO and CO_2.[8] For CO, the equilibrium constants, K_p, are on the order of 10^8 in the temperature range for pressure sintering and swelling, and these K_p *in*crease with falling temperatures (Gaskell, 1973; Bennison and Harmer, 1985a). Consequently, equilibrium partial pressures of O_2 (in pores with $C\text{-}O_2\text{-}CO$ mixtures) are negligible ($\approx 10^{-5}$) relative to pCO.

When final stage pressure sintering then proceeds to $P_{eff} = 0$, driven by a high P^{PS}_{app} (e.g. 20-40 MPa; Dorre and Hubner, 1984), such trapped gas mixtures, while based on a chemical equilibrium, will behave *as if* the gases were *inert*.[9] That is, as far as pore

---

[8] Controlled by temperature ($K_p\{T\}$), carbon activity (a_C) and pO_2.

[9] Because $K_p \approx 10^8$, so $pO_2 \approx 10^{-5} \cdot (pCO)$. $K_p \equiv K_X \cdot P_{tot}^{1/2}$ for C oxidation to CO (Gaskell, 1973, p.226) where K_p and K_X are equilibrium constants defined in terms of partial pressures, pY, and mole fractions, $X(Y)$, respectively. So, if P_{tot} is

pressures are concerned, the gas mixtures are *functionally* inert — a large change can take place in the volume fraction porosity as the compact densifies in pressure sintering, without a corresponding change in the number of moles of gas trapped in pores.

The 'inert' P^I_{int} term then represents a wider range of gas mixtures than simply proportions of N_2 or Ar, and many factors can make a pore gas mixture *functionally* inert; i.e. can hold the number of moles of gas trapped constant during densification or *de*densification.

A driving force for *swelling* based on such a functionally inert pore gas mixture will be self-dissipating (as is P^I_{int} in the current model). Reaction or mass transport kinetics can affect whether equilibrium gas pressures can be maintained during swelling to large V_v, over long periods of time. Such kinetic limitations are likely to be less important at sintering (1500 C) and high annealing temperatures (1600 C, Bennison and Harmer, 1983,1985a), but more important in the current tests (1250-1450 C). At low annealing tempertaures, a potentially reactive pore environment may *not* be able to maintain constant pore pressures

---

increased by 100 times (e.g. from 0.1-0.2 at pore closure to 20 MPa at the end of hot-pressing), the corresponding 10-fold *de*crease in K_x and 100-fold *in*crease in $X(O_2)$ would make *negligible* changes in X(CO) and the total number of moles of gas trapped.

(P^G_{int}). Such effects may be difficult to predict.[10]

From the above complications, as a first but general approximation, it is difficult to do better than the current two-term P_{int}, despite its being rather arbitrary and vulnerable to large temperature changes.

Given this, we can now consider whether we were justified in treating AVCO's swelling as driven by 'inert' gas. For the fit $(P_i V_v)_{ehp}$ value of 0.02 MPa, the functional inertness of its anticipated CO-rich pore atmosphere suggests that a P^G_{int} of approximately 0.2 MPa was established just after pore closure. This is close to atmospheric pressure (0.1 MPa). Fifty to 150 C lower, in air anneals, swelling was uniform, implying that local pore environments, and not the external furnace atmosphere, controlled swelling pore pressures.

If we assume that the implied $P_{int} \approx$ pCO of 0.2 MPa was maintained as a minimum value in pores *throughout* swelling, pore pressures in the HPA would have evolved as did those currently modeled, with P_{int} falling steeply towards a minimum value at this P^G_{int} (Figs. 5-9,-10). In the current numerical results for arbitrary P^G_{int} (Figs. 5-9,-10) chemically maintained pressures of

---

[10] Freund et al. (1984) discuss the complicated solid state chemistry of hydrogen and carbon dissolved in MgO.

0.2 MPa enhanced swelling rates little, relative to inert gas. Consequently, AVCO's swelling can be treated as driven by 'inert' trapped gas.

We now return to the questions originally raised in section 1.1, when, during creep fracture work on a model structural ceramic, unstressed controls swelled.

6.2 Swelling in creep fracture

When a pressure-sintered material which is to be used in creep fracture research or for structural components in creep service swells, it is important to be able to distinguish self-dissipating inert pore pressures from chemically-maintained internal pore pressures, and to estimate their magnitudes, from experimental data. Three questions can be asked: (1) what magnitude of internal gas pressure would enhance creep cavity nucleation and growth in creep fracture, (2) could such a biasing pressure be dissipated in a precreep anneal, and (3) what range of *pre*damaged microstructures could be generated by such an anneal, in order to test models for creep fracture?

For example, for the swelling work reported here, we could ask: in a predamage anneal, what driving force for pore growth would be available? How would that driving force change with time and temperature? Could we tell if it was simply self-dissipating, or was chemically-maintained? Could we dissipate it through anneals which generate a useful range of *pre*damaged microstructures?

The following discussion derives from work on monolithic, single phase ceramic polycrystals, and is oriented to such materials.

Variables are listed in section 6.3.

6.2.1 Could an inert internal pore pressure component be distinguished from a chemically-maintained component, using experimental data from early swelling?

If it is possible to distinguish such ideal pore pressure components in a swelling polycrystal, we anticipate that it will be because an inert component ('I') is self-dissipating in swelling, in contrast to a chemically-maintained component ('G'):

$$P_{int}\{V_v\} \equiv P^I_{int}\{V_v^{-1}\} + P^G_{int} \qquad (8)$$

That is, when a chemically-generated component is constant and has a magnitude that significantly enhances the swelling rate, the effective pressure which is driving swelling may pass through a minimum.[1]

While the model's complexity and coupling make it difficult to give a *general* answer to this question, the numerical results permit us to give initial answers to four related questions:

---

[1] For a case with a constant P^G_{int} of sufficient magnitude, the 'inert' pressure component is dissipated rapidly, but the P_{int} remains at or above its minimum value of P^G_{int}. Coalescence then progressively releases capillarity constraint, and P_{eff} passes through a minimum. We have discussed the *form* of P_{int} in section 6.1.6 and App. 4.

(1) What values of P^G_{int} would increase AVCO's swelling rate above that for inert trapped gas,

(2) how do these numerical P^G_{int} values compare to pressures predicted by thermochemical calculations for possible gas-generating reactions,

(3) relative to these pressures, could we estimate the P_{eff} or total P_{int} present in a final-stage polycrystal, from experimental data, in terms of the full swelling model, and

(4) in numerical calculations for AVCO HPA, how do P_{int} and P_{eff} evolve? In particular, how rapidly and how far do they fall, and do the P_{eff} pass through a minimum, when a significant gas-generating reaction is active?

We discuss these questions in the order in which they are listed.

6.2.1.1 Chemically-enhanced swelling

Fig. 5-9 predicts that, when AVCO HPA swells at between 1350 and 1450 C, P^G_{int} in the range of 0.1 to 10 MPa would change swelling from minimally enhanced, to rapid, to catastrophic (relative to the inert-trapped-gas case).[2] The model would require serious

---

[2] For these numerical results, the constant, chemically-maintained P^G_{int} component was independent of the inert-trapped-gas component; all parameters save P^G_{int} had their usual values. The results seem *insensitive* to δD_B.

modifications in order to handle the severe swelling possible at short times for large P^G_{int} — modifications for a continuous pore channel network developing, and for gas release (Rest, 1986; Gruber, 1986).

The P^G_{int} of most interest for the following questions are those *within* this *transitional* pressure range (≈ 1 MPa), as it is for such pressures that swelling rates may be moderate, but higher, at long times, than anticipated for 'inert' swelling.

6.2.1.2 Comparison with equilibrium thermochemical pressures

We have compared the above *transitional* P^G_{int} with the equilibrium pore pressures predicted by thermochemical calculations for likely gas-generating reactions, for limiting, chemically-open-pore and -closed-pore cases (App. 5).[3]

For *closed*-pore cases (for which we anticipate small P^G_{int}: App. A5-1.1; Fig. A5-1), over the temperature range 1350-1450 C, the predicted total pore pressures were below 10^{-4} MPa; i.e. at least

---

[3] For these calculations, we treated the pore as *mechanically closed* with respect to gas loss; what varied between limiting cases was whether the pore reactions were independent of, or in equilibrium with (chemically 'open' with respect to), the external pO_2.

three orders *smaller* than would noticeably affect AVCO's swelling. On the other hand, *open*-pore oxidation of dissolved C and S, in equilibrium with external furnace pO_2, can maintain high pore pressures. These are at least an order of magnitude *greater* than those the model predicts would cause rapid swelling (Bennison and Harmer's (1985a) Fig. 9; App. A5-1.2; Fig. 5-9).

Neither type of limiting-case calculation predicts P^G_{int} in the transitional pressure range. They lead instead either to a negligible effect, or to swelling occurring so rapidly that a final-stage microstructure cannot be assumed to hold for long times.

The high-pressure limiting-case results (e.g. for C or S oxidation, above) are not consistent with our swelling data. We find that swelling developed *uniformly* (i.e. porosity at the center of a specimen and near its external surfaces were comparable).[4] However, trapped *reactive* gases with *low* equilibrium pO_2 could generate partial pressures of CO or SO_2 which were in the transitional range of $P^G_{int} \approx 1$ MPa (Bennison and Harmer's (1985a) Fig. 9). For both CO and SO_2 reactions, the partial pressures of gaseous products would be proportional to the activity of the oxidized reactant (C or S). For our C and S

---

[4] At 1600 C in air, swelling was far more rapid at the specimen surface (Bennison and Harmer, 1985a).

impurity levels of about two orders less than Bennison and Harmer's (1985a), transitional pressures, in the swelling T range, could have been generated by oxidation reactions in *closed* pores, in which pore pO_2 were present on the order of 10^{-4} MPa for SO_2, and 10^{-11} MPa for CO.[5] In this T range, for every drop in temperature of 50 C, equilibrium partial pressures of SO_2 *increase* by a factor of between 2 to 5, and of CO by somewhat less (Bennison and Harmer, 1985a).[6]

6.2.2 Calculating P_{eff} and P_{int} from experimental data; detecting a chemically-maintained internal pore pressure

Given experimental $\{V_v, \bar{L}_2$ and $N_A\}$ data, the *effective* pore pressure driving a polycrystal's swelling can be calculated *in terms of the full swelling model* (App. 7):

$$P_{eff} = \phi_1 \cdot \frac{V_v^{1/2}}{B_3\{V_v\}N_A^{3/2}} \left(\dot{V}_v + |y_1| \frac{\dot{\bar{L}}_2}{\bar{L}_2} \right) \qquad (9a)$$

---

[5] These values can be taken directly from Bennison and Harmer's (1985a) Fig. 9a,b, which give pCO and pSO_2 at different temperatures and pO_2. Activities of C and S in AVCO and ARCO HPA are given in App. 5's Table A5-1..

[6] In contrast, *closed*-pore P_{int}^G *decrease* with temperature (App. 5-1.1).

where $$\phi_1 \equiv 9\left(\frac{6}{\pi}\right)^{1/2} \frac{kT}{\beta\delta D_B \Omega} \qquad (9b)$$

and B_3 is defined both in the swelling model and in App. 8. The values of y_1 are path-dependent:

Case (i)	Parameter held constant	y_1
1	(N_V)	0
2	N	- 8/9
3	f_3	- 8/3

The total *internal* pore pressure component, P_{int}, then can be calculated from the effective pressure:

$$P_{int} = P_{eff} - P_{cap} - P_{app} \qquad (10)$$

in which, given the dihedral angle for internal pores, P_{cap} can be calculated from (Apps. 3,6):

$$P_{cap} = 2\left(\frac{2\pi}{3}\right)^{1/2} g\{\psi\}\ \gamma_B \left(\frac{N_A}{V_V}\right)^{1/2} \qquad (11)$$

P_{app} is a known constant.[7]

These equations should permit testing a swelling (or densifying) polycrystal for any characteristic patterns in P_{eff} or P_{int}, with time or grain size. In particular, they should permit detecting a minimum in P_{eff}, when it occurs in swelling in which P^{G}_{int} are significant.

However, the numerical results for AVCO suggest that the anticipated minimum in P_{eff}, for cases with such P^{G}_{int}, may not in general occur, or may not be observed within the time frame of typical swelling tests. Figs. 5-7,-8 and -10 show that, when δD_B were small enough that numerical $\{r-\bar{L}_2\}$ and $\{V_v-\bar{L}_2\}$ results were linear, consistent with experimental data, then, for cases with only inert trapped gas, as well as those with a transitional, chemically-maintained pressure component (P^{G}_{int} = 1. MPa) both P_{eff} and P_{int} decreased *monotonically*, over the time span and temperature range of the current swelling tests.

---

[7] Hsu and Solomon (1983) develop a similar equation, for arbitrary *n*, for determining experimentally the driving force for swelling, P_{eff}, and from it, the driving force exponent, *n*. They included no pore coalescence, despite acknowledging grain growth (their Fig. 13) and pore 'interconnection' (their p. 459) and made no dihedral angle correction to P_{cap}. Their V^{o}_{v} and r_o were one to two orders higher than expected for hot-pressed ceramic polycrystals.

In contrast, for Cannon et al.'s (1980; App. 15) higher, *nonlinear* δD_B, for P_{int}^C in the same transitional pressure range, *but only for high enough temperatures and long enough times*, the calculated effective pressure *did* pass through a minimum, and then increased, as anticipated. At the same time, for this nonlinear δD_B, when swelling was driven solely by an inert trapped gas, P_{eff} decreased monotonically.[8]

The above results suggest that even though P_{eff} could be calculated for a swelling polycrystal, the P_{eff} minimum anticipated for transitional P_{int}^C may not be observed in typical swelling experiments, especially at low temperatures.

6.2.3 What P_{int} would enhance cavity growth rates in creep fracture?

We draw no general conclusions in this section. Instead, referring back to the driving force equations given in section 1.2.5, we outline certain basic issues which will have to be addressed when specific cases are examined.

In considering what effect a P_{int} from sintering or swelling would have on cavity *growth* rates, it is important to specify

---

[8] We do not show these results.

carefully where the creep cavities are located, how the components of P_{int} relate to fabrication and service conditions, and what mechanism(s) control creep fracture.

An internal pore pressure is potentially a significant bias in failure times modeled by cavity growth to coalescence. The sintering stress, P_{cap}, often is ignored in such models (Riedel, 1987: p.155-6). When it is included, it is because it increases the predicted times to pore coalescence, by opposing the normal stress in the driving force for cavity growth — particularly for small cavities. For such small cavities, both the sintering stress and an internal pore pressure due to trapped gas would be large. For somewhat larger cavities, when P_{cap} and σ_{∞}^{net} might still roughly balance each other, and an inert trapped-gas P_{int} component would be largely dissipated, even a small chemically-maintained P_{int}^{C} could be a significant bias *against* the capillarity stress, in favour of the applied stress.

Current data suggest that metal polycrystals creep damage via cavity *arrays*, while HPA damages via *single* cavities (Riedel, 1987, Ch. 11,12; Porter et al., 1981; Ch.4, Fig. 4-1). The present swelling model was developed for a representative (uniformly-distributed)[9] four-grain-junction pore.

---

[9] The same microstructural chemical heterogeneities that can lead to inhomogeneous creep cavity growth rates (Hsueh and Evans,

In a creep-cavitating, pressure-sintered polycrystal, in which residual, four-grain junction pores were present at the start of creep, there are two limiting cases. First, two-grain facet cavity *arrays* could nucleate — either on loading or continuously; spatially uniform or inhomogeneous — and then grow, dominating cavitation in the polycrystal.[10] In such cases, the array cavities would *not* have pressure driving forces due to inert trapped gas, predicted by the sintering/swelling model for four-grain junction residual pores, but could have internal pressure driving forces due to gas-generating chemical reactions. Alternatively, the polycrystal could creep damage by *single* four-grain junction cavities — spatially uniform or inhomogeneous — elongating rapidly down three-grain edges, and then growing laterally (Hsueh and Evans, 1981). In such cases, both inert trapped gases *and* chemically-generated gases could contribute to cavity growth driven by applied stresses.[11]

1981; Handwerker et al, 1984), also could cause the porosity in and after final-stage pressure sintering — and during swelling anneals — to be *non*uniformly distributed.

[10] High levels of swelling predamage can be generated in AVCO (Fig. 4-1); it is likely that such damage *would* be important in subsequent creep cavitation.

[11] However, the inert trapped gas component likely would be largely dissipated by the time an equiaxed four-grain cavity had elongated along a three-grain edge.

Creep fracture in commercial metals, and damage zone spreading in alumina (Hsueh and Evans, 1981) have been modeled as *constrained* cavitation. Constrained models should be readily extensible to include P_{int}, when the driving force is expanded, as in section 1.2.5.

It is important to distinguish a P_{int} bias in a *cavity growth* model from a bias in a *component lifetime* model — models for macroscopic failure lifetimes of a polycrystalline structural component are far more controversial than are models for cavity growth rates.[12]

---

[12] The controversy arises in part because it is difficult to model the interactive issues of an equilibrium-to-cracklike growth transition, cage constraint and continuous nucleation. More important, however, is that while constrained coalescence models fit creep lifetime data for commercial metals, using coalescence to predict constrained lifetimes is physically suspect (Riedel, 1987, p.181,2). In general engineering cases, then, some form of damage accumulation will be important — but the range of time-dependent spatial inhomogeneities it is often associated with are difficult to handle, theoretically and experimentally (e.g. Bogdanoff and Kozin, 1985, and section 9.1).

6.2.4 What range of *pre*damaged microstructures is available, for testing creep failure models?

If no *new* cavities nucleated in HPA during subsequent creep, then residual sintering porosity, or porosity from a swelling anneal, could be treated as H_2O bubbles or strain predamage have been in experiments with metals (review: Riedel, 1987, p.169, 182). However, creep damage in HPA occurs by single cavities growing laterally from three-grain edges, and not by cavities growing in arrays on two-grain facets.

A parameter for the intensity of predamage must be defined in terms of a specific creep fracture model. As noted in the previous section, in general, creep fracture in commercial materials generally involves some form of damage accumulation.[13]

---

[13] There is also the issue of generalized cavitation enhancing slow crack growth rates (Pilkington et al., 1981). Swelling predamage might be a useful approximation either for generalized creep damage, or for residual sintering porosity. Whether to use N and f_3 as a predamage measure depends on whether the crack growth model included a grain structure in the crack-tip cavitation zone. N would be more appropriate for continuum models which effectively ignore grains (e.g. Wilkinson and Vitek, 1982), while f_3 would better suit a damage zone approach in which grains, and cavities at specific boundary locations, were considered (e.g. Hsueh and Evans, 1981).

When justified by the experimental data, the relevant microstructural scale for modeling creep fracture in HPA can be taken to be small — say, one to several grains. For such a local scale, distinct *pre*damaged microstructures would have (1) different numbers of pores per grain (f_3; equivalently, per oriented facet) with (2) the grain size (or pore size/grain size ratio) constant,[14] and (3) P_{int} dissipated in all cases to levels that would not bias subsequent creep cavity growth.

Experimental data from anneals show (Figs. 4-7, and 4-9 to -12),[15] and the swelling/sintering model predicts — for limiting microstructural paths — the range of r, N and f_3 available from air anneals of AVCO HPA, at constant grain size (Fig. 5-4). From Fig. 4-10, the extreme range of pore number densities available in AVCO, in the current work, was about *one* pore per grain (600 h air anneals of AVCO at 1350 C) to about *two* per grain (40 h at 1450 C). For these extreme microstructures, the grain size was constant at $\bar{L}_2 \approx 2.5$ μm. The range of experimental pore sizes was rather narrow, being between 0.30 to 0.35 μm (Fig. 4-7), and so, because grain size was constant between these two

---

[14] The $(r/\bar{L}_2)$ ratio is important in the transition from quasi-equilibrium to crack-like growth modes (Hsueh and Evans, 1981); however, this transition is difficult to model.

[15] Data were tested for stereological errors due to nonequiaxed pores (App. 13). Because estimated errors were relatively small, data points were not corrected on plots.

microstructures, the $(r/\bar{L}_2)$ ratio was narrow also.[16]

Longer 1350 C anneal times would extend the range of f_3 available at constant grain size (Figs. 4-7,-10). Both experimental and model microstructures evolved with pore size linear in grain size. During such anneals, then, the range of $(r/\bar{L}_2)$ ratios, which is narrow in the above extreme microstructures, should change little. If variable grain size could be handled in tests of creep fracture models (Sundararajan, 1986), a much wider range of initial damage levels would be available (Fig. 4-10).

However, there are two complications for wider ranges of f_3. First, the idealized microstructures which have been used to model single/lateral cavity growth have distinguished only one *vs* two pores per oriented two-grain facet (Hsueh and Evans, 1981). No data have yet been generated for the effect on the time to form full-facet cavities, or to macroscopic failure, of *more* than two pores per grain or oriented facet; moreover, Hsueh and Evans'

---

[16] The proportion of *non*equiaxed pores also varies with time and temperature (App. 13). However, if we assume that four-grain junction pores elongate rapidly to three-grain edge cylinders on stressing at the start of a creep test (Hsueh and Evans, 1981), and if we correct for stereological errors due to the fraction of cylindrical pores in swelling being time- and temperature-dependent, this variation of predamage cavity shape should not be an important bias in using precreep damage anneals to test creep fracture models.

(1981) model will be difficult to extend beyond one *vs* two pores per facet.

Second, the microstructural scale that should be considered for creep fracture in HPA, and so, the pore parameter that indicates distinct predamaged microstructures, depends on how the material creep damages. If AVCO's one pore per oriented facet were uniformly distributed spatially, *no* constraint on cavity growth should develop during subsequent creep cavitation; i.e. *un*constrained growth models should apply. However, from the SEM micrographs, the spatial distribution of pores is *in*homogeneous after annealing (Fig. 4-1).[17] After swelling (and on loading) the material consists of regions which, on average, have more than one spherical-tetrahedral cavity per oriented facet, and regions with little or no predamage.

In uniaxial tensile creep tests on ARCO HPA, creep damage accumulation was far from spatially homogeneous.[18] At stresses

---

[17] It may be inhomogeneous in the *unannealed* material also; however, the as-received cavities had radii on the order of 0.1 μm, and were difficult to detect by the SEM techniques used. TEM micrographs sample a very small volume of polycrystal per foil (Fig. 4-13) and are poorly suited to characterizing spatial patterns which have dominant wavelengths longer than several grains.

[18] We discuss these results in the second part of this report.

sufficiently far below the transition to rapid failures, generalized cavity growth and coalescence generated multi-grain microcracks, and so competed with cracks growing by local cavitation from microstructural heterogeneities. We anticipate that constraint on cavity growth in more-heavily damaged regions will develop for low strain rates.

The observed spatial heterogeneities in predamage and creep damage suggest that a second relevant microstructural scale — larger than one to several grains, but currently undefined — may need to be considered in determining a parameter for the range of distinct predamaged microstructures. Data for this would include characterizing the time- and predamage-dependent heterogeneity of creep cavitation, as well as the predamage influence on the competition between crack propagation from initial heterogeneities and generalized (heterogeneous) cavitation. This is a large experimental project.

In summary, the current results for AVCO show that *early* swelling was controlled by P^{I}_{int}, and was rather *in*sensitive to temperature. *Later* swelling was controlled by pore coalescence rates, driven by (and so coupled to) grain growth. Consequently, only a rather restricted range of predamaged microstructures can be generated in air anneals, from the standpoint of homogeneous damage models. The range depends on coalescence rates being weakly temperature dependent. No data yet are available for the

range of spatially-inhomogeneous predamage, for use in constrained damage models.

In a final stage material whose internal pore pressures were independent of the external atmosphere, global porosity parameters and grain size should be rather *in*dependently variable in *pressure anneals* (which may be extended pressure sintering or HIPping runs). In such anneals, the pressure driven component of pore growth (though not the coalescence component) could be suppressed.

6.2.5 Could a potentially biasing P_{int} be dissipated by a *pre*creep anneal?

Figs. 5-7,-8 show how rapidly AVCO's total P_{int} would be dissipated by predamage anneals. Applying such results to the expanded driving force for creep cavity growth (section 1.2.5), we can predict what anneals would reduce P_{int} sufficiently to prevent it biasing cavity growth in subsequent creep cavitation studies. This can only be done with reference to a specific damage model and service conditions; in particular, constraint must be handled carefully, as it controls the magnitude of the mean stress normal to the cavitating boundary. As noted previously, no general analysis is available for the effect of a P_{int} on constrained cavitation.

For example, in the current numerical results, in the extreme 2.5 μm microstructures compared above, with one *vs* two pores per grain, *internal* pore pressures had been dissipated from on the order of 24 MPa, to values of between 2 and 3 MPa (Figs. 5-7b,-8b). (For this material, linearity in pore size and volume fraction porosity *vs* grain size set upper limits on the boundary diffusion coefficient, and so limited the maximum rates for P_{int} and P_{eff} decreasing. That is, the actual δD_B should have been no larger than the fit value; so, at a given time, the real P_{int} was no *lower* than that predicted.)

Similar calculations could be done for any material for which appropriate values were assigned to the in the swelling model.

6.3 Variables

All variables are defined in section 3.7, except:

DF driving force for diffusional cavity growth; [N/m^2]

f the area fraction of oriented two-grain facet that is cavitated; [-]

ϕ_1 materials parameter introduced in Eq. (2b)

σ_∞^{net} net applied far-field stress; [N/m^2]

y_1 dimensionless, path-specific multiplier; [-]

7 Conclusions

1 A general model was developed for final-stage polycrystals swelling due to gas trapped at high pressure in intergranular pores during hot-pressing. During swelling, pore and grain growth occur simultaneously. The model can be applied to final-stage pressure sintering, and likely can be extended rather simply to severe swelling and intermediate-stage pressure sintering.

2 In numerical simulations, swelling depended rather sensitively on the values of M_B and ωD_S, which interacted as a pair in controlling grain growth. Swelling depended sensitively on the value for δD_B, and was very sensitive to $(P_i V_v)_{ehp}$, which reflects the gas pressure in pores just after pore closure. $(P_i V_v)_{ehp}$ and δD_B interacted strongly in controlling the rate of pressure-driven diffusional pore growth at short times.

3 The boundary diffusion coefficient was a key materials parameter in numerical simulations of swelling. It controlled whether swelling and pore size were linear in grain size, and the value fit for $(P_i V_v)_{ehp}$. Linearity in the corresponding

experimental swelling data set upper limits on the value of δD_B. The δD_B parameters chosen were consistent with available diffusivity data.

4 Air anneals were carried out on AVCO and ARCO HPAs, at temperatures between 1250 and 1450 C, and at times up to 600 h. In this temperature range, swelling was uniform, suggesting that swelling was independent of the furnace atmosphere.

5 AVCO swelled nearly six times faster than ARCO (on a grain size basis) even though its C concentration was half of ARCO's, and their S concentrations were comparable.

6 AVCO's as-received pores were intergranular spherical tetrahedra, with equivalent radii of about 0.1 μm. ARCO's as-received pores were intragranular spheres with radii below 80 nm, and often occurred in clusters. Early in ARCO's swelling, they reattached to sweeping grain boundaries.

7 In both HPAs, all swelling data was bounded by pore coalescence occurring at a constant number of pores (1) per unit area grain boundary and (2) per grain. The pore coalescence rates were weakly temperature dependent, but in opposite directions in the two aluminas. The temperature dependence of the microstructural paths was insensitive to stereological errors due to our having treated all polish

plane pores as equiaxed.

8 In numerical simulations, early swelling was dominated by pressure-driven pore growth, and grain growth occurred under M_B control. Swelling rates were insensitive to the microstructural path during this stage. Later swelling was dominated by path-specific coalescence, which released capillarity constraint. Grain growth occurred largely under pore drag control. When coalescence was *excluded* from numerical simulations, swelling ceased after the initially high pore pressures had dissipated themselves by pore growth.

9 In numerical simulations, chemically-maintained pore pressures less than 0.1 MPa did not enhance swelling markedly above rates for inert gas. However, chemically-maintained pore pressures of 10 MPa or more caused very rapid swelling in the temperature range 1350 to 1450 C. Limiting-case thermochemical calculations for C oxidation predicted equilibrium pore pressures well outside this transitional pore pressure range.

10 Time-dependent effective pore pressures can be estimated from experimental data for a swelling polycrystal. However, from results of numerical simulations, the anticipated minimum in P_{eff} may not be observed in typical swelling experiments, for cases in which for chemical reactions maintain transitional pore pressures.

11 Only a limited range of predamaged microstructures can be generated in air anneals. The range depends on the (weak) temperature dependence of coalescence rates. In AVCO, in the current tests, the range was between about one and two pores per grain, at a mean grain size ($\bar{L}_2$) of approximately 2.5 μm. Pressure anneals should widen this range.

12 Models were reviewed for the effect of internal pore pressures in cavity nucleation and growth in creep fracture. The swelling model permits predicting the rate at which such pore pressures would be dissipated in preanneals or in creep service.

8 Recommended future work

1 Extend the swelling model to pressure sintering, including HIPping and HIP mapping. Extend the model to the intermediate stage, beginning with Tucker's (1981) work on the ψ-dependent geometry of three-grain edge channel networks, Occhionero's (1984) results for the mobility of cylindrical pores, and Wilkinson's (1978) diffusional, final-stage densification model (which needs to be recast for a cylindrical geometry).

2 Test the combined pressure sintering/swelling model on a material/processing system that is well characterized (i.e. M_B known, only intergranular pores, pressure sintering conditions known, gas-generating reactions controlled, gas entrapment known). With a HIP outfitted with an internal LVDT for continuous shrinkage measurements, tests could be carried out which were the high temperature/pressure/relative density equivalents of the studies Solomon and coworkers have performed (e.g. Hsu and Solomon, 1983).

3 Determine global boundary driving pressure (App. 10) and proportionality constants a_x and a_{ix} (App. 9), from

quantitative grain growth studies in which an automatic image analyzer, driven directly from SEM image signals, characterizes polish planes. Compare the results with similar measurements made on numerically grown microstructures (Anderson, 1986).

4 Develop a general analysis for P_{int} effects in constrained cavitation (see sections 1.2.5 and 7.2).

5 Generate TEM data for pore evolution in ARCO HPA, and analyze its swelling.

6 Test whether AVCO's swelling is atmosphere sensitive, by carrying out anneals at low pO_2. From C and S oxidation reactions (App. 5), H_2/H_2O equilibria likely will be necessary to achieve sufficiently low pO_2.

7 Extend the model to include severe swelling, with three-grain channel formation and gas release (e.g. Rest, 1986; Gruber, 1986).

8 Modify the microcomputer version of the swelling program (probably in FORTRAN, but perhaps in a modern compiled BASIC, Pascal or C — these offer integrated development environments). Plot up to, say, six on-screen graphs *during* a run, with hardcopy of the finished plots available at the end

of the run (inexpensive, high-level plotting routines are available commercially).[1] Currently, working with the model is slowed markedly by the time required to plot results with a standalone package. If necessary, add adaptive step size control to speed up the program (e.g. Press et al., 1986, p.554).

---

[1] For example, 'HGraph', Heartland software, Inc., Ames, Iowa; 'Geograph', Geocomp Corp., Concord, Massachussetts; 'Plot88', Plotworks, Inc., Ramon, California.

Part B

Creep and creep damage accumulation in hot-pressed alumina

9 Introduction

In Ch.1, we noted that the research project originally was concerned with creep damage accumulation, and that the swelling work was done with a view to controlling pore pressures and cavitation *pre*damage in creep fracture. Section 1.2.5 in that chapter indicates that constrained cavity growth models are physically suspect in predicting creep failure in commercial or spatially heterogeneous materials, in which, in general, some form of creep damage accumulation will be important.

In this section, we review damage accumulation, static fatigue (creep fracture) data for structural ceramics, HPA's role as a model material in such work, and the creep fracture and damage data which have been generated for HPA. We then list the objectives of the current work.

9.1 Literature review: creep fracture damage accumulation

As damage accumulates synergistically with deformation, and secondary creep accelerates into tertiary, a structural component's deformation resistance and reliability against creep

fracture degrade along with its microstructure. In metallic components, ductilities tend to be high, and tertiary creep makes important contributions to the total lifetime, strain and stress redistribution. Designing for arbitrary load and temperature schedules, predicting residual life from microstructural data, choosing conditions for accelerated creep tests, and extrapolating from such tests to long term service, demands understanding the micromechanisms of interactive tertiary deformation and damage.

Penny and Marriott (1971, p.192-238), Cocks and Ashby (1982) and Riedel (1987, p.22-6) review *empirical* extrapolation methods for fracture and deformation rates (e.g. Larson-Miller or Sherby-Dorn parameters). Such preliminary design aids persist because engineering test results often include relatively large scatter, but no strain or damage data. None of these global methods reliably can handle load or temperature changes during a component's lifetime; this requires a differential method based on, for example, damage mechanics (Cocks and Ashby, 1982).

In continuum damage mechanics (CDM), two coupled constitutive equations describe isothermal strain and damage rates respectively (e.g. Evans, 1984; Ashby and Dyson, 1984; Leckie, 1978,1986; Kachanov, 1986):

$$\dot{\varepsilon} = f\{\sigma,\omega\} \qquad \dot{\omega} = g\{\sigma,\omega\}$$

The strain rate typically depends on the equivalent stress only (e.g. Saanouni et al., 1986), but the dependence of damage rate on the stress *state* is materials specific. The functions f and g can be determined systematically, but the labor involved is prohibitive (Leckie, 1986). Typically, constitutive equations of Kachanov/Rabotnov form are adopted.

In the damage mechanics developed by Leckie, Hayhurst and coworkers (e.g. Leckie, 1986), the parameters characterizing a material's creep fracture behavior are determined experimentally from creep deformation rates and fracture times in thin-walled tubes subject to combined tension and torsion. Reversing the direction of torsional load generates nonproportional loading, and tests the stress state dependence and isotropy of damage (Trampczynski et al., 1981; Murakami and Sanomura, 1985).[1]

Damage may or may not be readily interpretable in terms of a microstructural parameter. As originally defined, as an internal variable, it was measurable only through its effect on the deformation behavior (Riedel, 1987, p.350). Cocks and Ashby (1982), Ashby and Dyson (1984), and Leckie (1978, 1986) discuss how compatible the continuum damage mechanics and micromechanical damage models are. This issue is still in development.

---

[1] In proportional loading, while the magnitudes of stress components may change, their *ratios* remain constant.

Damage mechanics is developing rapidly as an engineering design tool (Lemaitre, 1984, 1986; Saanouni et al. 1986). Applied locally in finite element analyses, it is better suited than its complement, fracture mechanics, to structures with highly dissipative large-scale yielding, time-dependent behavior (such as creep crack growth), three-dimensional effects (such as nonproportional loading) and damage accumulation. It can predict local stress, strain and damage fields in arbitrary components — ductile or brittle — fields which are coupled, and which redistribute, varying in time and space. It has been applied in fracture limits in metal forming, creep damage and creep fatigue interaction in metals, three-dimensional crack paths with history/orientation effects, and cracking in reinforced concrete.

A damage accumulation approach to fracture requires at least one damage variable — preferably one that can be measured from direct microstructural observations. It needs some measure of isotropy and stress state dependence, in a constitutive damage law, and a local fracture criterion. Because damage *in*homogeneity seems generally important in creep failures (Riedel, 1987, pp. 172-85), some measure of inherent spatial damage heterogeneity

likely will be required,[2,3] and a way to include such materials variation in CDM. From a materials science standpoint, spatial heterogeneity has been modeled as cavities on two-grain facets (Wilkinson, 1988), as isolated constrained facets (e.g. Riedel, 1987, pp. 172-85), as homogeneously distributed constrained facets (Cocks and Ashby, 1982), as constrained, spreading, multi-facet damage zones (Hsueh and Evans, 1981), and as randomly distributed cumulative cavitation (Evans and Rana, 1980). Within a mechanics framework, spatial heterogeneity in cavitation has been modeled by Burke and Cozzarelli (1984). Much work remains to combine the two approaches.

Ceramics such as silicon nitrides and silicon carbides have potential as structural materials for higher temperature applications than metallic alloys. Relative to metals, their ductilities in lab and service environments tend to be low. 'Tertiary' creep occurs in *flexural* (Grathwohl, 1984), and in uniaxial tensile tests (Gruffel et al., 1988), but high

---

[2] As opposed to that generated by inhomogeneous stress fields arising from component geometry and localized loading.

[3] Two scales of damage characterization are relevant: (1) materials-dependent ceramography on a given polish plane image field, and (2) processing sufficient image fields to determine damage distributions — calling for one to two orders of magnitude more data, generated by image analysis (Diggle, 1983).

temperature mechanical properties data are very limited, both in quantity and in variety of stress states. Little is known of damage accumulation. It is too early to say how CDM can be applied to the different families of ceramics.

The data which raise most clearly the issue of damage accumulation in high temperature structural ceramics are the static fatigue results of Grathwohl (1984), Quinn (1984) and Wiederhorn (1983), from which Quinn generated a fracture mechanism map for HPSN, and Wiederhorn generated strength degradation maps. When monolithic HPSN's are tested in flexural static fatigue in air, there is a region in service space, at low stress and temperature, within which the materials are *insensitive* to surface damage (Figs. 9-1,-2). As reviewed by Wiederhorn and Fuller (1985), HPSNs fail at high temperature and stress by crack growth from mechanical surface damage arising in machining — linear scratches, with associated plastically deformed material and subsurface cracks. At lower stress, the residual stresses around the dominant scratches in such a layer have sufficient time to decay, cracks heal and glass forms at crack tips. Specimen lifetimes increase sharply. At low stress and long times, a new population of flaws develops by pitting corrosion, and, if creep deformation occurs, by cavitation and cavity coalescence. From $\{\sigma\text{-}t_f\}$ slopes and crack origins, Grathwohl and Quinn concluded that long term failures were due to such strain-driven cumulative damage processes.

At high stress and short times, then, failure can be predicted by established methods for crack growth at high temperature (Wiederhorn, 1983). However, at long times, the flaw population is evolving by different mechanisms, and life prediction methods are not well developed. As Wiederhorn and Fuller (1985) note, whether a structural ceramic has a glassy grain boundary phase is a key factor in deformation and damage mechanisms. And, they note, existing mechanism models of creep fracture in ceramics are difficult to test experimentally, and either have not been so tested, or are inconsistent with test results. As well, no general framework has been developed for handling spatial damage heterogeneity.

There are two parts to experimental materials studies of creep fracture in ceramics: (1) locating conditions under which it occurs and (2) describing the damage processes. Generalizing results is complicated by damage processes depending on processing defects and test conditions ('materials quality'). There are two interactive experimental challenges: (1) microstructural instability (e.g. glass phases changing composition and viscosity), (2) mechanical testing (e.g. gripping and extensometry in uniaxial tensile tests). From creep fracture results for metals, and from cavitation damage modeling (Cocks and Ashby, 1982) we anticipate stress *state* effects; however, high temperature multiaxial tests are difficult. Bend tests are

the simplest way to generate tensile data; compressive tests are perhaps more difficult experimentally, and are limited to low strains.

Though it is easy to generate tensile stresses in *bend* tests, it is difficult to control them. Two-phase polycrystals, such as Si/SiC or glass-bonded HPSNs, deform at different rates in tension and compression. Flexural specimens in such materials have transiently mobile neutral axes, even when the glass is stable (Cohrt et al., 1984a,b; Chuang and Wiederhorn, 1988; Wiederhorn et al., 1988). However, in HPSNs creep tested in air, the glass phase is *un*stable: time-dependent composition and viscosity gradients develop near free surfaces (Lange, 1980), and the glass gradually crystallizes. As well, creep fracture in HPSNs is complicated by flaw healing and pitting (Wiederhorn, 1983), and by the fine-scale, felted-needle microstructure and low cavitation tolerance (M. Chadwick and R. Jupp, unpublished research). Glass-bonded aluminas (as model systems) undergo crystallization biased by proximity to surfaces and by stress, and have mobile neutral axes in bending (Wiederhorn et al., 1986a). For these reasons, detailed damage work on HPSNs (or their oxide analogs) has not been pursued, and in any systematic creep studies, there is pressure to use uniaxial tests.

Because of these experimental difficulties, the initial data on creep fracture in ceramics have simply been from parametric tests

— generally in bending. As reviewed by Wiederhorn and Fuller (1985), failure times do not, in general, follow a Monkman-Grant relation, in which they are proportional to the inverse of the steady state strain rate: $t_f \propto \dot{\epsilon}^{-\alpha}$, $\alpha \approx 1$. Mg-HPSNs in uniaxial tension and bending fit a Monkman-Grant relation. HPA and glass-bonded alumina, in bending, fit a stress-modified relation: $t_f \propto \dot{\epsilon}^{-1} \cdot \sigma^{-\ell}$, $\ell \approx 4\text{-}6$. Y-HPSN undergoes a change in grain boundary phase at 1300 C, and so a Monkman-Grant relation does not hold.

More detailed damage accumulation work has been done on two very different ceramics: Si/SiC and HPA. Si/SiC is a multiphase[4] material with potential for high temperature industrial applications. It has low oxidation rates, and is microstructurally relatively stable. Its materials parameters are known. Its damage tolerance and creep failure strains are low, but cavitation can be measured by SEM (Wiederhorn et al., 1986c,1988). Its tensile and compressive creep behaviors are very different (which complicates flexural tests; Carroll and Tressler, 1985, 1988; Wiederhorn et al., 1988). Both its SiC network and the interpenetrating Si are spatially heterogeneous.

---

[4] For example, a typical microstructure may have a spatially inhomogeneous network of SiC particles (e.g. 5 μm diam.) interpenetrated by free silicon (eg. $V_v^{Si} \approx 0.3$).

In contrast, HPA is a single phase, model structural ceramic. It is microstructurally rather stable in creep tests in air,[5] and its materials parameters are known (App. 15). Creep cavitation ceramography can be done by SEM, and the damage tolerance and creep ductility are high enough to suggest that damage accumulation approaches from structural metals eventually could be applied rather directly. It damages by cavitation only,[6] has high damage tolerance and creep failure strains (e.g. Dalgleish et al., 1985),[7] and similar deformation rates in tension and compression (Gruffel et al., 1988). To this point, the HPA tested has been spatially heterogeneous, with localized microstructural heterogeneities (e.g. Dalgleish and Evans, 1985). The character of heterogeneity is very different in HPA and Si/SiC.

Between 1981 and 1987, Evans and coworkers characterized flexural creep damage processes in HPA. As reviewed by Dalgleish et al. (1985), large-grained or chemical heterogeneities nucleate either cracks normal to the applied stress axis, or multiple cavitating

---

[5] See Chs. 1-8.

[6] This is materials quality dependent (e.g. Dalgleish and Evans, 1985); HPAs damage by global, generalized cavitation, driven by applied stress or by internal pore pressures, and by local cavitation at creep crack tips.

[7] Flexural failure strains on the order of 0.1 were reported by Dalgleish and Evans (1985) and Dalgleish et al. (1985).

bands inclined at 60° to the stress axis — 'shear bands' (SBs).[8] Cracks propagate by localized cavitation in a damage zone, but the material exhibits a threshold K_{Ic}, and so a transitional stress, below which strain-driven damage controls lifetimes. SB cavitation is broadly important: SB intersections can nucleate macrocracks, macrocracks can nucleate SBs, and adjacent macrocracks can link prior to failure, vis SBs.

In Dalgleish et al.'s (1985) results, a transitional stress was found at approximately 175 MPa (elastic), but the $\{t_f$-$\sigma\}$ slope below the transition was about -1, and not $-1/n$, as would be expected for strain-driven damage accumulation to a critical strain (Grathwohl, 1984).[9] They expressed concern at flexural stress redistribution being enhanced by cavitation, which could

---

[8] Dalgleish and Evans (1985) developed no model for cavity nucleation and growth in shear bands. Their calculations for the periphery of large-grained heterogeneity in a diffusionally creeping polycrystal show that, at 55° inclination to the applied stress, the shear strain is at a maximum, and the mean stress is still 0.1 of its maximum value (in line with the applied stress). They connected these results qualitatively to shear band orientation by noting that cavity nucleation occurs at three-grain junctions subject to a shear stress transient; cavity growth by diffusion requires normal stresses on facets.

[9] Cao et al.'s (1987) stress corrosion results, for cracks nucleated at 30-80 μm diameter glass spots on lapped tensile faces, are consistent with Dalgleish et al.'s (1985) static fatigue data for natural heterogeneities.

influence damage accumulation. Materials heterogeneities played a major role in crack and SB nucleation, and SBs were widespread. Their tests were performed at strain rates of approximately 10^{-5} s^{-1}, which is high for creep tests. Also, they generated no *internal* damage data — data which likely will be important in higher quality materials.

Concerns exist as to how general these results are for HPAs. Currently, it is uncertain whether low materials quality, high strain rates and temperature, and test configuration-specific, damage-enhanced stress redistribution (uniaxial tensile *vs* flexural) are important in the dominance of shear banding, and in the subtransition slope. Further, although several cases of heterogeneous cavitation have been modeled (e.g. Hsueh and Evans, 1981; Dalgleish et al., 1984), no systematic approach to spatial heterogeneity, appropriate to a range of *high quality* polycrystals, has been developed, and developing and applying such an approach almost certainly will require *internal* damage data.

9.2 Objectives of the current work

In this work, we generated flexural and uniaxial tensile data for creep deformation, cavitation and fracture in HPA — a model, high temperature structural ceramic.

The overall aims were:

(1) on the basis of both internal *and* surface damage data, to locate a creep fracture regime in HPA, at lower temperatures and strain rates (10^{-8} to 10^{-6} s^{-1}) than in previous work; i.e. a region in $\{\sigma\text{-}T\text{-}\varepsilon\{t\}\}$ space in which generalized cavitation damage controlled failure,

(2) to develop and validate a uniaxial tensile creep test system for a range of structural ceramics, and to apply it to creep fracture in HPA,

(3) to compare flexural and tensile creep deformation, damage and fracture in HPA, and

(4) to describe generalized damage fields over the course of creep fracture, in order to define the microstructures a computerized image analysis systems will have to characterize in developing damage constitutive laws and local fracture criteria. In particular, to generate qualitative data on the level of damage as cavity coalescence creates macrocracks, and on the character of spatial heterogeneity in cavitation fields.

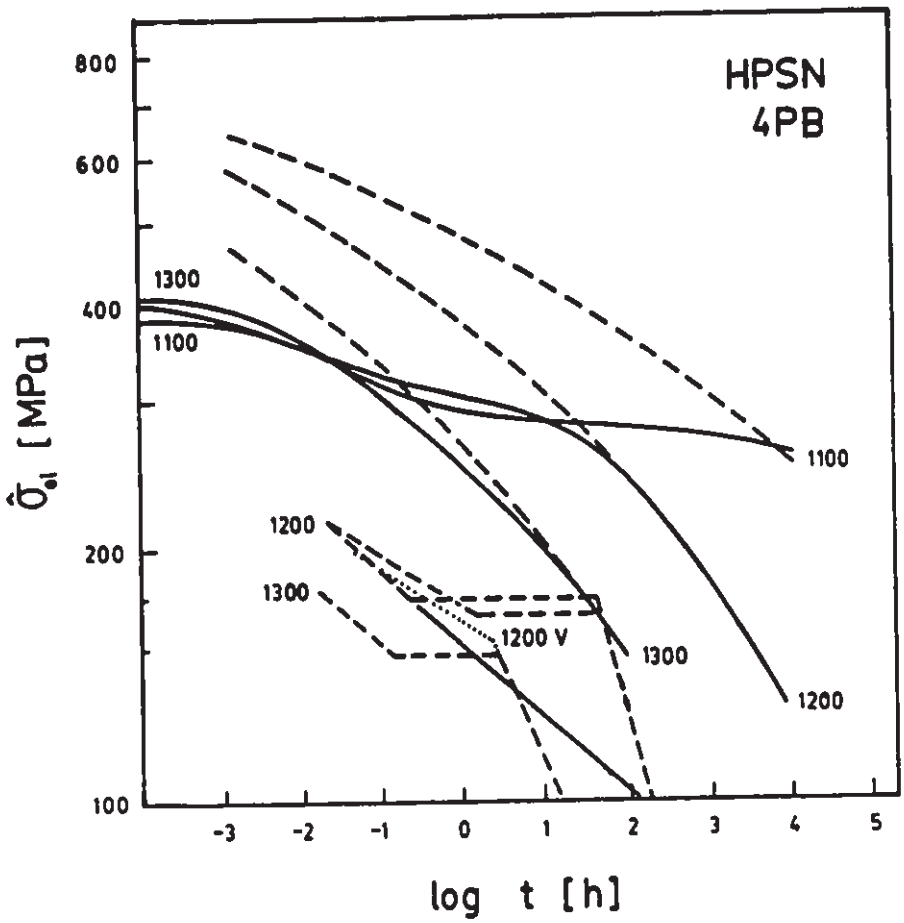

Fig. 9-1: Flexural static fatigue for HPSNs. The lower curves, for NH206, are after Grathwohl (1983,4); the upper curves, for NC132, after Quinn (1984). Dashed lines are tests in air with 'natural' flaws; solid are tests in air with artificial (Knoop) precracks on the tensile face; the dotted line is for vacuum. Temperatures are in C. The 'creep fracture' regime's border follows points where curves for naturally- and artificially-flawed failure times first coincide (see Fig. 9-2).

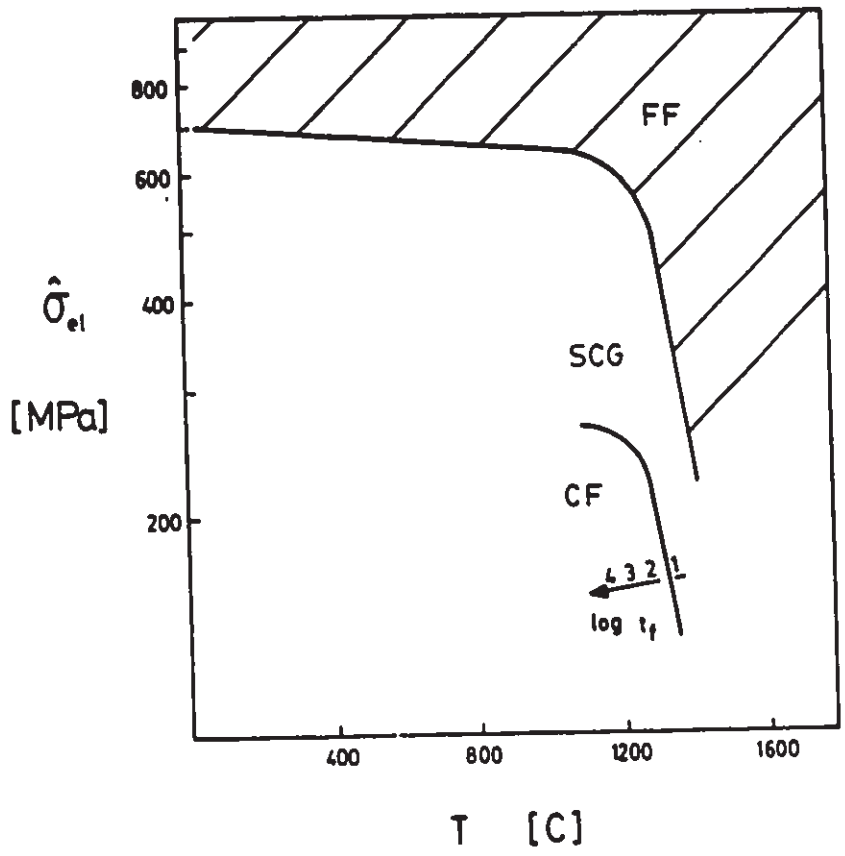

Fig. 9-2: Flexural static fatigue for NC132 HPSN, after Quinn (1984). Initial elastic stress at the tensile face *vs* failure time. The three fields are fast fracture (FF), slow crack growth (SCG) and creep fracture (CF). The failure time contours within the CF field are marked. The diagram is simplified — distributions of lifetimes (at a stress) or strengths (at a t_f) are not shown (Wiederhorn, 1983).

10 Experimental: creep and creep damage accumulation

10.1 High-temperature *flexural* creep tests

Rectangular specimens, approximately 4w x 6h x 651 mm,[1] were machined either on campus, using schedules outlined for swelling specimens (Table 2-2), or off campus (for which schedules were not available). Specimens were machined in both ARCO and AVCO HPA. The tensile face of a bar was always the face closest to the center of a billet; the creep loading and original hot pressing directions were parallel. Long edges adjacent to the future tensile face were beveled on a water-lubricated, 600 mesh, resin-bonded plate (Struers 'Planopol' 'GRASI'). The tensile face (and bevels) then were ground and lapped to a 0.25 μm diamond paste finish, following a schedule outlined for ceramography of swelled specimens (Table 2-4).

A polished specimen's cross section was measured with a vernier caliper, then the specimen was glued into a ceramic four-point

[1] Dimensioning abbreviations are: ϕ (diameter), w (width), h (height) and l (length).

bend rig with five-minute epoxy, using a custom aluminum jig and vernier caliper for alignment. The silicon nitride rig had load and support pin spacings of 28.5 and 54.0 mm; the pins were of 6 ϕ x 10 mm, ground, high-purity alumina rod. When the glue had set, the rig was placed in position in a furnace.[2] The rig was loaded lightly, to prevent it collapsing when the epoxy burned off at 300-400 C.

---

[2] The furnace, with loading and extensometer assemblies, was originally built by D. Watt of the University of Windsor, Windsor, Ontario. Though a new control system was added, few other changes were made.

The furnace was a simple box type, similar to that described by Quinn (1983), save that the lever arm/load rod socket assembly, and the extensometer, were somewhat more complicated. Also, a 25 mm layer of insulating board was placed outside the hot face of insulating fire brick, to permit operating at high temperatures. The four SiC heating elements were driven by a Eurotherm PID temperature controller and power controller, with a variable transformer to compensate for the U-shaped specific resistance curve of the SiC elements. See App. 18.

Because of the cost of modifying the current bend rig or having a new one made, these exploratory studies did *not* conform to MIL-STD 1942(MR) (Quinn, 1984).

The bend test system described by Govila et al. (1985) sets a standard for controlling rig/load train misalignment.

The extensometer consisted of three LVDTs (HP 24DCDT-250; linear error < 0.5%; ± 6.4 mm full scale displacement range). Each spring-loaded LVDT core contacted a specimen's tensile face via a 3 ϕ x ≈ 150 mm alumina rod. The tip of the central rod was ground and polished to a very shallow dome, to prevent errors from the tip being driven slowly into the tensile face by the spring pressure; those of the outer two rods were tapered to a similar shallow dome about 0.5 mm diameter, to minimize both penetration *and* displacement errors at high bar curvatures. The outer rods were 25 mm apart.[3]

The core/probe assemblies were checked for free travel and minimal spring pressure. The alumina probes were correctly spaced (via a fork-like jig) while in contact with the tensile face. Each LVDT was zeroed, by a leadscrew to which its cylindrical body was clamped. The furnace was heated. Typically, heating to 1200-1300 C required 1.5-2 h. After a 10-20 min equilibration, the full load was applied smoothly by manually lowering a support elevator.

---

[3] If the neutral axis position is known, such a three-probe extensometer permits determining tensile face strain rates more reliably than either single probe or ram displacement methods. Previous work established that, for AVCO, the neutral axis was stable at the centerline of a rectangular test bar (Robertson and Wilkinson, unpublished reesults).

During a test, LVDT voltages were recorded periodically by a microcomputer. If a specimen broke, the power to the furnace heating elements was interrupted automatically by a microswitch on the load lever arm, which was in the 4-20 mA circuit between (PID) temperature and power controllers. A specimen that did not break was cooled rapidly under full load to about 900 C, after which it was furnace cooled under the small preload used in heatup.

The two halves of *broken* specimens were treated differently. For damage surveys, one half was cut at 45 degrees some 5-10 mm back from the fracture surface, and was mounted with silver paint on this sloping face, on an SEM pin mount.[4] An angled cut permitted coating both fracture and tensile surfaces with gold, without a rotary base, and in one operation. Also, both faces could be examined by SEM without a specimen change or special adapter, simply by tilting and rotating the stage.

For detailed *internal* damage studies, the other half was cut 5-10 mm back from the fracture surface, then was sectioned near the bar centerline, parallel to the loading direction. This internal face was polished to 0.25 μm diamond, and then was thermally etched, following schedules for swelled specimens (Tables

---

[4] Care was taken to clean mount and specimen. See Ch. 2.

2-2,-4). A lapped, etched specimen was mounted on an SEM pin mount with high purity silver paint, on the original cut end, with the fracture surface 'up'. It then was coated with gold using a motorized rotary base (in order that, in *one* operation, the fracture, tensile and lapped internal surfaces were coated). With a small 90° adapter, any of these three faces could be examined in the SEM, by opening the specimen chamber and adjusting the specimen.

10.2 High-T *uniaxial tensile* creep testing

The furnace and load train designed and constructed for this test program are described in App. 18 (see Figs. 10-1,-2). Design issues are discussed in App. 19, and a second-generation design is described in App. 20.

The design and construction of the tensile rig was time-consuming. When it was begun, few such rigs existed in North America, and there were few guidelines for inexpensive rigs with extensometry (Pears and Digesu, 1965; Lange et al., 1979; Govila, 1982). Materials for pullrods, for example, were uncertain, and waits for materials and machining often long. Furthermore, at the time the furnace was built, it was seen as inevitable that compression and flexural tests, as well as tensile, eventually would be carried out in it. With tensile results uncertain, and

delays forseen for any change of focus which required a new test configuration, a test system was built which was capable of carrying out all three types of test. Optical extensometry was provided for tensile tests, and differential LVDT extensometry for the other two types. Tensile tests could be run under dead load or computer control, using different load frames; the compression and flexural tests were to be run under computer control.

Specimens were commercially machined, off campus, in ARCO HPA (Fig. 10-1a).[5] Flat faces were subsequently lapped to 3 or 1 μm diamond by hand, while a specimen was hot-waxed to an aluminum metal carrier (25 x 25 x 100 mm). The diamond polishing sequence was similar to that used for swelled specimens (Table 2-4).

Bevels on the long edges of the gauge length and flared sections were to be ground in and polished using a hand-held, 1/10 hp, commercial die grinder (Dumor, Model 10-351). However, the tooling for this operation — diamond wheels with a radius less than but close to the flare radius, with a *durable* coating of abrasive *in the* 1-10 μm *size range* — was not located. Standard toolmakers' wheels and grinding pins typically are no finer than 250 mesh; such tools chipped the gauge length edges. One set of

---

[5] Too little AVCO was on hand; no tensile tests were done on this HPA.

custom wheels (3 and 10 μm) were obtained by special order, but wore quickly. The technique adopted as an interim measure involved 'filing' off the initial material *transversely*, using 200 through 600 mesh SiC paper, wrapped around a rod of about 20 mm diameter. Final *longitudinal* lapping was done with the die grinder, using cylindric felt bobs 20 ϕ x 25 mm, which had been charged with 15, 6 and 1 μm diamond paste and polishing oil.[6] The bevels were checked for chips with a low power optical microscope. Narrow faces of gauge length and flares were lapped with the felt bobs.

A lapped specimen's gauge length cross section was measured, using a vernier caliper. The specimen then was pinned into the SiC pull rods of the load train, and was centered carefully in each rod slot with a thickness gauge (e.g. Mitutoyo 184-306). While the load train was unloaded, and with the clamshell furnace open, the extensometer telescope was focused on either upper or lower flags, while the load train was rotated from the *upper* SiC rod, with the lower rod following freely, until the specimen was normal to the telescope's line of sight.[7]

---

[6] This operation was awkward and tedious. In App. 20, we propose a specimen which needs *no* beveling, and perhaps no hand-lapping.

[7] A specimen was normal when *both* left and right flags were in focus, as the telescope was rotated by hand between them, with

A small (20 mm diam.) electric lightbulb then was placed in the rear half of the furnace, to illuminate the inside the cold furnace when it was closed. Its power leads were run alongside the upper pull rod, in the ≈ 2 mm gap between rod and furnace roof. The load train was loaded just enough to bring the lower nut of the load train against the lower plate of the test machine frame, so that the specimen was at the height it would be at when creep tested. The furnace was closed carefully. The alignment of the specimen flags with both radiation plugs was checked, with and without the telescope, by the light of the small bulb.[8] If it was necessary to shift the specimen *vertically*, the lower nut on the load train was adjusted gently; if *side-to-side* alignment was unsatisfactory, the *furnace* was shifted or rotated on its locating studs. The furnace was reopened, the light removed, and gaskets, and draft and heat radiation seals were adjusted. The furnace was reclosed, and 1/8" thick refractory felt seals placed around the pull rod on the top face of the furnace.

---

the rotary base disengaged from its micrometer drive.

[8] During a test, visual contrast depended on the radiation plug cooling the well in the rear furnace wall, and on the specimen being aligned between well and sight tunnel, such that each flag could be seen through its cutout in the sight tunnel plug, silhouetted in front of its cutout in the well plug.

Typical heating times were 2 h to 1250 C, during which the specimen was maintained under a small preload (equivalent to a gauge section stress of ≈ 5 MPa). At the test temperature, the flag locations were determined during an equilibration soak under the preload only. The specimen then was loaded smoothly, over a period of 30 to 60 s, via an elevator driven through a gear reduction box by a variable-speed, reversible DC electric motor. The flag locations were recorded again, and then periodically throughout the test, at a frequency that varied with the elongation rate for that test, considered in relation to the typical uncertainty of the optical extensometer.

'Left' and 'right' elongations, at a given time, were calculated from the positions of the four flags, and were determined as follows. A target point on each flag knife-edge, on which the cross-hairs would be set, was chosen and recorded.[9] During the test, care was taken to handle the telescope's inverting and reversing the images, and to relocate specific targets. A flag height was determined by locating its target point at the telescope crosshairs, using micrometer drives on the vertical stage and rotary base. With the rotary position set, four vertical readings were taken for a flag — two coming from above,

---

[9] This allowed for variations in the exact profile of each shoulder flag — variations due to both machining and hand-lapping.

and two from below the target — from which an average and standard deviation were calculated. A typical uncertainty for such a set of four readings was ± 5-10 μm.[10]

The micrometer drive of the rotary base was unlocked, and the assembly was rotated by hand until the other flag at this level was seen in the telescope. The base was relocked onto its micrometer, and this flag's location determined. Then, with the base still locked, the stage was raised or lowered, with the sight port's insulating door closed, until the flag above or below it came into view, and the process was repeated. When all four flags had been located — which might take 5 to 10 min[11] — the insulating door was closed to reduce heat flux onto the glass window.

In the initial series of tests, five of seven specimens were permitted to creep until they broke. When a specimen broke, the load pan fell back onto the elevator, displacing a pin which rotated a pair of mercury switches. This interrupted the 4-20 mA signal to the power controller (so cutting off power to the furnace), as well as the power to an electric clock (which recorded the exact failure time).

---

[10] Wiederhorn et al (1986) report ± 2 μm for their indented wire extenders.

[11] At an elongation rate of, say, 20 μm per *hour*.

Two of seven specimens were given step-stress change tests, as follows.[12] With the variable speed motor driving the Satec's elevator up beneath the test load, a specimen was rapidly unloaded, until the lower end of the load train was felt to be loose at the lower frame plate. At this point, the elevator fully supported the test load. The load was adjusted, and the specimen was reloaded by the variable speed motor, at the slower rate typical of standard teats (≈ 60 s to load a specimen).

A specimen's fracture strains were estimated by measuring the area of its fracture surface with a toolmakers' optical comparator (Bausch and Lomb, 10-50X).

For SEM, the two halves of a broken tensile specimen were treated as were those of a broken flexural specimen (Sectn. 10.1), save that the 'survey' half was cut normal to the long axis of the specimen, rather than at 45 degrees.

---

[12] One specimen broke, due to faulty stress-change technique; the other was given three different loads.

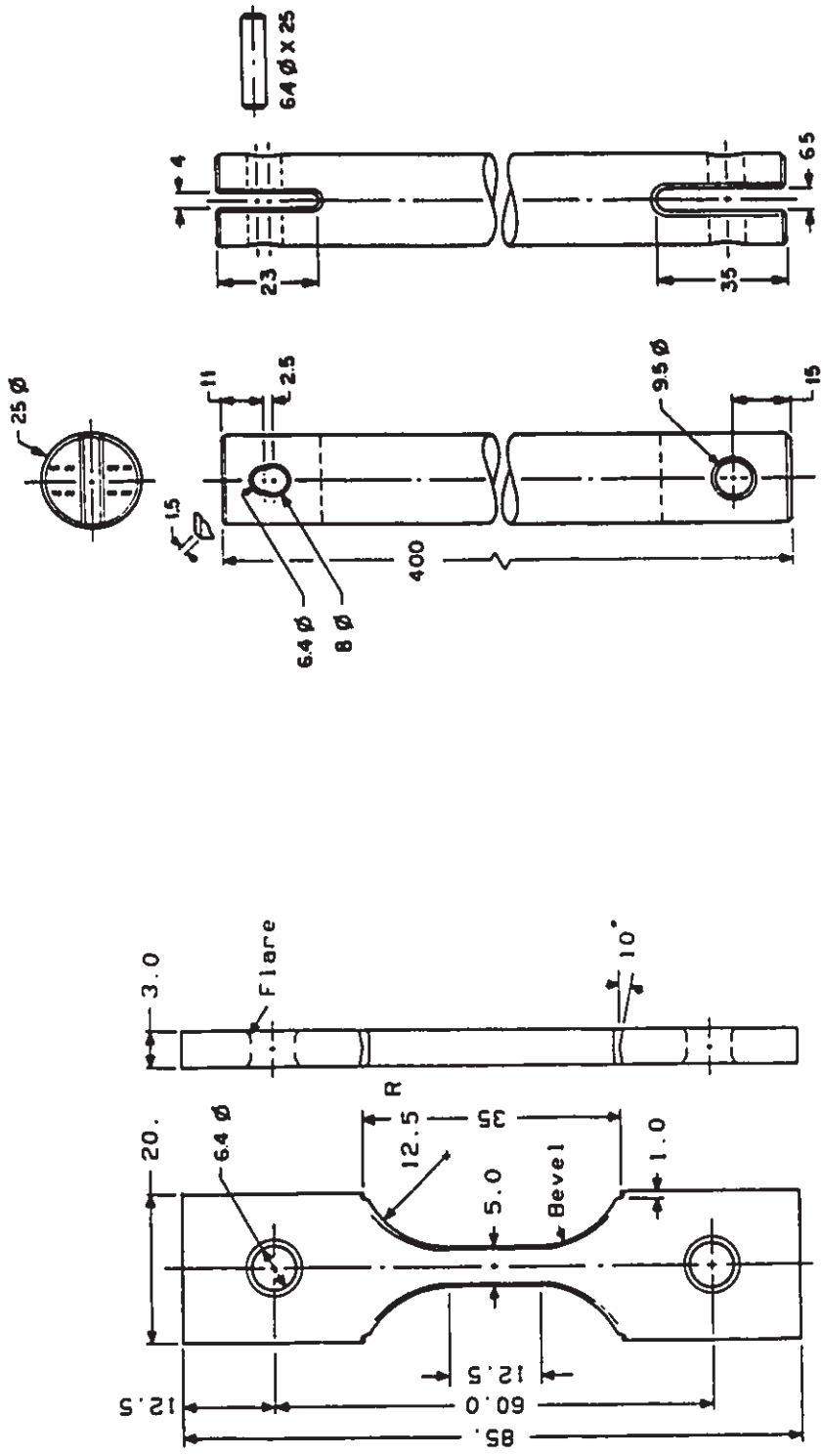

Fig. 10-1: Uniaxial tensile test rig (first generation; see Apps. 18-20).

a) Specimen (alumina).

b) Pull rod (recrystallized SiC) and hot pin (HP/SiC).

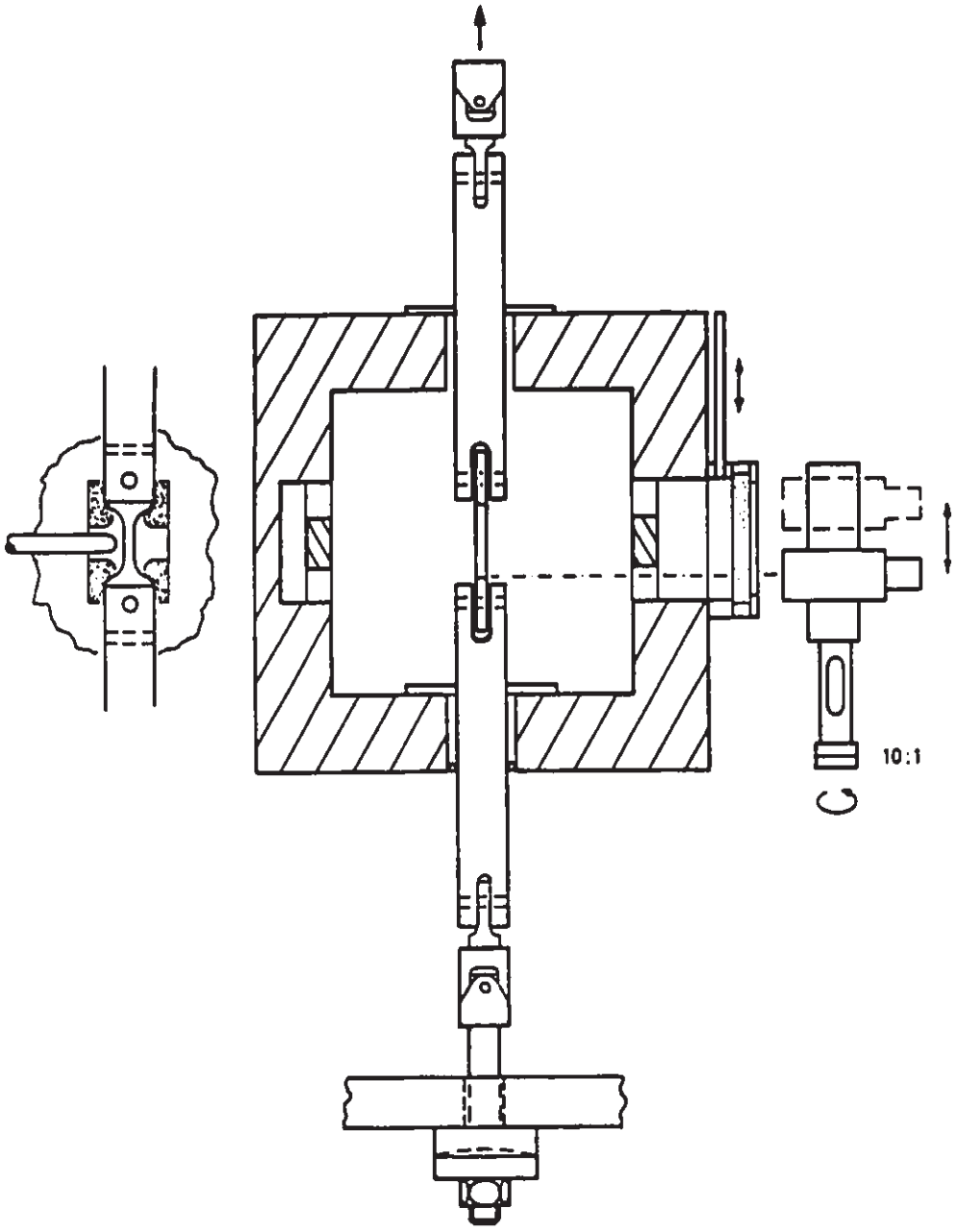

Fig. 10-2: Uniaxial tensile creep test rig.
(Schematic; see App. 18).

11 Experimental results

Variables are listed in section 11.3. While flexural data were generated in both HPAs, only ARCO was tested in uniaxial tension. Most of the flexural data given in this section is for that HPA.

11.1 Flexural results

All flexural strains, strain rates and steady state stresses in this section (Figs. 11-1,-2,-3 and -5) were calculated assuming that the Norton creep *pre-exponentials* were the same in tension and compression. We discuss this issue in App. 21.[1]

ARCO's strain-time data for flexural tests at 1250 C (Fig. 11-1) are typical of flexural results at all temperatures in both ARCO

[1] For flexural tests, stresses quoted are at the tensile face. Because stresses redistribute (App. 21), stresses must be specified as being either elastic or steady state. Fig. 11-1 shows steady state stresses, 11-2 shows both elastic and steady state, and 11-3 shows stress trajectories in time, from elastic to steady state.

and AVCO HPAs. Highly-stressed specimens failed at low ε and t. Specimens stressed below 170 MPa(ss) crept to the limit of strain possible in the rig (≈ 0.035 for ARCO, ≈ 0.055 for AVCO).[2]

Fig. 11-2 shows overall patterns in flexural deformation and failure for the two aluminas, determined during survey work in which we sought to locate conditions in which creep fracture due to generalized cavitation, at low strain rates and temperatures. AVCO was surveyed over two orders of magnitude in strain rate, and ARCO over one order.

Both aluminas showed a transitional stress near 200 MPa (elastic; see below) for strain rates between 10^{-7} to 10^{-6} s^{-1} (Fig. 11-2). At higher stresses, bars failed rapidly from a crack which propagated from a microstructural heterogeneity. At lower stresses, although cracks grew from many heterogeneities (see below), bars did not break by the time they had accumulated the maximum strains possible for the rig. Because micrographs of fracture surfaces and tensile faces showed heterogeneities and cracks similar to those of Johnson et al. (1984), Dalgleish and

---

[2] The maximum strains, $\hat{\varepsilon}$, were limited by the tensile face approaching the lower block of the bend rig. For a given material and rig (including load pin diameter), $\hat{\varepsilon}$ varies linearly with bar height (Hollenberg et al., 1971; Chuang and Wiederhorn, 1988). ACVO's bars were somewhat deeper than ARCO's.

Evans (1985) and Dalgleish et al. (1985), they are not presented here.[3] However, in contrast to that work, in the current work microstructural damage data were generated not just from these two surfaces, but from internal polish planes as well, and tensile face damage was correlated with polish plane damage (section 11.2; Ch.12; e.g. Fig. 11-7; 11-9 *vs* 11-10).[4]

The stress exponent, n, and activation energy, Q, were estimated, for a constitutive law of the form:[5]

---

[3] We list the types of heterogeneity later in this section. Surface damage seen on specimens tested below the transitional stress was for strains up to $\varepsilon \approx \varepsilon_f/3$ or $\varepsilon_f/2$. The papers referred to show damage in subtransitional specimens at higher strains.

[4] Earlier work (Robertson and Wilkinson, 1986) had shown a low-damage 'skin' some 15 μm thick at the tensile face of bend bars. There was therefore doubt that surface data *alone* could be used to characterize damage accumulation. We present no new data on this; however, edge rounding in polishing can be held to low levels (Ch.2; e.g. Fig. 11-7) so that such data now readily can be generated.

[5] Strain rates were calculated from Hollenberg et al. (1971), using earlier data showing that the neutral axis was stable (Robertson and Wilkinson, unpublished results). In Gruffel et al.'s (1988) uniaxial results at 1450 C, tensile and compressive strain rates were close, up to strains of 0.1 to 0.15. No grain growth occurred during the current tests. See also App. 21.

$$\dot{\epsilon}_{ss} = B_o \exp\left(\frac{-Q}{RT}\right) \hat{\sigma}_{ss}^{n} \qquad (1)$$

The stress exponent, n, can be estimated from the slope of isothermal ($\log \hat{\sigma}_i - \log \dot{\epsilon}_{ss}$) bend data. The initial elastic stress at the tensile face is independent of n; however, throughout most of a long-term test, the tensile face region will be subject to a smaller, redistributed stress, $\hat{\sigma}_{ss}$ (Chuang and Wiederhorn, 1988; Chuang, 1986; Cohrt et al., 1984a; App. 21). In the simplest case, uniaxial tensile and compressive constitutive laws are equal, and the neutral axis remains at the centerline of a rectangular test bar. Then $\dot{\epsilon}_{ss}$ can be calculated directly from bar curvature rates, which were available from our three-probe extensometry, assuming constant curvature within the gauge length (Hollenberg et al., 1971;[6] Jakus and Wiederhorn, 1988),[7] and $\hat{\sigma}_{ss}(n)$ is related to $\hat{\sigma}_{el}$ by a simple function of n (Cohrt et al., 1981, 1984b):

$$\frac{\hat{\sigma}_{ss}}{\hat{\sigma}_{el}} = \frac{2n+1}{3n} \qquad (2)$$

In such a case, *secondary* creep $\dot{\epsilon}_{ss}$ will yield an n when plotted against *initial* $\hat{\sigma}_{el}$, even though the steady-state $\hat{\sigma}_{ss}$ cannot be

---

[6] Limited to small curvatures; see original reference.

[7] Jakus and Wiederhorn (1988) show that this is *approximately* the case for two glass-bonded aluminas.

calculated from $\hat{\sigma}_{el}$ *until n is known.*

In these dead-load, four-point bend tests, $\dot{\epsilon}_{ss}$ were estimated from strain-time plots, from the data between the end of the primary transient (Fig. 11-1,-2) and the point at which the progressive fall in $\hat{\sigma}_{ss}$ with decreasing moment arm became significant.[8]

Bars tested *below* the transitional stress ($\hat{\sigma}_{el} \approx 200$ MPa) had strain-time curves with clear primary and secondary sections, but no tertiaries (Fig. 11-1).[9] For tests at stresses *above* the transition stress (in which bars broke at short times) calculated (ϵ–t) plots still seemed to have primary transients followed by secondary creep (Fig. 11-1b). However, the plotted $\dot{\epsilon}_{ss}$ were inconsistent with matrix deformation rates extrapolated, to high

---

[8] The moment arm decreased because, as bar curvature increased with ϵ, the bar/load pin contact points, on each inner/outer pin pair, moved towards each other, around the circumference of their load pins. (The relative decrease can be estimated from Hollenberg et al. (1971), but is not marked on Fig. 11-2.). At high elongations the decreasing moment was offset by the loss of cross sectional area near the tensile face.

[9] Tertiaries reported for structural metals are for uniaxial tensile tests, not for flexural tests. Physical interpretations of flexural primaries and tertiaries are complicated by stress redistribution (Cohrt et al., 1984b; Chuang and Wiederhorn, 1988).

stresses, from tests below the transition (Fig. 11-2). Rather, they likely reflected a bar deforming locally, like a hinge, about the gauge length's growing dominant flaw. So, for such tests, neither $\dot{\varepsilon}_{ss}$, nor the apparent length of the primary transients, were taken as representing *matrix* deformation.

Primary transients were clearest in low-stress tests (Fig. 11-1). For tests below the transitional stress, transients were complete in about 1 to 5 hours, and after strains of less than 0.005 (Figs. 11-1,-3).

Bending stress exponents, n, in the range 1.5–2.0, were estimated for both HPAs, from bars which did not fail (Fig. 11-2). For AVCO, the exponent was 2.0; for ARCO, it was approximately 1.8. Uncertainties in both were ±0.2.

Data for AVCO (1150, 1200 and 1350 C) suggested an activation energy for deformation of $Q \approx 480$ kJ/mol (Fig. 11-2). For ARCO, data at 1200 and 1250 C suggested $Q \approx 390$ kJ/mol.

AVCO deformed far more readily in creep than ARCO (Fig. 11-2). At a given *sub*transitional stress, their bending creep strain rates were approximately equal when AVCO was 100 C cooler than ARCO

(1150 vs 1250 C).[10]

Fig. 11-3 shows flexural static fatigue data for ARCO HPA at 1250 C in a form directly comparable to the original HPSN data of Quinn (1984) and Grathwohl (1984; Fig. 9-1) and to the HPA data of Dalgleish et al. (1985).[11]

Specimens which failed rapidly are denoted by vertical bars. Because their strain rates are uncertain (Fig. 11-2), stresses are as well; upper and lower bar ends give the two *limiting* stresses for these specimens (elastic and stationary). Open symbols denote specimens which did not fail. During a test, as stresses redistributed, material at a tensile face was subject to a falling stress trajectory (shown schematically by a curved line). The ends of the primary transients were determined from raw strain-time plots, as were strain contours. Because of the anomalous strain rates, strain contours do *not* apply to the specimens that failed at short times. *Transitional* stresses are given as elastic and steady state values.[12]

---

[10] As their Q's differ, this relation will change with temperature.

[11] Because we have uniaxial tensile data only for ARCO, and because the patterns in static fatigue behavior were similar in the two HPAs, we show only ARCO's data in this form.

[12] See first paragraph in this section (11.1).

For rapid failures above the transitional stress, the two orders of magnitude scatter in failure times discouraged determining a slope. On fracture surfaces in such specimens, crack origins included:

1. ARCO

a) a 50 μm diam. region containing large (10 μm) equiaxed grains.
b) an elliptical cluster, 100 x 200 μm, containing 10 μm diameter, platelike grains.
c) a single equiaxed 100 μm grain, intersecting the tensile surface.
d) a flat elliptical region 200 μm long, normal to the original hot-pressing direction, with a hollow, cracklike core extending most of its length.

2. AVCO

a) a blocky-grained cluster, similar to (b), above.
b) a 75 μm spherical hollow.[13]

On a fracture surface, the heterogeneity which was the crack

[13] On one fracture surface; the other was not examined.

origin was encountered at a range of depths, relative to the tensile face. Some fatal cracks originated from flaws cut by the lapped tensile face; others from flaws within the flexural specimen, at depths of up to maximum of approximately 700 μm from that face.

In tests *below* the transition, in both HPAs, no delayed creep failures occurred, up to the maximum strains possible in the rig. (This was the case even when AVCO was *pre*damaged with grain-boundary cavities by swelling in pressureless, high-T anneals.)[14] In these specimens, multiple sub-critical cracks developed from several classes of tensile face heterogeneity. These included:

a) circular or elliptical regions about 100 μm in diameter, consisting of large equiaxed grains (10 μm diameter), either (i) with or (ii) without a porous core.
b) circular regions about 10-30 μm in diameter, with grains of normal size, but either (i) porous or (ii) preferentially etched (either during creep, or in a ceramographic etch).
c) large blocky grains, 10-20 μm long, with aspect ratios of 2:1 to 5:1, occurring either (i) individually or (ii) in

---

[14] Preanneals were 1450 C, 50 h. See Ch. 4 for the *pre*damage levels introduced by such anneals.

loose clusters up to 100 μm long, consisting of two to ten grains.

From the regions of low surface relief around them, these cracks appeared to slow or stop after their initial growth.[15] At the lowest stresses tested, many such cracks developed.

No shear band cavitation[16] developed around heterogeneities — only cracks normal to the applied stress. For ARCO tested in bending at 1200 and 1250 C, (1) cracks with *coplanar* damage zones only were seen over a K_I range of 0.9 to 1.8 MPa$\sqrt{m}$ (Broek, 1982, p.82),[17] (2) cracks with either one or two *non*coplanar damage zones[18] were seen at K_I of between 0.9 to 1.5 MPa$\sqrt{m}$, and (3) *no* cracks with *non*coplanar damage zones were seen at K_I greater than 1.5 MPa$\sqrt{m}$.

---

[15] Such cracks were seen on tensile faces as diameters of circular regions almost free of the surface relief that developed at higher strains, as grains rotated and slid on their neighbors. Corresponding low-damage regions were encountered *on internal polish planes*, on either side of a crack (Fig. 11-8).

[16] See Ch.9.

[17] Interpreting surface cracks as *half-pennies*.

[18] Noncoplanar damage zones are heavily cavitated regions or bands which develop on either side of but ahead of the crack tip; that is, 'above' and 'below' the plane of the crack (Blumenthal and Evans, 1984).

11.2 Uniaxial tensile results

To the present time, we have uniaxial tensile creep fracture data for *four* specimens of *ARCO* HPA, tested in air at 1250.[19] The range of applied stresses was approximately 40 to 100 MPa; the corresponding failure times were about 250 to 20 h (Figs. 11-4,-6).

Strain rates were estimated directly from elongation data (Figs. 11-4,-5):[20]

$$\dot{\varepsilon}(t) = \dot{\ell}(t)/\ell(t) \qquad (3)$$

Elongation rates were measured at the shoulders of a specimen

---

[19] *Seven* ARCO specimens were tested. The first was lost through faulty stress change technique in a multiple stress test, the second was tested at three different stresses in the same test, and the fifth failed from both in the head and in the gauge length, 10 s after applying 140 MPa. The AVCO HPA was out of production by the time of the tensile tests, and too little of it was on hand to permit it to be tested.

[20] Because of complications in including the flared region of a specimen into a tensile strain analysis, particularly at high strains, we present no such analysis at this time. In App. 20 we recommend a specimen design which permits a very simple and direct translation of flag elongation to gauge length strain, which eliminates these complications

(Fig. 10-1a). For the rather low stress exponents ($n \approx 2$), deformation rates decreased slowly as the cross sectional area increased through the flares, between the gauge length and the flags. As a result, the effective gauge length was uncertain. An effective *initial* gauge length of 20 mm was assumed for plotting $\dot{c}$ (Fig. 11-5), and vertical error bars were marked, corresponding to the limits of 12.5 mm (the nominal gauge length) and 35 mm (the flag separation).

Tensile strain rates from *six* specimens are plotted in Fig. 11-5. For the four static fatigue specimens, *approximate* stress-strain rate paths were calculated from Fig. 11-4 (using Eq. 3 and ℓ_o = 20 mm), and are given as dashed lines. Physical primary creep occurred in all cases.[21] At the two higher stresses, specimens broke while in primary creep. Tertiary acceleration was evident at 55 MPa, and was stronger at 40 MPa. In such a ductile material, tested in dead-load, the change of applied stress with elongation became significant at low stress. Between-test scatter was about half that due to the uncertain effective gauge length. The tensile data confirm the flexural value for the stress exponent: $n = 1.8 \pm 0.2$.

For comparison, ARCO's flexural strain rates at 1250 C,

---

[21] The primaries follow from Eq. (3) and the long period in which the slope of each line in Fig. 11-4 was constant.

calculated assuming a stable neutral axis and an n of 1.8, also are given in Fig. 11-5. The tensile strain rates are approximately an order of magnitude higher than the flexural (see App. 21).[22]

Though gauge length widths were not systematically measured by optical comparator, no necking was evident in any specimen.

Failure strains were calculated assuming constant-volume deformation, from the ratios of initial gauge length cross sectional area (measured by vernier caliper) to the area of the fracture surface (measured by optical comparator; Fig. 11-15):[23]

$$\varepsilon_f = ln\ (A_o/A_f) \qquad (4)$$

At 100 and 77 MPa, failure strains were 0.08; at 55 MPa, 0.09. At 40 MPa, ε_f doubled to 0.17.

---

[22] The error bars and dashed lines correspond to the uncertainties in R, the ratio of the stress-independent factors for uniaxial tensile *vs* compressive creep (Eq. 1; see App. 21).

[23] Determining uniaxial tensile failure strains from gauge length cross sections ignores the cavitation component of strain. For the generalized damage levels evident in Fig. 11-10, the failure strains for low stress were significantly larger than the minimum values reported here. Raj (1982b) describes how to separate constant-volume and dilational creep strain components experimentally.

On a static fatigue, {log t_f–log stress} plot (Fig. 11-6), the three data points at high stress extrapolated back to the *maximum* flexural failure times in the flexural transition stress range near 200 MPa (≈ 5 h; Fig. 11-2).[24] The slope of the data was about −1/3 at high stress, increasing to between −1/2 and −1/1.5 at stresses between 55 and 40 MPa.

As stresses decreased, the amount of internal and external cavitation damage, at failure, increased. Fig. 11-7a shows a crack which propagated inwards from the surface of the sample, as cut by the polish plane. This specimen was crept at 77 MPa, to a failure strain of 0.08. Fig. 11-9 shows a crack of similar length (≈ 115-120 μm) on the polish plane of the specimen crept at 55 MPa to ε_f of about 0.09. This specimen is shown in Fig. 11-8.[25] At failure, the crack in the 55 MPa specimen had opened far more than the corresponding crack in the 77 MPa specimen. Its damage zone was larger and more complicated, and showed signs that, at an earlier stage, the crack advanced along one of two noncoplanar

---

[24] Uniaxial tensile tests are currently too expensive to use to explore the variable, flaw-size sensitive region at high stress, near the transition, *in a material of the quality used.*

[25] The crack in Fig. 11-9 is at the right hand side of the polish plane in Fig. 11-8a, and at the left hand side of the external surface in Fig. 11-8b.

damage zones. Generalized damage is much heavier in the second specimen, and the damage levels above and below the crack itself are low (Figs. 11-7a,b and 11-9,10b). At the lower stress, cumulative damage levels were high enough that cavities coalesced to generate flaws on the order of the size of the initial microstructural heterogeneities (Fig. 11-10b).

Figs. 11-7c and 11-12 show external surfaces of specimens crept at 77 and 55 MPa respectively. The surface relief is due to grains sliding and rotating during creep; such relief is more exaggerated in the 55 MPa specimen. Generalized cavitation levels at failure were far heavier in the 55 MPa specimen. In the 77 MPa specimen, cavitation levels appear somewhat lower on the external surface than on the polish plane. Surface relief complicates estimating external cavitation levels, particularly at low stresses (Fig. 11-12). In the 55 MPa specimen, a crack origin is indicated by the dark lobes above and below the crack, in which the surface relief is low.

In the 77 and 55 MPa specimens, little shear banding occurred *between crack tips* — internally or externally (Figs. 11-7,-9,-12). However, on *in*ternal cracks, noncoplanar damage zones were rather common (e.g. Fig. 11-9,-11). In some of these inclined lobes, cavity coalescence nucleated several small cracks, each normal to the applied stress (e.g. at the left end of the crack in Fig. 11-11). In the 100 MPa specimen, a survey

(by optical microscope, at 65 X) suggested that noncoplanar damage was common at the tips of the many surface cracks nucleated.

On fracture surfaces, the critical crack at failure became much larger as stress decreased, and the crack peripheries changed from sharp to poorly defined (Fig. 11-13). At lower stresses, multiple cracks were seen on fracture surfaces, and generalized damage levels became so high that crack tips advanced by linking with multi-grain cracks which developed ahead of the main tip, by cavities coalescing in extended damage zones (Figs. 11-9, and particularly 11-12).

Despite this, the critical K_{Ic} values calculated from the size of fracture surface cracks (Newman and Raju, 1981) were rather insensitive to stress, strain and cumulative damage at failure, having values close to 3 MPa$\sqrt{m}$ (Fig. 11-14).

In the 100 MPa specimen, the crack originated in a heterogeneity some 50-100 μm from the surface (a high magnification SEM micrograph is not yet available). In the 77 MPa specimen, the origin was a 200 μm diameter cluster of plate-like grains, 10-20 μm in diameter, similar to origins seen in rapid *flexural* failures. In the 55 MPa specimen, no heterogeneity was evident at high SEM magnification, but the crack was centered on a poorly beveled edge. Mechanical damage in manual beveling may have

caused the crack.[26] In the 40 MPa specimen, a planar region some 15 x 50 μm, about 50 to 100 μm beneath the specimen surface, was the apparent crack origin. This type of flaw was not encountered previously in flexural failures. One or several large planar grains could have caused such a feature in a fracture surface, by failing along the interface with the polycrystal matrix (e.g. at the right of Fig. 11-11); the mating fracture surface has not yet been examined by SEM to verify this.

11.3 Variables

$A_{o,f}$ initial and at-fracture cross sectional area of gauge length; [m^2]

B_o temperature-dependent, stress-independent pre-exponential factor in creep deformation law; [

ε strain; [-]

ε_f failure strain; [-]

$\dot{\varepsilon}_{ss}$ steady state strain rate; [s^{-1}]

K_{Ic} critical, mode one stress intensity factor; [MPa$\sqrt{m}$]

ℓ, ℓ_o effective gauge length; effective *initial* gauge length; [m]

n stress exponent for creep deformation; [-]

N stress exponent for creep crack growth; [-]

Q activation energy; [J/mol]

---

[26] The specimen recommended in App. 19 *eliminates* beveling.

R gas constant; [J/mol·K]

σ stress; [N/m^2]

$\sigma_{el,ss}$ elastic (steady state) stress; [N/m^2]

t_f failure time; [s] or [h]

Diacriticals

$\hat{}$ maximum (for a bend specimen, this refers to the tensile face).

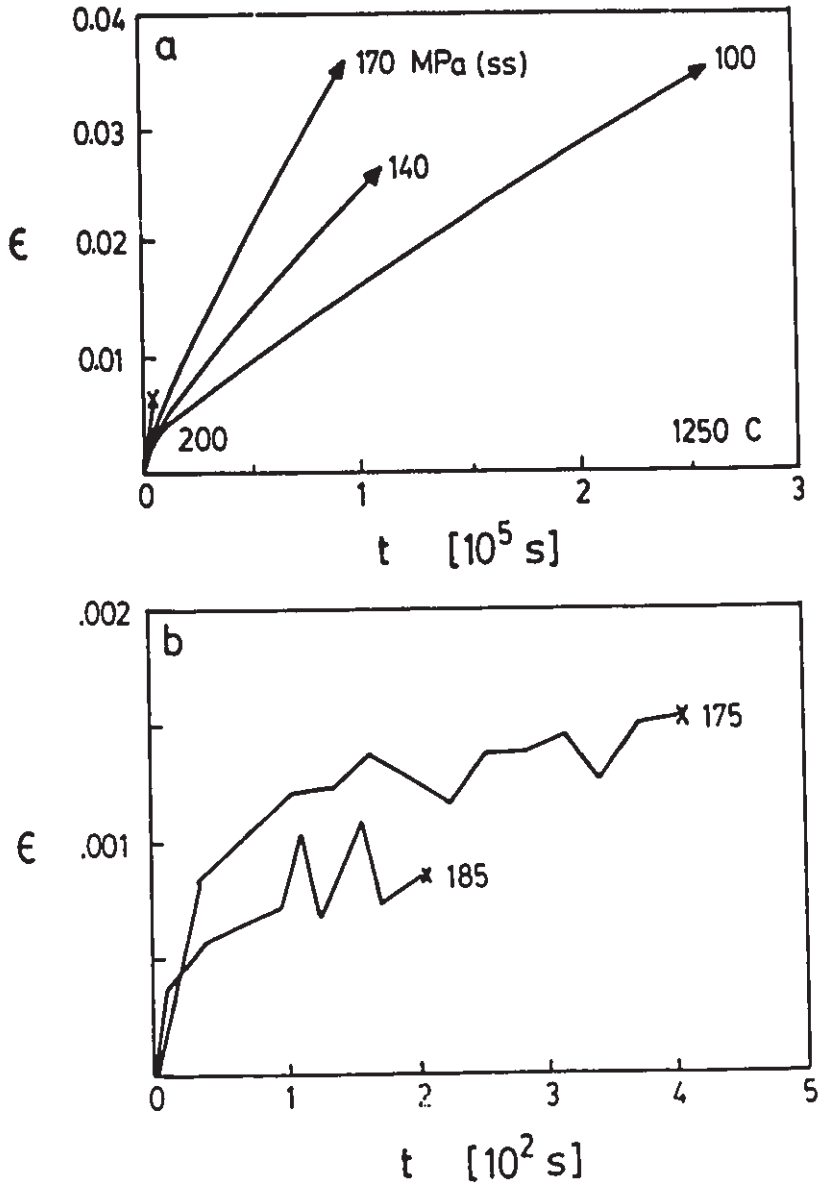

Fig. 11-1: Flexural creep deformation in ARCO HPA at 1250 C. Strains and *steady state* stresses are calculated for a stable neutral axis and an *n* of 1.8. See App. 21.

a) Above (200 MPa, ss) and below (100-170 MPa, ss) the transition.

b) Above the transition (175, 185 MPa, ss)

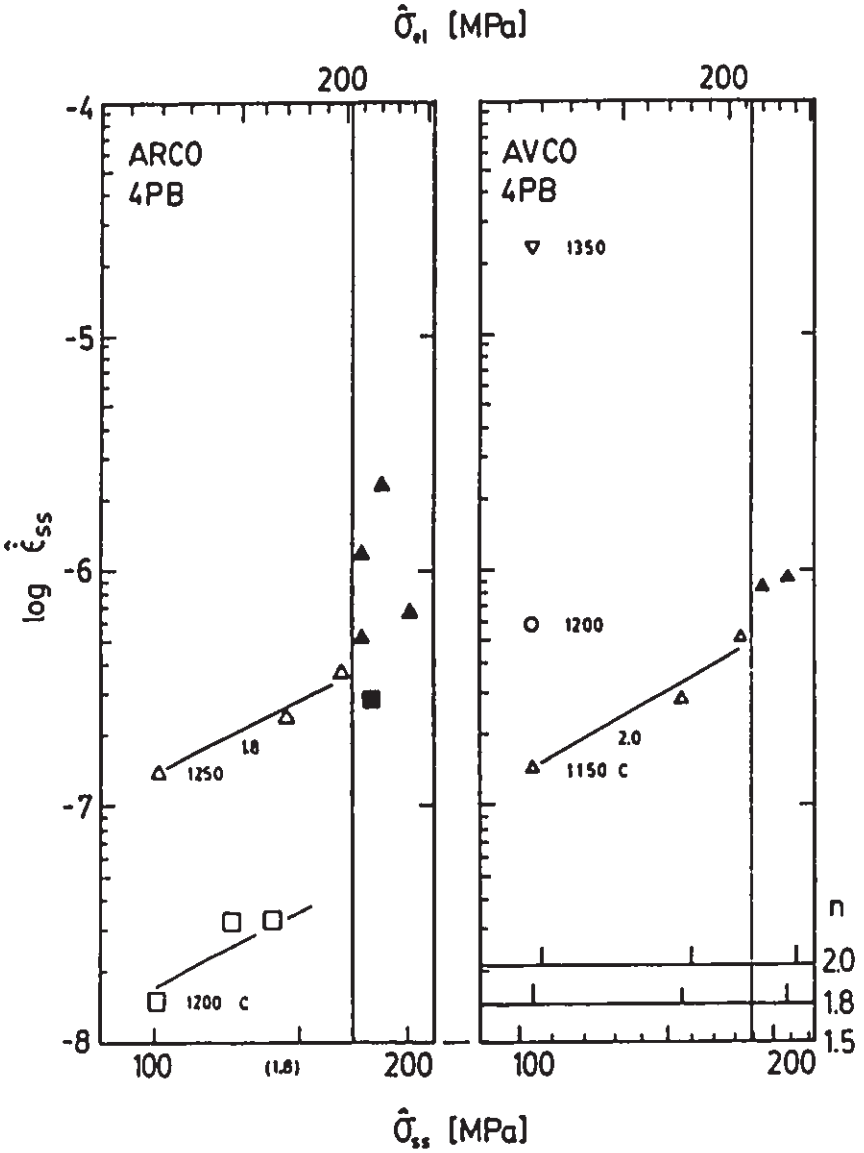

Fig. 11-2: Flexural creep deformation and failure in AVCO and ARCO HPAs as a function of stress (initial, $\hat{\sigma}_{el}$, and stationary, $\hat{\sigma}_{ss}$)and temperature. Open symbols are for specimens unbroken to the strain limit for the rig ($\hat{\epsilon} \approx 0.05$); filled are for specimens that failed during a test.

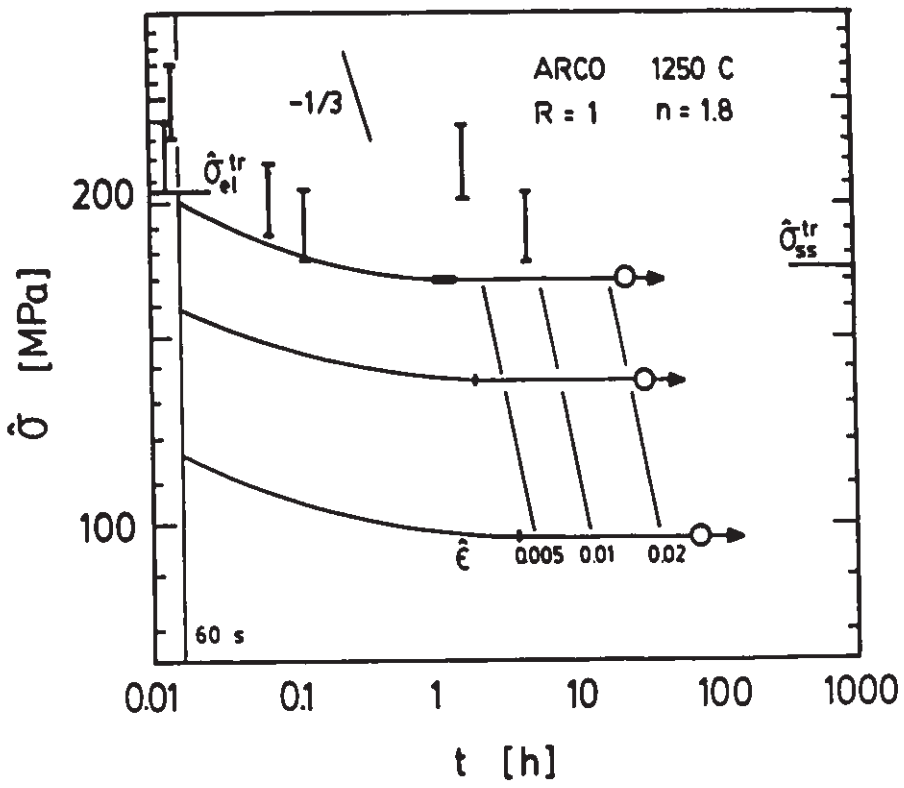

Fig. 11-3: Flexural static fatigue in ARCO HPA at 1250 C: time vs elastic and stationary stresses at the tensile face. Specimens which failed rapidly are denoted by vertical bars; open symbols denote specimens which did not fail. Stress redistribution at tensile faces followed trajectories shown schematically by curved lines. Strain contours do *not* apply to the specimens that failed at short times. The vertical line at 60 s denotes a typical loading time.

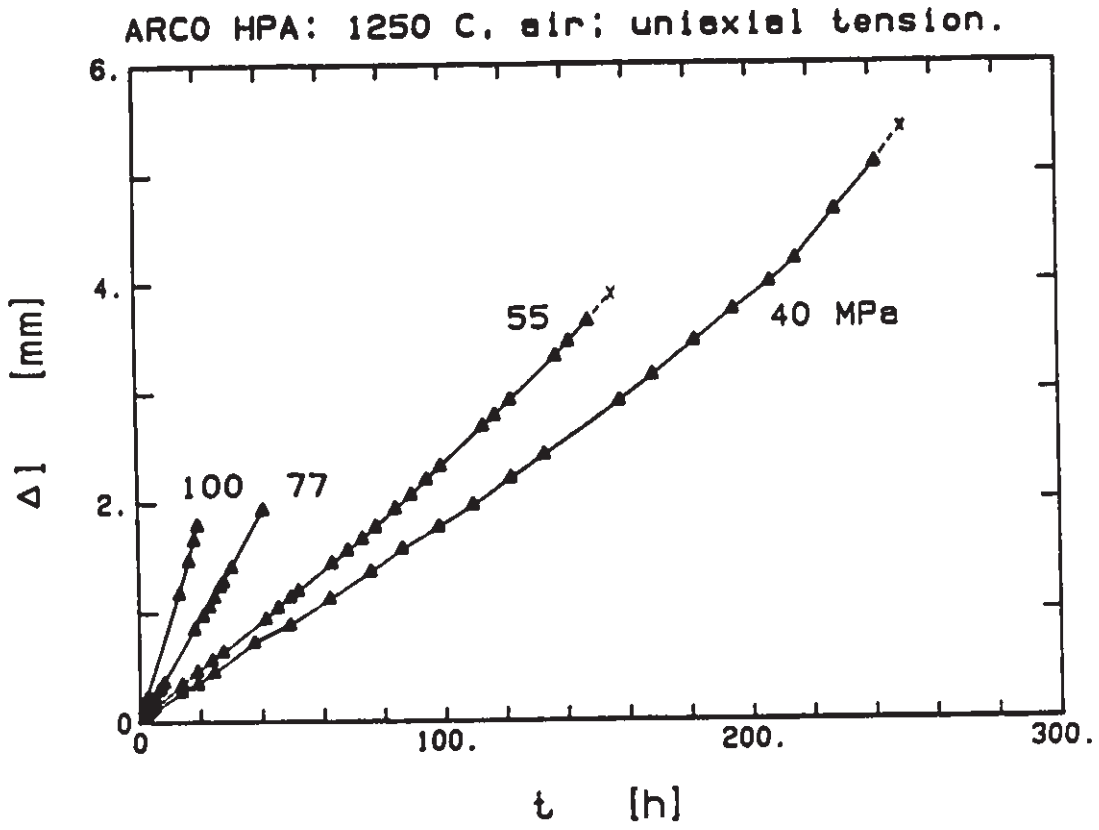

Fig. 11-4: Uniaxial creep elongation in ARCO HPA at 1250 C in air. The failure times for the two higher stresses coincide approximately with the ends of the plotted lines; for the lower two stresses, bars failed at the marked 'X's.

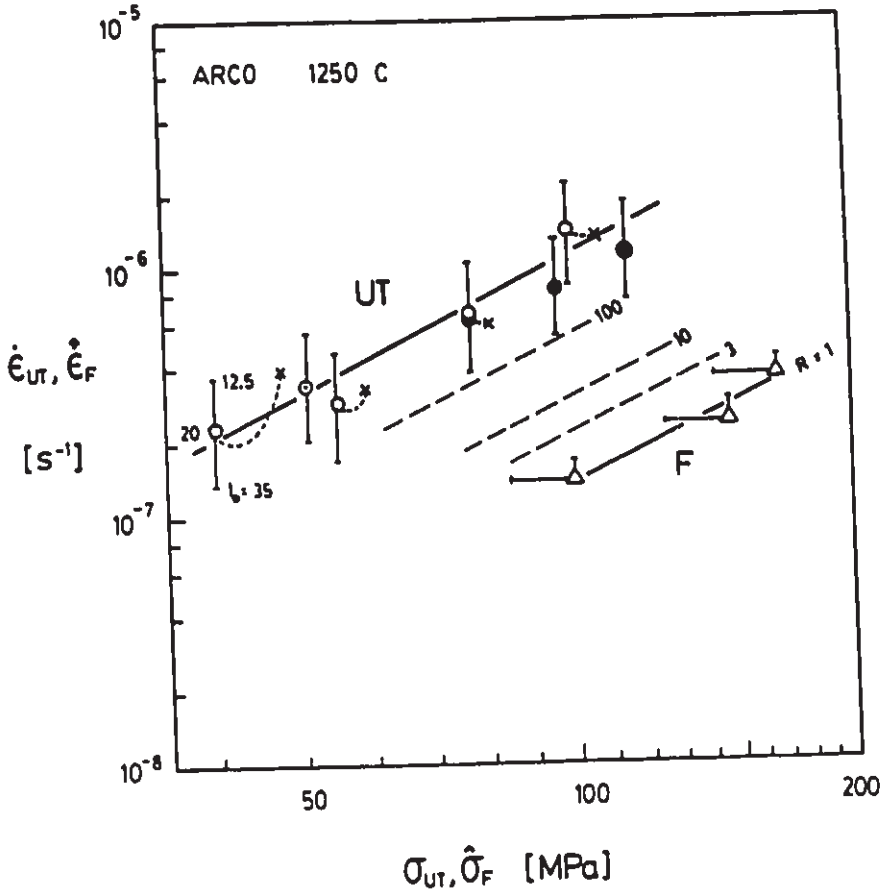

Fig. 11-5: Uniaxial tensile (UT) *vs* flexural (F) creep rates in ARCO HPA at 1250 C. See App. 21.

Solid UT symbols are for a step-stress-change test on *one* specimen. Dashed lines are approximate *dead-load*, static fatigue trajectories, estimated from Fig. 11-4. UT error bars are for extreme effective initial gauge lengths, ℓ_o, of 12.5 and 35 mm; plotted points assume ℓ_o = 20 mm.

F error bars are for $1 \leq R \leq 3$ (App.20); plotted points assume $R = 1$. Dashed F lines are for R = 3, 10, and 100.

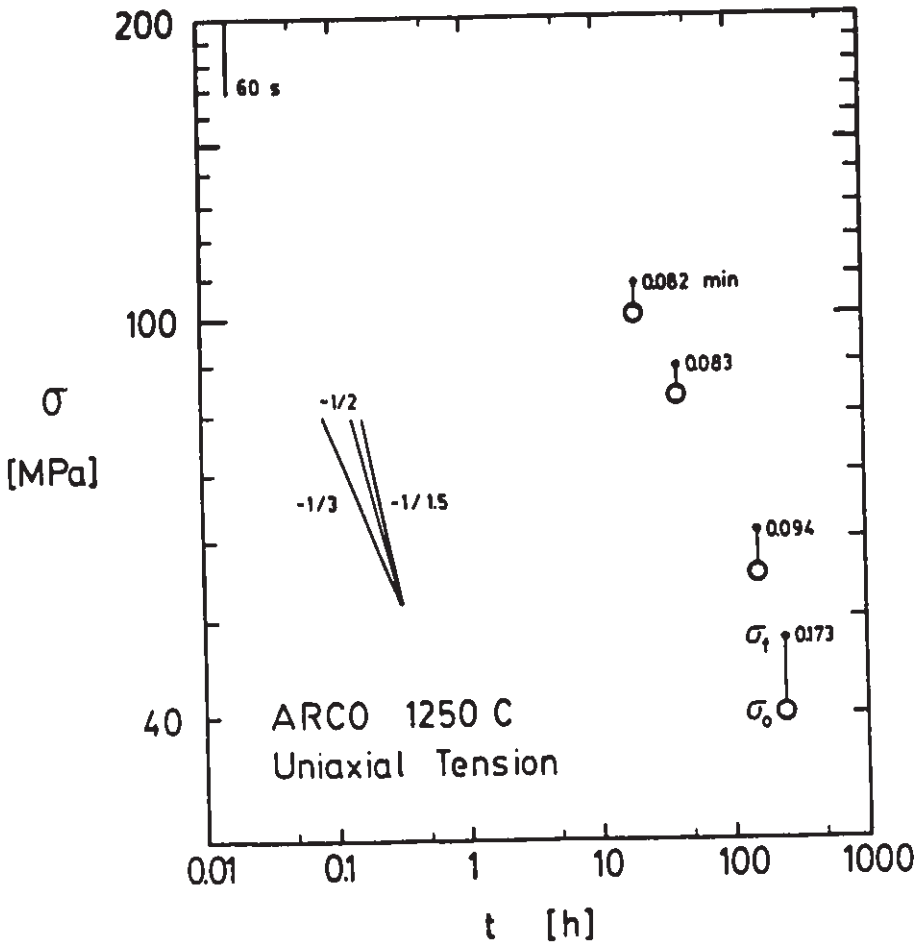

Fig. 11-6: Uniaxial tensile static fatigue in ARCO HPA at 1250 C: failure time vs (dead-load) stress. The large symbol denotes the *initial* stress for a specimen; the small symbols denote the macroscopic stress *at failure*, based on the external dimensions of the fracture surface. The minimum failure strains are marked (see Fig. 11-14). The short vertical line at 60 s denotes a typical loading time.

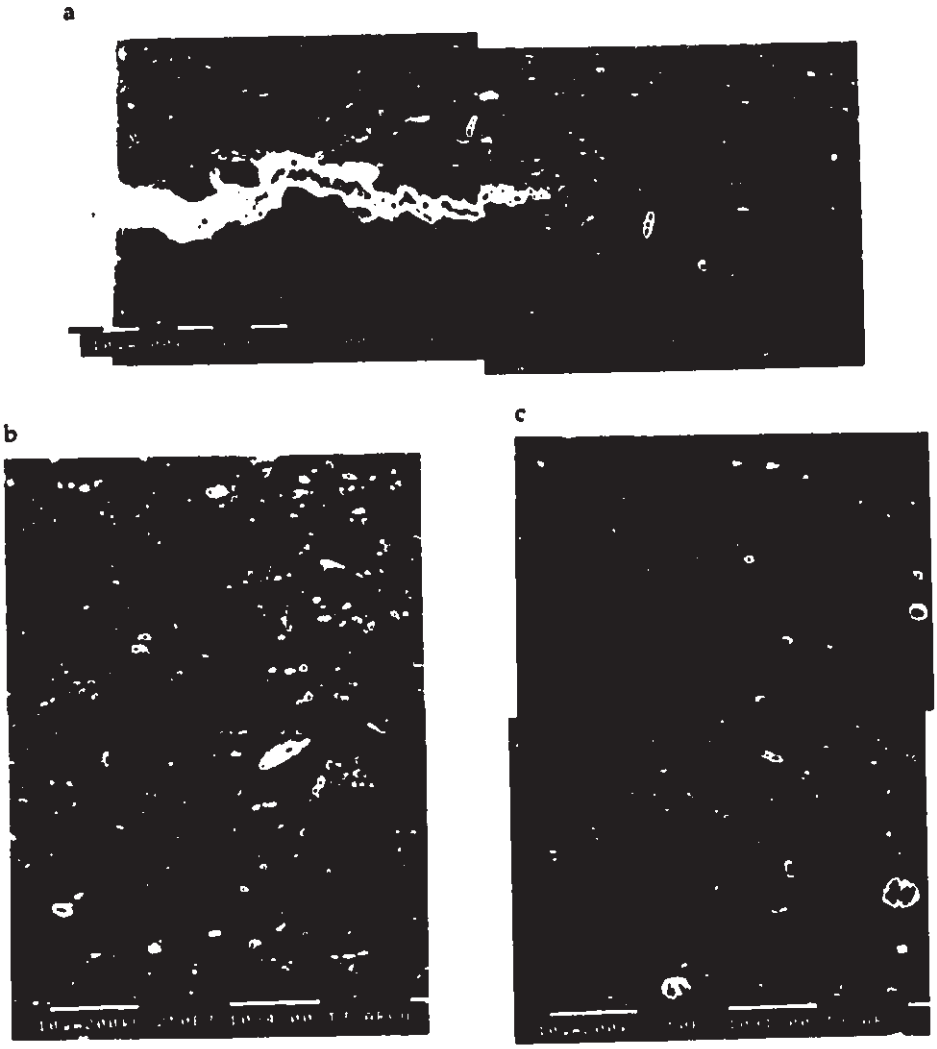

Fig. 11-7: Creep damage at failure in ARCO HPA, crept in uniaxial tension in air, at 1250 C, at 77 MPa. Failure at $t_f \approx 40$ h, $\varepsilon_f \approx 0.08$. SEM micrographs from an internal section about 0.5 to 1 mm from an external surface; polished, thermally etched and gold coated. The applied stress axis is vertical.

a) Internal polish plane: crack growing from the external surface (at left), its damage zone, and typical internal damage.

b) Typical *internal* cavitation damage.

c) Typical *external* cavitation damage.

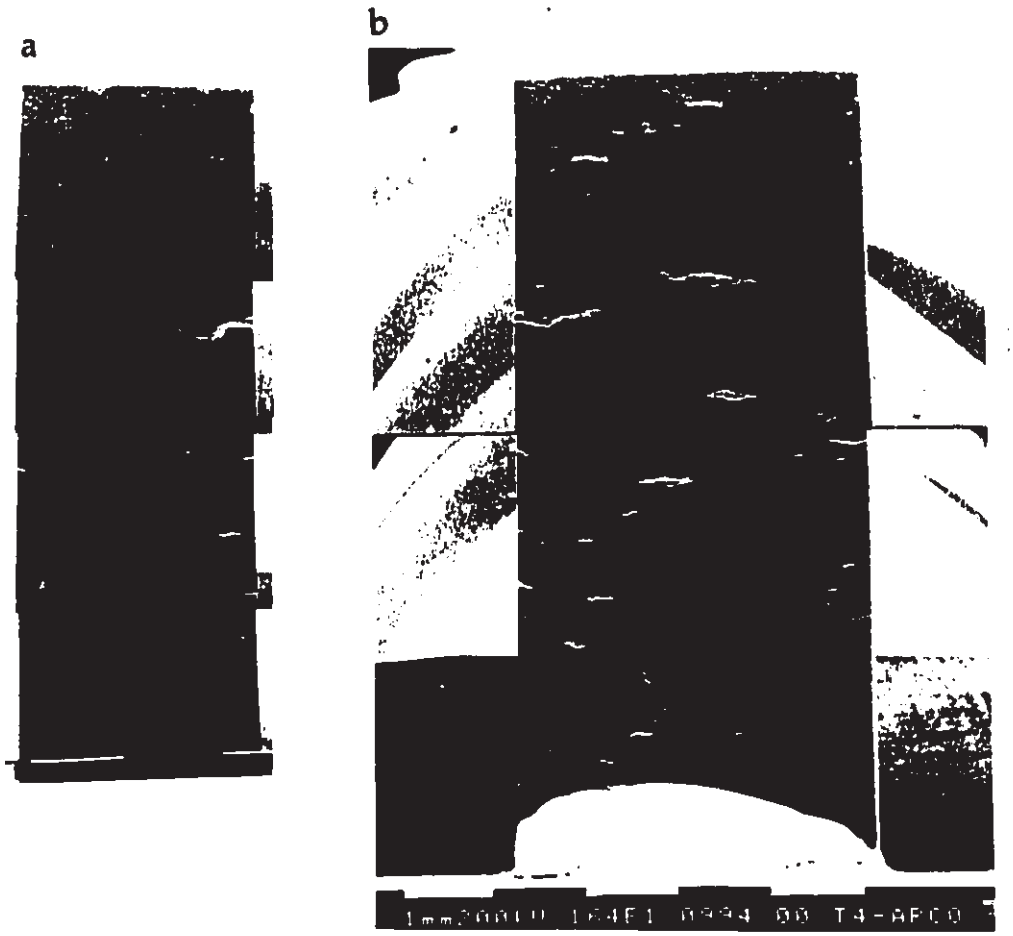

Fig. 11-8: *Internal* (a) and *external* (b) macroscopic damage at failure in ARCO HPA, crept in uniaxial tension in air, at 1250 C, at 55 MPa. Failure at $t_f \approx 150$ h, $\varepsilon_f \approx 0.09$. Adjoining surfaces. Thermally etched and gold-coated for SEM. The applied stress axis is vertical.

a) Internal polish plane about 0.5 to 1 mm from an external surface (the original specimen was 5 mm wide). Right surface is external face, (b).

b) External tensile face. Left surface is internal plane, (a).

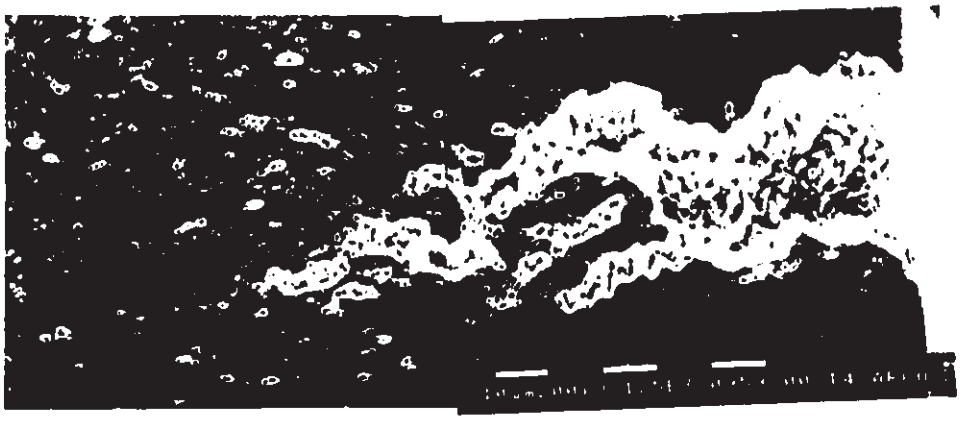

Fig. 11-9: Surface crack from the specimen shown in Fig. 11-8. Internal polish plane, thermally etched and gold-coated for SEM. The external face is the surface at the right.

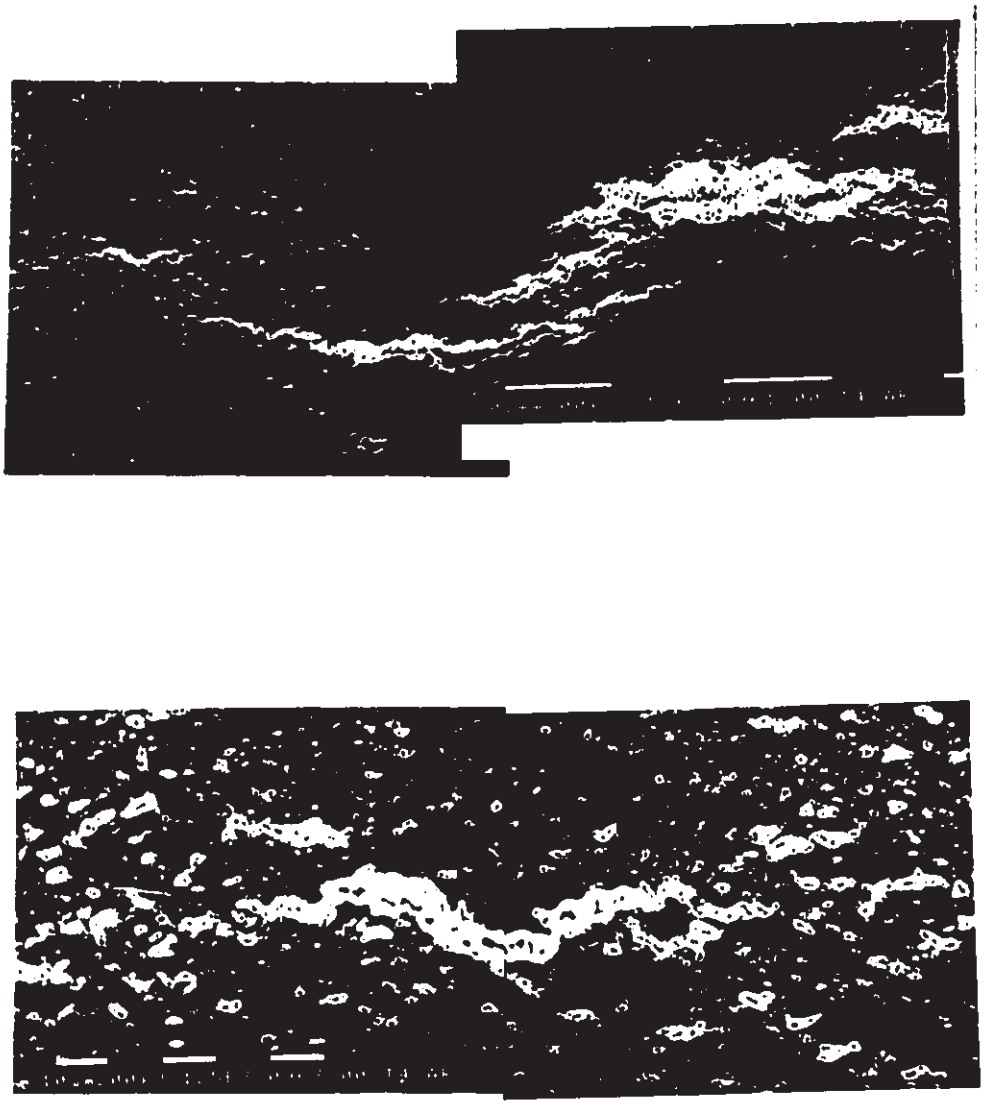

Fig. 11-10: Internal damage, at failure, in ARCO specimen shown in Figs. 11-8,-9. Internal polish plane, thermally etched and gold-coated for SEM. The applied stress axis is vertical.

a) The largest crack on the polish plane.

b) Internal crack generated by cavity coalescence, near tip of crack shown in (a).

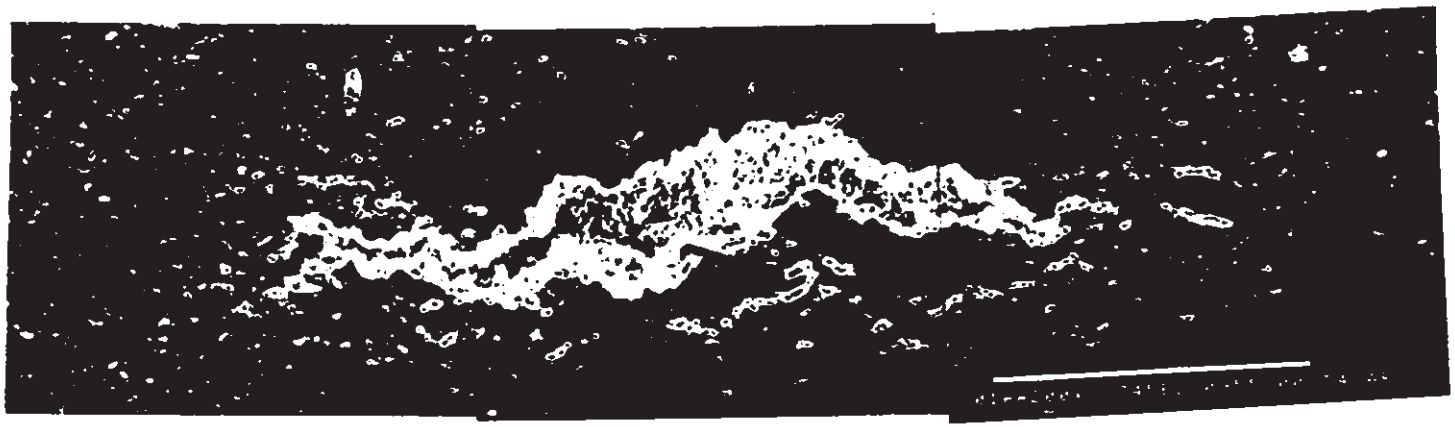

Fig. 11-11: Internal crack in ARCO specimen shown in Figs. 11-8 to 11-10. Crack may be a later stage of the type shown in Fig. 11-10b. Internal polish plane, thermally etched and gold coated for SEM. The applied stress axis is normal to the crack.

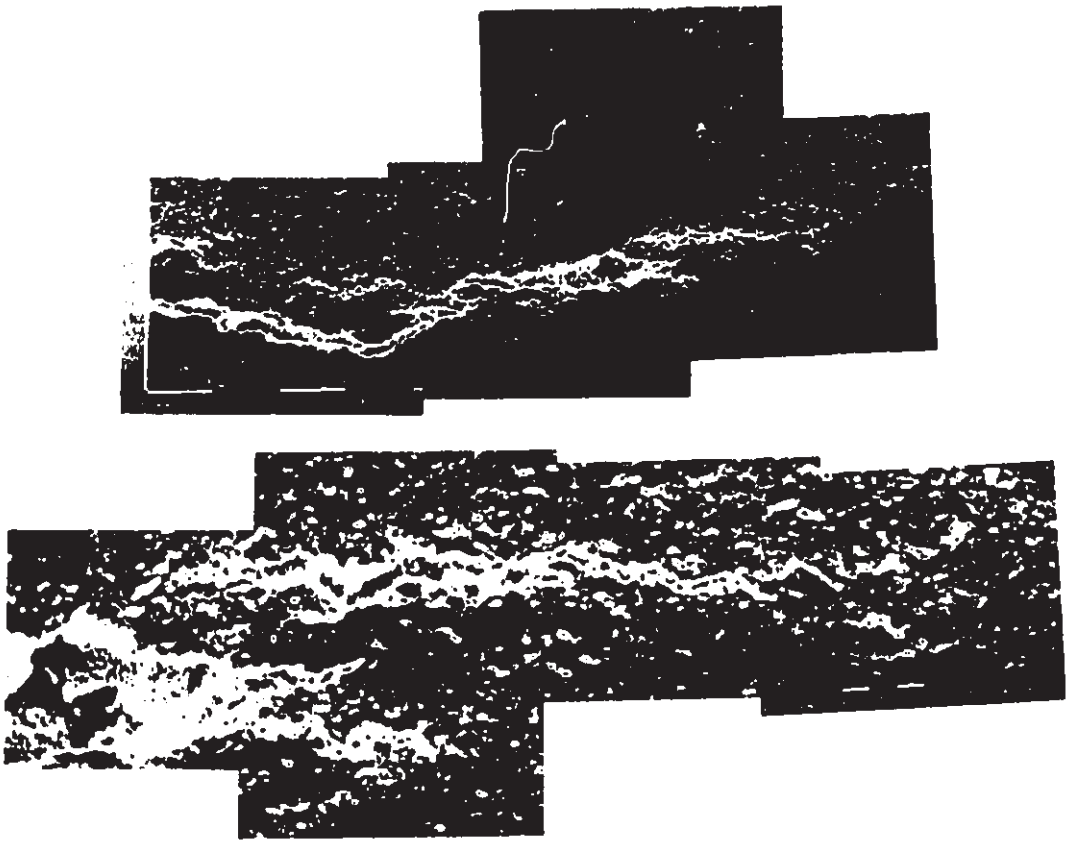

Fig. 11-12: External damage at failure in ARCO specimen shown in Figs. 11-8 to 11-11. The applied stress axis is vertical.

a) The largest crack on external surface. Dark bilobed regions have low surface relief, and denote the crack origin.

b) Tip of crack shown in (a).

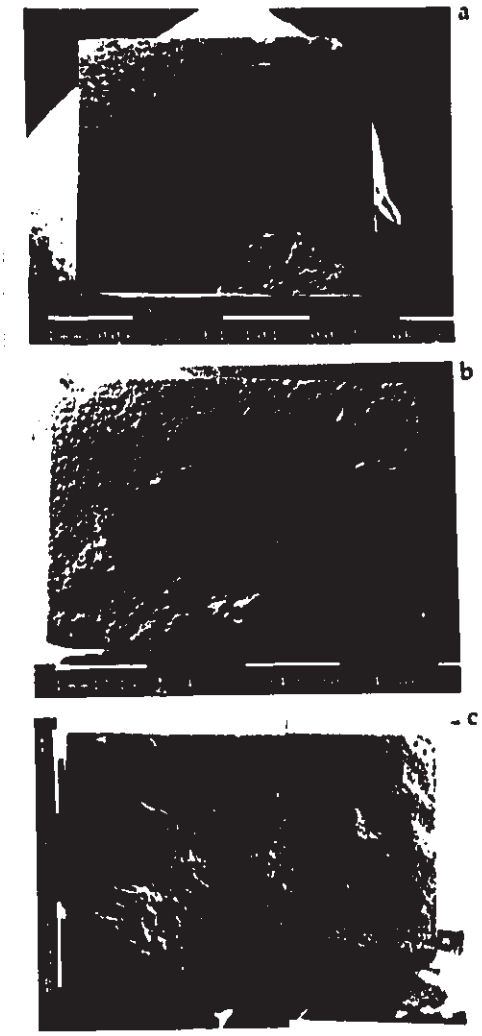

Fig. 11-13: Fracture surfaces of three ARCO HPA specimens, crept to failure in uniaxial tension in air, at 1250 C, at (a) 77 MPa, (b) 55 MPa and (c) 40 MPa (Figs. 11-4 to -6). Secondary crack growth is occurring from one site in (b), and from at least four sites in (c). Specimens are *as-fractured;* gold-coated for SEM. The applied stress axis is normal to the micrograph.

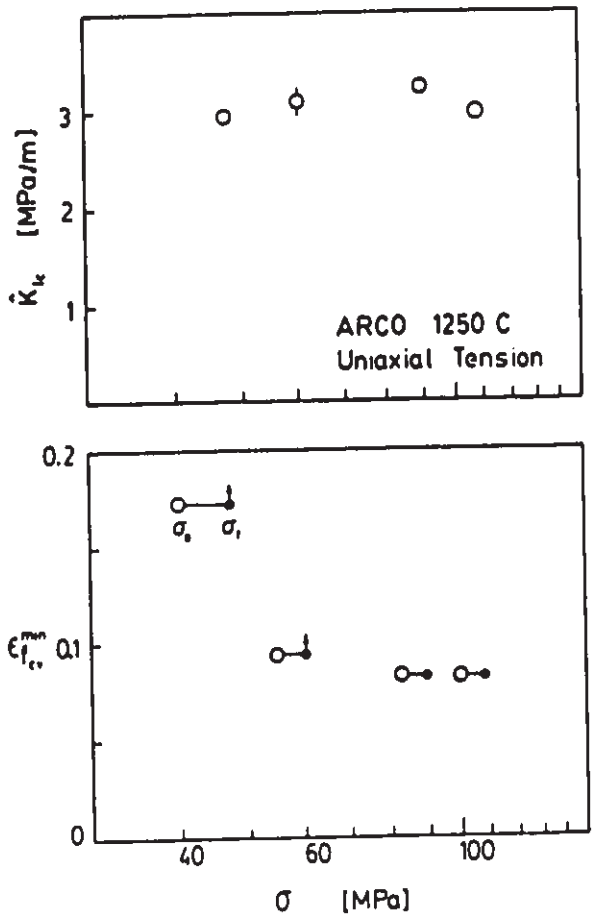

Fig. 11-14: Long-term creep fracture toughnesses, K_{Ic}, in ARCO HPA at 1250 C, as a function of applied stress *at failure*, calculated from the external dimensions of the fracture surface.

Fig. 11-15: Minimum failure strains in ARCO HPA at 1250 C, as a function of applied stress. The horizontal stress range for each specimen reflects the loss of gauge cross sectional area. The small vertical a[illegible] denote specimens in which the cavitation component of [illegible] strain, which is not included in the calculated failure [illegible]rains, is significant.

12 Discussion

In this section we discuss creep deformation data, then creep fracture and damage accumulation data.

12.1 General

Both aluminas were microstructurally stable with respect to swelling and grain growth, at the temperatures at which most creep data were generated (1150 C for AVCO, and 1250 C for ARCO; Figs. 4-3,-4).[1]

12.2 Creep deformation

Stress redistribution complicates interpreting primary creep in flexural tests (Chuang and Wiederhorn, 1988); however, uniaxial

[1] For AVCO, most creep data were generated at 1150 C — 200 C below the *lowest* swelling temperature. The swelling data strongly suggest AVCO was stable in creep at this temperature. ARCO's swelling data included 1250 C, its creep test temperature; because it *was* stable at that temperature, the data were *not* included in Ch. 4.

tensile data for ARCO (Figs. 11-4,-5) show primary creep.

Gruffel et al. (1988) explained uniaxial primaries in Mg, Mg-Y and Mg-Ti/HPAs as due to concurrent grain growth. However, as noted above, no significant grain growth occurred in ARCO HPA at 1250 C (Ch.4). ARCO's flexural primary transients (Figs. 11-1,-3) were complete in one half the flexural strains reported by Chokshi and Porter (1986) for an HPA similar to AVCO (<0.005, vs <0.01). They eliminated dislocation density increases and concurrent grain growth as possible physical causes, but did not identify the physical basis for the transients.

Diffusion-induced primary transients can be estimated from Frost and Ashby (1982) p.2,98,119. For the flexural data for ARCO at 1250 C (Fig. 11-2), strains of approximately 0.001, with a time constant of about 0.6 h are predicted. The transients seen (Figs. 11-2,-3) had larger strains and decayed more slowly, diverging farther from these predictions as stress decreased. The physical basis for the observed physical primary transients is therefore unclear.[2]

Tertiary creep was reported by Grathwohl (1984) in dead-load

---

[2] Chuang and Wiederhorn (1988) analyze transient flexural stress redistribution. Their analysis has not yet been applied to the current results.

flexural tests on HPSN, and by Gruffel et al. (1988) in uniaxial tensile, constant-stress tests on Mg-, Mg-Y and Mg-Ti HPAs. In the current work, at the relatively low strains achieved in the flexural tests,[3] no tertiary acceleration was noted (Fig. 11-1a). However, in dead load uniaxial tensile tests to failure, tertiary acceleration developed in 55 and 40 MPa tests (Fig. 11-4,-5).

In the current work, no necking was observed to strains of at least 0.17, consistent with the high-elongation uniaxial data of Gruffel et al. (1988; $\varepsilon_f \approx 0.4$-$0.5$).

For AVCO, the measured stress exponent of 2.0 was close to the value of 1.7-1.8 determined for other MgO-HPAs from the same manufacturer (Porter et al., 1981; Johnson et al., 1984), and close to the value of 1.9 determined for a similar HPA by Chokshi and Porter (1986). ARCO's exponent of 1.8 ± 0.2 was similar.

Comparing experimental activation energies for creep deformation with previous values determined for similar materials confirms that controlling mechanisms and diffusion coefficients are uncertain (particularly when determined from measurements over narrow temperature ranges) and are specific to particular materials. The range of activation energies expected for Coble

---

[3] Strains of about $\varepsilon_f/3$ to $\varepsilon_f/2$ were reached in the stress range at which $\varepsilon_f \approx 0.1$.

creep in HPA is that for aluminum boundary diffusion;[4] i.e. between perhaps 420 kJ/mol (Frost and Ashby, 1982, p.99,101-2) and 684 kJ/mol (Dynys et al. (1980); App.15). AVCO's apparent Q ≈ 480 kJ/mol (Fig. 11-2) is close to Porter et al.'s (1981) value of 460 kJ/mol, and Johnson et al.'s (1984) 480 kJ/mol, for other AVCO MgO-HPAs. However, Chokshi and Porter (1986) reported 635 kJ/mol for a similar HPA.

For ARCO, flexural creep deformation data over a narrow temperature range (1200-1250 C) suggest a much lower activation energy of approximately 390 kJ/mol. However, in the swelling work, we fit a boundary diffusion activation energy of 500 kJ/mol (Ch.5). These two values are not necessarily inconsistent. The activation energy for *creep* was calculated from data taken over a narrow temperature range, and at low temperature, relative to diffusion data. In a study of neck growth between alumina spheres between 1500 and 1900 C, Dynys et al. (1980) found Al control of boundary diffusion at high temperature, and O control at low; their mixed Q_B was 684 kJ/mol. In the current work, the activation energy for *swelling* was calculated from data for intermediate temperatures, and had an intermediate value between

---

[4] From TEM micrographs of grain boundaries at much higher magnification than Fig. 4-13 (not shown here), grain boundaries were free of glassy phases in both aluminas.

the creep energy and Dynys et al.'s (1980) mixed energy.

Generating high temperature creep data would permit comparing the activation energies for swelling and creep more reliably. Concurrent grain growth will occur at high temperature (Ch.4), which will have to be taken into account; however, such tests likely will be short. Fortunately, ARCO swells slowly at high temperature, and the swelling kinetics are known (Chs. 1-8). For fine-grained HPA, the controlling deformation mechanism should not change to lattice diffusion at higher temperature (Frost and Ashby, 1982, p.98-100).

The reason for the large difference in deformation resistance between the two HPAs tested is unclear. AVCO's as-received grain size, $\bar{L}_2$, was 1.6 μm, vs ARCO's of 1.0 μm (Ch.4). For boundary diffusion controlled creep described by $\dot{\epsilon} \propto \delta D_B/\bar{L}_2^3$ (Frost and Ashby's (1982) Eq. 2.29), ARCO's δD_B would need to be some 40 times smaller than AVCO's, at the same temperature, to explain the difference in deformability shown in Fig. 11-2. Impurity and dopant levels are different in the two HPAs, but it is difficult to anticipate how these differences would affect δD_B.[5]

---

[5] ARCO's lower swelling rate, relative to AVCO, is consistent with its low deformation rate, in that both should be controlled by grain boundary diffusion. However, pore pressures in ARCO are uncertain (Chs. 4,6).

12.3 Creep damage and fracture

For rapid failures *above* the stress transition, the large scatter in *flexural* failure times discouraged determining a slope for this regime (Fig. 11-2). Dalgleish et al.'s (1985, their Fig. 4) short-term failure times also show strong scatter, and have an uncertain slope. For a single type of fracture origin,[6] the slope should relate to the stress exponent for slow crack growth (*N;* Grathwohl, 1984), which is tentatively[7] on the order of three in HP/alumina (Blumenthal and Evans, 1984). Possible slopes were far from -1/3, consistent with the different types, sizes and

---

[6] And, for flexural tests, for heterogeneities of sufficiently high number density, N_v, that in *each* specimen, a dominant flaw is near the tensile face...

[7] Blumenthal and Evans (1984) present V-K data for *extrinsic* (i.e. Knoop) cracks in their Figs. 4 and 14. For 1300 C, data points are not consistent between the two figures, and slopes of two and three, respectively, were fit. The exponent at 1400 C is between 1.5 and 2-3, depending on the points included. In Cao et al. (1987), failure times for *artificial intrinsic* cracks were consistent with those for *natural intrinsic* cracks in Dalgleish et al. (1985), both above *and* below the high transitional stress. At 1250 C, ARCO deforms comparably to AVCO at 1150 C (Fig. 11-2); i.e. some 150 C below the lowest temperature for for Blumenthal and Evans' (1984) V-K data. Low temperature V-K kinetics are uncertain at this time.

locations of the dominant flaw seen by SEM in different bars.[8] As noted in section 11.1, the types of heterogeneity seen at fracture origins were consistent with those reported by Johnson et al. (1984), Dalgleish and Evans (1985) and Dalgleish et al. (1985).

Below the transitional stress, our failure data are from uniaxial tensile tests. The three data points at high stress ($\sigma \geq 55$ MPa; Fig. 11-5) extrapolated to higher stresses, were consistent with the maximum *flexural* failure times, in the flexural transition stress range near 200 MPa (≈ 5 h; Fig. 11-2).[9] For stresses between 70 and 170 MPa, Dalgleish et al.'s (1985, their Fig. 4) and Cao et al.'s (1987, their Fig. 4) flexural subtransition slopes were close to -1, and were not explained. In contrast, here, the slope of the uniaxial high-stress data was about $-1/3$, tentatively consistent with Blumenthal and Evans' (1984) V-K kinetics for extrinsic creep crack growth in HPA. As the stress was reduced from 55 to 40 MPa, the slope increased to between $-1/2$ and $-1/1.5$, consistent with ARCO's deformation exponent,

---

[8] At this stage in the overall project, it was too time-consuming to test enough bars to generate a representative slope.

[9] At this stage of the project, uniaxial tensile tests were too expensive to use to characterize the flaw-size sensitive region at high stress, near the transition, in a material of the quality used.

$n \approx 1.8$, in this work (Fig. 11-2,-5).

These data indicate a second transition in this lower stress range — apparently more gradual, re. t_f, than the transition at high stress. The transition appears to be from crack growth controlled failures (slope = $-1/N$; Grathwohl, 1984) towards failures from strain-controlled damage accumulation (for a critical strain, slope = $-1/n$; Grathwohl, 1984). (Dalgleish et al.'s (1985) and Cao et al.'s (1987) lowest stresses, 65 and 75 MPa respectively, was well *above* this second transition.)

This is supported by micrographs of both internal and external cavitation. Failure by generalized cavitation will only be seen in HPA of high enough quality; otherwise, failure will be controlled by localized cavitation at crack tips, in cracks propagating from as-received heterogeneities. From SEM examinations of fracture surfaces (e.g. Figs. 11-13),[10] in this work, all failures (flexural *and* tensile) could be assigned to crack propagation from either as-received microstructural heterogeneities (consistent with Dalgleish et al., 1985), or specimen bevels.[11]

---

[10] The higher magnification SEM micrographs of crack origins are not shown here.

[11] In App. 20 we recommend a specimen which requires *no* beveling.

However, in contrast to their flexural results at $\dot{c} \approx 10^{-5}$ s^{-1}, and to the internal damage data for constant-stress uniaxial tests at 1450 C (Gruffel et al., 1988), little shear banding between crack tips was evident on external surfaces or polish planes of tensile specimens crept at 77 and 55 MPa (e.g. Fig. 11-6). Further, only cracks, and no shear bands, were observed to nucleate at heterogeneities.

That such cracks propagated from *intrinsic* heterogeneities at K_I less than the extrinsic threshold K_I^{th}, and then stopped, or grew very slowly, is consistent with results given by Blumenthal and Evans (1984) and Cao et al. (1987).[12]

Noncoplanar damage zones were encountered at tips of cracks on

---

[12] As reviewed by Blumenthal and Evans (1984), only at steady state in a linearly viscous creeping continuum, and for a stationary crack, can K_I be used as a crack loading parameter (because, for that case, $C^* \propto K_I^2$). However, as they note, (1) C^* *cannot* be controlled experimentally for small cracks, and (2) their data for crack opening displacement rates in AVCO HPA at 1300 and 1400 C do not support using K_I. In this work we present no data justifying K_I as a loading parameter at our lower test temperature. Despite this, we estimate K_I from elastic formulae for crack size and shape, in order to compare our results with previous data on, for instance, crack propagation thresholds (e.g. Blumenthal and Evans, 1984).

the tensile face of *flexural* specimens in ARCO HPA, for K_I below the threshold, $K_I^{th} \approx 1.5$ MPa$\sqrt{m}$, determined by Blumenthal and Evans (1984) and Evans and Blumenthal (1984) on an AVCO HPA at 1300 and 1400 C. In the current work, only coplanar damage zones were seen for cracks with K_I greater than this K_I^{th}. In tensile specimens, at much higher strains than in these flexural specimens, noncoplanar damage zones were rather common (e.g. Fig. 11-8), and crack nucleation in inclined lobes occurred, as seen by Dalgleish and Evans (1985). Such lobes and heavily damaged inter-crack bands (e.g. Fig. 11-9) were smaller in the current work than those seen at 1450 C and strains of 0.4 to 0.5 by Gruffel et al. (1988), and by Dalgleish and Evans (1985).

That few cracks joined by shear bands in this work may reflect materials quality differences, through the number density of heterogeneities available to generate cracks (which will interact via shear bands if they are close enough). Also, cracks interacting by shear bands, and shear bands nucleating from heterogeneities, may occur more readily at high temperature, when plastic and cavitation regions around heterogeneities and crack tips can develop more rapidly. In the case of Dalgleish et al.'s (1985) results (and acknowledged by them) the stresses in the tensile face region were uncertain in the later stages of creep, as heavy damage redistributes stress.

Because subtransitional failure strains were two to three times

higher than those achievable in the current bend rig (≈ 0.09 vs 0.035 for ARCO), at this time we have no data for comparing flexural and uniaxial creep damage at high strains in ARCO. In particular, we have no data on the relative importance of shear bands in crack linkage in tensile and flexural failures. However, it now would be straightforward to generate such flexural data, using deep bend bars.[13]

Comparing internal (polish plane) and surface cavitation damage shows that, at the high failure strains achieved at low stress, the grain-scale topographic relief that develops on external surfaces (e.g. Fig. 11-12), obscures details of cavities coalescing to form macrocracks, relative to internal polish planes (e.g. Fig. 11-10). Such surface relief would interfere with characterizing surface cavitation fields by automatic image analyzers.[14]

---

[13] Say, bars 12 to 15 mm high. Maximum strain is linear in bar height; load (for a given stress at the tensile face) varies as the square of bar height. Our data indicate that the relevant stress range for tensile comparisons is below 100 MPa, there now should be no immediate concerns about overloading the bend rig.

[14] If an initially-lapped surface *could* be relapped for image analysis of damage on the external surface, during an interrupted set of tests on a single specimen, this would be an efficient way to study damage evolution. However, for such data be useful in failure prediction, in cases in which internal

Two aspects of the data suggest that, as the stress was reduced to 40 MPa, the HPA was close to a border of a field for creep fracture by generalized cavitation. First, the tensile failure slope changed from that for creep crack growth towards that for creep deformation. Second, the internal cavitation level increased to levels where cavity coalescence generated cracks *as large as the as-received heterogeneities*, both away from and near crack tips (Figs. 11-10,-12). Failures still occurred by slow crack growth from as-received microstructural heterogeneities; but generalized cavitation was playing a larger role, both in strain and in crack growth from heterogeneities.

Tensile failure strains, at stresses between 100 and 55 MPa, were close to the flexural values of at least 0.08 reported by Dalgleish et al. (1985); however, at 40 MPa, the failure strains were at least 0.17 (Fig. 11-12b). Gruffel et al.'s (1988) failure

---

damage controls creep lifetimes, it would be necessary that surface damage be correlated with internal damage.

However, experimental lapping could be eliminated by studying specimens which have a ground surface finish comparable to that anticipated for production parts. Surface damage then would not be as readily compared to internal; however, (materials specific) data on controlling damage processes for practical industrial surface finishes would be generated.

strains in HPAs were on the order of 0.5 at 1450 C and $\dot{\varepsilon} \approx 10^{-4}$ s^{-1}.

The pattern for creep failure in HPSN, in bending, in air, is a single transition from slow crack growth (SCG) to damage accumulation with decreasing stress (Grathwohl, 1984; Quinn, 1984). Dalgleish et al. (1985) and Cao et al. (1987), in flexural tests on AVCO HPA at 1300 C and $\dot{\varepsilon} \approx 10^{-5}$, encountered a single abrupt transition at high stress, but the subtransitional (σ-t_f) slope did not correspond to the expected $-1/n$, and microstructural heterogeneities (and possible damage-enhanced stress redistribution) were important.

In contrast to these results, in the current combined flexural/ tensile data set, *two* transitions were encountered — in t_f, ε_f and damage patterns. The first, at 200-210 MPA (elastic), was similar to that reported by Dalgleish et al. (1985) and Cao et al. (1987). Abrupt in t_f and ε_f, the change, with decreasing stress, was from rapid and scattered failures, by crack growth from one of a number of types of microstructural heterogeneity, to delayed failure — still by a crack growing from a heterogeneity, but with significant multiple crack growth occurring at the same time.

The second transition occurred in uniaxial tensile tests on ARCO at 1250 C, at lower stresses — between 40 and 55 MPa. It was

more gradual in t_f, though rather abrupt in ε_f. Multiple crack growth occurred internally and externally, and growing cracks interacted if they were close enough. Generalized internal damage accumulated to levels where cavity coalescence generated cracks as large as the original heterogeneities, and large cracks advanced by multi-facet plates of damage. The large damage zones were in contrast to the compact zones seen internally in uniaxial specimens at higher stress (Fig. 11-6), and those shown on the tensile face of flexural specimens by Blumenthal and Evans (1984) for higher temperature and strain rates in AVCO HPA.

That the high-stress uniaxial tensile t_f extrapolated back to the envelope of *flexural* t_f ($\approx$ 5h) suggests that *no* abrupt transition in t_f should be encountered in uniaxial tests in this stress range, in contrast to the flexural results. Because $N > n$, and the slope of the high stress t_f is close to the expected $-1/N$, we expect a *gradual* fall in ε_f as stress increases towards and across the flexural transition. The uniaxial results support the flexural transition being due to stress redistribution (possibly enhanced by tensile face damage) and perhaps assisted in some cases by locally high 'intrinsic' V-K kinetics (Blumenthal and Evans, 1984; Cao et al., 1987).

The K_{Ic} value suggested by the tensile data — just over 3 MPa$\sqrt{m}$ — is consistent with the value determined for extrinsic cracks at 1300 and 1400 C by Blumenthal and Evans (1984).

12.4 Flexural test conditions

Test conditions were selected on the basis of many interrelated factors. Creep test acceleration is always a concern. Dalgleish et al.'s (1985) static fatigue results identified the stress range 100-200 MPa as a starting point, but their failures at low stress were unexplained, and were strongly influenced by material heterogeneities, and, perhaps stress redistribution.[15] Even though HPA, as a model structural ceramic, has different chemistry, and different deformation and damage mechanisms than HPSN, the original HPSN data prompted interest in damage processes at *low* stresses and temperatures (Figs. 9-1,-2) — low stresses for failure by generalized cavitation; low temperature for structurally reasonable strain rates.

It is important that the same deformation and damage mechanisms control failure lifetimes in lab tests and in service. Currently, because there are too few data on damage mechanisms in HPA to permit choosing test conditions, it seems reasonable to use the lowest strain rates typical of similar studies. Wiederhorn et al.

---

[15] Their test conditions are somewhat uncertain: the legends given in their Figs. 4 and 5 report no unique relation between stress and steady state strain rate, at a given temperature.

(1986c, 1988) used strain rates of 10^{-9} to 10^{-7} s^{-1} in systematic studies of Si/SiC (for $\varepsilon_f \approx 0.01$). Dalgleish et al.'s (1985) bending strain rates were around 10^{-5} s^{-1}, while Chokshi and Porter's (1986) were 10^{-7} to 10^{-4} s^{-1}. For materials as damage-tolerant as HPA, tests at strain rates below 10^{-8} s^{-1} are uncomfortably long; in the current tests, a strain rate range of 10^{-8} to 10^{-6} s^{-1} was used. Such rates typically yielded the maximum strains possible in the bend rig (≈ 0.05), within 100-500 h, at stresses between 100-200 MPa. Test temperatures were chosen which were low, but still high enough to permit maintaining these deformation rates at loads that would not damage the test rig, for bend specimens deep enough to give these maximum strains, at the low curvatures called for by Hollenberg et al.'s (1971) deformation analysis.

12.5 Maximum flexural strains

Maximum flexural strains imposed (Figs. 11-1,-3) were lower than those of Dalgleish et al. (1985), and it is likely that failures similar to theirs would have been encountered at similar strains.

However, by the time their data were published, our flexural rig and specimen design were in use. Machining a new test rig would have been expensive; with the current rig, their large failure

strains required flexural tests on bars 12 to 15 mm deep,[16] or else uniaxial tensile tests. For flexural tests, the maximum strain possible is linear in bar depth, but the load required for a given tensile face stress increases as the square of bar depth. We were concerned about damaging the bend rig and load train if deep bars were used, particularly at lower temperatures.[17]

Most important, SEM data from the current work and for Dalgleish et al. (1985) showed HPA to be capable of sustaining very high levels of internal damage. This likely would enhance stress redistribution (Chuang and Wiederhorn, 1988), and would complicate interpreting bend test results. Dalgleish et al. (1985) acknowledged this, and were unable to explain their results. Instead of increasing bending strains, then, tensile tests were undertaken as offering large strains, and uniform, controlled deformation conditions throughout a specimen's gauge length.

---

[16] In order to keep curvatures at maximum strains low, in accord with Hollenberg et al.'s (1971) recommendations. Dalgleish et al.'s (1985) 3 x 3 mm bars would have had very high curvatures at strains of 0.08.

[17] A flexural rig capable of sustaining higher loads has been constructed.

12.6 Head failures

It is important to discuss an experimental problem which was encountered in the uniaxial tensile tests, as it raises issues for materials-specific test system design.

The current specimen had a gauge width of 5.0 mm, which was intended to give a high signal-to-noise ratio in a 10 mm diameter neutron beam, in planned cavitation kinetics determinations by SANS. Peterson's (1953) Fig. 83 suggests this to be rather large, relative to the head dimensions: the *initial* maximum stresses at the pin hole were larger than the steady-state stresses in the gauge length. (A reduced gauge cross section — say, a width of 4.0 mm — would correct this.

In the tensile tests reported here, cracks grew from up to three locations around the peripheries of pin holes in one or both specimen heads.[18] In the 77 MPa test, the specimen broke *only* within the gauge length. However, in the other three tests (at 100, 55 and 40 MPa), the specimens broke not only within the gauge length, but also within the upper head, from cracks from the load pin hole. For these three cases, which were run at

---

[18] Fig. 10-1a; from both extreme stress locations on the hole diameter normal to the specimen axis (Peterson, 1953), as well as from the point opposite the gauge length, of one or both loading pin holes.

stresses *both above and below* the fourth, it is likely that the *initial* failure occurred at a side crack which propagated from a load pin hole; nucleated either at a microstructural heterogeneity or at machining damage.[19] That a specimen at an *intermediate* stress did *not* fail from head cracks indicates the uncertainty introduced into testing by a combination of variable machining damage and large, random microstructural heterogeneities.[20,21]

However, this head cracking invalidates neither the trends in results, nor the conclusions drawn from them — neither trends in K_{Ic} nor failure times, with stress, indicate *strongly* premature failure in the three uncertain cases. The 77 MPa specimen's K_{Ic} was perhaps 0.1-0.2 MPa$\sqrt{m}$ higher than the test set mean of about 3 MPa$\sqrt{m}$, and was consistent with K_{Ic} determined by Blumenthal and Evans (1984). Failure *strains* may be low when head failures

---

[19] Generated on breakthrough in drilling, and not removed completely by beveling.

[20] Perhaps also randomly high *misalignment* in the specimen which failed only in the gauge length. No specimens were strain-gauged to estimate misalignment at loading. The failure strains show the material to be so ductile under the current test conditions that minor misalignment is unlikely to have been important in failure times.

[21] Over the set of *flexural* bars that failed rapidly, fracture surfaces showed several types of large heterogeneity.

occur, particularly when such premature failure occurs during an accelerating tertiary phase of a test. However, rather *moderate* tertiary acceleration occurred in low stress tests (Fig. 11-4). Static fatigue slopes at long times (Fig. 11-6) are rather *in*sensitive to premature failure, from the numerical compression inherent in a log-log plot. Finally, the trends in the character of the fracture surfaces (Fig. 11-13), and in internal and surface damage levels (Figs. 11-7 to -12), remain meaningful.

When we compare our results and specimen dimensions with the maximum test times, the flare radius, and head and pin hole dimensions of Wiederhorn et al.'s (1988) similar "pin and clevis" tensile specimen in Si/SiC, we infer that crack initiation and propagation are materials/materials quality specific, and that HPA is more susceptible to this than Si/SiC. In particular, Si/SiC should resist crack propagation, as the Si 'pools' should blunt crack tips. That is, not only are heterogeneities materials specific, but their consequences are materials specific (and perhaps test condition specific).

The current specimen's gauge cross section should be reduced, or the pin hole eliminated by loading under flare shoulders, as in the proposed new specimen design (App. 20).

13 Conclusions

1 In contrast to flexural results of Dalgleish et al. (1985) and Cao et al. (1987), *two* transitions occurred in failure times and strains, and in cumulative damage patterns, over the stress range 40 to 230 MPa, at 1250 C in ARCO HPA.

The first, a sharp and expected *flexural* transition, occurred in both HPAs at elastic stresses of 200-210 MPa. The transition, as stress was reduced, was from rapid and scattered failures (by crack growth from one of a number of types of microstructural heterogeneity) to delayed failure at ϵ_f of 0.08, and multiple crack growth from heterogeneities.

The second transition occurred in uniaxial tensile tests on ARCO HPA, at stresses between 40 and 55 MPa, and $\dot{\epsilon}$ between 10^{-7} and 10^{-6} s^{-1}. Failure times above this transition extrapolated back to the flexural failure envelope, and the failure strains and multiple crack growth were consistent with Dalgleish et al. (1985), although little shear band cavitation occurred, either at heterogeneities or between macrocracks. At the lowest stress, however, the failure strain more than

doubled to at least 0.017. At transitional stresses (55 to 40 MPa), (1) multiple crack growth was evident on fracture *as well as* external surfaces, (2) generalized internal damage accumulated to levels where cavity coalescence generated cracks on the order of the size of the initially present heterogeneities, and (3) large creep cracks advanced by multi-facet 'plates' of damage.

Across this transition, the slope of failure times *vs* stress, on a log log plot, changed from the (negative inverse of the) stress exponent for extrinsic crack growth, above the transition, towards that for creep deformation, below the transition. The data suggest that a border was approached or encountered, for failure controlled by strain-driven, generalized creep cavitation.

2 In *flexural* specimens, *non*coplanar damage zones developed in surface cracks at K_I below approximately 1.5 MPa$\sqrt{m}$, consistent with Blumenthal and Evans (1984). However, only cracks, but no shear bands formed at heterogeneities, in contrast to results of Dalgleish et al. (1985). In uniaxial *tensile* specimens, *non*coplanar damage zones developed at internal crack tips. These were consistent in form with, but on a smaller scale than Gruffel et al.'s (1988) damaged bands between internal cracks at higher temperatures and strain rates.

3 K_{Ic}'s for uniaxial tensile failures were just over 3 MPa$\sqrt{m}$, and were essentially independent of the sharp increase in failure strain and cavitation level across the lower stress transition. In three of four specimens, K_{Ic} was reduced by some 0.1-0.2 MPa$\sqrt{m}$ by premature failures, caused by cracks propagating from rims of pin holes in specimen heads.

4 An HPA doped with 800 ppm Y/200 Mg (ARCO) was far more deformation resistant than one doped with 3000 ppm Mg. (AVCO). For these two materials, the creep stress exponents were 1.8 and 2.0 (±0.2), and the approximate activation energies were approximately 390 and 480 kJ/mol, respectively.

5 Studying creep fracture in a damage-tolerant material like HPA requires uniaxial tensile tests. Because of the high failure strains, integral flags machined into the gauge length are recommended, with a hybrid flat/axisymmetric specimen. Because of materials-specific crack nucleation and propagation, shoulder, and not through-pin loading, is advised. Given the high creep failure strains, constant-stress tests are indicated, rather than dead-load. Two systems permitting such tests are noted in App. 20.

14 Recommended future work

Experimental data to consolidate the work reported here could be generated rather quickly. At the same time as this is done, longer term issues need to be addressed, concerning both the materials tested and the test system.

1 Initially, it is important to resolve the offset of uniaxial tensile and flexural creep rates in Fig. 11-5. Specific action is recommended at the end of App. 21.

2 The current batch of ARCO HPA is of moderate quality only; in creep fracture, cracks originating in heterogeneities compete with generalized cavitation over a wide stress range. However, the material now is well characterized. It swells slowly, and undergoes no grain growth at current creep test temperatures. Also, three HP billets currently are on hand from the original batch, each of which should yield six to eight uniaxial tensile specimens. A number of standard and deep bend bars are also on hand. For comparison with HPA of higher quality in later tests, at least one billet of ARCO HPA should be

reserved.

To consolidate the initial results:

- Determine flexural deformation data at higher temperatures in ARCO (up to 1450 C), and compare its creep activation energy to the current low value for low temperature deformation, and to the value fit for swelling. (These data should be generable quickly and economically: several temperatures can be tested on *each* of a small number of specimens. Also, they should not be sensitive to the uncertainty discussed in App. 21.)

- Determine V-K kinetics for intrinsic and extrinsic cracks at the low temperatures used for creep fracture studies, in order to verify the high-stress slope of uniaxial tensile static fatigue data. Probably such tests will be done flexurally, including the transient analysis of Chuang and Wiederhorn (1988). Briefly extend the tests to the higher temperature range of Blumenthal and Evans (1984), to check that low temperature techniques give results consistent with theirs.

- Have second-generation uniaxial tensile specimens (App. 20) machined in ARCO, with new pull rods. (Alternatively, retain the current pull rods, and use a single-pin version of the

new specimen, relying on the smaller gauge length cross section to eliminate head failures.)

- With these new specimens, extend static fatigue data to stresses below 40 MPa. Verify that $(t_f-\sigma)$ slopes, above and below this transition, are consistent with the respective stress exponents, as indicated by current data. Generate accurate strains, to failure, particularly below the lower transition. Record primary and tertiary transients carefully. Characterize internal damage below the transition, especially cavity coalescence and macrocrack emergence. (Macrocrack emergence can be nondestructively monitored by X-ray microtomography (Sawicka and Palmer, 1988). This technique should be applied to the new tensile specimens.) Check origins of cracks *on fracture surfaces* for consistency with failure controlled by cavity coalescence.

- Determine whether transitions in t_f and ε_f, similar to those seen in flexural tests, occur at *high* stress. (At present, it is uncertain at what stress the scatter in t_f seen in flexural tests will become important, as the applied stress is increased. Rig misalignment also may play a larger role at high stresses, and should be estimated experimentally, by strain-gauging before a test, and measuring specimen curvature after.)

- For deep flexural bars,[1] compare failure strains and shear banding between multiple cracks in bending and uniaxial tensile tests in ARCO HPA, to demonstrate whether damage-enhanced stress redistribution is important in damage processes in a material of this quality. (From the unresolved difference in uniaxial and flexural strain rates (App. 21), all comparative tests should be done in the same furnace. See note on shear bands, below.)

3 The next, higher level of HPA creep fracture tests would include at least:

- mapping the border of the creep fracture regime experimentally, at *higher and lower temperature*, and characterizing how the transitions in t_f, ε_f and damage processes change with temperature. This would permit drawing a three-dimensional fracture mechanism map similar to Fig. 9-2, in which, on the third axis — strain — strain contours to failure can be drawn.[2] (From the data of Gruffel et al. (1988), in HPA of high quality there may be a

---

[1] Permitting high flexural strains to be achieved; see also App. 21.

[2] And, with damage data, damage contours as well. However, this would call for far more specimens, as, unless flared regions can be used as well, only one damage point can be generated per specimen.

transition to high elongations or superplastic behavior at high temperatures.) Given the differences noted between shear banding in this work (Ch.11) and that reported by Dalgleish and Evans (1985), generate tensile and flexural data on the temperature dependence of the role of shear bands in damage processes.

- determining the *scatter* in failure times for groups of specimens across the creep fracture transition(s). That is, generating data on probabilistic *vs* deterministic strength degradation as damage accumulates, after Wiederhorn's (1983) work on HPSN.

4 The next higher level of creep fracture tests on HPA would be to compare the high temperature performance of an HPA of the highest quality currently available, to that of ARCO.

5 All of the above are straightforward extensions of the work begun in this study. On HPA, a model material, they represent a considerable basic research investment. If carried out, it would generate a broad understanding of a well-characterized monolithic ceramic system. However, it is worth keeping in mind the strong industrial interest in nitride and carbide systems, and in whisker-reinforced ceramics. In particular, the research group is well prepared to study deformation and damage in SiC_w/HPA — a model reinforced system.

6 The high elongations possible in high quality HPA (Ch.11; Gruffel et al., 1988), the systematic mechanical behavior data generated by Wiederhorn et al (1988) on Si/SiC, and the currently unresolved offset in plotted tensile and flexural results (Fig. 11-5; App.21) suggest that uniaxial deformation and damage laws need to be generated for HPA, which are more detailed and precise than the data from this work (in which considerable effort was invested in establishing techniques, equipment and overall patterns in behavior). Damage laws likely should be generated by direct image analysis of polish planes *in the SEM* (though post-analysis of SEM micrographs likely would be adequate for global damage determinations in fairly homgeneous material).

Also, the above data strongly suggest that, for ductile polycrystals such as HPA, *dead-load* tensile loading should be replaced by *constant-stress* loading. This will require continuous strain feedback from the creeping specimen, for control of an automated test machine. While the rig described by Gruffel et al. (1988) is very attractive, a more practical route for this lab — in the short term or indefinitely, depending on the results — may well be to adopt the new specimen and to change to a side-mounted contact extensometer (App. 20). (The uniaxial *compressive* test rig designed and built in the course of this work already makes continuous,

differential LVDT signals available to a test machine.)

7 In addition, preliminary work should be begun on the design of a high temperature tension/torsion rig for damage mechanics studies on thin-walled tubes machined from hot-pressed billets, based on the principles outlined in Ch.9 and early in App. 19.

8 Finally, for modeling deformation and damage mechanisms at high temperature, it would be useful to have a computer program available for plotting deformation mechanism maps of the types given in Frost and Ashby (1982), in order that the implications of uncertainties in, or alternative values of materials parameters can be evaluated for specific materials. To facilitate this, evaluate inexpensive, commercial, *high-level* graphics software for compiled FORTRAN, BASIC and Pascal (see Ch.8, item 8).

Appendices

Appendix 1

Grain size in the ideal microstructure

In this section we summarize geometric relations for an ideal truncated-octahedral polycrystal, and establish the grain size which gives equal specific boundary areas (S_v) in ideal and real polycrystals. Variables are listed in section A1-2.

We set the specific boundary areas equal, because stereology will give us fairly accurate *volume* number densities of pores, N_v, and S_v can be determined directly from the mean linear intercept grain size (Apps. 6,13). Consequently, the *area* number density of pores attached to grain boundaries, N, which is a key parameter in the phenomenological model of pore drag, should be close in real and ideal microstructures.

A1-1 Analysis

We idealize the three-dimensional microstructure as a space-

filling assemblage of identical truncated octahedra[1] (Fig. 3-1a; Yan et al., 1980).[2] The specific grain boundary area in this ideal polycrystal is (Table A1-1):[3]

$$S_v = 1.450 / R_o \qquad (1)$$

where R_o is half the true, three-dimensional distance between opposite hexagonal faces of an idealized grain.[4]

On a random polish plane, in a single-phase polycrystal which is close to theoretical density, a direct and general relation holds between the specific boundary area and grain size, regardless of grain shape and grain size distribution. As long as no strong

---

[1] After Pearce (1978, p.5) and Budworth (1970), we reserve the term 'tetrakaidecahedra' for similar polyhedra with *curved*, as opposed to plane, faces.

[2] A broader view of the ideal microstructure can be built from these additional references: Hull and Houk, 1953; DeHoff and Rhines, 1968, pp.91ff; Budworth, 1970; Pearce, 1978, pp.5ff; Kasper and Lonsdale, 1959; Gasson, 1983; and Cwajna et al., 1986.

[3] Budworth (1970) shows that S_v for ideal truncated-octahedral and minimum-S_v tetrakaidecahedral polycrystals are very close.

[4] The truncated-octahedral facet edge length, ℓ, is a more common reference length. Table A1-1 summarizes geometric relations for both ℓ and R_o.

texture is present (DeHoff and Rhines, 1968, p.79,233):[5]

$$S_v = 2 / \bar{L}_2 \qquad (2)$$

To hold specific grain boundary areas equal in real and idealized microstructures, set Eq. (1) equal to Eq. (2):

$$R_o = (1.450/2.0)\ \bar{L}_2$$

$$= 0.725\ \bar{L}_2 \qquad (3)$$

We will write this as:

$$R_o = \bar{L}_2/\alpha_L \qquad (4a)$$

where $$\alpha_L = 1.379 \qquad (4b)$$

The radius of a sphere, r_s, which has the same volume as the equi-S_v unit grain is:

$$(4\pi/3)\ r_s^3 = 6.155\ R_o^3 \qquad (5a)$$

---

[5] Further, for a lognormally distributed, truncated-octahedral microstructure, the *arithmetic* means of linear intercept and volume-equivalent grain diameter are nearly equal (DeHoff and Rhines, 1968, p.234-5). Consequently, in this work we use $\bar{L}_2$ as the most physically appropriate and unambiguous measure of grain size, rather than the 'spherical' diameter typically used ($\bar{G} \equiv 1.5\ \bar{L}_2$; Fullman, 1953; Gifkins, 1970, p. 178-84). Because the V_v are low, we have not corrected the raw $\bar{L}_2$ for porosity, after Wurst and Nelson (1972).

from which $r_s = 1.137\ R_o$ (5b)

$= 0.825\ \bar{L}_2$ (5c)

The diameter of this sphere, $d_s = 1.65\ \bar{L}_2$, is close to, but larger than Fullman's (1953) $\bar{G} = 1.5\ \bar{L}_2$.

The following table summarizes geometric relations for the ideal, equi-S_v microstructure. The data in it are derived from the references given with Eq. (1), and extend those references to the parameter R_o. Entries not provided can be generated from those given in the table.

Table A1-1: Parameters of a regular truncated-octahedral polycrystal, in terms of ℓ, $\bar{L}_2$, and R_o.

Param.	ℓ	$\bar{L}_2$	R_o
ℓ		$0.592\ \bar{L}_2$	$0.816\ R_o$
R_o	$1.225\ \ell$	$0.725\ \bar{L}_2$	
S_3^{iso}	$26.79\ \ell^2$		
$S_3^{px} = S_3^{iso} / 2$			
V_3	$11.314\ \ell^2$	$2.347\ \bar{L}_2^3$	$6.155\ R_o^3$
$S_V = S_3^{iso} / 2\ V_3$			
$G_3 = 1/V_3$			$0.162\ R_o^{-3}$
$J_{4V} = 6\ G_3 = 6 / V_3$			$0.975\ R_o^{-3}$
$N_V = f_3 \cdot J_{4V}$		$2.557\ f_3 \bar{L}_2^{-3}$	$0.975\ f_3 R_o^{-3}$

A1-2 Variables

α_L factor set to give equal S_v in real and ideal polycrystals; [-]

c_1 constant introduced to simplify equations

d_s diameter of spherical grain with same volume as ideal equi-S_v grain; [m]

f_3 fraction of four-grain junctions cavitated in ideal microstructure; [-]

$\bar{G}$ equivalent 'spherical' grain size; [m]

G_3 number of ideal grains per unit volume; [m^{-3}]

J_{4V} number of four-grain junctions per unit volume ideal polycrystal; [m^{-3}]

ℓ facet edge length of the polyhedron used as an ideal grain; [m]

$\bar{L}_2$ mean linear intercept on a random polish plane in a real microstructure; [m]

N number density of pores attached to grain boundaries; [m^{-2}]

N_V number of pores per unit volume solid; [m^{-3}]

R_o true distance between opposite hexagonal faces in the ideal, truncated-octahedral grain; [m]

R_o half the distance between opposite hexagonal faces in a truncated octahedron; [m]

$S_3^{iso,px}$ surface area per ideal, truncated-octahedral grain, either of an isolated grain (*iso*), or of a grain in the ideal polycrystal (*px*); [m^2]

S_v specific grain boundary surface area per unit volume polycrystal; $[m^2 \cdot m^{-3}]$

V_3 volume of an ideal grain; $[m^3]$

• Starred variables are constants.

Appendix 2

Pore coalescence rates in the ideal porous microstructure

In this section we develop expressions for coalescence rates (with respect to grain size) for an ideal truncated-octahedral polycrystal with pores only at four-grain junctions. The relations are between (1) the mean linear intercept grain size, $\bar{L}_2$ and (2) the pore number density parameters N_v, N and f_3. We develop these relations for the three limiting microstructural paths solved for in the swelling model: constant-N_v, constant-N and constant-f_3. Variables are listed in section A2-2.

A2-1 General relations

In the idealized, equi-S_v microstructure (Table A1-1):

$$N_v = c_1 \cdot f_3 \cdot \bar{L}_2^{-3} \qquad (1a)$$

where $$c_1 = 2.557 \qquad (1b)$$

so $$f_3 = c_1^{-1} \cdot N_V \bar{L}_2^3 \quad (2)$$

For cavities attached to grain boundaries:

$$N = N_V / S_V \quad (3a)$$

which, from Eq. (1a) in this appendix, and Eq. (2) in App. 1:

$$N = (c_1/2) f_3 \bar{L}_2^{-2} \quad (3b)$$

which, from Eq. (3) in this appendix, and Eq. (2) in App. 1:

$$N_V = N \cdot S_V \quad (4a)$$

$$= 2 N \bar{L}_2^{-1} \quad (4b)$$

From Eqs. (2) and (3):

$$f_3 = (N \cdot S_V / c_1) \bar{L}_2^3$$

$$= (2/c_1) N \bar{L}_2^2 \quad (5)$$

A2-1.1 Case: constant $N_V = N_V^*$

This case gives *upper* bounds to N_V, N, and f_3 values; that is, the number of pores remains constant, and is not reduced by coalescence.

From Eq. (3a) in this appendix, and Eq. (2) in App. 1:

$$N = (N_V^{\bullet} / 2)\, \bar{L}_2 \qquad (6)$$

From Eq. (2): $$f_3 = (N_V^{\bullet} / c_1)\, \bar{L}_2 \qquad (7)$$

From Eq. (7), f_3 will increase past its physically meaningful maximum value of one, at a grain size of:

$$\bar{L}_2^{\bullet} = (c_1 / N_V^{\bullet})^{1/3} \qquad (8)$$

However, this poses no real problem, because, when significant grain growth occurs in a porous polycrystal, a constant-N_V path is hypothetical. Coalescence *will* occur.

A2-1.2 Case: constant $N = N^{\bullet}$

This case gives values of N_V, N, and f_3, at a given grain size, which are *intermediate* between the higher values for a constant-N_V case and the lower values for a constant-f_3 path.[1]

From Eq. (4):

$$N_V = 2\, N^{\bullet}\, \bar{L}_2^{-1} \qquad (9)$$

---

[1] Given that the initial microstructures for all three paths were identical...

From Eq. (5): $f_3 = (2/c_1)\, N^{\bullet}\, \bar{L}_2^{\,2}$ (10)

From Eq. (10), f_3 will increase past its physically meaningful maximum value of one, at a grain size of:

$$\bar{L}_2^{\,\bullet} = (\, c_1 / \, 2\, N^{\bullet})^{\,1/2} \qquad (11)$$

A real microstructure — if its pores still were to remain at four-grain junctions only — would at this point change to a constant-f_3 path, with $f_3^{\bullet} = 1$.

A2-1.3 Case: constant $f_3 = f_3^{\bullet}$

This case gives *lower* bounds to N_V, N, and f_3 values at a given grain size. The permissible values for $f_3^{\bullet}$ are between zero and one.

From Eq. (1a):

$$N_V = c_1\, f_3^{\bullet}\, \bar{L}_2^{\,-3} \qquad (12)$$

From Eq. (3): $N = (c_1/2)\, f_3^{\bullet}\, \bar{L}_2^{\,-2}$ (13)

A2-2 Variables

c_1 constant introduced to simplify equations

equi-S_v grain; [m]

f_3 fraction of four-grain junctions cavitated in ideal microstructure; [-]

$\bar{L}_2$ mean linear intercept on a random polish plane in a real microstructure; [m]

N number density of pores attached to grain boundaries; [m^{-2}]

N_v number of pores per unit volume solid; [m^{-3}]

R_o distance between opposite hexagonal faces in the ideal, truncated-octahedral grain; [m]

S_v specific grain boundary area of the polycrystal; [m^2/m^3]

---

* Starred variables are constants.

Appendix 3

Dihedral angle correction to P_{cap}, for a four-grain junction pore

In this section, we generate a first-order correction to the pressure-driven, diffusional pore growth model of Wilkinson (1978), by reducing the predicted capillarity pressure of a pore attached to a four-grain junction. We do this simply by acknowledging that the pore will be not a sphere, but rather a spherical tetrahedron,[1] with a surface curvature appropriate to its dihedral angle. Variables are listed in section A3-3.

A3-1 Analysis

A dihedral angle correction is more important in swelling than in creep fracture, in which the sintering stress may be neglected, relative to a constant applied stress (Riedel, 1987, p.155-6). In

[1] That is, a tetrahedral pore whose faces have a common spherical curvature.

swelling driven by inert trapped gas, the internal pore pressure falls very sharply at short times (Fig. 5-8). For the rest of swelling, the effective pressure is strongly influenced by the opposing capillarity constraint. The geometric uncertainties which make dihedral angle corrections of uncertain value in *initial* stage microstructures (Handwerker et al., 1984) are far less important in final stage microstructures.

When surface energy is isotropic, an equilibrium, *four-grain junction* pore will take the shape of a spherical tetrahedron (Raj and Ashby, 1975). Surface curvature and capillarity pressure in such a pore will be lower than in a *spherical* pore of the same volume:

$$P_{cap} = \gamma_s \cdot \kappa \tag{1a}$$

where

$$\kappa = (1/r_1 + 1/r_2) \tag{1b}$$

$$= 2/r \tag{1c}$$

in which r_1 and r_2 are the principal radii of curvature (for an ideal spherical tetrahedron, they both equal the common r).

However, assuming *spherical* pores simplifies calculating average pore population parameters from swelling data (App. 5), and equivolume spheres and spherical tetrahedra should have reasonably similar mean tangent diameters, $\bar{D}_v$ (DeHoff and Rhines,

1968, p.131).[2] So, in the stereological calculations, and in most parts of the swelling model, we treat pores as spheres. At the same time, we estimate below a numerical factor $g\{\psi\}$ which depends only on the dihedral angle,[3] ψ, which can be used to adjust the P_{cap} predicted for a spherical pore, to the lower and physically more reasonable spherical-tetrahedral value. That is, we will replace:

$$P_{cap} = 2\,\gamma_s/r \qquad (2a)$$

with:[4,5]

$$P_{cap} = 2\,g\{\psi\}\,\gamma_s/\,r \qquad (2b)$$

'where 'r' is the spherical radius calculated from experimental data as in App. 5, and:

---

[2] For polished, thermally-etched HPA, in which pores are counted by SEM, as in this work, *practical* $\bar{D}_v$ values likely are close to *theoretical* $\bar{D}_v$, for spherical-tetrahedral pores.

[3] This is the *full*, not the half-angle. While the results are presented only for the four-grain junction pore, formulae given by Raj and Ashby (1975) permit the same analysis to be applied to three-grain edge and two-grain facet pores.

[4] Using this form simplifies comparing the P_{cap} of equivolume spherical and spherical tetrahedral pores.

[5] In calculating $g\{\psi\}$, we note that ψ is held *constant* in models for how cavities (and grain boundaries) distort as they are dragged by moving boundaries during grain growth (Hsueh et al., 1982; Spears and Evans, 1982).

$$0 \leq g\{\psi\} \leq 1 \tag{2c}$$

Raj and Ashby (1975, Eq. A1.3) present results for the volume of a spherical tetrahedron. Using their notation for a spherical tetrahedron of dihedral *half*-angle α (where $\psi = 2\alpha$) and face radius ρ:

$$V_{st} = F_v\{\psi\} \cdot \rho^3 \tag{3}$$

where the subscript 'st' refers to a spherical tetrahedron, and:

$$F_v\{\psi\} = 8\left[\frac{\pi}{3} - \cos^{-1}\left(\frac{2^{1/2} - \cos\alpha\cdot(3-A^2)^{1/2}}{A\sin\alpha}\right)\right] + A\cos\alpha\left[(4\sin^2\alpha - A^2)^{1/2} - \left(\frac{A^2}{2^{1/2}}\right)\right] - 4\cos\alpha\cdot(3-\cos^2\alpha)\cdot\sin^{-1}\left(\frac{A}{2\sin\alpha}\right) \tag{4a}$$

where: $$A = \left(\frac{2}{3}\right)\left[2^{1/2}(4\sin^2\alpha - 1)^{1/2} - \cos\alpha\right] \tag{4b}$$

For a spherical pore of radius r:

$$V_s = c_s \cdot r^3 \tag{5a}$$

where: $$c_s \equiv \frac{4\pi}{3} \tag{5b}$$

Setting the volumes of the spherical tetrahedral and spherical pore equal, then for equal γ_s in both pores, the ratio of the capillarity pressures is:

$$\left.\frac{P^{st}_{cap}}{P^{s}_{cap}}\right|_{V} = \left.\frac{\gamma_s(\kappa_1^{st} + \kappa_2^{st})}{\gamma_s(\kappa_1^{s} + \kappa_2^{s})}\right|_{V} \qquad (6a)$$

$$= \left.\frac{2/r}{2/r}\right|_{V}$$

$$= \left.\frac{r}{r}\right|_{V} \qquad (6b)$$

$$\equiv g\{\psi\} \qquad (6c)$$

From Eqs. (3) and (5a):

$$g\{\psi\} = \left(\frac{F_V(\psi)}{c_s}\right)^{1/3} \qquad (7)$$

Then, with an estimate of average *spherical* pore size (r) from stereological data, we assume that such an estimate is insensitive to pore shape, for typical ψ. That is, for $V_{st} = V_s$ we assume (DeHoff and Rhines, 1968, p. 131):

$$\bar{D}_v^{st} \simeq \bar{D}_v^{s} \qquad (8)$$

from which:

$$P^{st}_{cap}\{\psi\} = g\{\psi\} \cdot P^{s}_{cap} \qquad (9a)$$

$$= 2\, g\{\psi\} \cdot \frac{\gamma_s}{r} \qquad (9b)$$

A3-2 Results

Fig. A3-1 shows that $g\{\psi\}$ is close to linear in the full equilibrium dihedral angle, for the range of angles possible for

a four-grain junction pore in systems with isotropic γ_s. The lower limit to ψ is that for a planar tetrahedron (just over 70.5°; Tuma, 1979, p.24), while the upper limit is that for a sphere (180°).

Experimental values reported for ψ for alumina vary considerably (App. 15). A reasonable first approximation for generic alumina would set $\psi \simeq 120°$ and $g(\psi)$ to 0.5 (Coble, 1970, p.4805). Francois and Kingery (1967; UO_2) and Handwerker et al. (1984; MgO) note that ψ determined from internal pores will be smaller by 30 to 45° than ψ determined from thermal grooving data.[6] This would be the case when the internal pore atmosphere lowered γ_s, relative to its value when in contact with the external atmosphere.

Approximate mean ψ determined experimentally in this work, by TEM of internal pores, are (see Chs. 2,4):

	ARCO	AVCO
ψ (deg)	90-120	80-100

For AVCO HPA, we used $\psi = 90°$, and the corresponding value of

[6] Both papers present data on the *distribution* of ψ.

$g\{\psi\} = 0.3$, in the numerical model.

As swelling proceeded in pressureless anneals, pores developed which were no longer equiaxed. An increasing fraction of the pore population seen on internal etched polish planes appeared to be cylinders along three-grain edges, or disks covering two-grain facets (App. 13). So, although an approximate correction to P_{cap} was important in predicting P_{cap}, it did not seem worthwhile to refine that estimate.[7]

A3-3 Variables

α	$\psi/2$; [deg]
A	Factor in $F_v(\psi)$; [-]
c_s	$F_v(\psi)$ for a spherical pore (= $4\pi/3$); [-]
$\bar{D}_v$	stereological mean tangent diameter; [m]
$F_v(\psi)$	function of dihedral angle, relating volume of a spherical-tetrahedral, four-grain junction pore to radius of curvature of its surfaces (after Raj and Ashby, 1975); [-]

[7] Kingery and Francois (1967) present an initial analysis which predicts that an internal pore pressure will reduce ψ. Because of complications acknowledged in their analysis, the complexity of the current model and uncertainties in model parameters, we do not include this effect.

$g(\psi)$	multiplier reducing P_{cap} from value for a spherical pore to value appropriate to a spherical tetrahedron of the same volume, with $\psi = \psi$.
γ_s	surface energy; [J/m^2]
κ	sum of the two local principal curvatures of pore surface; [m^{-1}]
ψ	(full) equilibrium dihedral angle at pore surface/grain boundary junction; [m^{-2}]
P_{cap}	capillarity pressure of a pore; [N/m^2]
r	radius of faces of *spherical-tetrahedral* pore; [m]
r_1, r_2	local principal radii of curvature of pore surface; [m]
r	radius of surface of *spherical* pore; [m]
s, st	subscripts denoting spherical/spherical tetrahedral
V	pore volume; [m^3]

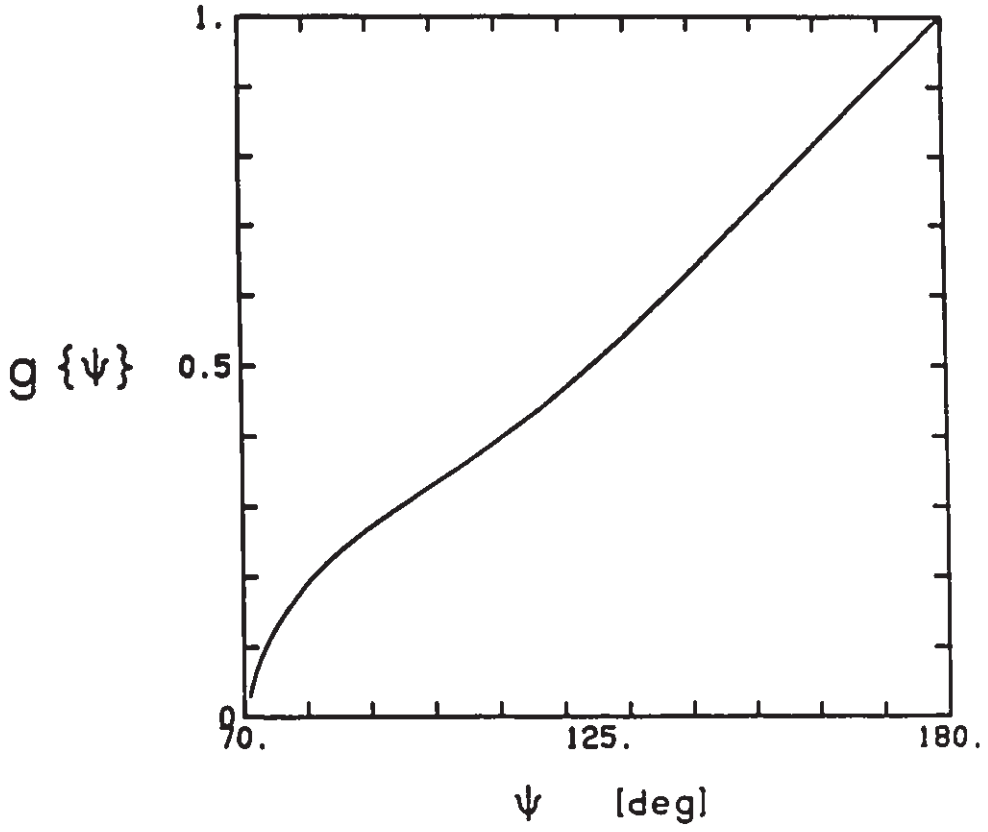

Fig. A3-1: The capillary pressure correction factor, $g(\psi)$, as a function of the full dihedral angle, for an equilibrium four-grain pore.

Appendix 4

Pressure-volume relations for *inert* gas trapped in closed pores

---

The internal pore pressure (Eq. 19 in Ch.3) contains two terms: one for inert trapped gas, and one for a gas-generating reaction:

$$P_{int} = P^{I}_{int} + P^{G}_{int}$$

In this section, we develop expressions for the trapped-gas component, P^{I}_{int}, for the case when no pore gas is lost or generated during final-stage pressure sintering or swelling. Also, we show that the *initial* effective pore pressure is roughly equal to the applied pressure during hot-pressing. (We discuss the chemically-maintained P_{int} component in App. 5, and in the discussion, Ch.6.) Variables are listed in section A4-3.

A4-1 The inert trapped-gas component, P^{I}_{int}

We assume that the total number of moles of gas trapped in pores per unit volume porous polycrystal, n_v^{tot}, is constant during swelling. That is, no significant amount of gas dissolves or

exsolves, adsorbs or desorbs, is generated by internal chemical reaction or lost by, for example, boundary diffusion[1] (Coble, 1962; Rice, 1969; Bennison and Harmer, 1985a):

$$n_{V_o}^{tot} = n_V^{tot}(t) \qquad (1)$$

where

$$n_V^{tot} = N_V \cdot \bar{n}_c \qquad (2)$$

We assume that the trapped gas behaves ideally (Raj, 1982a; Riedel, 1987, pp.132-5). Then, for the average pore, at t = 0:[2]

$$P_i^o \; V_c^o = \bar{n}_c^o \; R \; T \qquad (3a)$$

i.e.

$$\bar{n}_c^o = \left(\frac{1}{RT} \right) P_i^o \; V_c^o \qquad (3b)$$

From Eq. (2), multiplying Eq. (3b) by N_V^o:

$$n_{V_o}^{tot} = \left(\frac{1}{RT} \right) P_i^o \; (N_V^o \; V_c) \qquad (4a)$$

$$= \left(\frac{1}{RT} \right) P_i^o \; V_v^o \qquad (4b)$$

And similarly, at any t ≥ 0:

---

[1] The polycrystal (de)densifies by, for example, P_{eff}-driven boundary diffusion of *matrix* atoms or ions.

[2] In this section, often we will write P_{int} as P_i, for compactness. *Initial* values are denoted by a sub- or superscript 'o'.

$$n_V^{tot}\{t\} = \left(\frac{1}{RT}\right) P_i\{t\}\cdot N_V\{t\}\cdot V_C\{t\} \qquad (5a)$$

$$= \left(\frac{1}{RT}\right) P_i\{t\}\cdot V_V\{t\} \qquad (5b)$$

So, from Eqs. (1), (4b) and (5b):

$$P_{int}^{I}\{t\} = \frac{(P_i V_V)_o}{V_V\{t\}} \qquad (6)$$

where, for compactness, we have written $P_i^o V_V^o$ as $(P_i V_V)_o$.

From Eq. (6), the inert-trapped-gas component of the internal pore pressure is a *self-dissipating* driving force for diffusional pore growth.

A3-2 The temperature dependence of $(P_i V_V)_o$

A3-2.1 General

Assuming, as above, a constant amount of gas trapped in the porous polycrystal between the end of hot-pressing at T_{HP} (subscript 'f') and the start of the anneal at T_{ann}:

$$n_{Vf}^{tot}\Big|_{T_{HP}} = n_{Vo}^{tot}\Big|_{T_{ann}} \qquad (8)$$

Then, from Eq. (8), and either (4) or (5):

$$\frac{1}{RT_{HP}} (P_i V_v)_f^{HP} = \frac{1}{RT_{ann}} (P_i V_v)_o \qquad (9)$$

i.e. $$(P_i V_v)_o = \left(\frac{T_{ann}}{T_{HP}} \right) (P_i V_v)_f^{HP} \qquad (10)$$

Typical temperature ratios for these tests show that $(P_i V_v)_f^{HP}$ will be within 15% of $(P_i V_v)_o$:

T_{ann} / T_{HP} [K/K]		
T_{ann}	T_{HP} [C]	
[C]	1500	1550
1450	0.97	0.95
1350	0.92	0.89
1250	0.86	0.84

We now establish an approximate value for $(P_i V_v)_f^{HP}$, and so for $(P_i V_v)_o$, for the limiting case in which the total amount of gas trapped in pores remains constant throughout the final stage of pressure sintering.

A3-2.2 Case: Constant n_v^{tot} during final stage densification

At pore closure (subscript 'pc') during pressure sintering at T_{HP}, for ideal gas behavior in the average pore, from Eq. (5):

$$P_i^{pc} \cdot V_v^{pc} = n_{v,pc}^{tot} \cdot R\, T_{HP} \qquad (11)$$

If the gas mixture within the hot-pressing furnace is at a pressure of one atmosphere:

$$P_{ext}^{HP} = P_{i,pc}^{HP} \qquad (12a)$$

$$= 0.1 \quad \text{MPa} \qquad (12b)$$

For *global* pore closure occurring at a relative density of at least 0.9 (Budworth, 1970; Rosolowski and Greskovich, 1975; Beeré, 1975a, pp.134-5):

$$\tilde{\rho}_{pc} \geq 0.9 \qquad (13a)$$

i.e. $$V_{v,pc} \leq 0.1 \qquad (13b)$$

From Eqs. (12) and (13):

$$(P_i V_v)_{pc} \leq 0.01 \quad \text{MPa} \qquad (14)$$

Grain growth-driven coalescence will decrease N_v and increase the mean cavity size (and so $\bar{n}_c$) during final stage pressure sintering (Yan et al., 1980). We assume, however, a constant *total* amount of trapped gas in the densifying polycrystal, as in Eq. (1):

$$n_{v,f}^{tot} = n_{v,pc}^{tot} \qquad (15a)$$

That is, for the $(N_v - n_c)$ *products*:

$$N_V^f \cdot \bar{n}_c^f = N_V^{pc} \cdot \bar{n}_c^{pc} \qquad (15b)$$

Throughout final stage sintering, for ideal gas behavior in the average pore, from Eq. (15):

$$\bar{n}_c^{fs} = \left(\frac{1}{RT_{HP}} \right) (P_i \; V_c)_{fs} \qquad (16a)$$

i.e.

$$(N_V \; \bar{n}_c)_{fs} = \left(\frac{1}{RT_{HP}} \right) (P_i \; V_v)_{fs} \qquad (16b)$$

So, from Eqs. (14-16):

$$(P_i \; V_v)_f^{HP} \leq 0.01 \quad \text{MPa} \qquad (17)$$

Eqs. (15-17) hold only if, for example, no gas-generating chemical reactions are active during final-stage pressure sintering.

For this case, from Eqs. (10) and (17):

$$(P_i V_v)_o \leq 0.01 \left(\frac{T_{ann}}{T_{HP}} \right) \qquad (18)$$

where the temperature ratio has been given above.

A3-3 The relation between P_{app}^{HP} and P_{eff}^{o}

Assuming negligible microstructural and dimensional changes between the end of hot-pressing and the start of the anneal:

$$V_{V,f}^{HP} \approx V_V^o \tag{19}$$

Then, from Eq. (10):

$$P_i^o = \frac{T_{ann}}{T_{HP}} \cdot P_i^f \tag{20}$$

For the swelling tests on Al_2O_3 reported here, the temperature ratio in Eq. (20) is between 0.85 and 1.

Surface energies, and so, capillarity pressures, are rather insensitive to temperature over the range T_{HP} to T_{ann} (Davidge, 1979, p.77). So, again assuming negligible microstructural change between the end of hot-pressing and the start of the anneal:

$$P_{cap,f}^{HP} \approx P_{cap}^o \tag{21}$$

For the high relative densities achieved in the polycrystal at the end of the hot-press final stage — which it retains at the beginning of the anneal — no $\tilde{\rho}$ correction to P_{app} is required (Coble, 1970; Vieira and Brook, 1984).

Define $$\Delta P \equiv P_{eff}^o - P_{eff,f}^{HP} \tag{22}$$

We assume that, at the end of the final stage of hot-pressing:

$$P_{eff,f}^{HP} \approx 0 \tag{23}$$

Then, from Eq. (22): $$\Delta P = P_{eff}^o \tag{24a}$$

where, at any time, the effective pressure is defined as:

$$P_{eff} \equiv P_{int} - P_{cap} - P_{app} \tag{24b}$$

From Eqs. (23) and (24b):

$$P^{HP}_{int,f} = P^{HP}_{cap,f} + P^{HP}_{app} \tag{25a}$$

Multiplying Eq. (25a) by the temperature ratio:

$$\left(\frac{T_{ann}}{T_{HP}}\right) P^{HP}_{int,f} = \left(\frac{T_{ann}}{T_{HP}}\right) P^{HP}_{cap,f} + \left(\frac{T_{ann}}{T_{HP}}\right) P^{HP}_{app} \tag{25b}$$

Substituting Eqs. (19), (20) and (25b) into (24b): (26a)

$$\Delta P = \left(\frac{T_{ann}}{T_{HP}}\right) P^{HP}_{cap,f} + \left(\frac{T_{ann}}{T_{HP}}\right) P^{HP}_{app} - P^{HP}_{cap,f} - P_{app}$$

$$= P^{HP}_{cap,f}\left(\frac{T_{ann}}{T_{HP}} - 1\right) + \left(\frac{T_{ann}}{T_{HP}}\right) P^{HP}_{app} - P_{app} \tag{26b}$$

In the swelling tests reported here, $T_{ann} \approx T_{HP}$ and $P^{HP}_{app} \gg P_{app}$ (20 to 40 MPa $\gg$ 0.1 MPa). So, Eq. (26b) can be simplified:

$$P^{o}_{eff} \leq \left(\frac{T_{ann}}{T_{HP}}\right) P^{HP}_{app} \tag{27a}$$

$$\approx P^{HP}_{app} \tag{27b}$$

A4-3 Variables

n_c	moles of gas trapped in the average pore; [moles]
N_V	pores per unit volume porous polycrystal; [m^{-3}]
n_V^{tot}	total number of moles of gas trapped in pores, per unit volume porous polycrystal; [$moles.m^{-3}$]
P_{app}	applied hot-pressing (ram) pressure; [N/m^2]
P_{atm}	external furnace atmosphere pressure during hot-pressing; [N/m^2]
P_{cap}	pore capillarity pressure; [N/m^2]
P_{int}, P_i	internal pore pressure; [N/m^2]
ΔP	defined in Eq. (22); [N/m^2]
R	gas constant; [J/mol.K]
$\tilde{\rho}$	relative density; [-]
T	temperature
V_c	volume of the mean pore; [m^3]
V_V	volume fraction porosity; [-]

Subscripts and superscripts

ann	anneal
f	end of hot-pressing
HP	hot-press...
o	initial
pc	pore closure

Appendix 5

The internal pore pressure component maintained by internal, gas-generating chemical reactions, P^{G}_{int}

In this section we establish a simple form for a P_{int} which includes both inert and chemically-maintained components. Then, from thermochemical data, we predict minimum and maximum equilibrium pore pressures, for certain gas-generating pore reactions.

In Ch.5, we compare these results to the range of P^{G}_{int} predicted by numerical solutions to enhance swelling rates relative to rates due to trapped gas alone. The results are (1) total pore pressures for pO_2 liberated by MgO-doped HPA dissociating are far too low to enhance swelling, and (2) in the temperature range for swelling, pCO in equilibrium with external furnace pO_2 are at least an order of magnitude higher than the P^{G}_{int} (10 MPa) that will cause runaway swelling.

Variables are listed in section A5-4.

A5-1 General

Many pore gas mixtures are possible, depending on the ceramic materials/processing system, the press dies and the furnace atmosphere and schedule (App. 4). Consequently, choosing a general *form* for a P_{int} which includes both trapped-gas and gas-generating reaction components, and estimating pore pressures during final-stage hot-pressing and swelling, are complicated by, for example:

1) Dopants and impurities segregating to grain boundaries and pore surfaces (Bennison and Harmer, 1985a).
2) Pore atmospheres after pore closure and in the as-received material serving as oxygen reservoirs — perhaps of limited capacity — and so permitting large pore pressures to develop *independently* of the furnace atmosphere.
3) Internal gas generating reactions occurring not only during swelling, but also during final-stage hot-pressing (such that $(P_i V_v)_o \geq 0.01$).
4) Kinetics of diffusional mass transport to and from pores invalidating equilibrium pressure calculations.
5) Gas-forming reactions and diffusional mass transport having different temperature dependencies.

Given such uncertainties, we choose an internal pore pressure with the simple form:

$$P_{int}\{V_v, T\} = P^{I}_{int}\{V_v^{-1}, (T)\} + P^{G}_{int}\{T\} \qquad (1)$$

where the self-dissipating, inert trapped gas component (I) is *weakly* temperature dependent (App. 4) and the component related to gas-generating-reactions (G) is taken as a temperature-dependent constant. Such a form is flexible, accommodating a range of pore gas mixtures, from limiting 'inert' gases (in which the number of moles of trapped gas remains constant during swelling; this need not be, for example, N_2 or Ar), to those in which ongoing chemical reactions maintain a constant internal pore pressure (e.g. CO_x or SO_2; Bennison and Harmer, 1985a). We discuss it more fully in section 6.1.6.

Numerical swelling calculations for a P_{int} of this form, with parameter value sets appropriate to specific materials, will permit calculating (1) the maximum P^{G}_{int} that does *not* enhance swelling rates above those for inert trapped gas, and (2) the minimum P^{G}_{int} that will cause rapid swelling to gas release. In Chs.5 and 6, we compare such predicted transitional partial pore pressures with equilibrium pore pressures predicted here for specific gas-generating reactions. Of the range of potential calculations for *equilibrium* pore pressures implied by the above,

we will discuss two limiting cases:[1]

1. Case: *Minimum* equilibrium pore pressures: pores are mechanically *and* chemically closed. Gas-solid equilibria within pores — such as MgO and Al_2O_3 dissociating, and the O_2 liberated reacting with dissolved carbon to form CO and CO_2 — are independent of the external furnace environment.

2. Case: *Maximum* equilibrium pore pressures: pores are mechanically closed (re. diffusional loss of oxidation product gases; Coble, 1962), but chemically open (re. oxygen grain boundary diffusion; Coble, 1962). Gas-solid reactions within pores — such as dissolved C and S reacting to generate CO, CO_2 and SO_2 (Bennison and Harmer, 1985a) — are equilibrated with the pO_2 in the external furnace atmosphere.

A5-2 Minimum pore pressure case

For (MgO)-Al_2O_3-[C],[2] JANAF free energy functions and standard

---

[1] In carrying out these calculations, we have considered Pasco's (1980) work on Al-O-C equilibria. Throughout the SEM and TEM for this work, we detected no Al_4C_3 or Al_4O_4C.

[2] We use round brackets to denote a dopant (e.g. (MgO)-Al_2O_3),

formation enthalpies can be used, in conjunction with an elemental mass balance for the *dominant* gas phase species, to calculate equilibrium partial and total pore pressures (JANAF, 1974; Lupis, 1983, p.130-32).

A5-2.1 System: Al_2O_3-[C]

This system is presented for comparison with MgO-doped cases (below).[3] We can write a reaction equation set based on CO(g), with temperature-dependent equilibrium constants of standard form:

$$\frac{1}{2}\,Al_2O_3 + \frac{3}{2}\,C = Al(g) + \frac{3}{2}\,CO(g) \qquad K_{a1} \qquad (2)$$

$$\frac{1}{2}\,Al_2O_3 + \frac{3}{2}\,C = \frac{1}{2}\,Al_2O(g) + CO(g) \qquad K_{a2} \qquad (3)$$

$$Al_2O_3 + C = 2AlO(g) + CO(g) \qquad K_{a2} \qquad (4)$$

$$2CO(g) = C(gr) + CO_2(g) \qquad K_{CO} \qquad (5)$$

$$C(gr) + \frac{1}{2}\,O_2(g) = CO(g) \qquad K_{CO_2} \qquad (6)$$

A gas-phase mass balance for the *elemental* Al and O liberated by

---

and square brackets to denote a dissolved impurity (e.g. Al_2O_3-[C]).

[3] Similar calculations could be done for oxidation of S, instead of C.

Al_2O_3 dissociation is:

$$n^{(el)}_{Al,gas} = \frac{2}{3} n^{(el)}_{O,gas} \qquad (7)$$

In terms of *all* gas phase components, this is:

$$n_{Al(g)} + n_{AlO(g)} + 2n_{Al_2O(g)} = \qquad (8)$$

$$\frac{2}{3}\left[n_{AlO(g)} + n_{Al_2O(g)} + n_{CO(g)} + 2n_{CO_2(g)} + 2n_{O_2(g)} \right]$$

Taking Al, Al_2O and CO as the dominant gas phase components,[4] and for ideal gas behavior at the low pore pressures calculated, Eq. (8) can be written as:

$$p_{Al(g)} + \frac{4}{3} p_{Al_2O(g)} - \frac{2}{3} p_{CO(g)} = 0 \qquad (9)$$

Substituting for p_{Al} and p_{Al_2O} from K_{a1} and K_{a2}, from Eqs. (2) and (3):

$$K_{a1}\left(\frac{a_c}{p_{CO}}\right)^{3/2} + \frac{4}{3}\left(K_{a2}\frac{a_c}{p_{CO}}\right)^{2} - \frac{2}{3} p_{CO} = 0 \qquad (10)$$

or $$a \cdot p_{CO}^{3} + b \cdot p_{CO}^{1/2} + c = 0 \qquad (11)$$

where, at a given temperature and carbon activity:

---

[4] Assumed on a trial basis, and verified by the numerical results (Fig. A5-1; Lupis, 1983: p.130-32).

$$a = 2/3 \qquad (12a)$$

$$b = - K_{a1}\, a_C^{3/2} \qquad (12b)$$

and

$$c = - \tfrac{4}{3} K_{a2}^2\, a_C^2 \qquad (12c)$$

The equilibrium constants are calculated from JANAF data. For any chemical reaction:

$$\Delta G^\circ\{T\} = T \cdot \Delta fef_{298}\{T\} + \Delta H^\circ_{f,298} \qquad (13a)$$

and

$$K\{T\} = exp\left(- \frac{\Delta G^\circ\{T\}}{R\,T} \right) \qquad (13b)$$

where $\Delta fef_{298}\{T\}$ is the reaction's free energy function difference, and $\Delta H^\circ_{f,298}$ is its standard formation enthalpy difference, both referred to 298 K (Gaskell, 1973, p.452-56).

Given a carbon activity, a_C (Table A5-1), the coefficients *a*, *b* and *c* are fixed, and Eq. (11) can be solved numerically for p_{CO} over the temperature range 1000 - 2000 K. Eqs. (2) - (6) then can be used to calculate the remaining partial pressures.

A5-2.2 System: (MgO) - Al_2O_3 - [C]

To the above system of reaction equations (1-5) we add:

$$MgO(c) + C(gr) = Mg(g) + \tfrac{3}{2} CO(g) \qquad K_m \qquad (14)$$

The elemental gas-phase mass balance must now include the oxygen

liberated by MgO dissociation:

$$n_{O,gas}^{(el)} = n_{Mg,gas}^{(el)} + \frac{3}{2} n_{Al,gas}^{(el)} \qquad (15)$$

That is:

$$2n_{O_2(g)} + 2n_{CO_2(g)} + n_{CO(g)} + n_{Al_2O(g)} = \qquad (16)$$
$$n_{Mg(g)} + \frac{3}{2}\left[n_{Al(g)} + 2n_{Al_2O(g)} + n_{AlO(g)} \right]$$

For Mg, CO, Al and Al_2O dominant in the gas phase,[5] and for ideal gas behavior, the dominant mass balance can be written as:

$$p_{CO} - p_{Mg} - \frac{3}{2} p_{Al} - 2 p_{Al_2O} = 0 \qquad (17)$$

Substituting from Eqs. (2-6) and (14), this is equivalent to:

$$a \cdot p_{CO}^{3} + b \cdot p_{CO} + c \cdot p_{CO}^{1/2} + d = 0 \qquad (18)$$

in which the temperature-dependent constants are:

$$a = 1.0 \qquad (19a)$$

$$b = - K_m \cdot a_{MgO} \cdot a_C \qquad (19b)$$

$$c = - \frac{3}{2} K_{a1} \cdot a_C^{3/2} \qquad (19c)$$

$$d = - 2 (K_{a2} \cdot a_C)^2 \qquad (19d)$$

---

[5] The results show $p_{Mg} \approx p_{CO} > p_{Al} > p_{Al_2O}$, so a simpler mass balance could have been used.

The results are shown in Fig. A15-1, and are discussed below, in section A15-2.4.

A5-2.3 System: ($MgO - Y_2O_3$) - Al_2O_3 - [C]

Thermochemical data over a wide temperature range were located only for Y and Y_2O_3 (Barin and Knacke, 1973); only 298 K data were available for $Y_2(g)$, YO(g), $Y_2O(g)$ and $Y_2O_2(g)$ (Wagman et al., 1971). However, we can estimate whether Y-bearing species should give significant partial pressures in closed pores. The Ellingham Y-O-Y_2O_3 reaction is about 40 kcal/mol O_2 more negative than that for Al_2O_3 (Barin and Knacke, 1973). Further, Y_2O_3 activities are low in the HPAs studied (Table A5-1), and equilibrium partial pressures of Y-bearing gas mixture components will be proportional to some positive power of these Y_2O_3 activities. So, we anticipate negligible changes in predicted total pore pressures, relative to the above calculations without Y_2O_3.

A4-2.4 Results

Numerical results for the (MgO)-Al_2O_3-[C] case described in section A5-2.2 are shown in Fig. A5-1.

Total pore pressures for ARCO (heavy dashed lines) and AVCO (heavy solid lines) are rather similar, despite the differences in MgO and C concentrations. The upper line for each corresponds to estimated (high) *segregated* concentrations; the lower lines to bulk concentrations (1000 times lower; see text accompanying Table A5-1). In the temperature range for swelling, total pore pressures were between 10^{-6} and 10^{-4} MPa, increasing with temperature. The partial pressures of the components of the gas mixture are small (the light lines are for the bulk concentration case).

MgO is more volatile than Al_2O_3 (Sata and Sasamoto's (1984) Fig. 9; Lou et al.'s (1985) Figs. 6 and 10). ARCO contains 200 ppm MgO; AVCO 3000. AVCO's total pore pressures being higher than ARCO's in Fig. A5-1 indicates the extent to which MgO doping increases pore pressures.

A5-3 Maximum pore pressure case

This case corresponds to C or S oxidation to CO_x and SO_x, in equilibrium with the external furnace pO_2.

Bennison and Harmer (1985a), using Raj's (1982a) activity

coefficients to correct for nonideal gas behavior,[6] predict large pore pressures for C and S oxidation in equilibrium with an external furnace p_{O_2}:

$$C(gr) + \tfrac{1}{2} O_2(g) = CO(g) \qquad K_{CO} \qquad (20)$$

$$C(gr) + O2(g) = CO_2(g) \qquad K_{CO_2} \qquad (21)$$

and

$$S(c) + O_2(g) = SO_2(g) \qquad K_S \qquad (22)$$

For the segregant concentrations they estimate by Auger spectra on quenched, fractured specimens, their Figs. 9a,b, predict pore pressures greater than 100 MPa for CO, and about 10^{-2} for SO_2, during swelling in air.[7] Consistent with these high pore pressures, their Fig. 5 shows that heavy cavitation develops rapidly in a *surface* layer at 1600 C. However, in the lower temperature results reported here, swelling was *uniform* across internal polish planes of annealed specimens. This observed uniformity is inconsistent with the oxygen attack described in this section, but is consistent with trapped pore gases containing very low pO_2, and with gas-generating reactions maintaining pore pressures not much greater than one atmosphere during swelling (Chs. 5,6).

---

[6] See also Riedel (1987) p.132-35.

[7] Similar calculations, not given here, predict pCO_2 close to pCO, depending on the temperature and pO_2.

No low-pO_2 swelling tests have yet been carried out, to verify that the uniform swelling is independent of the external furnace atmosphere.

Table A5-1: Activities ranges for C and MgO

Assuming ideal solutions, the activity of the *i*th component equals its mole fraction: $a_i = X_i$. To convert *x* ppmw of component *i*, whose molecular weight is M_i, into X_i in Al_2O_3:

$$a_i = X_i = (M_{Al_2O_3} / M_i) \; x_i \cdot 10^{-6}$$

Upper and lower limits on the activities of dopants and impurities active in the swelling cases discussed above were estimated as follows. For *minimum* values, the *bulk* concentrations were used ('Experimental': Table 2-1b).

For *maximum* values, Bennison and Harmer's (1985a) Auger data were applied to the present HPAs. Their bulk (combustion) C levels were similar to AVCO's, at about 120 ppm, with C segregating to grain boundaries by a factor of about 100. Bulk S levels were four times those reported here by XRF, at about 60 ppm, and the segregated grain boundary C:S concentration ratio was reported as on the order of 10:1. Applying these *ratios* to our *bulk* C and S values yields the *maximum* values in the table below.

(continued on next page)

Table A5-1 (continued)

i:	Al_2O_3	MgO	Y_2O_3	C	S
M_i	102.	40.3	226	12.	32.1
x_i(ARCO)*	*rem*	200	800	250	16
x_i(AVCO)*	*rem*	3000	10	140	17
a_i^{min}(ARCO)	1.	$0.5 \cdot 10^{-3}$	$4 \cdot 10^{-4}$	$\approx 2 \cdot 10^{-3}$	$5 \cdot 10^{-5}$
a_i^{min}(AVCO)	1.	$7.6 \cdot 10^{-3}$	$5 \cdot 10^{-6}$	$\approx 1 \cdot 10^{-3}$	$5 \cdot 10^{-5}$
a_i^{max}(ARCO)	1.			≈ 0.2	10^{-3}
a_i^{max}(AVCO)	1.			≈ 0.1	10^{-3}

* See 'Experimental', Table 2-1b for a more complete chemical analysis.

• *Minimum* and maximum values correspond to *bulk* and (higher) *segregated* concentrations, as described above.

A5-4 Variables and contractions

a,b,c,d constants in equations (10) and (17).

a_i activity of solution component *i*; [-]

fef	free energy function; [J/mol·deg] ?
ΔG°	standard Gibbs energy difference; [J/mol]
ΔH_f°	standard formation enthalpy; [J/mol]
K_j	equilibrium constant of *j*th chemical reaction; [-]
M_i	molecular weight of solution component *i*; [g/mol]
n_k	number of moles of component *k* in pore gas mixture.
p_k	partial pressure of component *k* in pore gas mixture; [N/m^2]
ppmw	parts per million by weight; [-]
rem	remainder
x_i	concentration of solution component *i*; [ppmw]
X_i	mole fraction of solution component *i*; [-]

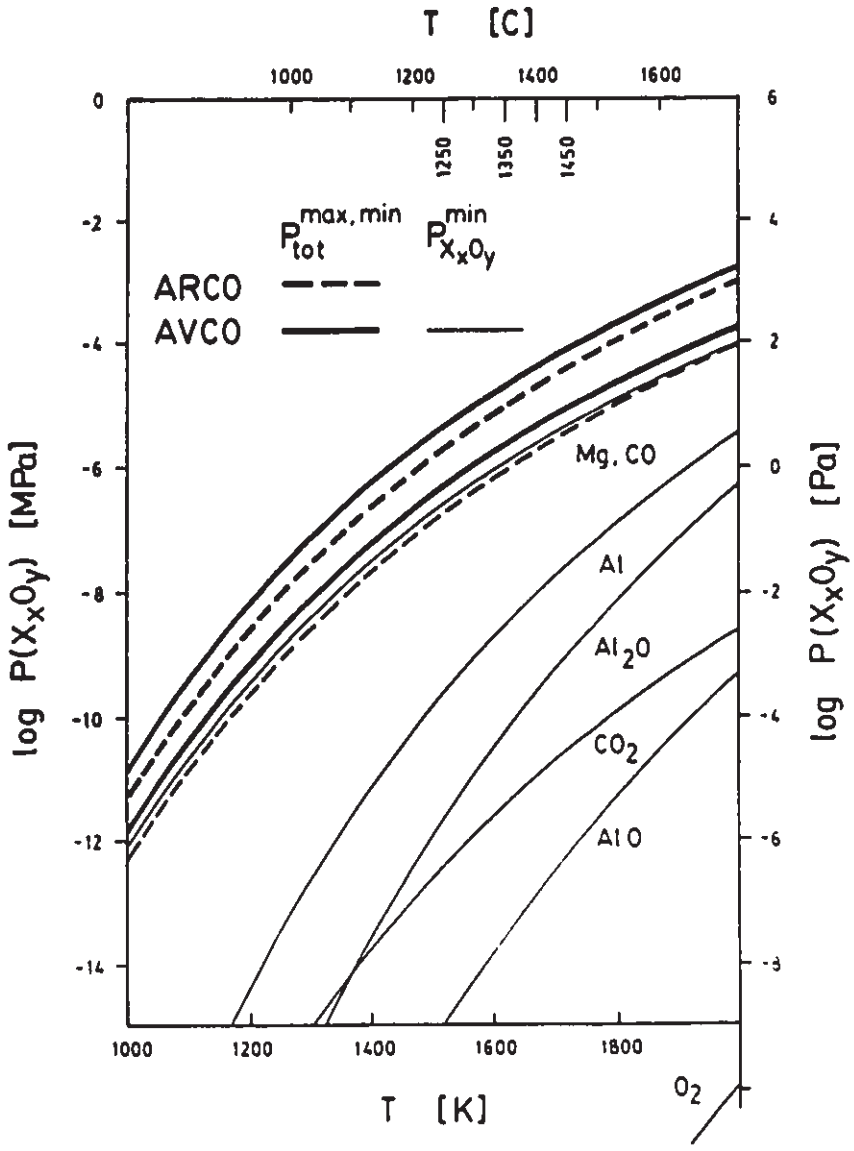

Fig. A5-1: *Minimum* equilibrium pore pressures (i.e. for disssociation of doped HPA and oxidation of dissolved C by the O_2 liberated). Calculated partial and total pore pressures as functions of temperature, for the system (MgO)-Al_2O_3-[C]. Minimum and maximum *total* pressures shown here correspond to bulk and segregated C levels, and are discussed in the text accompanying Table A5-1.

Appendix 6

Estimating microstructural parameters from experimental data

In this section we show how to calculate r, N_V, N, f_3, *b*, ℓ and β from stereological and density data. App. 7 deals with calculating volume fraction porosity (V_V) from density change data. Uncertainties in *raw* data, and error propagation (after Bevington, 1969, Ch. 4) are discussed in App. 14. Variables are listed in section A6-3.

A6-1 Basic microstructural relations

The specific grain boundary area in any polycrystal is (DeHoff and Rhines, 1968, p.79):

$$S_V = 2 / \bar{L}_2 \qquad (1)$$

and convex, second phase 'particles' particles are cut by a polish plane so that (DeHoff and Rhines, 1968, p.131):

$$N_A = N_V \cdot \bar{D}_V \qquad (2a)$$

where, for spherical pores, the mean tangent diameter is:[1]

$$\bar{D}_V = 2\,r \tag{2b}$$

The volume fraction of spherical pores is:

$$V_V = N_V \cdot \bar{V}_C$$

$$= N_V \cdot \left(\frac{4\pi}{3}\right) r^3 \tag{3}$$

We assume an idealized, truncated-octahedral microstructure, in which S_V is equal to that of the real polycrystal (App. 1), and pores occur only at four-grain junctions. From Eqs. (2) and (3), the mean pore size is:

$$r = \left(\frac{3}{2\pi}\right)^{1/2} \left(\frac{V_V}{N_A}\right)^{1/2} \tag{4}$$

Substituting Eq. (3) into Eq. (2), the number of pores per unit volume porous solid is:

$$N_V = \left(\frac{\pi}{6}\right)^{1/2} \left(\frac{N_A^{3/2}}{V_V^{1/2}}\right) \tag{5}$$

If all pores are attached to grain boundaries, the *area* number

---

[1] This appendix assumes spherical pores. We assume throughout that *practical* $\bar{D}_V$ are similar for spherical and spherical-tetrahedral pores of equal volume (App. 3). See App. 13 for the stereology of *mixed* sphere/cylinder pore populations.

density of pores is:

$$N = \frac{N_V}{S_V} \tag{6}$$

So, from Eqs. (1) and (6):

$$N = 0.362 \left(\frac{N_A^{3/2}}{V_V^{1/2}} \right) \bar{L}_2 \tag{7}$$

The *volume* number density of pores, N_V, in terms of the fraction of four-grain junctions cavitated, f_3, is (App. 1):

$$N_V = c_1 f_3 \bar{L}_2^{-3} \tag{8a}$$

where $$c_1 = 2.557 \tag{8b}$$

From Eqs. (5) and (8), the fraction of four-grain junctions with pores is:

$$f_3 = c_1^{-1} \left(\frac{\pi}{6}\right)^{1/2} \left(\frac{N_A^{3/2} \bar{L}_2^{3}}{V_V^{1/2}} \right) \tag{9}$$

A6-2 The spherical shell

For the representative, spherical, porous material element (Wilkinson, 1978, p.61-3) the relative density is:

$$\tilde{\rho} = 1 - V_V \tag{10a}$$

$$= 1 - \left(\frac{r}{b}\right)^3 \qquad (10b)$$

The volume of the spherical solid shell which surrounds an average pore, in terms of the shell radius, b, is:

$$\left(\frac{4\pi}{3}\right) b^3 = 1 / N_V \qquad (11)$$

Substituting N_V, from Eq. (5), the shell radius can be written as:

$$b = \left(\frac{3}{4\pi}\right)^{1/3} N_V^{-1/3} \qquad (12a)$$

$$= \left(\frac{3}{2\pi}\right)^{1/2} \left(\frac{V_V^{1/6}}{N_V^{1/2}} \right) \qquad (12b)$$

The dimensionless ratio of grain boundary area in the spherical shell of radius b, *in the ideal polycrystal*, to the area of the single flat boundary plane in the model spherical shell, is:

$$\beta \equiv \frac{A_{gb/c}}{\pi b^2} \qquad (13)$$

In deriving an expression for β in terms of stereological parameters, we ignore the grain boundary area occluded by a pore, on the grounds that pore volume fractions in the current data are low:

From Eq. (10), $$\left(\frac{r}{b}\right)^3 = V_V \qquad (14a)$$

so $$\frac{b}{r} = V_V^{-1/3} \qquad (14b)$$

Current $V_V\{t\}$ data give *minimum* values of:

$$\left(\frac{b}{r}\right)_{ARCO} \geq 5; \qquad \left(\frac{b}{r}\right)_{AVCO} \geq 4 \qquad (15)$$

That is, in Eq. (13), we can neglect the ($-\pi r^2$) correction to both numerator and denominator of the RHS.

Inverting Eq. (6), the grain boundary area per spherical shell of radius *b*; i.e. per average *attached* pore, is:

$$A_{gb/c} = \frac{S_V}{N_V} \qquad (16a)$$

or, from Eq. (1): $$= \left(\frac{2}{N_V \bar{L}_2} \right) \qquad (16b)$$

From Eq. (5): $$A_{gb/c}\{t\} = 2 \left(\frac{6}{\pi}\right)^{1/2} \left(\frac{V_V^{1/2}}{N_A^{3/2} \bar{L}_2} \right) \qquad (16c)$$

The spherical shell's volume is:

$$V_{shell} = 1/ N_V = \frac{4}{3} \pi b^3 \qquad (17a)$$

from which $$b = \left(\frac{3}{2\pi} \right)^{1/2} \frac{V_V^{1/6}}{N_A^{1/2}} \qquad (17b)$$

Given the ratio between the length of a facet edge in the equi-S_V

ideal grain, ℓ, and the mean linear intercept (App. 1):

$$\ell = 0.592\ \bar{L}_2 \tag{18}$$

then, from Eqs. (17b) and (18):

$$\left(\frac{b}{\ell}\right) = 1.167\ \frac{V_V^{1/6}}{N_A^{1/2}\ \bar{L}_2} \tag{19}$$

Substituting Eqs. (16c) and (17b) into Eq. (13), and as long as $b \geq \ell$:

$$\beta = 1.843\ \left(\frac{V_V^{1/6}}{N_A^{1/2}\ \bar{L}_2}\right) \tag{20a}$$

and from Eq. (19):

$$= 1.579\ \left(\frac{b}{\ell}\right) \tag{20b}$$

However, for *small* (b/ℓ), Eq. (20) does not hold. At an ideal, truncated-octahedral four-grain junction, six boundary facets converge. Four are corners of hexagonal facets, and two are corners of square facets. So, for b less than ℓ:[2]

$$A_{gb/c} = \left(\frac{4}{3} + \frac{2}{4}\right)\pi b^2 \tag{21a}$$

$$\approx 1.83\ \pi b^2 \tag{21b}$$

As a result, for $b \leq \ell$, β has a constant value of ≈ 1.83. From Eq. (21b), this value of β corresponds to $(b/\ell) \approx 1.14$. For all

---

[2] Budworth (1970) shows that S_V for ideal truncated-octahedral and minimum-S_V tetrakaidecahedral polycrystals are very close.

(b/ℓ) smaller than this, Eq. (20a) cannot be used to calculate β.

A6-3 Variables

$A_{gb/c}$ grain boundary area in the representative spherical shell of radius b, in the ideal polycrystal; $[m^2]$

b radius of representative spherical shell in diffusional pore growth model; [m]

β dimensionless ratio of the grain boundary area in polycrystal, per pore, to the area of the single grain boundary plane in the representative spherical shell of radius b; set at 1.8.; [-]

c_1 constant defined in Eq. (7b); [-]

$\bar{D}_V$ mean tangent intercept for a dispersed second phase; [m]

f_3 fraction of four-grain junctions cavitated in ideal microstructure; [-]

ℓ facet edge length in the ideal grain (App. 1); [m]

$\bar{L}_2$ mean linear intercept on a random polish plane in a real microstructure; [m]

N number density of pores attached to grain boundaries; $[m^{-2}]$

N_A number density of pores on an internal polish plane; $[m^{-2}]$

N_V number of pores per unit volume solid; $[m^{-3}]$

r	radius of average spherical pore; [m]
$\tilde{\rho}$	relative density; [-]
S_V	specific grain boundary area; [m^2/m^3]
V_C	volume of an average (spherical) pore; [m^3]
V_{shell}	volume of the representative material shell; [m^3]
V_V	volume fraction of pores; [-]

Appendix 7

Calculating V_v from Archimedes' density change data

In this section we develop formulae for calculating the volume fraction porosity during swelling, from density-change data (Ratcliffe, 1965), for purposes of testing a specific swelling model. We treat polycrystals with intergranular and intragranular *as-received* porosity differently. Variables are listed in section A7-3.

A7-1 Porosity as a function of density change.

The experimental density change data (Tables 4-1,-2) are of the form (Fig. A7-1; Ratcliffe, 1965):

$$\frac{\Delta\rho\{t\}}{\rho_o} = \frac{\rho_o}{\rho_{D_o}} - \frac{\rho_1}{\rho_{D_1}} \qquad (1a)$$

where $$\Delta\rho\{t\} \equiv \rho\{t\} - \rho_o \qquad (1b)$$

These data are 'buffered', in that the dummy specimens (ρ_{D_o}, ρ_{D_1})

correct for uncertainties in, for example, the temperature dependence of the density of the immersion liquid, and drift in the balance between 'before' and 'after' weighing sessions.

However, as discussed below, the *absolute* density of the immersion liquid must be determined accurately in order to calculate an as-received specimen density, by which density change data are converted to V_v. This step has no such buffering.

Density changes reflect whatever fraction of the porosity is in fact active in swelling. Inter and intragranular porosity must be handled differently.

A7-1.1 Case: Dominant initial porosity is intergranular

For the simple case of a polycrystal such as AVCO HPA, which has negligible intragranular porosity (Fig. A7-1a) and no pore separation during swelling, we transform this data into the volume fraction of active pores as follows:

$$V_v\{t\} = 1 - \tilde{\rho}\{t\} \qquad (2a)$$

$$= 1 - \frac{\rho_t}{\rho_{th}} \qquad (2b)$$

The left-hand side of Eq. (1) is:

$$\frac{\Delta\rho\{t\}}{\rho_o} = \frac{\rho_o - \rho_t}{\rho_o} \qquad (3a)$$

$$= 1 - \frac{\rho_t}{\rho_o} \qquad (3b)$$

Rearranging Eq. (3):

$$\frac{\rho_t}{\rho_o} = 1 - \frac{\Delta\rho\{t\}}{\rho_o} \qquad (4a)$$

so

$$\rho_t = \rho_o \left(1 - \frac{\Delta\rho\{t\}}{\rho_o} \right) \qquad (4b)$$

and

$$\tilde{\rho}\{t\} \equiv \frac{\rho_t}{\rho_{th}}$$

$$= \frac{\rho_o}{\rho_{th}} \left(1 - \frac{\Delta\rho\{t\}}{\rho_o} \right) \qquad (4c)$$

Then, from Eq. (2b):

$$V_v\{t\} = 1 - \frac{\rho_o}{\rho_{th}} \left(1 - \frac{\Delta\rho\{t\}}{\rho_o} \right) \qquad (5a)$$

$$= 1 - \tilde{\rho}_o \left(1 - \frac{\Delta\rho\{t\}}{\rho_o} \right) \qquad (5b)$$

From Eq. (5), calculated {volume fraction - time} trajectories are sensitive to uncertainties in as-received relative density ($\tilde{\rho}_o$); that is, to errors in both absolute as-received *and* theoretical densities (Bevington, 1969; see also App. 14).

A7-1.2 Case: Dominant initial porosity is intragranular

The above analysis must be modified for polycrystals which have significant intragranular porosity, as does as-received ARCO HPA (Figs. A7-1b, 4-1.2*j* and 4-2). Such porosity is present in the as-received material, when pores separate from sweeping grain boundaries during sintering. During subsequent anneals, under conditions in which δD_B controls the diffusional component of pore growth (the case for the tests reported here: App. 16) a pore's potential P_{eff}-driven contribution to swelling is expressed only if it contacts, or is very close to a grain boundary. (The *coalescence* component of pore growth rate, as modeled in the current work, also requires intergranular pores.)

At present, we have no data on how ARCO's as-received intragranular pores were distributed over its grain size range. SEM data showed that ARCO's pores rather quickly became intergranular (Table 4-2's Note 2). However, currently we lack TEM data showing how this occurs. In principle, pores which separated as a result of *normal* grain growth may continue to participate periodically in swelling, as sweeping boundaries pass them by. They also may remain attached when swept up, as the boundary driving pressure falls with grain growth. Pores present in the largest as-received grains, particularly if separated by *discontinuous* grain growth, we regard as permanently nonparticipatory.

ARCO requires that the analysis be performed for a time- and temperature-dependent fraction of intragranular pores, i.e. ρ_e, ($\rho_o < \rho_e < \rho_{th}$; Fig. A7-1b). Pending TEM data for its microstructural evolution during swelling, we do not, at this time, apply the model to this HPA. (AVCO is treated as $\rho_e \approx \rho_{th}$; that is, as all its pores participate in swelling; Fig. A7-1a).

A7-2. Initial volume fraction porosity, V_v^o

Eq. (5) shows that, in order to calculate $V_v(t)$ from buffered density change data, the Ratcliffe analysis requires an accurate *absolute* relative density for a specimen ($\tilde{\rho}_o$; Fig. A7-1). Accurate ρ_o and ρ_{th} were required.

The 'Experimental' section describes how absolute densities of the immersion *liquid* were determined. These were required for calculating ρ_o.

The theoretical densities of the *impure, doped* aluminas, ρ_{th}, were estimated as follows.

We calculated the theoretical density of *single crystal* Al_2O_3 from the unit cell volume, after Dorre and Hubner (1984: their p. 11), with atomic weights from Weast et al. (1985: their

p. B-2,3), and Avogadro's number from Cohen and Taylor (1986: their p. 18):[1,2]

$$\rho_{th}(Al_2O_3) \approx 3.9874(4) \pm 0.00016 \quad [Mg/m^3] \qquad (6)$$

No correction was made for grain boundaries lowering the theoretical density of a polycrystal relative to that of a *single* crystal of the same composition.

Approximate corrections to this theoretical density were made for dominant dopants and impurities, based on the XRF analysis (Table 2-1b). For MgO and SiO_2, the data of Rasmunssen and Kingery (1970) was used. For MgO, the $V_O^{\cdot\cdot}$ line of their Fig. 1c was used; for SiO_2, the $V_{Al}^{'''}$ line of their Fig. 1d. In both cases, the *oxide* dopant was converted first to elemental or atomic ppm (ppm $A_aO_b \rightarrow$ ppm A). An approximate solid solution correction for yttrium (as Y_{Al}°) was made, using the difference in atomic weights of Y and Al (Weast et al., 1985), and assuming the lattice parameter remained constant despite the solid solution. The corrections, $\Delta\rho_{th}$, and the final estimates for the two ρ_{th}^{HPA} were:

---

[1] Table 2.1 of Dorre and Hubner (1984) gives a slightly different value. Averaging the three most recent entries, the theoretical density of single crystal Al_2O_3 is about 3.986(1) ± 0.001 Mg/m^3.

[2] Digits in brackets are being carried against future calculations.

AVCO:	ppm A_aO_b	ppm A	$\Delta\rho_{th}$ (Mg/m^3)
SiO_2	140	65.5	$-0.66(10^{-4})$
MgO	3000	1809	$-27.1(10^{-4})$
Y_2O_3	——	10	$+0.28(10^{-4})$
ρ_{th} (Mg/m^3)		3.9846(9) ± 0.0002	

ARCO:	ppm A_aO_b	ppm A	$\Delta\rho_{th}$ (Mg/m^3)
SiO_2	200	93.5	$-0.94(10^{-4})$
MgO	200	121	$-1.81(10^{-4})$
Y_2O_3	——	800	$+22.8(10^{-4})$
ρ_{th} (Mg/m^3)		3.9874(4) ± 0.0002	

No other corrections were made to ρ_{th}. The uncertainties in the above theoretical densities are root mean square propagations from reported uncertainties in physical data (Bevington, 1969), conservatively increased by about one-half, to allow for, for example, impurities for which no density corrections were available.

Experimental data for absolute and relative, *as-received* HPA densities, and the corresponding calculated initial porosities, V_V^o, are summarized in the following table:

		ARCO	AVCO
ρ_o^{abs}	(Mg/m^3)	3.9844(0)±0.0002	3.9818(4)±0.0004
$\tilde{\rho}_o$	(-)	0.9987(5)±0.0002	0.9992(9)±0.0001
V_V^o	(-)	$(1.25\pm0.21)10^{-3}$	$(0.71\pm0.11)10^{-3}$

A7-3 Variables

ρ, ρ^{abs} absolute density; [Mg/m^3]

$\tilde{\rho}$ density relative to theoretical; [-]

$\rho_{o,1}$ ρ at t=0 or t_o, t_1; [Mg/m^3]

ρ_o absolute density of as-received material; [Mg/m^3]

$\rho_{D_{o,1}}$ ρ of a dummy specimen at t=t_o, t_1; [Mg/m^3]

ρ_t ρ at t=t; i.e. $\rho\{t\}$; [Mg/m^3]

ρ_{th} theoretical density; [Mg/m^3]

ρ_* border between porosity fractions which are active (intergranular) and nonactive (intragranular) in swelling, on a $\{\rho$-t$\}$ Ratcliffe swelling plot

(Fig. A7-1); [Mg/m^3]

V_v volume fraction porosity; [-]

V_v^o initial volume fraction porosity; [-]

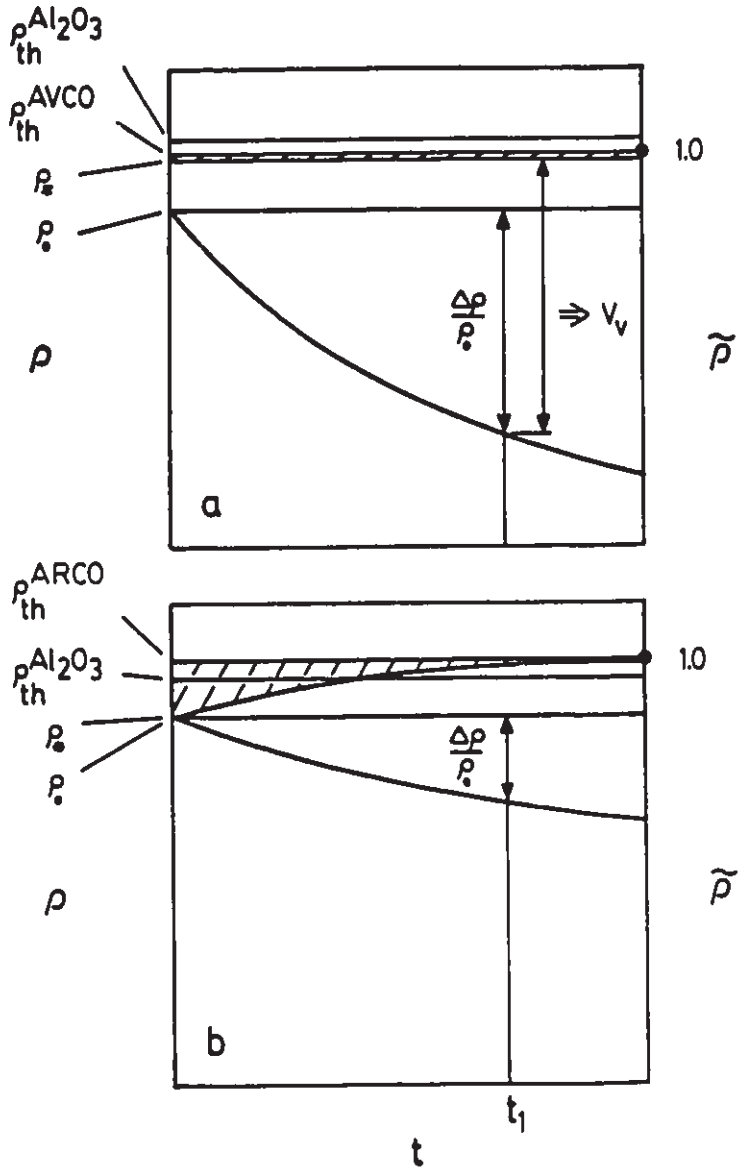

Fig. A7-1: Models for density changes and porosity in swelling, for ACVO and ARCO HPA (schemetic). The hatched band, in each case, is intragranular porosity which is inactive in swelling.

a) AVCO

b) ARCO

Appendix 8

Calculating $P_{eff}\{t\}$ and $P_{int}\{t\}$ from experimental data

In this section, we rearrange the swelling model (Ch.3) to give expressions by which the effective pore pressure, P_{eff}, and its internal component, P_{int}, can be estimated from experimental V_v, N_A and $\bar{L}_2$ data. Variables are listed in section A8-2.

A8-1 Analysis

For spherical pores, the volume fraction porosity is:

$$V_v\{t\} = N_v\{t\} \cdot \frac{4}{3} \pi \cdot r\{t\}^3 \qquad (1)$$

As developed in the swelling model, the overall pore growth rate includes pressure-driven ('P') and coalescence ('L') components (section 3.2):

$$\dot{r} = \dot{r}_P + \dot{r}_L \qquad (2)$$

in which (Ch.3's Eq. 31):

$$\dot{r}_L = - x_i \, r \cdot \frac{\dot{\bar{L}}_2}{\bar{L}_2} \tag{3a}$$

Case (i)	Parameter held constant	x_i
1	N_v	0
2	N	1/3
3	f_3	1

(3b)

Differentiating Eq. (1) with respect to time:

$$\frac{\dot{V}_v}{V_v} = \frac{\dot{N}_v}{N_v} + \frac{1}{3}\frac{\dot{r}}{r} \tag{4}$$

Substituting Eq. (2) into Eq. (4), we can separate the overall swelling rate into two components — $\dot{V}_{vp}$, which includes only the pressure-driven pore growth rate, $\dot{r}_p$, and $\dot{V}_{vL}$, which includes only rates related to pore coalescence:

$$\dot{V}_v = V_v \left[\frac{\dot{r}_p}{3r} + \left(\frac{\dot{N}_v}{N_v} + \frac{\dot{r}_L}{3r} \right) \right] \tag{5a}$$

$$= V_v \left(\frac{\dot{r}_p}{3r} \right) + V_v \left(\frac{\dot{N}_v}{N_v} + \frac{\dot{r}_L}{3r} \right) \tag{5b}$$

$$\equiv \dot{V}_{VP} + \dot{V}_{VL} \qquad (5c)$$

The coalescence component of the overall swelling rate, $\dot{V}_{VL}$, can be simplified for the three limiting microstructural trajectories: constant N_V, N and f_3. To do this, we substitute Eq. (3) and the results of App. 2 into Eq. (6):

A8-1.1 For a constant-N_V trajectory:

$$\dot{r}_L = 0 \text{ and } \dot{N}_V \equiv 0 \qquad (7a,b)$$

so, from Eq. (6): $\dot{V}_{VL} = 0 \qquad (8)$

A8-1.2 For constant N ($N = N^*$):

From Eq. (3): $$\dot{r}_L = \frac{r}{3} \cdot \frac{\dot{\bar{L}}_2}{\bar{L}_2} \qquad (9)$$

from App. 2's Eq. (9):

$$N_V = 2 N^* \bar{L}_2^{-1} \qquad (10)$$

from which:

$$\dot{N}_V = -2 N^* \bar{L}_2^{-2} \dot{\bar{L}}_2 \qquad (11)$$

so, from Eq. (6): $$\frac{\dot{V}_{VL}}{V_V} = -\frac{8}{9} \frac{\dot{\bar{L}}_2}{\bar{L}_2} \qquad (12)$$

This term is negative, because, in equation (5), $(\dot{N}_v/N_v)$ is negative and larger than $(\dot{r}_L/3r)$.

A8-1.3 For constant f_3 ($f_3 = f_3^*$):

From Eq. (3):
$$\dot{r}_L = r \cdot \frac{\dot{\bar{L}}_2}{\bar{L}_2} \tag{13}$$

From App. 2's Eq. (12):
$$N_v = c_1 f_3^* \bar{L}_2^{-3} \tag{14}$$

from which:
$$\dot{N}_v = -3\, c_1 f_3^* \bar{L}_2^{-4}\, \dot{\bar{L}}_2 \tag{15}$$

so, from Eq. (6):
$$\frac{\dot{V}_{vL}}{V_v} = -\frac{8}{3}\frac{\dot{\bar{L}}_2}{\bar{L}_2} \tag{16}$$

Following Eq. (3), we can summarize Eqs. (8), (12) and (16) as:
$$\frac{\dot{V}_{vL}}{V_v} = y_1 \cdot \frac{\dot{\bar{L}}_2}{\bar{L}_2} \tag{17}$$

Case (ℓ)	Parameter held constant	y_1
1	N_V	0
2	N	- 8/9
3	f_3	- 8/3

The coalescence component of the swelling rate is never positive and nonzero.

We will now use these results to develop equations for calculating P_{eff} and P_{int} from experimental data. From the swelling model (section 3.3), the pressure-driven component of the pore growth rate is:

$$\dot{r}_P = \beta \frac{\delta D_B \Omega}{4\pi r^2 kT} B_3\{V_V\} \cdot P_{eff} \qquad (18)$$

in which:

$$B_3\{V_V\} = \left(\frac{2\pi(1-V_V^{2/3})}{(1+V_V^{2/3})\ \ln(V_V^{-1/3}) - (1-V_V^{2/3})} \right) \qquad (19)$$

Rearranging Eq. (16), and using Eqs. (4) and (6):[1]

[1] While we develop only the case $n = 1$, in $\dot{r}_P \propto DF^n$, the relations readily can be modified for general n (Hsu and

$$P_{eff} = \frac{4\pi kT}{\beta\delta D_B \Omega} \frac{r^2}{B_3\{V_V\}} \dot{r}_P \qquad (20a)$$

$$= \frac{12\pi kT}{\beta\delta D_B \Omega} \frac{r^3}{V_V \cdot B_3\{V_V\}} \dot{V}_{VP} \qquad (20b)$$

$$= \frac{12\pi kT}{\beta\delta D_B \Omega} \frac{r^3}{V_V \cdot B_3\{V_V\}} \left(\dot{V}_V + |y_1| \frac{\dot{\bar{L}}_2}{\bar{L}_2} \right) \qquad (20c)$$

The mean pore radius can be calculated from experimental data by (App. 6, Eq. 4):

$$r = \left(\frac{3}{2\pi}\right)^{1/2} \left(\frac{V_V}{N_A} \right)^{1/2} \qquad (21)$$

When this is substituted into Eq. (20c):

$$P_{eff} = \phi_1 \cdot \frac{V_V^{1/2}}{B_3\{V_V\} \cdot N_A^{3/2}} \left(\dot{V}_V + |y_1| \frac{\dot{\bar{L}}_2}{\bar{L}_2} \right) \qquad (22a)$$

where $$\phi_1 = 9\left(\frac{6}{\pi}\right)^{1/2} \frac{kT}{\beta\delta D_B \Omega} \qquad (22b)$$

Of the experimental parameters required, all but $N_A\{t\}$ are smooth and monotonic (Chs. 4,5). The area number density, N_A, on the

---

Solomon, 1983).

other hand, increases sharply early in swelling, passes through a maximum, then decreases more slowly (Figs. 4-6,5-5). So, early in swelling, N_A and P_{eff} will be uncertain.

The *internal* pore pressure, P_{int} (rather than the effective pressure, P_{eff}) can be calculated from (section 3.3):

$$P_{int} = P_{eff} - P_{cap} - P_{app} \tag{23}$$

in which, for spherical-tetrahedral pores, from App. 3 and Eq. (21):

$$P_{cap} = 2\, g(\psi)\, \frac{\gamma_s}{r} \tag{24a}$$

$$= 2\left(\frac{2\pi}{3}\right)^{1/2} g(\psi)\, \gamma_s \left(\frac{N_A}{V_v}\right)^{1/2} \tag{24b}$$

P_{app} is a known, applied external pressure.

A8-2 Variables

All variables are defined in section 3.7, except for the following:

ϕ_1 Constant introduced to simplify Eq. (20).

y_1 Dimensionless, trajectory-specific multiplier; [-]

Appendix 9

Grain boundary mobility

In this section we relate 'intrinsic' grain boundary mobility, M_B, in the swelling model's phenomenological grain growth equations, to experimental grain growth kinetics. Variables are listed in section A9-2.

A9-1 Analysis

Phenomenological pore drag models include an effective boundary mobility, M_B^{eff} (e.g. Yan et al.'s (1977) Eq. 22; Ch.3):

$$M_B^{eff} = \frac{M_P}{N + (M_P / M_B)} \qquad (1)$$

The boundary mobility of the pore-free matrix, M_B, can be eliminated by assuming pore drag control (*pdc*; e.g. Yan et al., 1980, p.6):[1]

---

[1] We retained M_B and the potential for mixed control of grain

$$M_B^{eff}(pdc) \equiv M_p/N \qquad (2)$$

Such an assumption permits an analytic solution to be generated for the two differential equations for microstructural evolution — pore and grain growth rates.

In the current swelling model, however, we retain mixed control, and so retain M_B in M_B^{eff}. (The system evolved towards pore drag control, but we did not impose that control.) For the general case of *non*parabolic grain growth for the pore-free matrix (App. 8, Table A8-1), M_B is defined as the ratio of mean boundary velocity to global driving pressure (Yan et al., 1977):

$$M_B \equiv \frac{v_B}{\bar{P}_B} \qquad (2)$$

It is not constant, but depends on grain size, as follows. For grain growth kinetics based on the mean linear intercept:

$$\Delta_L^m \equiv \bar{L}_2^m - \bar{L}_2^{o\,m} \qquad (3a)$$

---

growth in order to develop a *general* numerical model which could be applied in ongoing research programs. For example, if independent control of porosity and grain size is sought by pressure anneals (Ch.7), the polycrystal may spend extended periods under M_B control at high temperature. In such cases, predictions of microstructural evolution may be inaccurate if grain growth rates are assumed to be controlled by pore drag (Fig. 5-2).

$$= K_L\{m\} \cdot t \qquad (3b)$$

the experimental rate constant $K_L\{m\}$ and exponent m are determined by a linear regression of Δ_L^m against time. Yan et al. (1977) define boundary mobility for such general kinetics as:[2,3]

$$M_{B,L} \equiv \frac{K_L\{m\}}{m\,\gamma_B\,\bar{L}_2^{\,m-2}} \qquad (4)$$

The form of the right hand side of Eq. (4) arises from Yan et al.'s (1977) Eqs. (39, 30, 31, and 34), as follows. Substitute, into the right hand side of Eq. (2), the corresponding expressions from the swelling model (Ch. 3):[4]

---

[2] We have written this equation in terms of $\bar{L}_2$, instead of the $\bar{G}$ which they used.

[3] We distinguish grain size defined as mean linear intercept, $\bar{L}_2$, from the corresponding 'spherical' measure, $\bar{G} \equiv 1.5\,\bar{L}_2$ (Fullman, 1953; Yan et al., 1977), because many of the parameters used in this section have values specific to the grain size basis: $K_x\{m\}$, M_{Bx}, a_x, a_{1x}; x = L or G, i = 1,2. The exponent m and activation energy Q_K (below) are *in*dependent of the basis.

[4] From $\bar{G} \equiv 1.5\,\bar{L}_2$, the values of a_x, a_{1x} and a_{2x} for different grain size bases ($\bar{L}_2$ or $\bar{G}$; x = L or G) are related:

$$a_{1G} = 1.5\,a_{1L}, \quad i = 1,2 \qquad (f1a)$$

$$a_G = (1.5)^2 \cdot a_L \qquad (f1b)$$

$$v_B \equiv \dot{\bar{L}}_2 / a_{2L} \tag{5}$$

and

$$\bar{P}_B \equiv a_{1L} \gamma_B / \bar{L}_2 \tag{6}$$

We discuss the proportionality constants a_{1L} and a_{2L} in App. 10. With this substitution, Eq. (2) becomes:

$$M_B \equiv \bar{L}_2 \cdot \dot{\bar{L}}_2 / a_L \gamma_B \tag{7a}$$

in which

$$a_L \equiv a_{1L} \cdot a_{2L} \tag{7b}$$

When $a_L = 1$, then by setting Eq. (4) equal to Eq. (7a), we recover Eq. (3).

Yan et al. (1977, p.292-4) use $\bar{G}$ as the grain size, set $a_G \equiv 1$, and then omit that factor in their subsequent discussion. However, because a_x (x = L,G) need not in general have this value (App. 10),[5] we retain it explicitly, and redefine (compare to Eq. 4):[6]

---

[5] While the range of possible values for the geometrical parameter a_{2x} is limited, a_{1x} can be reduced to very small values by narrowing the size distribution in the polycrystal (e.g. by sintering a monodisperse powder compact).

[6] In their review, Yan et al. (1977) give more complicated forms for different M_B mechanisms. Yan et al. (1983) and Handwerker et al. (1984) work with a more complicated expression for

$$M_{BL} \equiv \frac{K_L\{m\}}{a_L m \gamma_B \bar{L}_2^{m-2}} \qquad (8)$$

For arbitrary a_L, we set Eq. (8) equal to Eq. (7a) to recover Eq. (3).

From Eqs. (4) and (8), M_{Bx} (x = L,G) is *in*dependent of grain size only when $m = 2$.[7] In typical engineering materials, this is not the case (Brook, 1976). In such materials, $m > 2$, and, for a given set of $\{\bar{L}_2\text{-}t\}$ or $\{\bar{G}\text{-}t\}$ grain growth data, M_{Bx} will decrease as grain growth proceeds.[8]

When temperature-dependent values of M_B are sought for a system or composition for which no grain growth data are available (for

---

impurity drag controlled M_B.

[7] Using a grain size-*in*dependent $M_{Bx}\{T\}$:

$$M_{Bx}\{T\} = M^o_{Bx} \cdot exp\ \{ -Q/RT \} \qquad (f2a)$$

with

$$M^o_{BG} = (1.5)^2 \cdot M^o_{BL} \qquad (f2b)$$

is equivalent to assuming $m = 2$ for the pore-free matrix (App. 8).

[8] Mean grain sizes increase by factors of three to four in typical grain growth experiments (Mocellin and Kingery, 1973; Bennison and Harmer, 1985b); for an m of three, M_B would decrease by corresponding factors in such experiments.

the pore-free matrix) Yan et al.'s (1977) *normalized* Fig. 8[9] could be used to estimate the pre-exponential and activation energy in a K_x (x = L,G) for Eq. (8), in which:[10]

$$K_L\{m,T\} \equiv K_L^o\{m\}\cdot exp\{ -Q_K/RT \} \qquad (9)$$

However, in order to do this, we need to deal with their a_G, γ_B and $\bar{G}$ normalizations. From the intercept and slope of an $\tilde{M}_{BG}$ line in their figure, we can convert back to an approximate $K_G^o\{m,T\}$:

$$\tilde{M}_{BG}\{T\} = \tilde{M}_{BG}^o \cdot exp\{ -Q_K/RT \} \qquad (10)$$

$$\equiv \left(\frac{K_G^o\{m\}}{a_G^{*m}\, \gamma_B^{*}\, (\bar{G}^{*})^{m-2}} \right) exp\{ -Q_K/RT \} \qquad (11)$$

Their normalizing parameters have the values $a_G^* = 1$, $\gamma_B^* = 0.3$ J/m^2 and $\bar{G}^* = 90$ μm). Their figure includes no m information — a reasonable value will have to be estimated. However, Q_K can be estimated from that figure, and should be consistent with the activation energy of the original grain growth data, because Yan et al. (1977) normalize by a temperature-*in*dependent $\bar{G}$.

---

[9] See App. 15's Fig. A15-1d.

[10] K_x's temperature dependence is far more significant than γ_B's (Davidge, 1979, p.77). Also, from $\bar{G} \equiv 1.5\ \bar{L}_2$:

$$K_G^o\{m\} = (1.5)^m \cdot K_L^o\{m\} \qquad (f3)$$

When possible, however, it is best to use *original* $\Delta_L^m(T)$ grain growth data, to get m, $K_x(m,T)$ and Q_K. If m and $K_x(m,T)$ are available, but the activation energy, Q_K, is not, it can be estimated (as we did in this work) from theoretical arguments for mechanisms implied by experimental m, using corresponding diffusion data (Ch. 4 and Apps. 8,15). Alternatively, if Yan et al.'s (1977) Fig. 8 contains data for a similar material tc the one in question, Q_K can be calculated from that figure. Despite the comment in the previous paragraph, however, some of the plotted data are for systems with second phase (e.g. pore) drag, and the activation energies in such cases can*not* be asssumed to apply to the pore-free matrix.

A9-2 Variables

a_{ix}, $(i = 1,2;\ x = L,G)$ proportionality constants; [-]

Δ_L^m differential grain size; [m^m/s]

$\bar{G}$ equivalent 'spherical' grain diameter; [m]

γ_B mean energy of grain boundaries; [J/m^2]

K_x experimental rate constant for grain growth; [m^m/s]

$\bar{L}_2$ mean linear intercept on a random polish plane; [m]

m grain growth exponent; [-]

M_B intrinsic grain boundary mobility; [$m^3/N\cdot s$]

M_B^{eff} effective boundary mobility; [$m^3/N\cdot s$]

N area number density of pores on grain boundaries; [m^{-2}]

$\bar{P}_B$ mean boundary driving pressure; [N/m^2]

Q_K activation energy for the grain growth rate constant, K_x; [J/mol·deg]

v_B global boundary velocity; [m/s]

Sub/Superscripts:

x L or G, denoting grain size as $\bar{L}_2$ or as $\bar{G} = 1.5w$

o pre-exponential or initial value

$*$ normalizing parameters in Yan et al.'s (1977) Fig. 8.

$\sim$ normalized parameter

Appendix 10

Boundary driving pressure, $\bar{P}_B$, as a function of grain size, $\bar{L}_2$

In this section we establish an approximate value for $\bar{P}_B$ for normal grain growth, in terms of the mean linear intercept grain size ($\bar{L}_2$). Variables are listed in section A10-2.

A10-1 Analysis

The simplest possible relation for the global boundary pressure which drives normal grain growth (Ashby, 1980), expresses it in terms of the mean grain size (Yan et al., 1977, Eq. 34):

$$\bar{P}_B = \bar{P}_B\{\bar{L}_2\} \qquad (1)$$

The grain size *dispersion*, which also should be a factor, effectively is included in Eq. (1), in an approximate way, by assuming a stationary grain size distribution typical of normal grain growth (Hillert, 1965).

Hillert's (1965) rate equation for steady state, normal grain

growth is:

$$\frac{d}{dt}\left(R_{cr}^{2}\right) = (\alpha/2)\,\gamma_B\,M_B \qquad (2)$$

where γ_B is the mean grain boundary energy, and M_B is the mean grain boundary mobility, and for a three dimensional microstructure:

$$R_{cr} = (9/8)\,\bar{R} \qquad (3)$$

R_{cr} is the (equivalent spherical) grain size for which $\bar{\kappa}_{gn}$, the average curvature per grain which is available to drive grain growth (Srolovitz et al., 1984) is zero.[1]

From Eqs. (1) and (2), using an intrinsic boundary mobility for

---

[1] The dimensionless parameter α arises when Hillert (1965) chooses the simplest possible form for an expression for the product, $g\cdot\bar{\kappa}_{gn}$. This value is difficult to estimate for a real microstructure: averaged over all grains in the size class of radius R:

$$g\{R\}\cdot\bar{\kappa}_{gn}\{R\} = \alpha\,(\,1/R_{cr} - 1/R\,) \qquad (f1a)$$

where g, defined by:

$$\dot{R} \equiv g\cdot\bar{v}_{gn}\{R\} \qquad (f1b)$$

relates $\bar{v}_{gn}\{R\}$, the grain boundary velocity averaged around a grain of the size class R, to the rate of grain growth for that class.

the single-phase polycrystal, M_B:

$$\dot{R}_{cr} = (\alpha/2)\ (\ M_B\ \gamma_B\ /\ 2\ R_{cr}) \qquad (4)$$

$$\dot{\bar{R}} = (8/9)^2(\alpha/4)\ \gamma_B\ M_B\ /\ \bar{R}$$

Using a value for α of 1, for a three-dimensional microstructure (Hillert, 1965):

$$\dot{\bar{R}} = 0.20\ \gamma_B\ M_B/\ \bar{R} \qquad (5)$$

We convert Eq. (5) to an equation based on $\bar{L}_2$ in two ways. For the first, we use the ideal, equi-S_V microstructure described in App. 1. The ideal grain size, R_o, giving ideal and real microstructures the same specific grain boundary area is:

$$R_o = \bar{L}_2\ /\ 1.379 \qquad (6)$$

We take $\bar{R}$ to be the radius of the sphere whose volume is equal to that of the unit grain in the ideal microstructure, r_s (App. 1; Hillert, 1965):

$$\bar{R} = r_s = 1.137\ R_o \qquad (7)$$

From Eqs. (6) and (7):

$$\bar{R} = 1.137\ (\ \bar{L}_2\ /\ 1.379\ )$$

$$= 0.825\ \bar{L}_2 \qquad (8)$$

Substituting Eq. (8) into Eq. (5):

$$\dot{\bar{L}}_2 = 0.29\ \gamma_B M_B / \bar{L}_2 \qquad (9)$$

Referring to Eqs. (39) to Eq. (43) in the swelling model:

$$\dot{\bar{L}}_2 = a_L\ \gamma_B M_B / \bar{L}_2 \qquad (10)$$

from which, from Eq. (9), the proportionlaity constant, a_L is:

$$a_L \approx 0.3 \qquad (11)$$

For comparison, we generate a second estimate for a_L by following Yan et al. (1977, p. 292), and substituting $\bar{G} = 2 \cdot \bar{R}$ into Eq. (5), rather than the r_s used above:

$$\dot{\bar{G}} = 0.79\ \gamma_B M_B / \bar{G} \qquad (12)$$

the proportionality constant, a_G, has a value somewhat less than the $a_G = 1$ given, with no derivation, by Yan et al. (1977, Eq. 34). If we then substitute the standard $\bar{G} = 1.5\ \bar{L}_2$ (Fullman, 1953; Yan et al., 1977, p.292) into Eq. (12), we get (compare with Eq. 11):[2]

$$a_L \approx 0.35 \qquad (13)$$

The proportionality factor a_x (x = L,G) is the product of two

---

[2] Effectively, instead of Eq. (8), we've substituted:

$$\dot{\bar{R}} = \dot{\bar{G}}/2 = 0.75\ \dot{\bar{L}}_2 \qquad (f2)$$

separate factors (Ch.3, Eq. 40), the values of which depend on the grain size basis ($\bar{G}$ or $\bar{L}_2$: App. 9). For $\bar{L}_2$ as the grain size:

$$a_L \equiv a_{1L} \cdot a_{2L} \tag{14}$$

If we accept Yan et al.'s (1977: Eq. 30) $a_{2G} \approx 2$, and use the a_{1x} relations given in App. 9, we get $a_{2L} \approx 1.33$. Then, from Eqs. (11, 13 and 14), we calculate:

$$a_{1L} \equiv a_L / a_{2L} \tag{15a}$$

$$\approx \{0.3 \text{ to } 0.35\}/1.33$$

$$\approx 0.23 \text{ to } 0.26 \tag{15b}$$

Yan et al.'s (1977) a_L of 0.44 is equivalent to an a_{1L} of 0.33.

Yan et al. (1977) note that the density of grain boundary energy is:

$$\hat{P}_B = \gamma_B \cdot S_V \tag{16a}$$

$$= 2 \gamma_B / \bar{L}_2 \tag{16b}$$

From Eqs. (15b) and (16b), about one eighth of the boundary energy density is available to drive normal grain growth. Yan et al. (1977) estimate a factor of one sixth.

The global driving pressure should depend on the grain size

dispersion, as well as on the mean grain size. Zhao and Harmer (1988a,b) estimate such a relation as:

$$\bar{P}_B = \frac{c\gamma_B}{\bar{G}} \left(1 - \frac{\bar{G}}{\hat{G}} \right) \tag{17}$$

For normal grain growth, $c = 1.25$ (Yan et al., 1977), and for a steady state grain size distribution (Hillert, 1965):

$$\bar{R}/\hat{R} = 0.56 \tag{18}$$

Substituting Eq. (18), $(\bar{G}/\hat{G})$ for $(\bar{R}/\hat{R})$, and $\bar{G} = 1.5\ \bar{L}_2$ into Eq. (17) gives:

$$\bar{P}_B \approx \frac{1.25\ \gamma_B}{1.5\ \bar{L}_2} \left(1 - 0.56 \right) \tag{19a}$$

$$\approx \frac{0.37\ \gamma_B}{\bar{L}_2} \tag{19b}$$

from which:

$$a_{1L} \approx 0.37 \tag{21}$$

This value is somewhat larger than the range of 0.23-0.26 estimated previously, but is closer to Yan et al.'s 0.33. When grain growth is controlled largely by pore drag, uncertainties of this order in a_x will be outweighed by uncertainties in ωD_s. (Particularly when accurate grain growth data are available for the pore-free matrix (App. 9), the surface diffusion coefficient will be the parameter whose value is most directly affected; Ch.6, App. 17).

Global mean curvatures of a three-dimensional structure — such as a grain boundary network — can be determined *directly* from experimental polish plane data (DeHoff and Rhines, 1968, Ch. 10: esp. pp.322-3). It now should be possible to determine *experimentally* the boundary driving pressures in polycrystals, using image analysis systems.

The numerical results in Ch.5 were generated with an a_L value of 0.3, as in Eq. (11), above (Table 5-1).

A10-2 Variables

a_{ix}, (i = 1,2; x = L,G) proportionality constants; [-]

α dimensionless parameter in Hillert (1965); [-]

c proportionality factor; [-]

γ_B mean energy of grain boundaries; [J/m^2]

g dimensionless parameter in Hillert (1965); [-]

$\bar{G}$ equivalent 'spherical' grain diameter; [m]

$\hat{G}$ maximum grain size; [m]

$\bar{\kappa}_{gn}$ mean boundary curvature of a grain; [m^{-1}]

$\bar{L}_2$ mean linear intercept on a random polish plane; [m]

M_B intrinsic grain boundary mobility; [$m^3/N \cdot s$]

$\bar{P}_B$ mean boundary driving pressure; [N/m^2]

$\hat{P}_B$ boundary driving pressure density; [N/m^2]

$\bar{R}$ equivalent spherical grain radius; [m]

$\hat{R}$ maximum grain size; [m]

R_{cr} R for which $\bar{\kappa}_{gn} \rightarrow 0$ (Hillert, 1965); [m]

R_o grain size in the ideal, truncated-octahedral microstructure (App. 1.1); [m]

r_s radius of spherical grain with same volume as ideal grain; [m]

S_v specific grain boundary area; [m^2/m^3]

Appendix 11

Phenomenological pore drag and separation

Phenomenological drag analyses in sintering typically mark, on a grain size/pore size diagram, a field within which pores should separate from sweeping grain boundaries (e.g. Carpay, 1977). Pore drag control often is assumed, and limiting-case coalescence rates (unsupported by experimental data, e.g. $f_3 = 1$).

In this section, we extend grain size/pore size diagrams for phenomenological drag by developing equations for *arbitrary contours* for *two* summary descriptors of an evolving porous microstructure. These are (1) $\tilde{v}_p$, the pore velocity, normalized by the velocity at separation,[1] and (2) $\tilde{M}_B^{eff}$, the effective

---

[1] In App. 12, we develop expressions for $\hat{v}_p$, the *non*-phenomenological pore velocity at separation. It is normalized by the phenomenological separation velocity of a (spherical) pore of the same volume, and can take values greater than one. The normalized pore velocity developed in *this* appendix, $\tilde{v}_p$, is the phenomenological pore velocity divided by the phenomenological separation velocity.

boundary mobility, normalized by the intrinsic boundary mobility, M_B (App. 9).[2]

At separation, $\tilde{v}_p$ has a value of one. However, the phenomenological analysis is approximate, and, based on work in App. 12, we permit $\tilde{v}_p$ to take values greater than one. In this section, we show that $\tilde{M}_B^{eff}$ is equal to $\tilde{P}_B^{eff}$, the normalized boundary driving pressure; that is, that this parameter is a general pore drag index.

The equations we develop for these two families of contours are for the current swelling analysis, for a general experimentally-determined boundary mobility, M_B, and for both constant-N and constant-f_3 paths. (A porous microstructure would have a constant-N_v path only if little or no grain growth occurred, so drag and separation are not issues for such a path.)

We do not plot the results at this time. However, the analysis given here leads to plots in which both families of contours are drawn on diagrams with grain size *vs* pore size axes, and experimental swelling (or pressure sintering) paths for real

---

[2] A third set of contours would be potentially useful: those for $\tilde{M}_2^{-1}$, the ratio of M_B^{eff} for a microstructure at a given time, for pore drag control, to that for mixed M_B/pore drag control (see Fig. 5-6). This ratio relates to whether pore drag control can be assumed.

materials are superimposed. Such plots would permit testing whether, in real microstructures, $\tilde{v}_p$ exceed values of one. Diagrams with families of contours would give better bases for evaluating how closely a given sintering or heat treating schedule approaches separation, and why, than current diagrams.[3]

Variables are listed in section A11-5.

A11-1 Pore drag, as a function of normalized pore velocity

In this section we develop the basic equations for the phenomenological drag formulation, explicitly showing the relation between pore drag, boundary contact angle, and normalized pore velocity. We use many of these relations in the subsequent two sections, in which we develop the expressions for $\tilde{M}_B^{eff}$ and $\tilde{v}_p$ contours on swelling or sintering diagrams. Previously, drag relations have been developed for limited cases of microstructural evolution, including constant-N_v (Carpay, 1977) and specific constant-f_3 cases (Carpay, 1977; Brook, 1976;

---

[3] Detailed diagrams have been drawn for more complicated forms for M_B, and for distributions in pore and grain size (Yan et al., 1983; Handwerker et al., 1984; Zhao and Harmer, 1988a). While promising, these are, as yet, unsupported by experimental data. The current analysis is explicitly framed for the experimental M_B data which would be the first generated for a new material.

Yan et al., 1980).

We use Heuer's (1979) notation for the phenomenological boundary intersection angle θ (Fig. A11-1), but Ashby's (1980) boundary driving *pressure* $\bar{P}_B$ [N/m^2] instead of a driving *force* F_B [N] per atom or $\Omega^{2/3}$ [m^2] on the grain boundary, (Carpay, 1977; Heuer, 1979; and Hsueh et al., 1982).

The phenomenological force [N] exerted by the sweeping grain boundary on an attached (rigid, spherical) pore is (Heuer's (1979) notation):

$$F_{PX} = 2\pi\, r\, \gamma_B \cdot \cos\theta \cdot \sin\theta \qquad (1a)$$

$$= \pi\, r\, \gamma_B \cdot \sin\{2\theta\} \qquad (1b)$$

From this, $$\hat{F}_{PX} = \pi\, r\, \gamma_B \qquad (2)$$

at $$\hat{\theta} = \pi/4 \quad \text{(radians)} \qquad (3)$$

where the 'hat' denotes the maximum value; i.e. the value *at pore separation.*

Defining mean pore and boundary velocities[4] as force- and pressure-mobility products respectively (Carpay, 1977; Brook,

---

[4] In the following text, boundary (v_B) and pore (v_p) velocities are global means; however, for clarity, for these variables, the implied superscript bars are *not* shown.

1969):

$$v_P \equiv F_{PX} \cdot M_P \tag{4}$$

The global boundary velocity can be expressed as two equivalent products (Brook, 1976): (1) a driving pressure which is unchanged by pore drag, times an effective boundary mobility, reduced by pore drag, or (2) an effective driving pressure, reduced by pore drag, times a boundary mobility which is unchanged by pore drag:

$$v_B \equiv \bar{P}_B \cdot M_B^{eff} = P_B^{eff} \cdot M_B \tag{5}$$

We write global boundary pressure and velocity for normal grain growth as (Ch.3; Apps. 9 and 10):[5]

$$v_B \equiv \dot{\bar{L}}_2 / a_{2L} \tag{6}$$

and

$$\bar{P}_B \equiv a_{1L} \gamma_B / \bar{L}_2 \tag{7}$$

The *effective* boundary mobility and driving pressure are (Brook, 1976):

$$M_B^{eff} \equiv \frac{M_P}{N + (M_P/M_B)} \tag{8}$$

---

[5] Values of a_i (i=1,2) are specific to $\bar{L}_2$ as the grain size measure (see App. 9).

and, as $F_{Px} = F_D$:

$$P_B^{eff} = \bar{P}_B - N \cdot F_D \tag{9}$$

We define a normalized pore velocity as:[6]

$$\tilde{v}_p = \frac{v_p}{\hat{v}_p^o} \tag{10}$$

where $\hat{v}_p^o$ is the maximum *phenomenological* pore velocity (Hsueh et al., 1982).

We can regard normalized, effective, boundary driving pressure and boundary mobility as dimensionless measures of pore drag (Carpay, 1977):

$$\tilde{P}_B^{eff} \equiv P_B^{eff} / \bar{P}_B \tag{11}$$

and

$$\tilde{M}_B^{eff} \equiv M_B^{eff} / M_B \tag{12}$$

in which $\bar{P}_B$ and M_B are the values for the equivalent pore-*free* system. From Eqs. (5, 11 and 12), these drag measures are equal:

---

[6] In App. 12, we discuss Hsueh et al.'s (1982) prediction that $\tilde{v}_p > 1$ at separation. In the following discussion, which is strictly within the conventional $\tilde{v}_p \leq 1$ limit, inconsistencies arise for $\tilde{v}_p > 1$.

$$\tilde{P}_B^{eff} = \tilde{M}_B^{eff} \tag{13}$$

For attached pores:[7]

$$v_P \equiv v_B \tag{14}$$

Substituting into Eq. (14) from Eqs. (4 and 5), and noting that both the boundary's force on a pore, and the pore drag are functions of the pore velocity:

$$F_{PX}\{v_P\} \cdot M_P = \bar{P}_B \cdot M_B^{eff}\{v_P\} \tag{15}$$

From Eqs. (1b, 7 and 8), this is equivalent to:

$$\pi r \gamma_B \sin\{2\theta\} = \frac{a_{1L}\gamma_B}{\bar{L}_2} \cdot \frac{M_B}{M_P + N \cdot M_B} \tag{16}$$

The boundary contact angle, θ, is (Fig. A11-1):

$$\theta = 0.5 \sin^{-1}\{ \mathcal{T} \} \tag{17}$$

in which the dimensionless parameter $\mathcal{T}$ is given by:

$$\mathcal{T} \equiv \frac{a_1}{\pi r \bar{L}_2} \cdot \frac{M_B}{M_P + N \cdot M_B} \tag{18}$$

From Eq. (3), we define a normalized boundary contact angle as:

---

[7] This can be regarded as global or local.

$$\tilde{\theta} \equiv \theta / \hat{\theta} \tag{19a}$$

$$= \frac{2}{\pi} \sin^{-1}_{rad} \{ \mathcal{T} \} \tag{19b}$$[8]

From Eqs. (1b, 2 and 4) the normalized pore velocity is:

$$\tilde{\upsilon}_P \equiv \sin \{2\theta\} = \mathcal{T} \tag{20}$$

and so the normalized boundary contact angle is:

$$\tilde{\theta} \equiv \frac{2}{\pi} \sin^{-1}_{rad} \{ \tilde{\upsilon}_P \} \tag{21}$$

For steady pore velocity; i.e. $\dot{\upsilon}_P = 0$:

$$F_{Px} = F_D \tag{22}$$

so normalized drag force and boundary/pore forces are equal:

$$\tilde{F}_D = \frac{F_{Px}}{\hat{F}_{Px}} \equiv \tilde{F}_P \tag{23a}$$

and, from Eqs. (1b, 2):

$$\tilde{F}_D = \sin 2\theta \tag{23b}$$

From Eqs. (20, 23), the normalized drag force and normalized pore

---

[8] For the given $(2/\pi)$ factor, the subscript specifies that the inverse sin return a value in *radians*. The factor would be 0.011 for a value returned in *degrees*.

velocity are equal:[9]

$$\tilde{F}_D = \tilde{\upsilon}_P \tag{24}$$

From Eqs. (6, 9):

$$P_B^{eff} = \bar{P}_B - N \cdot \hat{F}_D \tilde{F}_D \tag{25a}$$

which, from Eq. (22, 23a) is:

$$P_B^{eff} = \bar{P}_B - N \cdot \hat{F}_D \cdot \tilde{\upsilon}_P \tag{25b}$$

and, from Eqs. (11, 13):

$$\tilde{M}_B^{eff} = \tilde{P}_B^{eff} = 1 - \left(\frac{N \cdot \hat{F}_D}{\bar{P}_B} \right) \tilde{\upsilon}_P \tag{26}$$

The normalized, effective boundary mobility and driving pressure, the dimensionless measures of pore drag, are linear in normalized pore velocity. From Eqs. (2, 7 and 22), the bracketed term in Eq. (26), i.e. the slope of a plot of $\tilde{\upsilon}_P$ *vs* $\tilde{P}_B^{eff}$ is:[10]

$$\text{Slope} = - \frac{N \cdot \hat{F}_D}{\bar{P}_B} \tag{27a}$$

$$= - \frac{\pi}{\bar{a}_{1L}} \cdot N \, r \, \bar{L}_2 \tag{27b}$$

---

[9] See footnote with Eq. (7), concerning $\tilde{\upsilon}_P \geq 1$.

[10] The slope is equal to (-1/Q), where Q is Brooks's (1969) parameter.

The slope was derived without assuming a specific M_P mechanism or form for M_B. It is independent of temperature, even though both M_B and M_P are temperature-dependent.

At phenomenological pore separation, $\tilde{\upsilon}_P \equiv 1$, and, from Eqs. (26 and 27b):

$$\tilde{M}_B^{eff} \longrightarrow \hat{\tilde{M}}_B^{eff} = 1 - \frac{\pi}{a_{1L}} \cdot N\, r\, \bar{L}_2 \qquad (28a)$$

$$= 1 - \left(\frac{N \cdot \hat{F}_D}{\bar{P}_B} \right) \qquad (28b)$$

A11-2 $\tilde{M}_B^{eff} = \tilde{P}_B^{eff}$ ('drag') contours on ($\bar{L}_2$-r) plots

The normalized, effective boundary driving pressure, $\tilde{M}_B^{eff}$, is relative to the boundary mobility of the equivalent, pore-free matrix. It, and the equivalent normalized, effective boundary driving pressure, $\tilde{P}_B^{eff}$, give dimensionless measures of how effectively phenomenological pore drag is retarding grain growth. As such, it is a useful descriptor of a porous microstructure undergoing grain growth.

A11-2.1 General

Simplifying the notation of Eqs. (8) and (12) for clarity, by replacing $\tilde{M}_B^{eff}$ with $\tilde{M}$:

$$\tilde{M} \equiv \tilde{M}_B^{eff} \equiv \frac{M_P}{M_P + N \cdot M_B} \tag{28a}$$

$$= \left(\frac{N \cdot M_B}{M_P} + 1 \right)^{-1} \tag{28b}$$

i.e. $$\frac{N \cdot M_B}{M_P} = \left(\tilde{M}^{-1} - 1 \right) \tag{29}$$

This is independent of an assumed M_p mechanism.

A general matrix boundary mobility, which uses experimental $\{t - \bar{L}_2\}$ grain growth data directly,

$$\bar{L}_2\{t\}^m - \bar{L}_2^{o\,m} = K_L\{m\} \cdot t \tag{30}$$

can be defined as (Yan et al., 1977; App. 9):

$$M_B\{m\} \equiv \frac{K_L\{m\}}{a_L m \gamma_B \bar{L}_2^{m-2}} \tag{31a}$$

$$\equiv \mu_o\{m\} \cdot \bar{L}_2^{2-m} \tag{31b}$$

where the parameter μ_o is defined as:

$$\mu_o \equiv \frac{K_L\{m\}}{a_L m \gamma_B} \tag{32}$$

A11-2.2 Case: Constant-N microstructural evolution

From Eq. (29):

$$M_P^{-1} = \frac{1}{N \cdot M_B}\left(\tilde{M}^{-1} - 1 \right) \tag{33}$$

which, for surface diffusion controlled M_P:

$$M_P \equiv \frac{\omega D_S \Omega}{\pi k T r^4} \tag{34}$$

gives:

$$r\{m\}\Big|_{\tilde{M},\bar{L}_2} = \left(\frac{\omega D_S \Omega}{\pi k T \; N \; \mu_o} \right)^{1/4} \left(\tilde{M}^{-1} - 1 \right)^{1/4} \bar{L}_2^{\left(\frac{m-2}{4}\right)} \tag{35}$$

For $m = 2$, this gives vertical (i.e. $\bar{L}_2$-independent) contours of $\tilde{M}$ on an ($\bar{L}_2$ - r) plot, which can be summarized as a single sigmoid curve, for a given temperature. However, for $m > 2$, M_B is grain size dependent. For example, for $m = 3$, and surface diffusion controlled pore mobility:

$$r\{m=3\}\Big|_{\tilde{M},\bar{L}_2} = \left(\frac{\omega D_S \Omega}{\pi k T \; N \; \mu_o} \right)^{1/4} \left(\tilde{M}^{-1} - 1 \right)^{1/4} \bar{L}_2^{1/4} \tag{36}$$

A11-2.3 Case: Constant-f_3 microstructural evolution

For attached pores at four grain junctions in an idealized, equi-S_V microstructure (App. 1):

$$N = N^{att} \tag{37a}$$

$$= N_V / S_V \tag{37b}$$

$$= \frac{f_3}{c_f \bar{L}_2^{\,2}} \quad , \quad c_f = 4.694 \tag{37c,d}$$

Substituting Eq. (37c) into (28a):

$$\tilde{M}\Big|_{\bar{L}_2, r} \equiv M_P\{r\} \left(\frac{f_3 M_B}{c_f \bar{L}_2^{\,2}} + M_P\{r\} \right)^{-1} \tag{38a}$$

$$= \frac{c_f M_P \bar{L}_2^{\,m}}{f_3 \mu_o + c_f M_P \bar{L}_2^{\,m}} \tag{38b}$$[11]

Substituting Eqs. (30b, 36c) into Eq. (29) and rearranging:

$$\bar{L}_2\Big|_{\tilde{M}, r} = \left(\frac{f_3 \mu_o}{c_f M_P\{r\}} \right)^{1/m} \left(\tilde{M}^{-1} - 1 \right)^{-1/m} \tag{39}$$

For *surface diffusion* controlled M_P (Eq. 33), $\tilde{M}$ contour on a grain size/ pore size plot follows:

---

[11] Two limiting cases exist: M_B control, for which:

$$f_3 \mu_o \ll c_f M_P \bar{L}_2^{\,m} \quad , \text{ so that } \quad \tilde{M} \approx 1 \tag{f1a}$$

and pore drag control, for which:

$$f_3 \mu_o \gg c_f M_P \bar{L}_2^{\,m} \quad , \text{ so that } \quad \tilde{M} \approx \frac{c_f M_P \bar{L}_2^{\,m}}{f_3 \mu_o} \tag{f1b}$$

These relations are independent of an assumed M_P mechanism.

$$r\Big|_{\tilde{M}} = \left(\frac{\omega D_s \Omega}{\pi k T} \frac{c_f \bar{L}_2^{\,m}}{f_3 \mu_o} \left(\tilde{M}^{-1} - 1 \right) \right)^{1/4} \qquad (40)$$

A11-3 $\tilde{\upsilon}_p$ contours on ($\bar{L}_2$ - r) plots

A11-3.1 General

From Eqs. (5-7):

$$\dot{\bar{L}}_2 = (a_L \gamma_B M_B^{eff}) / \bar{L}_2 \qquad (41)$$

where $$a_L = a_{1L} \cdot a_{2L} \qquad (42)$$

From Eqs. (2, 4, 6, 8, 10, 14, and 41):

$$\tilde{\upsilon}_p = \frac{a_{1L} \gamma_B}{\bar{L}_2} \frac{M_B^{eff}}{\hat{\upsilon}_p^o} \qquad (43a)$$

$$= \frac{a_{1L}}{\pi r} \left(\frac{\mu_o \bar{L}_2^{\,1-m}}{N \mu_o \bar{L}_2^{\,2-m} + M_p} \right) \qquad (43b)$$

which rearranges to give the general equation for an arbitrary $\tilde{\upsilon}_p$ contour:

$$\pi r \tilde{\upsilon}_p M_p \bar{L}_2^{\,m-1} + \pi r N \mu_o \tilde{\upsilon}_p \bar{L}_2 - a_{1L} \mu_o = 0 \qquad (44)$$

A11-3.1.1 Locus for $\tilde{v}_p \equiv 1$

The general locus for phenomenological pore separation is at $\tilde{v}_p \equiv 1$:[12]

$$\pi\, r\, M_p\, \bar{L}_2^{m-1} + \pi\, r\, N\, \mu_o\, \bar{L}_2 - a_{1L}\, \mu_o = 0 \qquad (45)$$

For $m = 3$, this locus is:

$$\pi\, r\, M_p\, \bar{L}_2^{2} + \pi\, r\, N\, \mu_o\, \bar{L}_2 - a_{1L}\, \mu_o = 0 \qquad (46)$$

Eq. (44) was derived without assuming either an M_p mechanism or a microstructural trajectory. For surface diffusion-controlled pore mobility, and $m = 3$:

$$\left(\pi\, N\, \mu_o\, \bar{L}_2 \right) r - a_{1L}\, \mu_o + \left(\frac{\omega D_s\, \Omega}{kT}\, \bar{L}_2^{2} \right) r^{-3} = 0 \qquad (47)$$

A11-3.2 Case: Constant-N microstructural evolution

Constant - $\tilde{v}_p\big|_N$ contours on an ($\bar{L}_2$ - r) plot can be calculated directly from Eq. (44), for an assumed M_p mechanism (e.g. for ωD_s control).

---

[12] Hsueh et al., (1982), for $\psi < \pi$ radians, predict steady state, two-grain facet pore velocities in excess of $\tilde{v}_p = 1$. A tentative separation field boundary may better be placed not at $\tilde{v}_p = 1$, but between $\tilde{v}_p = 1 - 3$ (App. 12).

A11-3.3 Case: Constant f_3 microstructural evolution

Substituting for N from Eq. (37b) into Eq. (44):

$$\pi\, r\, \tilde{\upsilon}_p\, M_p\, \bar{L}_2^{\,m} - a_{1L}\, \mu_o\, \bar{L}_2 + \pi\, c_f^{-1}\, f_3\, \mu_o\, \tilde{\upsilon}_p\, r = 0 \qquad (48)$$

A11-3.3.1 Locus for $\tilde{\upsilon}_p \equiv 1$

The general locus for phenomenological pore separation is at $\tilde{\upsilon}_p \equiv 1$:[13]

$$\pi\, r\, M_p\, \bar{L}_2^{\,m} - a_{1L}\, \mu_o\, \bar{L}_2 + \frac{\pi}{c_f}\, f_3\, \mu_o\, r = 0 \qquad (49)$$

For $m = 3$, this locus is:

$$\pi\, r\, M_p\, \bar{L}_2^{\,3} + \frac{\pi}{c_f}\, f_3\, \mu_o\, r\, \bar{L}_2 - a_{1L}\, \mu_o = 0 \qquad (50)$$

For surface diffusion-controlled pore mobility, and $m = 3$, it is:

$$\left(\frac{\pi}{c_f}\, f_3\, \mu_o\, \bar{L}_2 \right) r - a_{1L}\, \mu_o + \left(\frac{\omega D_s \Omega}{kT}\, \bar{L}_2^{\,3} \right) r^{-3} + = 0 \qquad (51)$$

---

[13] See previous footnote.

A11-4 Summary

1. Equations are developed for plotting, on grain size/pore size diagrams, families of contours at arbitrary values of:
   a) $\tilde{\upsilon}_p$, the pore velocity, normalized by the velocity at separation ($\tilde{\upsilon}_p = 1$ at phenomenological separation), and
   b) $\tilde{M}_B^{eff} = \tilde{P}_B^{eff}$, the effective boundary mobility, normalized by the intrinsic boundary mobility, M_B.
2. The equations are developed for constant-N and constant-f_J paths, and for a general, *m*- and grain size-*de*pendent M_B.
3. These two families of contours describe, in terms of the phenomenological theory of pore drag and separation, a porous microstructure which is undergoing simultaneous pore and grain growth, in which pore coalescence is occurring at specific rates, with respect to grain size.
4. No diagrams are plotted. When they are, they will permit experimentally testing phenomenological pore separation velocities.

A11-5 Variables

$a_{L,1L,2L}$ parameters in grain growth model which convert local to global parameters; $a_L = a_{1L} \cdot a_{2L}$; [-]

c_f numerical constant defined in Eqs. (22c,d)

D_S surface diffusion coefficient; [m^2/s]

f_3 fraction of four-grain junctions cavitated in ideal microstructure; [-]

F_D phenomenological drag force exerted on sweeping grain boundary by a pore; [N]

F_P, F_{Px} phenomenological force exerted on an attached pore by a sweeping grain boundary; [N]

γ_B mean energy of grain boundaries; [J/m^2]

k Boltzmann's constant; [1.381E-23 J/atom·K]

L contraction of $\bar{L}_2$; [-]

$\bar{L}_2$ mean linear intercept on a random polish plane in a real microstructure; [m]

$\tilde{M}$ contraction of $\tilde{M}_B^{eff}$; [-]

M_B global mobility of pore-free grain boundary (App. 9); [$m^3/N \cdot s$]

M_B^{eff} phenomenological effective grain boundary mobility with attached pores; [$m^3/N \cdot s$] = [$(m/s)/(N/m^2)$]

M_P phenomenological pore mobility; [(m/s)/N]

μ_o parameter introduced to simplify equations containing M_B; [$metres^{m+1}/N \cdot s$]

N number density of pores attached to grain boundaries; [m^{-2}]

N_V number of pores per unit volume solid; [m^{-3}]

$\tilde{v}_P$ the pore velocity normalized by the phenomemological pore velocity at separation; [-]

Ω atomic or molecular volume, or volume of controlling diffusing species (App. 15); [m^3]

$\bar{P}_B$ global average curvature pressure driving grain growth;

$[N/m^2]$

r radius of average spherical pore; [m]

S_V specific grain boundary area; $[m^2/m^3]$

$\mathcal{T}$ dimensionless factor defined in Eq. (5b); [-]

θ pore/boundary intersection angle; [rad] or [deg] $\bar{v}_B$ global grain boundary velocity; [m/s]

v_P pore velocity; [m/s]

$\tilde{v}_P$ the phenomenological pore velocity divided by the phenomenological separation velocity; [-]

v_P^o phenomenological (spherical) pore velocity; [m/s]

ω width for surface diffusion; [m]

Diacriticals

$\sim$ normalized value

$\hat{}$ maximum value

$-$ mean value

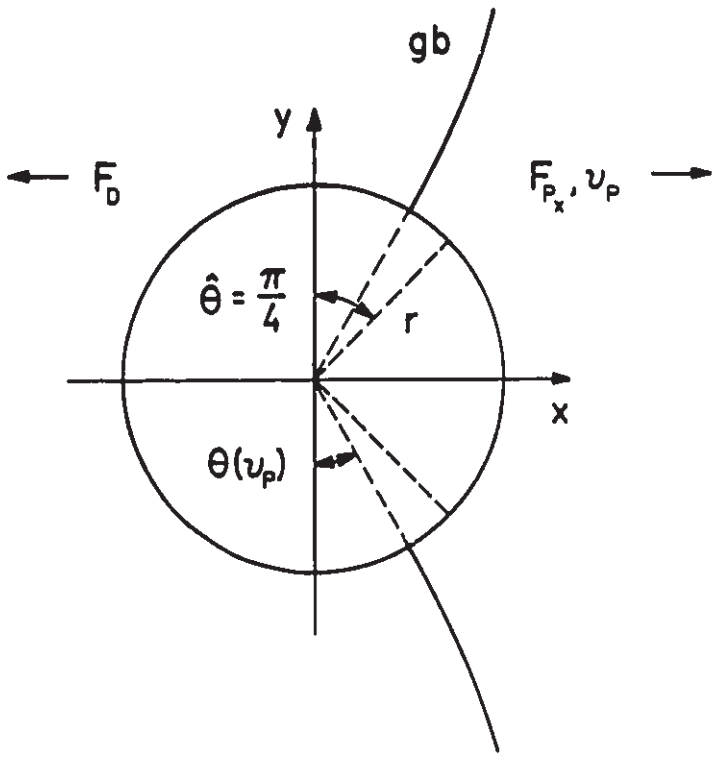

Fig. A11-1: A phenomenological pore attached to a sweeping two-grain boundary facet.

Appendix 12

Renormalization of the maximum, steady-state, surface diffusion controlled velocity of a *two-grain facet* pore with arbitrary dihedral angle

---

The approximations which make the phenomenological theory of pore drag and separation so physically unsatisfying are emphasized by Hsueh et al.'s (1982) analysis, in which a two-grain facet pore, with an arbitrary dihedral angle, distorts when it moves with a sweeping grain boundary. The analysis indicates that pores with the low dihedral angles typical of internal pores in HPA will remain 'attached' to boundaries at velocities up to order of magnitude greater than the phenomenological separation velocity. The issue is important, because the phenomenological model remains the only drag/separation model *globally* applicable to *arbitrary porous microstructures*, and so generally applicable in sintering and swelling analyses.

In this section, we renormalize Hsueh et al.'s (1982) results, so that the pore velocity at separation, as a function of dihedral angle, ψ, relates more directly to experimental data for porous

microstructures. (Instead of normalizing on the basis of a constant zero-velocity pore radius on the boundary, we use a constant pore volume.) In contrast to their results, the renormalized peak pore velocity is rather *in*sensitive to pore dihedral angle, having values between two and three. This suggests that the phenomenological separation predictions be retained, but extended to such values.

Variables are listed in section A12-4.

A12-1 Overview

Hsueh et al. (1982), Spears and Evans (1982) and Hsueh and Evans (1983) developed specific *local* models for surface diffusion- and evaporation/condensation-controlled motion of pores attached to sweeping grain boundaries. In these models, the interdependent pore/boundary distortions predicted are physically more satisfying than the phenomenological drag formulation.[1]

---

[1] The gap between the phenomenological and such alternative approaches will be difficult to close. For example, the local boundary distortion, or change in boundary curvature, due to an attached pore on a two-grain facet, as calculated by Hsueh et al. (1982), failed to include how the facet's distortion must also depend on its being attached to the local grain boundary network through its peripheral three-grain edges, and so being influenced by the time-dependent, historically-biased processes

Their results can be related more directly to phenomenological separation than was done in the original papers. As in Hsueh et al.'s (1982) analysis, and as in the phenomenological approach, we consider here time- and travel distance-*in*dependent predictions for a single nonphenomenological (i.e. nonspherical) pore separating from an isolated two-grain facet.

Hsueh et al. (1982) consider a series of single pores, in which ψ varies. However, in practice, we will apply pore drag and separation theory not to single pores, but to porous polycrystals for which the experimental data available are the volume fraction porosity, V_v, the grain size, $\bar{L}_2$ and the area number density of pores on the polish plane, N_A.[2] From these data, we will calculate the pore number densities, N_v and N (App. 6). To refer the ψ-sensitivity of the maximum steady state pore velocity, demonstrated by Hsueh et al. (1982), to such a microstructure and data, we need to consider a hypothetical series of *microstructures* with constant porosity, grain size and number densities of pores, in which only ψ varies. As the following

---

in the microstructural neighborhood Srolovitz et al. (1984). (See also Handwerker et al., 1984).

[2] It is possible that data for the *distribution* of ψ, and of pore and grain size will be available; we do not include such distributions in the present argument.

equations show, this requires normalizing on the basis of a constant pore volume.

A12-2 Analysis

Stating first the general stereological relation (DeHoff and Rhines, 1968, p.131):

$$N_V = N_A / \bar{D}_V \qquad (1)$$

For attached pores, the area number density is (DeHoff and Rhines, 1968, p.79):

$$N = N_V / S_V$$

$$= \frac{N_A / \bar{D}_V}{2/\bar{L}_2}$$

$$= \frac{N_A \bar{L}_2}{2 \bar{D}_V} \qquad (2)$$

The mean pore volume is then:

$$V_C = V_V / N_V$$

$$= \frac{V_V}{N_A} \bar{D}_V \qquad (3)$$

If N and N_V are to be independent of pore dihedral angle ψ, given constant experimental V_V, N_A and $\bar{L}_2$, then, from Eqs. (1) and

(2):[3]

$$N_V^{\circ}\ \{\ N_A, \bar{D}_V^{\circ} = 2r\ \} \quad = \quad N_V^{\psi}\ \{\ N_A, \bar{D}_V^{\psi}\ \} \tag{4a}$$

$$N^{\circ}\ \{\ N_A, \bar{L}_2, \bar{D}_V^{\circ} = 2r\ \} \quad = \quad N^{\psi}\ \{\ N_A, \bar{L}_2, \bar{D}_V^{\psi}\ \} \tag{4b}$$

i.e.
$$\bar{D}_V^{\circ} \quad = \quad \bar{D}_V^{\psi} \tag{5}$$

But if Eq. (5) holds, then from Eq. (3):

$$V_C^{\circ} \quad = \quad V_C^{\psi} \tag{6}$$

That is, for N and N_V to be independent of ψ, both $\bar{D}_V$ and V_C must remain constant as ψ varies. We could carry the analysis further, via $\bar{D}_V$, by approximating a two-grain facet ψ-pore by an oblate, triaxial ellipsoid, for which $\bar{D}_V$ are available (DeHoff and Rhines, 1968, p.142-7). However, the phenomenological drag theory simplifies the real pore population to average spheres on an isolated boundary sheet, so $\bar{D}_V$ - ψ relations are obscure. It is easier — and, from Eq. (6), equivalent — to use Raj and Ashby's (1975) expressions for the volumes of intergranular pores of specific location and arbitrary ψ.

---

[3] Where the superscript '$\circ$' refers to a spherical (i.e. phenomenological: Hsueh et al., 1982) pore, for which $\psi = \pi$ radians (π-pore), and the superscript 'ψ' refers to a *non*phenomenological two-grain pore with *full* (not half-) dihedral angle $\psi < \pi$ radians (ψ-pore).

We want a peak velocity normalized on a *constant pore volume* basis, rather than the *constant boundary contact radius* normalization of Hsueh et al. (1982), which was: (7)

$$\left(\frac{\max \omega D_S \text{ s.s. } \hat{v}_P \text{ for 2/gn/fct pore with } a_o = a_o^{\psi}}{\max \omega D_S \, \hat{v}_P^{o} \text{ for spherical, phenomen. pore with } r=r} \right)_{V_C}$$

For a spherical, phenomenological (π-)pore:

$$V_C^{o} = \left(\frac{4\pi}{3}\right) r^3 \tag{8}$$

while for a two-grain ψ-pore of the same volume (Raj and Ashby, 1975):

$$V_C^{\psi} = F_V\{2;\psi\} \cdot r_o^3 \tag{9}$$

where, for constant γ_S , r_o is the zero-velocity, spherical caps radius, and the argument '2' notes that F_V is specific to a two-grain facet pore.

Setting Eq. (8) equal to Eq. (9):

$$F_V\{2;\psi\} \cdot r_o^3 = \left(\frac{4\pi}{3}\right) r^3$$

i.e.

$$\frac{r_o}{r} = \left(\frac{(4\pi/3)}{F_V\{2;\psi\}} \right)^{1/3} \tag{10}$$

To calculate r_o in terms of b_o, the zero-velocity ψ-pore radius *in the grain boundary plane*, we use Raj and Ashby's (1975) Eq. (3c) for the area of this boundary plane, $B\{\psi\}$:

$$B\{\psi\} = \pi \sin^2 (\psi/2) \cdot r_o^2 \qquad (11a)$$

By elementary geometry:

$$B\{\psi\} = \pi b_o^2 \qquad (11b)$$

Setting Eq. (11a) equal to Eq. (11b):

$$r_o = \frac{b_o}{\sin (\psi/2)} \qquad (12)$$

Substituting Eq. (12) into Eq. (10):

$$\left(\frac{b_o}{r \cdot \sin (\psi/2)} \right)_{V_c} = \left(\frac{(4\pi/3)}{F_v\{2;\psi\}} \right)^{1/3} \qquad (13a)$$

so

$$\left(\frac{b_o}{r} \right)_{V_c} = \frac{(4\pi/3)^{1/3} \sin (\psi/2)}{F_v\{2;\psi\}^{1/3}} \qquad (13b)$$

So, for a two-grain facet pore (Raj and Ashby, 1975):

$$F_v\{2;\psi\} = \left(\frac{2\pi}{3}\right) \left[2 - 3 \cos\left(\frac{\psi}{2}\right) + \cos^3\left(\frac{\psi}{2}\right) \right] \qquad (14)$$

so

$$\left(\frac{b_o}{r} \right)_{V_c} = \frac{2^{1/3} \sin (\psi/2)}{[\, 2 - 3 \cos(\psi/2) + \cos^3(\psi/2) \,]} \qquad (15a)$$

$$\equiv \mathcal{R}\{\psi\} \qquad (15a)$$

$\mathcal{R}\{\psi\}$ is a dimensionless function of ψ, decreasing monotonically from about 1.7 at $\psi = 60^\circ$ to 1.00 at $\psi = 180^\circ$. That is, for N and N_v independent of ψ, a ψ-pore has a larger (zero-velocity) radius

in the grain boundary plane than its equivolume phenomenological π-pore.

From Eq. (15b), the renormalized, constant-V_C, peak, steady-state, ωD_S velocity for a two-grain ψ-pore (without Hsueh et al.'s (1982) (γ_B/γ_S) factor) is:[4]

$$\hat{\nu}_P \equiv \left(\frac{\hat{\upsilon}_P^{\psi} \{ b_o = r \cdot \mathcal{R}\{\psi\}\}}{\hat{\upsilon}_P^{o} \{ \pi\text{-pore, } r=r\}} \right)_{V_C} \tag{16}$$

For ωD_S motion of a (phenomenological) spherical pore of radius r (App. 11):

$$\hat{\upsilon}_P^{o} \propto r^{-3} \tag{17}$$

so
$$\hat{\nu}_P \equiv \left(\frac{\hat{\upsilon}_P^{\psi} \{b_o\}}{\hat{\upsilon}_P^{o} \{r\}} \right)_{V_C} = \frac{\hat{\upsilon}_P^{\psi} \{b_o\}}{\hat{\upsilon}_P^{o} \{b_o\}} \cdot \frac{\hat{\upsilon}_P^{o} \{b_o\}}{\hat{\upsilon}_P^{o} \{r\}} \tag{18a}$$

$$= \frac{\hat{\upsilon}_P^{\psi} \{b_o\}}{\hat{\upsilon}_P^{o} \{b_o\}} \left(\frac{r}{b_o} \right)^3 \tag{18a}$$

$$= \frac{\hat{\upsilon}_P^{\psi} \{b_o\}}{\hat{\upsilon}_P^{o} \{b_o\}} \cdot \mathcal{R}\{\psi\}^{-3} \tag{18c}$$

---

[4] The initial footnote in App. 11 describes clearly the difference between the (re)normalized, *non*phenomenological separation velocity developed here, $\hat{\nu}_P$, and the normalized, phenomenological pore velocity developed in that appendix, $\tilde{\upsilon}_P$.

A12-3 Results

In Fig. A12-1, curves (a) and (b) correspond to Hsueh et al.'s (1982) strongly ψ-sensitive normalization. We have truncated the plot at $\psi \approx 150^{\circ}$, which is the maximum ψ for which their approximate linear expression — their Eq. 14 — fits their numerical results (their Fig. 7: $\hat{\nu}_p \equiv (17.9 - 6.2\ \psi_{rad})$. Curve (a) is their original result. Curve (b) gives the same results, but, as an alternative normalized velocity, eliminates the $2 \cdot \cos(\psi/2)$ factor from the RHS of their Eq. (14). It is less ψ-sensitive than (a), but still reaches high normalized velocities at low ψ.

Curves (c) and (d) are for the constant pore volume normalization calculated in this section, which we generate by dividing curves (a) and (b) by $\mathcal{R}\{\psi\}^3$ (Eq. 18: curve (d) corresponds to a renormalized (a); curve (c) to a renormalized (b)). Regardless of which original normalization is chosen, *both* renormalized curves are *insensitive* to ψ, and, over the range ψ = 60 to 150°, have normalized peak pore velocities of between one and three.

From these results, we suggest that phenomenological separation predictions be retained tentatively, but that separation need not occur at a normalized peak pore velocity of one. Rather, contours of two to three times the peak phenomenological velocity should

be drawn on plots (of, for example, grain size *vs* pore size; equations are given in App. 11), and the separation value for a given material be determined by experiment. Handwerker et al. (1984) suggest a similar strategy.

Because we have yet to plot experimental swelling results with normalized pore velocity and drag contours (App. 11), at this point we cannot say whether AVCO or ARCO exceeded phenomenological separation velocities in the current swelling work.

A12-4 Variables

a, b radius *in the plane of the grain boundary* of a non-phenomenological pore on a two-grain facet; [m]

B area of grain boundary occluded by attached pore; [m^2]

D_S surface diffusion coefficient; [m^2/s]

$\bar{D}_V$ mean tangent intercept for a dispersed second phase; [m]

F_V dimensionless pore volume function defined by Eq. (14); [-]

$\bar{L}_2$ mean linear intercept on a random polish plane; [m]

N number of attached pores per unit area grain boundary; [m^{-2}]

N_A number of pores per unit area internal polish plane; [m^{-2}]

N_V number of pores per unit volume porous polycrystal; [m^{-3}]

$\hat{\nu}_p$ peak pore velocity, (re)normalized on a constant pore volume basis; [-]

ψ pore dihedral angle; [rad] or [deg]

r radius of average *spherical* pore; [m]

ρ radius of curvature of two-grain facet pore with $\psi < \pi$ rad; [m]

$\mathcal{R}$ dimensionless function defined in Eq. (15); [-]

S_V specific grain boundary area; [m^2/m^3]

V_C volume of an average (spherical) pore; [m^3]

V_V volume fraction of pores; [-]

v_p pore velocity; [m/s]

ω width for surface diffusion; [m]

Diacriticals:

$\bar{a}$ denotes a mean value

$\hat{a}$ denotes a maximum value

$\tilde{a}$ denotes a normalized value

Superscripts:

a° denotes a phenomenological value; i.e. for a spherical pore ($\psi = \pi$).

a^ψ denotes a value for a pore with $\psi < \pi$ rad.

Subscripts:

a_o parameter value at zero pore/boundary velocity

rad denotes and angle in radians

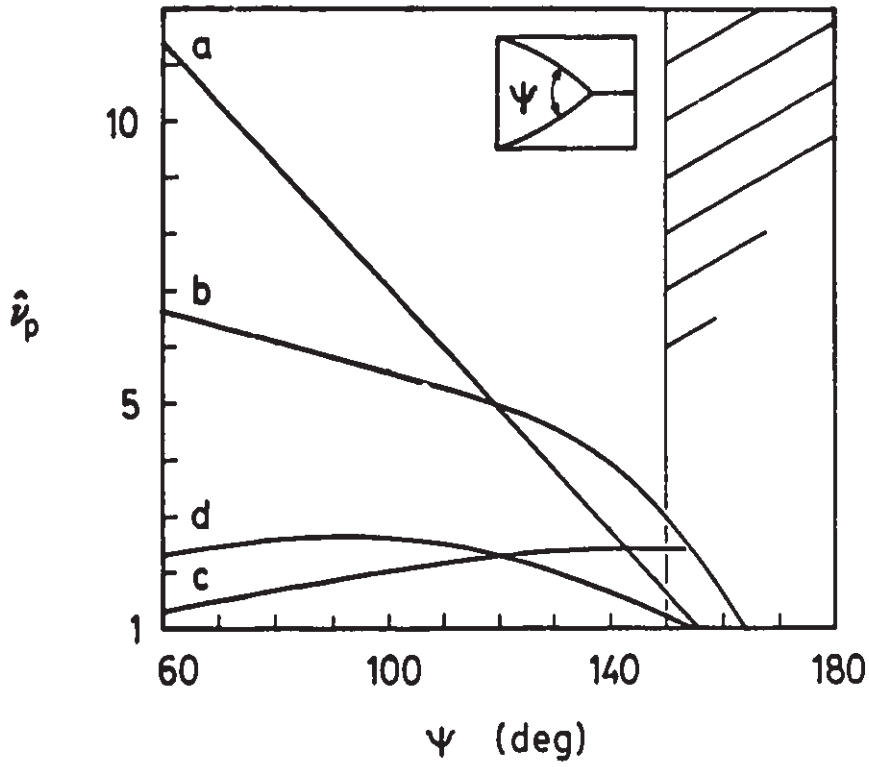

Fig. A12-1: Normalized, peak velocity of a pore on a two-grain facet, versus (full) dihedral angle, ψ.
Curve: a = $(17.9 - 6.2\ \psi_{rad})$
b = $a/[2\cos(\psi/2)]$
c = $b/\mathcal{R}^3$
d = $a/\mathcal{R}^3$
The dimensionless factor $\mathcal{R}$ is defined in Eq. (15). The plot is restricted to the range of ψ over which Hsueh et al's (1982) linear approximation (in their Fig. 7) is consistent with their numerical results; that is, to $\psi < 150^\circ$.

Appendix 13

Potential errors in calculated r, N_v, f_3 and N, arising from *non*-equiaxed cavities

---

In the current experimental work, the proportion of *non*equiaxed pores on internal polish planes gradually increased with time and temperature (Figs. 4-1.1,-1.2). However, for purposes of calculating microstructural parameters (App. 6), we treated *all* pores cut by polish planes as if they were equiaxed. This leads to errors in calculated r, N_v, N and f_3.

In this section we show that the observed temperature dependence of coalescence rates (with respect to grain size; Figs. 4-13,-14) is unlikely to be an artifact of this treatment.

It is important to demonstrate that the potential stereological errors are small, because the numerical results show that this temperature dependence is the only basis for generating *distinct* *pre*damaged microstructures in low temperature pressureless anneals, for subsequent creep fracture studies (see Ch.6).

Variables are listed in section A13-5.

A13-1 General

As HPA swells, an increasing fraction of grain-boundary pores seen on internal polish planes are not equiaxed, but are elongated, with aspect ratios *(on the plane)* in the range of two to three (Figs. 4-1.1,-1.2, A13-1). Both three dimensional, three-grain-edge (3GE) cylindrical pores and two-grain-facet (2GF) disk-shaped cavities could generate such elongated polish plane pore outlines. Furthermore, even equiaxed pores at polish plane 'triple-junctions' could be either sections through 3GE cylinders, or (as we assume) spherical tetrahedra at four-grain-junctions (4GJ).

Given the area number density of pores on the polish plane, N_A, it is possible to calculate the volume number density, N_V, and from it, given the grain size, the mean pore radius, number of pores per unit area grain boundary, N, and number per grain, $(6 \cdot f_3$; Apps. 1,6). The calculation requires assuming a characteristic shape for the average pore (DeHoff and Rhines, 1968, p. 131). Then, the mean tangent diameter of this representative pore, $\bar{D}_V$, defines the stereology:

$$N_A = N_V \cdot \bar{D}_V \qquad (1)$$

We treat pores as identical, average spheres,[1] and so assume $\bar{D}_v = 2r$, in calculating r, N_v, N and f_3. Our calculated pore parameters show progressive temperature-dependent trends in the rate of coalescence, within the bounds of constant-N and constant-f_3 microstructural trajectories (Figs. 4-13,-14). Because the swelling model predicts that the coalescence component of the pore growth rate ($\dot{r}_L$) — and so, the overall swelling rate, at long times — depends on the swelling trajectory, it is important to test whether the variation in trajectory is real.

Could simplifying to average spheres the observed, two-dimensional, *mixed* equiaxed/elongated pore populations seen on polish planes, introduce significant errors into the calculated, three-dimensional microstructural parameters? Would constant-N and constant-f_3 paths still bound experimental data, or would all data converge to a common, temperature-*in*dependent path?

Because the fraction of elongated pores increases with time and

---

[1] We treat pores (1) as spheres for stereology — assuming that $\bar{D}_v$ for a spherical tetrahedron (with dihedral angle, ψ, typical of HPA) are close, in practice, to $\bar{D}_v = 2r$ for spheres of the same volume — but (2) as spherical tetrahedra for P_{cap} calculations (App. 3).

temperature, we risk not offsets at constant slope, but rather errors in *slopes* on, for example, {log N - log $\bar{L}_2$} plots; Figs. 4-13,-14); that is, we risk errors in trajectory *character*.

A13-2 The ideal mixed pore population

We generate an estimate for the potential errors by assuming an idealized, three-dimensional pore population which is slightly more complicated in geometry and swelling kinetics than one consisting only of identical spheres. The analysis is approximate. It is intended to be only a first-order verification of the calculated trajectories, and a base to be extended when a physical model for intergranular pore coalescence by grain growth, supported by data from direct SEM image analysis systems — or one for swelling to gas release in these systems — becomes available. We apply the analysis only to AVCO's data (Fig. A13-1), because currently we are uncertain how to treat ARCO's initial intragranular porosity. When ARCO's swelling model is developed, however, this potential error should be tested for that model and those data.

We assume a uniform mixture of monodisperse spherical and cylindrical intergranular pore subpopulations (Fig. A13-2). The mixed population of N_v (total) pores per unit volume is described

by number fractions for spheres and cylinders:[2]

$$f_s + f_c = 1 \qquad (2)$$

The spherical pore's radius is equal at all times to the radius of the cylindrical pore's cross-section. This common radius increases with time and temperature, as the polycrystal swells. Cylinders are of common length $h\{t,T\}$, and are randomly oriented (on 3GE). As the microstructure evolves, we assume that the cylinders' true *three*-dimensional aspect ratio $X_3 \equiv h\{t,T\}/2r\{t,T\}$ remains constant,[3] but the fraction f_c of such cylinders in the mixed population increases linearly with $\tilde{L}_2$ (Fig. A13-1).

The *maximum two*-dimensional pore aspect ratio observed on SEM micrographs of internal polish planes, X_2, will be close to, and greater than, the true, three-dimensional X_3.[4] By elementary

---

[2] The corresponding polish-plane fractions will have a higher apparent f_s.

[3] The cylinder length, h, should be on the order of the mean facet edge trace length on the polish plane: $h \approx \ell\{t,T\}$; ie. it should be linear in $\bar{L}_2$ (App. 1). The experimental pore radius (for a spheres-only analysis) is approximately linear in grain size (Fig. 5-7).

[4] The real (etched) pore population appears to be more complicated than just spheres and cylinders — there are, no doubt, some coin-like, full-facet cavities as well — so we

geometry:

$$\hat{X}_2 \approx \frac{(4r^2 + h^2)^{1/2}}{2r}$$

$$= (1 + X_3)^{1/2} \qquad (3)$$

The maximum value observed, $\hat{X}_2$, was about three (Figs. 4-1.1,-1.2). The *average* polish plane aspect ratio, $\bar{X}_2$, will be somewhat less than X_3 (DeHoff and Rhines' (1968) Eq. 5-15):

$$\bar{D}_v\{cyl\} = 2r\left(\frac{\pi}{4} + \frac{X_3}{2}\right) \qquad (4)$$

Defining $$\bar{X}_2 \equiv \frac{\bar{D}_v}{2r} \qquad (5a)$$

it follows that $$\bar{X}_2 = \frac{\pi}{r} + \frac{X_3}{2} \qquad (5b)$$

Based on the arguments DeHoff and Rhines (1968, pp. 129ff) used to develop Eq. (1), we assume that a relation *of the same form* as Eq. (1) holds for the *mixed* sphere/cylinder pore population. That is, we assume:

---

estimate only a rough X_2. For monodisperse cylinders, extreme $\hat{X}_2$, which might be encountered for cylindrical pores in which $h_2 \approx h$, but $r_2 \ll r$, will seldom be counted, due to practical aspects of detecting pores by SEM on thermally etched polish planes. The highest observed aspect ratios may correspond to thin, coin-like 2GF pores which are cut by the polish plane.

$$\bar{N}_{A,mix} = N_{V,mix} \cdot \bar{D}_{V,mix} \quad (6)$$

where $$\bar{D}_{V,mix} = f_s \cdot \bar{D}_{V,s} + f_c \cdot \bar{D}_{V,c} \quad (7)$$

The mean tangent diameter for spherical pores is:

$$\bar{D}_{V,s} = 2r \quad (8)$$

while that for cylindrical pores has been given in Eq. (4).

We now modify previous stereological relations for calculating r, N_V and f_3 for *spherical* pores (App. 6) to apply to such a mixed pore population. Then, using these mixed relations, for experimental f_c and $\bar{X}_2\{t,T\}$ typical of annealed AVCO HPA (Fig. A13-1), we compare the mixed results with pore population parameters calculated assuming spherical cavities only (Table 4-3).

A13-3 Stereology of simple mixed sphere/cylinder pore populations

We simplify the following equations by dropping the subscript "3" from the three-dimensional X_3 — writing it simply as X. The subscript 'm' denotes a parameter of the *mixed* pore population.

From Eqs. (7) to (9), the mean tangent diameter for the mixed population is:

$$\bar{D}_{Vm} = f_s \cdot \bar{D}_{V,s} + f_c \cdot \bar{D}_{V,c} \qquad (10a)$$

$$= f_s \cdot 2r + f_c \cdot 2r(\pi/4 + X/2)$$

$$= 2r \left[f_s + f_c(\pi/4 + X/2) \right] \qquad (10b)$$

The volume fraction porosity can be written:

$$V_{Vm} = N_{Vs} \cdot \bar{V}_{sph} + N_{Vc} \cdot \bar{V}_{cyl} \qquad (11a)$$

$$= \pi r^2 N_{Vm} \left[(4f_s/3)\, r + h\, f_c \right] \qquad (11b)$$

A13-3.1 The mean pore radius for the mixed population, r_m

To derive the new, mixed relation for r, substitute Eq. (10b) into Eq. (1) and rearrange:

$$N_{Vm} = N_A / \bar{D}_{Vm} \qquad (12a)$$

$$= N_A \cdot \left(2r \left[f_s + f_c(\pi/4 + X/2) \right] \right)^{-1} \qquad (12b)$$

Substituting Eq. (12b) into Eq. (11b):

$$V_V = \frac{N_A}{2r \left[f_s + f_c(\pi/4 + X/2) \right]} \left[f_s \frac{4\pi}{3} r^3 + f_c \pi h r^2 \right]$$

$$= N_A \left(\frac{f_s\left(\frac{4\pi}{3}\right) r^2 + f_c \pi h r \left(\frac{2r}{2r}\right)}{2 [f_s + f_c(\pi/4 + X/2)]} \right)$$

$$= N_A \left(\frac{\pi (2f_s/3 + X f_c)}{f_s + f_c(\pi/4 + X/2)} \right) r^2 \qquad (13)$$

$$\text{so} \qquad r_m = \left(\frac{f_s + f_c(\pi/4 + X/2)}{\pi (2f_s/3 + X f_c)} \right)^{1/2} \left(\frac{V_V}{N_A} \right)^{1/2} \qquad (14)$$

In the limit $f_s \longrightarrow 1$, we have only spherical pores, and this reduces to the relation derived previously (App. 5's Eq. 5a):

$$r_s = (3/2\pi)^{1/2} \left(\frac{V_V}{N_A} \right)^{1/2} \qquad (15)$$

If we simplify this by defining:

$$F \equiv \left(\frac{f_s + f_c(\pi/4 + X/2)}{\pi (2f_s/3 + X f_c)} \right)^{1/2} \qquad (16)$$

we can write Eq. (14) as:

$$r_m = F \left(\frac{V_V}{N_A} \right)^{1/2} \qquad (17)$$

Given experimental V_V and N_A, when $F < (3/2\pi)^{1/2}$, the r_s calculated by assuming spherical pores only will be larger then the true r_m of the mixed population.

We do not give the results for r, but give N_V's results in the next section, as it is a parameter more diractly related to the issue of potential errors in coalescence strength. However, for r, the potential relative error could be estimated by plotting:

$$\tilde{F} \equiv F / (3/2\pi)^{1/2} \qquad (18)$$

against $\tilde{L}_2$, for f_c, $\tilde{L}_2$, and X_2 typical of the swelled HPA (such X_2 are given in Figs. A13-1, 4-1.1). As an extreme example for AVCO, for $f_c = 0.2$ and $X_2 \approx X = 3$, $\tilde{F}$ is 0.86; that is, the mixed r is 14% smaller than that calculated from the same density and stereological data, assuming spheres only.

A13-3.2 The volume number density of pores for the mixed population, N_{Vm}

To develop the N_{Vm} relation, substitute Eq. (16) back into Eq. (12a):

$$N_{Vm} = N_A \cdot \left[2 \left(F \, (V_V/N_A)^{1/2} \right) \left(f_s + f_c \left(\frac{\pi}{4} + \frac{X}{2} \right) \right) \right]^{-1}$$

$$= \left[2 F \left(f_s + f_c \left(\frac{\pi}{4} + \frac{X}{2} \right) \right) \right]^{-1} \left(N_A^{3/2} / V_V^{1/2} \right)$$

$$= \left(\frac{\sqrt{\pi} \ [\ 2f_s/3 + X f_c \ ]^{1/2}}{2 \ [\ f_s + f_c (\ \pi/4 + X/2 \ ) \ ]^{3/2}} \right) \frac{N_A^{3/2}}{V_V^{1/2}} \qquad (19)$$

Define $$N_{Vm} \equiv G \left(\frac{N_A^{3/2}}{V_V^{1/2}} \right) \qquad (20)$$

where, from Eq. (19):

$$G \equiv \frac{\sqrt{\pi} \ [\ 2f_s/3 + X f_c \ ]^{1/2}}{2 \ [\ f_s + f_c (\ \pi/4 + X/2 \ ) \ ]^{3/2}} \qquad (21)$$

In the limit $f_s \longrightarrow 1$, we have only spherical pores, and this reduces to the relation derived previously (App. 6's Eq. 6):

$$N_{Vs} = (\pi/6)^{1/2} \left(\frac{N_A^{3/2}}{V_V^{1/2}} \right) \qquad (22)$$

For the type of mixed pore populations assumed here, the mixed mean tangent diameter is always greater than that for the spherical pores alone: $\bar{D}_{V,mix} > \bar{D}_{V,sph}$. So, from Eq. (1):

$$G \leq (\pi/6)^{1/2} \qquad (23)$$

Given experimental N_A and V_V, the N_{Vm} calculated by Eq. (20) for the *mixed* cavity population will be *smaller* than that calculated assuming spherical cavities only, using Eq. (22).

For AVCO, we can estimate the potential errors in N_V, and so in

path character, by plotting (Fig. A13-3):

$$\tilde{G} \equiv G/(\pi/6)^{1/2} \leq 1 \qquad (24)$$

for f_c, X and $\tilde{L}_2$ typical of swelled AVCO HPA (Fig. A13-1). As an *extreme* example, for $f_c = 0.2$ and $X_2 \approx X = 3$, $\tilde{G} \approx 0.93$. $\tilde{G}$ is greater than 0.93 for all $\tilde{L}_2$ in AVCO's current data. That is, the true $N_{V,mix}$ is smaller than, but within, say, 10% of the N_V calculated throughout this report assuming equiaxed pores only, even in the AVCO samples annealed to the longest time, at the highest temperature.

A13-3.3 The fraction of four-grain junctions cavitated, f_3

The effect on f_3 follows directly from Eqs. (20), (22) and (24):

$$\left.\frac{N_{V,mix}}{N_{V,sph}}\right|_{t,T} = \tilde{G} \qquad (25)$$

and

$$f_3 \propto N_V \qquad (26)$$

so

$$\left.\frac{f_{3,mix}}{f_{3,sph}}\right|_{t,T} = \tilde{G} \qquad (27)$$

A13-3.4 The area number density of pores, N

Similarly, from Eqs. (20), (22) and (24):

as $$N^{att} = N_v \tag{28}$$

so $$\left.\frac{N_{mix}}{N_{sph}}\right|_{t,} = \tilde{G} \tag{29}$$

A13-4 Comments

Admitting *non*-equiaxed pores would require changes be made to the model. For example, parameters such as r and f_3, which are readily defined as long as we include only equiaxed pores at 4GJ, become physically messy. N would retain its meaning, but the phenomenological pore drag relations of which it is a part would need modifying (Occhionero and Halloran, 1984). Cylindrical pores will *have* to be included in a swelling model capable of handling swelling sufficient to generate continuous 3GE pore channels and gas release; precedents for the required changes are available for nuclear fuels (e.g. Rest, 1986; Gruber, 1986).

By assuming equiaxed (spherical) pores, then, (and keeping the above comments about physically imprecise parameters in mind) we are *over*estimating N_v, N and f_3. Pore radius is inverse in N_v, so we are *under*estimating it.

For AVCO, however, the anticipated corrections are *not* sufficient to compensate for the differences in {log N or log f_3 *vs* log $\bar{L}_2$} plots seen at different T (Figs. 4-11,12) — especially those between 1350 C and the higher T runs at 1400 and 1450 C. In particular, we cannot assume a constant f_3 for the higher T anneals in AVCO. That is, this simple stereological correction does *not* eliminate trends in AVCO's trajectory character with changing anneal temperature.

The uncertainties in calculated r, N_V, N and f_3 now are larger than, and more difficult to estimate (or express) than those shown in Figs. 4-7 to 4-12. However, given the number of uncertain parameters in the model, and the relatively small corrections suggested above, we have adjusted neither the plotted (spherical) experimental data points, nor their uncertainties (App. 14).

A13-5 Variables

$\bar{D}_V$	mean tangent intercept for a dispersed second phase; [m]
$\bar{D}_{V,cyl}$	$\bar{D}_V$ for cylindrical pores; [m]
$\bar{D}_{V,m}$	$\bar{D}_V$ for mixed sphere/cylinder population; [m]
$\bar{D}_{V,s}$	$\bar{D}_V$ for spherical pores; [m]

$f_{s,c}$ fraction of mixed pore population that is spherical and cylindrical, respectively; [-]

f_3 fraction of four-grain junctions cavitated in ideal microstructure; [-]

F dimensionless ratio defined in Eq. (16); [-]

G dimensionless ratio defined in Eq. (21); [-]

h common height (length) of cylindrical pores in assumed mixed pore population; [m]

J_{4V} number of four-grain junctions (3-dimensional vertices) per unit volume ideal truncated-octahedral microstructure; [m^{-3}]

ℓ length of facet edge in ideal, truncated-octahedral grain; [m]

$\bar{L}_2$ mean linear intercept on a random polish plane in a real microstructure; [m]

$\bar{L}_2^o$ $\bar{L}_2(t=0)$; [m]

N, N^{att} number density of pores attached to grain boundaries; [m^{-2}]

N_A number density of pores on an internal polish plane; [m^{-2}]

$N_{Vc,s}$ number of cylindrical and spherical pores per unit volume polycrystal in assumed mixed pore population; [m^{-3}]

N_V number of pores per unit volume solid; [m^{-3}]

r radius of average spherical pore; [m]

S_V specific grain boundary area; [m^2/m^3]

V_c volume of an average (spherical) pore; [m^3]

V_v volume fraction of pores; [-]

X, X_3 true aspect ratio of assumed cylindrical pores; [-]

X_2 apparent (2D) aspect ratio of assumed cylindrical pores, as seen on polish planes; [-]

Diacriticals:

$\bar{a}$ denotes mean value

$\hat{a}$ denotes maximum value

$\tilde{a}$ denotes value normalized by dividing by initial value.

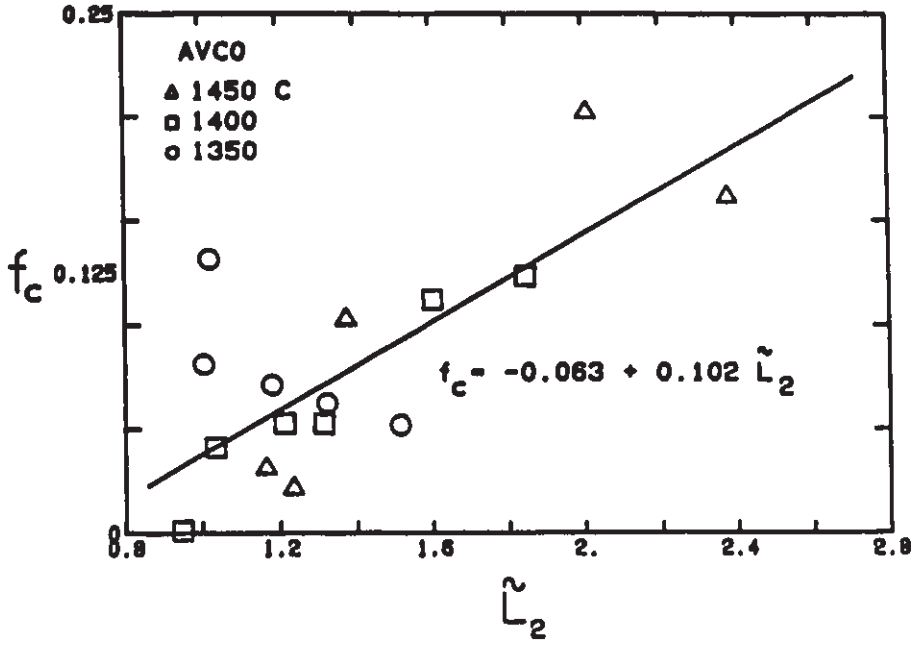

Fig. A13-1: Experimental fraction of pores on SEM polish planes which are cylindrical, as a function of the normalized grain size ($\tilde{L}_2 \equiv \bar{L}_2/\bar{L}_2^o$), for AVCO HPA.

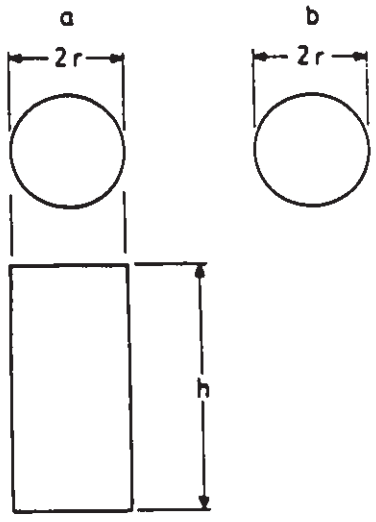

Fig. A13-2: The two pore types — (a) cylindrical and (b) spherical, in the idealized, mixed pore population.

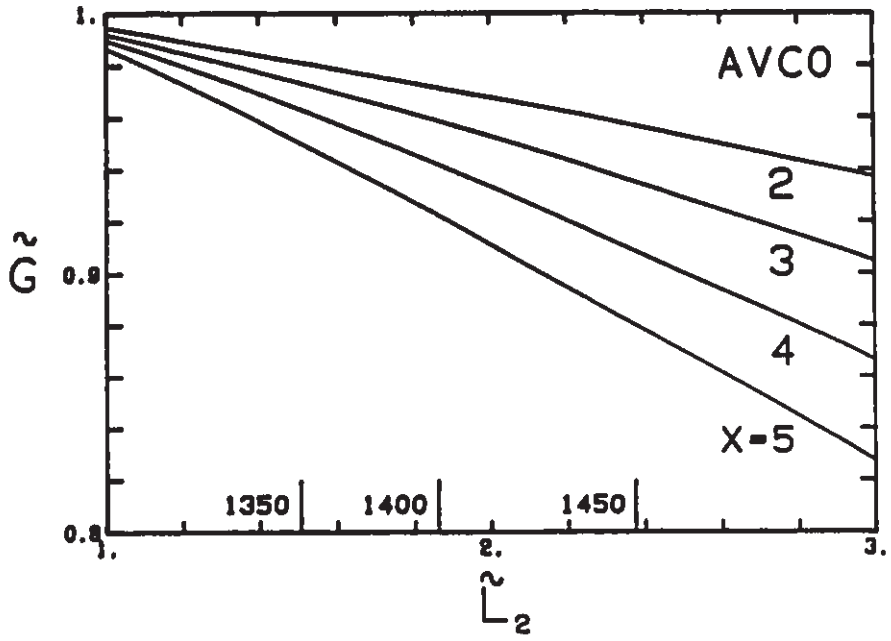

Fig. A13-3: The ratio of the true N_v for the *mixed* spherical/cylindrical pore population, to N_v calculated with the same experimental data, but assuming only spherical pores. The maximum $\tilde{L}_2$ for each annealing temperature in the current data are shown. X is the true aspect ratio for cylindrical pores.

Appendix 14

Uncertainties in experimental swelling data

In this section we discuss experimental uncertainties in the raw data. For V_v, we illustrate how such uncertainties propagated, when mean microstructural parameters were calculated in Apps. 6 and 7. Variables are listed in Ch.3, section 3.7.

A14-1 Volume fraction porosity, V_v

Systematic errors in calculated *as-received* relative densities ($\tilde{\rho}_o$) will propagate through the *entire* set of mean porosity parameters calculated for an HPA — V_v, r, N_v, N and f_3 (Apps. 5,6). So, despite the 'buffering' built into Ratcliffe's (1965) technique for determining density *changes* (see App. 7, section A7-1), for the work reported here it was important that an accurate *absolute* liquid density have been known at all temperatures for which as-received Al_2O_3 densities (ρ_o) were determined. (The pycnometer/hydrometer method used to determine liquid density was outlined Ch.2.)

It was important also that the absolute, theoretical densities of the doped, impure HPAs, ρ_{th}, were estimated closely (App. 7). While corrections to the theoretical densities of the HPAs were made for Si and Mg from Rasmunssen and Kingery's (1970) data, those for other dopants and impurities (e.g. Y) had to be estimated. The uncertainties in calculated theoretical densities due to impurities were small, relative to the calculated V_v^o. No single/polycrystal density correction for grain boundary density was applied; the anticipated corrections were small.

Calculated (V_v- t) trajectories were sensitive to uncertainties in the initial relative densities, $\tilde{\rho}_o$; that is, to errors in both ρ_o and ρ_{th} (App. 7). These raw uncertainties propagated as a sum of squares, to give an absolute uncertainty in V_v (Bevington, 1969, Ch. 4):[1]

$$\sigma\{V_v\} = V_v \left[\left(\frac{\sigma\{\rho_o\}}{\rho_o} \right)^2 + \left(\frac{\sigma\{\rho_{th}\}}{\rho_{th}} \right)^2 + \left(\frac{\sigma\{\Delta\rho/\rho_o\}}{\Delta\rho/\rho_o} \right)^2 \right]^{1/2} \qquad (1)$$

In the current density change data, the uncertainty in density

---

[1] In this section, we use $\sigma\{x\}$ to denote an absolute (as opposed to relative) uncertainty. In all other sections of this report (except Tables 4-1 and 4-2), σ denotes stress. Uncertainties for *all* calculated parameters were generated by similar root mean square equations.

change measurements — calculated by a similar sum of squares — was far larger than the other two uncertainty components, so Eq. (1) simplified to:

$$\sigma\{V_v\} \quad \propto \quad V_v \left(\frac{\sigma\{\Delta\rho/\rho_o\}}{\Delta\rho/\rho_o} \right) \qquad (2)$$

Mean pore radii determined by TEM (Figs. 4-13,-14) provided an independent check on absolute errors in $\tilde{\rho}_o$ (e.g. Fig. 4-7).

A systematic error in V_v^o, arising from $\tilde{\rho}_o$, via either ρ_{th} or ρ_o, (App. 7), would have generated progressively *less* important errors in calculated microstructural parameters as swelling proceeded, particularly in a material swelling as strongly as AVCO HPA. Consequently, the apparent common origins for AVCO's N and f_3, on log-log plots vs grain size (Figs. 4-13,-14), provided a check on its estimated V_v^o. For example, AVCO's common initial N was about $9(10^{10})$ pores per unit area of grain boundary (Fig. 4-13). With AVCO's initial mean pore radius estimated by TEM as 0.12 μm, this implied a V_v^o of $0.80(10^{-3})$, which was within the estimated uncertainty for the absolute V_v^o estimate from density measurements. ARCO's initial porosity was more difficult to deal with, within the current model (App. 7, sectn. A7-1.2).[2]

---

[2] While current pore size distributions probably are reliable (Fig. 4-3), more TEM data are needed for pore number densities, and for the proportion of pores occurring as individual pores *vs* clusters.

A14-2 Grain size, $\bar{L}_2$

Fig. 4-4 shows experimental grain growth kinetics. Systematic errors in $\bar{L}_2$ should have been small, because, although no calibrating microspheres were used (Bennison and Harmer, 1985b), the SEM's magnification was verified regularly by the instrument's technician. More data would resolve whether the calculated standard deviations reflect primarily the relatively small number of grains measured (especially at high $\bar{L}_2$), or were characteristic of the grain-growth dependent, grain size distributions. Both analytic and numerical models for normal grain growth (Anderson et al., 1986; Srolovitz et al., 1984) predict time-invariant *normalized* grain size distributions, which require *raw* distribution dispersions to increase with their means. Raw uncertainties were plotted in Fig. 4-4, and were propagated in calculating normalized grain sizes, $\tilde{L}_2$. Other porosity parameters which required $\bar{L}_2$ (i.e. N, f_3, (b/ℓ) and β) were calculated with a single, approximate global uncertainty in $\bar{L}_2$ for each HPA, estimated from a rough linear regression over all experimental uncertainties for that material (Tables 4-1,-3). (The positive slopes for both these regressed lines were justified by the above references.)[3]

[3] At the time the experimental data were generated, we were

A14-3 The area density of pores on polish planes, N_A

Calculated N_A values should be robust for pores larger than an minimum size (see below), given accurately known SEM magnifications, and subject to processing sufficient numbers of micrographs at appropriate magnifications. *Raw* uncertainties are plotted in Fig. 4-8; however, an approximate global *relative* uncertainty of 0.15 was assigned for both HPAs (Tables 4-1,4-2), in calculations depending on N_A (App. 6). This estimate could be refined by taking more data.[4]

Etching introduced uncertainties into N_A. Thermal etch cycles (Table 2-5) gradually were optimized to groove boundaries *minimally*, though no allowances across sets of specimens were made for the slower grooving observed in materials annealed at high temperatures for long times. The data presented here were taken from specimens etched with mature schedules, which *barely* rounded rims of pores cut by the polish plane.[5] We measured V_v by

---

unaware that Kumar and Johnson (1974) discuss experimental uncertainties in S_v (and so in $\bar{L}_2$), and that Aigeltinger and DeHoff (1970) discuss uncertainties in $\bar{L}_2$ and N_A.

[4] See footnote for section A14-2.

[5] This justifies not having determined pore parameters from *un*etched specimens, but grain size from etched specimens.

immersion densities, not via polish plane area fraction porosities, so the possiblity that etching enlarged pore cross sections was not a factor in calculated V_v, nor in the microstructural parameters calculated with V_v (App. 6). No trials were made of etched vs unetched polish planes in the same specimen, or of progressively etched sets on the same specimen. Errors in N_A for small pores were revealed by inconsistencies in the calculated early microstructural parameters r, N_v, N and f_3, relative to trends predicted by the model.

The *early* pore size data for ARCO were inconsistent with numerical results for swelling at short times, in directions implying that the corresponding raw N_A values were too low (Tables 4-2,-4, and their Note 1). We discuss this in Ch.4; ARCO's initial porosity was intragranular, and progressively reattached to sweeping boundaries.

However, for AVCO, the one apparently low N_A value (1350 C, 8 h) probably was due to the HPA surface smearing plastically during polishing. (We describe this in Ch.4.) The resulting 'SEM detection limit' for intergranular pores, 0.1 to 0.15 μm, was four times larger than a detection limit reported by Handwerker et al. (1984) for MgO. From the entire data set (Figs. 4-9 to 4-14), only this one point seems to be affected; the magnitude of the steep early rise in AVCO's experimental N_A is otherwise accurate in Fig. 4-8.

A14-4 The dihedral angle, ψ

Dihedral angles for grain-boundary pores in both aluminas were estimated from TEM micrographs of a small number of carefully selected four-grain junction and three-grain edge pores (Fig. 4-13).[6] Dihedral angles tended to vary within one pore and between pores, depending on the crystal faces exposed. As a rule, not all corners of one pore were well resolved, in a given micrograph. Foils had to be tilted in the TEM, to ensure that geometric errors due to pore edges being misaligned with respect to the electron beam were minimized. For this, a two-axis stage whose height easily can be adjusted to locate the axes of rotation at the focus point is desirable; we used a one-axis stage. It was important to determine whether a pore is tetrahedral or cylindrical: the minimum dihedral angles are 71.5 and 60 degrees, respectively (Kaspar and Lonsdale, 1959), and the potential geometric errors across a pore are different. Pores should be selected that have not been eroded during ion thinning; preferably, they should be completely within the foil.

---

[6] Handwerker et al. (1984) and Francois and Kingery (1967) show that ψ determined from internal pores can be 30 to 45° smaller than those estimated from thermal grooving.

Appendix 15

Materials property data for hot-pressed alumina

In this section we discuss the materials parameters values used in the numerical swelling calculations. We summarize data for lattice, boundary and surface diffusion, and for boundary mobility, in Figs. 15-1a-d. We discuss parameter fitting for the swelling model in the section on numerical results (Ch.5), and give the parameter values used in the numerical solutions for AVCO's swelling in Table 5-1. All variables are explained in the text.

A15-1 'Atomic' volume for diffusional processes

The molecular volume of Al_2O_3 can be calculated from the geometric information given by Dorre and Hubner (1984, p.11):

$$\Omega\ (Al_2O_3) = \frac{a_o^2 c_o}{4\sqrt{3}} \qquad (1)$$

Lattice parameters a_o and c_o are given in their Table 2.1. The volume calculated using these agrees with the value given by

Frost and Ashby (1982, p. 99):

$$\Omega\ (Al_2O_3) = 4.246(10^{-29})\quad [m^3] \tag{2}$$

For every O or Al atom arriving at a surface, work:

$$\sigma \cdot \Omega\ (Al_2O_3) \ /\ n_1 \tag{3}$$

is done, where n_1 = 2 for Al and 2 for O (Frost and Ashby, 1982, p.100). Al controls *boundary* and *lattice* diffusion (Frost and Ashby, 1982, p.98,100).[1] For *surface* diffusion, Al control "is frequently assumed" (Dynys et al., 1980; Robertson and Chang, 1966). So, for diffusional processes in these studies, the effective atomic volume is:

$$\Omega_{eff}(\text{Al control}) = \Omega\ (Al_2O_3) \ /\ 2 \tag{4a}$$

$$= 2.12(10^{-29})\quad [m^3] \tag{4b}$$

A15-2 Lattice diffusion

Fig. A15-1a summarizes lattice diffusion data.

Frost and Ashby (1982: 'FA82') use parameter values which generate coefficients which are within a factor of five, over the temperature range for swelling, of those of Cannon et al. (1980:

---

[1] However, see Dynys et al.'s (1980) mixed δD_B in sectn. A15-3.

'C80', in Dorre and Hubner's (1984): Table 2.6.A).[2] Yan et al. (1980: their Table 3), referring to Cannon and Coble (1974), calculate an 1800 C coefficient very close to that given by Cannon et al.'s (1980) parameters.

Because, for these parameter values, surface diffusion is predicted to control pore mobility, we did not include D_L in the numerical calculations. However, we test for D_L *vs* δD_B control in pressure driven pore growth (App. 16), and use the D_L data to set bounds on the activation energies for grain boundary mobility (Section A15-5, below).

$D_L = D_L^o \cdot exp\ (- Q_L / RT\ )$

Refs	D_L^o [m^2/s]	Q_L [kJ/mol]	D_L(1450 C) [m^2/s]	Compn
FA82	$2.8(10^{-3})$	477.	$9.7(10^{-18})$	
C80	13.6	577.	$4.4(10^{-17})$	$\frac{1}{4}$% MgO

[2] The temperature range for swelling was well below the ranges in which most diffusion data were generated.

A15-3 Boundary diffusion

Fig. A15-1b summarizes boundary diffusion data.

Frost and Ashby (1982, p.100,102), use Cannon and Coble's (1974) values, which are the same as Cannon et al.'s (1980: 'C80'), in Dorre and Hubner's (1984) Table 2.6.B and Fig 2.9). We take this coefficient as an upper bound. As a lower bound, Dynys et al. (1980: 'D80') found mixed control — Al control at high temperatures, and oxygen control at low. The mixed activation energy was high, and diffusion coefficients were about two orders of magnitude smaller than C80's, when extrapolated into the temperature range for swelling.

The effect of Mg effect on δD_B is not fully understood. Dynys et al. (1980) claim no Mg effect. However, Berry and Harmer (1986) show that 250 ppm atomic Mg/Al increase the densification rate via δD_B by a factor of three in pressureless sintering at 1600 C. Dorre and Hubner (1984, p.37) report that allovalent doping enhances δD_B^O, but not δD_B^{Al}.

In the current work, a δD_B intermediate between C80 and D80 was chosen. The activation energy, Q_B, was decreased towards C80's value, until the early pressure-driven pore growth rates were large enough that numerical $\{\bar{L}_2\text{-}V_v\}$ and $\{\bar{L}_2\text{-}r\}$ results were no longer linear, as were the experimental data (Figs. 4-4,-6). For

each such trial Q_B, the pre-exponential, δD_B^o, was set to maintain the coefficient values at high temperature to which both C80 and D80 converged. The coefficient used corresponds to the line marked with an 'X' in Fig. A15-1b.

$$\delta D_B = \delta D_B^o \cdot exp\ (-\ Q_B / RT\ )$$

Ref.	δD_B^o [m^3/s]	Q_B [kJ/mol]	δD_B(1450 C) [m^3/s]
C80	$8.6(10^{-10})$	418.	$1.71(10^{-22})$
Fit	$5.5(10^{-8})$	500.	$3.82(10^{-23})$
D80	$2.3(10^{-3})$	≈ 684.	$4.19(10^{-24})$

A15-4 Surface diffusion

Fig. A15-1c summarizes surface diffusion data. Surface diffusion values are uncertain for gas-filled pores in impure materials.

For temperatures in the range for the current swelling work, Dynys et al.'s (1980: 'D80') diffusion coefficient is very close to Cannon et al.'s (1980; 'C80'), which was used by Yan et al.

(1980).[3] Dynys et al. (1980) conclude, from grain-boundary grooving data for pure bicrystals and Lucalox (Mg-doped), that Mg doping has little effect on ωD_s, and that the data within a narrow band, which is centered on the coefficient mentioned above, "are essentially independent of an air versus vacuum environment". However, Berry and Harmer (1986) claim that Mg doping (250 ppm atomic Mg/Al) "raised the surface diffusion coefficient relative to the undoped material by a factor of 2.5 ...".

We used a coefficient which was very close to Dynys et al.'s (1980) in the temperature range for swelling, with, however, a higher Q_s of 650 kJ/mol. High Q were necessary for both surface diffusion and boundary mobility, in order to fit the grain growth data; however, as discussed in Ch.5, *the numerical results were rather insensitive to these activation energies.*

The fit diffusion coefficient corresponds to the line marked with an 'X' in Fig. A15-1c.

---

[3] The width for surface diffusion, ω, is $5 \cdot (10^{-10})$ m (Hsueh and Evans, 1983; their Table 1). Al is assumed to be controlling (Dynys et al., 1980).

$$\omega D_S = \omega D_S^o \cdot exp\ (-\ Q_S /\ RT\ )$$

Ref.	ωD_S^o [m^3/s]	Q_S [kJ/mol]	ωD_S(1450 C) [m^3/s]
D80	$6.0(10^{-6})$	547.	$1.6(10^{-22})$
Fit	$7.5(10^{-3})$	650.	$1.5(10^{-22})$
C80	$8.6(10^{-10})$	418.	$1.8(10^{-22})$

A15-5 'Intrinsic' grain boundary mobility, M_B

We summarize boundary mobility data for alumina in Fig. A15-1d, and discuss mobility in App. 9.

Yan et al. (1977) present data for alumina systems (their *normalized*[4] Fig. 8). For the general case of arbitrary grain growth exponent, m, in:

$$\bar{L}_2(t,T)^m - \bar{L}_2^{o\ m} = K_L(m,T) \cdot t \qquad (5)$$

the global grain boundary mobility (for $\bar{L}_2$ as the grain size) is defined as (App. 9):

[4] Re. a_C, γ_B and $\bar{G}$; see App. 9.

$$M_{BL}\{m,T\} \equiv \frac{K_L\{m,T\}}{a_L m \gamma_B \bar{L}_2^{m-2}} \qquad (6)$$

in which the experimental rate constant, $K_L\{m,T\}$ is:

$$K_L\{m,T\} \equiv K_L^{\circ}\{m\} \cdot exp\ \{-Q_K/RT\} \qquad (7)$$

From Eq. (7), M_{BL} is independent of grain size only when $m = 2$. In this work, experimental grain growth exponents (with pore drag) were between three and four, so the exponent for the matrix was taken to be three, after Bennison and Harmer (1985b), corresponding to impurity drag control (Brook, 1976). Though the concentration of dopant in their study was an order of magnitude less than AVCO's, it is not clear what change a higher [Mg] should generate in the mobility (Yan et al., 1977, p.300). Because of this, and because the data for doped alumina systems in Yan et al.'s (1977) Fig. 8 were for polycrystals with second phase drag,[5] we retained Bennison and Harmer's (1985b) 1600 C data point.

For impurity drag control, the activation energy for boundary mobility should be closer to that for lattice than for boundary

---

[5] The saturation limit of MgO in Al_2O_3 is about 100 ppm (expressed either as oxides or as elements; Roy and Coble, 1968). Despite this, no dispersed solid second phase was seen by TEM in AVCO, which XRF data reported as 3000 ppm MgO, and which the manufacturer stated to be 2500 ppm MgO.

diffusion ($Q_K = Q_L$; Yan et al., 1977). Dorre and Hubner (1984: their Table 2.6.A) report activation energies for lattice diffusion ranging from 477±63 to 787±29 kJ/mol. The numerical results were insensitive to Q_K between Q_B^{Al} of 419 kJ/mol, and a high Q_L^{Al} of 600 kJ/mol.[6]

The results presented here used Cannon et al.'s (1980) Q_L of 577 kJ/mol, as fitting grain growth data required high activation energies for both boundary mobility and surface diffusion. The fit boundary mobility, normalized after Yan et al.'s (1977) Fig. 8, corresponds to the line segment marked with an 'X' in Fig. A15-1d.

$K_L(3,T) \equiv K_L^o(3) \cdot exp\{-Q_K/RT\}$

Ref.	$K_L^o(3)$ [m^3/s]	Q_K [kJ/mol]
Fit	$3.8(10^{-5})$	577.

[6] In fitting, given the constant 1600 C data point, the corresponding factor of two in the range of M_B, over the swelling temperature range, was easily accommodated by small adjustments in the ωD_S parameters.

A15-6 Evaporation/condensation; Vapor diffusion

Data are available in Hsueh and Evans (1983), and in Yan et al. (1980, their Table 3 and p. 20). Hsueh and Evans (1983) calculate that evaporation/condensation is unimportant in controlling pore mobility for pore diameters less than 20 μm. We do not include this mechanism in calculating pore mobilities.

A15-7 Surface and grain boundary energies

We follow Yan et al. (1980) in assuming that the surface and boundary energies are equal, and use Davidge's (1979, p.77) temperature-*in*sensitive mean value for Al_2O_3:

$$\gamma_S \approx \gamma_B \approx 1 \qquad [J/m^2]$$

A15-8 Dihedral angle

Experimental values for Al_2O_3 show a wide spread; details of experimental procedures need to be considered (App. 14; Francois and Kingery, 1967; Dynys et al., 1980; Porter et al., 1981; Dorre and Hubner, 1984, p.12; Handwerker et al., 1984; Bennison and Harmer, 1985a).

In the present calculations, we used an mean ψ of 90° for AVCO HPA, which we determined experimentally by TEM, from a number of internal pores in one foil (Ch.4). We used this to correct the capillarity component of the effective pore pressure (App. 3).

Fig. A15-1: Experimental diffusion and boundary mobility data for alumina. Values used in the numerical calculations for AVCO are marked with an 'X'.

a) Lattice diffusivities, after Dorre and Hubner's (1984) Fig. 2.8, with Dynys et al's (1980) data added.
b) Grain boundary diffusivities, after Dorre and Hubner's (1984) Fig. 2.9, with Dynys et al's (1980) data added.
c) Surface diffusivities, after Dynys et al's (1980) Fig. 4.
d) Boundary mobilities, normalized after Yan et al's (1977) Fig. 8 (see App. 9). The dotted line is the theoretical intrinsic mobility for pure alumina. Bennison and Harmer's (1985b) two data points are marked as 'd' for doped, and 'u' for undoped. The fan of three lines, from their doped point, correspond to activation energies of 400 to 600 kJ/mol.

continued...

Fig. A15-1 (continued)

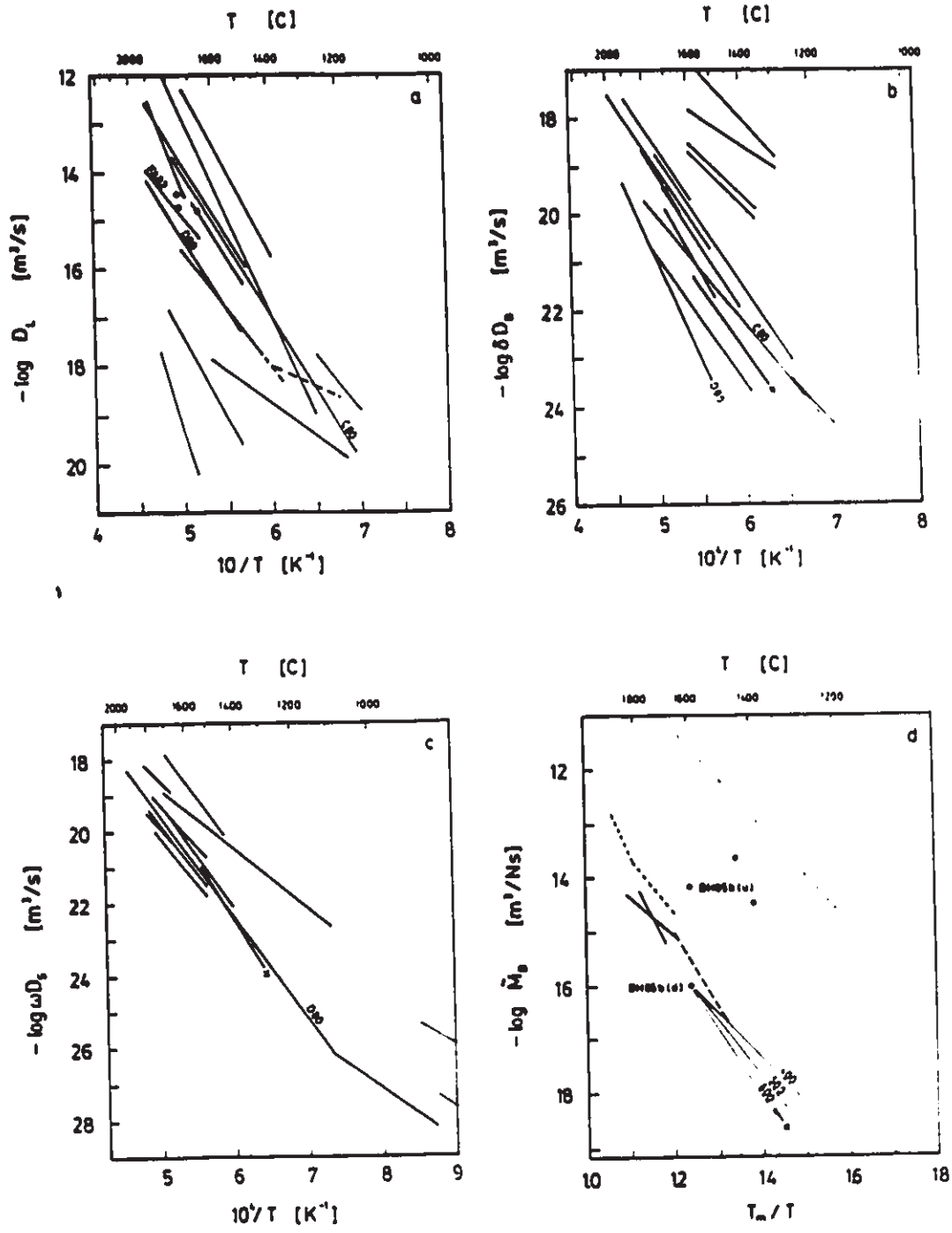

Appendix 16

Lattice and boundary control in diffusional pore growth

In the current numerical swelling calculations, we assume that the pressure-driven component of the pore growth rate, $\dot{r}_p$, was controlled by boundary diffusion. In this section, we justify that assumption by showing what contribution lattice diffusion should make to $\dot{r}_p$. Variables are listed in section A16-2.

A16-1 Analysis

The relative contributions of lattice and boundary diffusion to pressure-driven pore growth rate, $\dot{r}_p$, can be calculated by Wilkinson's (1978, p.31-4) scaling. Because he includes no coalescence, his *overall* pore growth rate is equivalent to our *pressure-driven* component. His rate of change of relative density (for either lattice or boundary control) can be written as:

$$\dot{\tilde{\rho}} = \left|\dot{V}_v\right|\Big|_{N_v} = 4\pi N_v r^2 \dot{r}_p \qquad (1)$$

From this, for lattice ('L') or boundary ('B') control:[1]

$$\frac{\dot{r}_p(L)}{\dot{r}_p(B)} = \frac{2}{\beta} \cdot \frac{rD_L}{\delta D_B} \qquad (2)$$

Substituting our ratio of grain boundary area per pore, $\beta = 1.8$, for his $n_B = 2$ (App. 6; Fig. 4-16), the transitional radius at which the contributions from the two mechanisms are equal is:

$$r_1 \approx \frac{\delta D_B}{D_L} \qquad (3)$$

For large pores ($r \gg r_1$), lattice diffusion controls. For small pores, ($r \ll r_1$), boundary diffusion controls.

From Eq. (2), with both lattice and boundary diffusion acting in parallel, the pressure-driven pore growth rate becomes:

$$\dot{r}_p(\text{mixed}) = \dot{r}_p(\delta D_B \text{ only}) \cdot \left(1 + \frac{r \cdot D_L}{\delta D_B} \right) \qquad (4)$$

from which $\dot{\mathcal{R}}$, the ratio of mixed to boundary-controlled diffusional pore growth rates can be written as:[2]

---

[1] Yan et al (1980, their Table 2) develop a similar expression for pressure*less* sintering, but omit the factor β.

[2] While this calculation is for a spherical pore, it should not change when the dihedral angle correction to P_{cap} is included (App. 3).

$$\dot{\mathcal{R}} = \left(1 + \frac{r \cdot D_L}{\delta D_B} \right) \qquad (5)$$

In Fig. A16-1, we plot the transitional radii, r_1, and the mixed/boundary pore growth rate ratio, $\dot{\mathcal{R}}$, for the boundary diffusion coefficient fit to the data (App. 15)), and two lattice diffusion coefficients: that given by Cannon et al. (1980: Q_L = 577 kJ/mol; marked as 'C' in Fig. A16-1 and as C80 in Fig. A15-1a), and that used by Frost and Ashby (1982: Q_L = 477 kJ/mol; marked as 'F' in Fig. A16-1 and as FA82 in Fig. A15-1a). Particularly for Cannon et al.'s (1980) D_L, we anticipate a significant lattice contribution to diffusional pore growth, for larger pores. In the current work, pressure-driven pore growth was rapid for small pore sizes only, so we did not add the D_L correction to $\dot{r}_p$.

A16-2 Variables

β dimensionless ratio of the grain boundary area in polycrystal, per pore, to the area of the single grain boundary plane in the representative spherical shell of radius *b*; [-]

D_B boundary diffusion coefficient; [m^2/s]

D_L lattice diffusion coefficient; [m^2/s]

δ width for grain boundary diffusion; [m]

N_V number of pores per unit volume solid; [m^{-3}]

r radius of mean pore; [m]

$\dot{r}_P$ pressure-driven pore growth rate component; [m/s]

r_1 transitional pore radius at which D_L and δD_B make equal contributions to $\dot{r}_P$; [m]

$\dot{\mathcal{R}}$ ratio of mixed pore growth rate to boundary-controlled pore growth rate; [-]

$\tilde{\rho}$ relative density; [-]

V_V volume fraction porosity; [-]

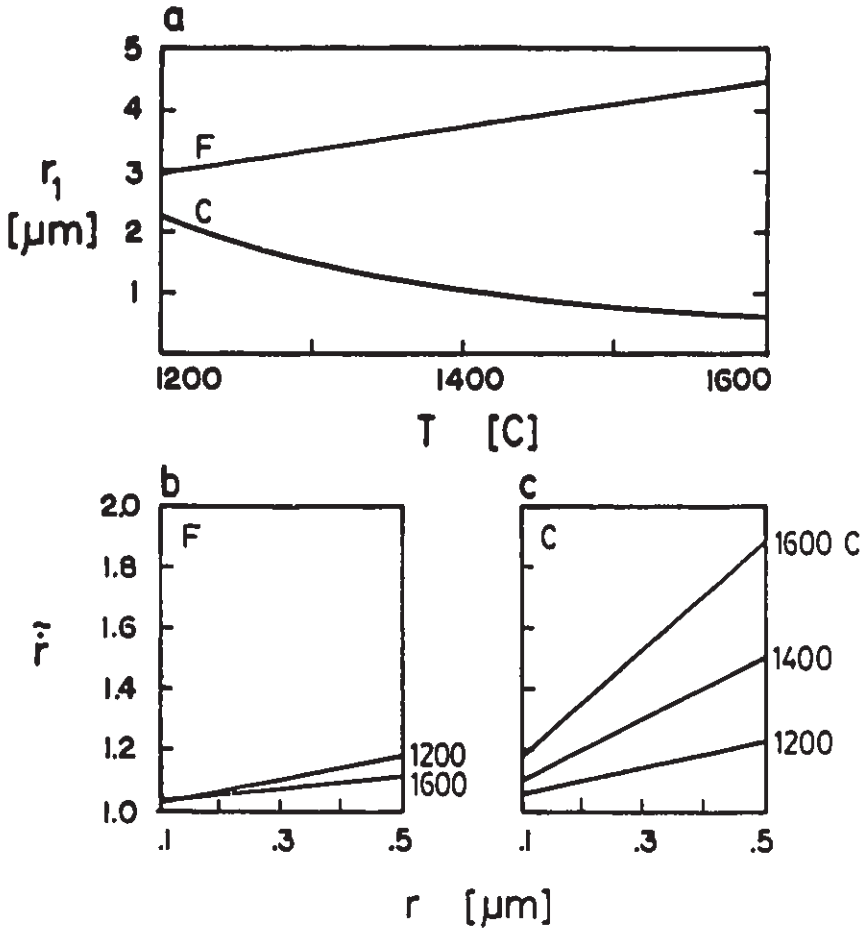

Fig. A16-1: Boundary vs mixed (boundary/lattice) control of the diffusional, pressure-driven pore growth rate, $\dot{r}_p$. 'F' denotes Frost and Ashby's (1982) D_L; 'C' denotes Cannon et al's (1980) D_L.

a) transitional pore radius, r_1, for which lattice and boundary diffusion make equal contributions.

b,c) ratio of $\dot{r}_p$ for mixed control, to that for boundary diffusion control alone.

Appendix 17

Determining model parameters

In this appendix, we discuss how values were determined for materials and adjustable parameters for the swelling model, during early numerical runs. We discuss first why $(P_i V_v)_{ehp}$ and T_{HP} were adjustable, then give a general picture of how the four main uncertain parameters interacted as two pairs (M_B and ωD_S, *vs* $(P_i V_v)_{ehp}$ and δD_B). Finally, we discuss M_B, Q_K, δD_B, $(P_i V_v)_{ehp}$ and T_{HP} individually. Variables are listed in sections 3.7 and 5.3.

A17-1 General

TEM data (Fig. 4-13) showed that AVCO's — but not ARCO's — as-received porosity was intergranular, as we assumed in the model. We therefore fit the numerical results *only to AVCO's* experimental data.

We fit several parameters simultaneously, comparing numerical to

experimental grain size, pore size and volume fraction porosity (Figs. 5-1,-3 and -4). Table 5-1 gives the final values used for AVCO, and also identifies appendices in which we discuss parameters in more detail. $(P_i V_v)_{ehp}$ and T_{HP} were treated as adjustable parameters,[1] because (1) the alumina was a commercial product, for which the exact fabrication conditions were not available, and (2) even if they *had* been available, gas-generating reactions may have occurred during hot-pressing, and the manufacturer could not be expected to have detailed data on this. For example, even though the press furnace may have been filled with Ar, or pumped towards a vacuum, the densifying compact would have outgassed during densification, so that the local atmosphere within the die and compact (which would be dependent on the materials and sintering schedule), would have controlled the composition of trapped gas, and so the pore pressures established in final-stage densification (e.g. Rice, 1969).

In general terms, the main results from fitting materials and adjustable parameters were the following. Although materials data for aluminas were available (App. 15), AVCO's lattice, boundary and surface diffusion coefficients, and boundary mobility parameters, were uncertain. During exploratory runs of the

---

[1] $(P_i V_v)_{ehp}$ was far more important an adjustable parameter than T_{HP}.

numerical model, during which parameters were fit, the intrinsic boundary *mobility* interacted strongly with surface diffusion coefficient, because pore mobility was linear in the surface diffusion coefficient, and together, boundary and pore mobilities controlled the grain growth rate, via M_B^{eff} (Ch.3's Eqs. 35,43; Fig. 5-1). At the same time, the boundary *diffusion* coefficient and $(P_i V_v)_{ehp}$ interacted strongly, because they controlled the *pressure*-driven pore growth rate, which, at short times, was far larger than pore growth rates due to grain growth-driven coalescence (Ch.3's Eqs. 17,19; Fig. 5-2). The two *pairs* of parameters interacted, because early pore growth rates (dominated by $(P_i V_v)_o$ and δD_B, via $\dot{r}_p$) largely dissipated the trapped gas driving force, and so strongly influenced grain and pore sizes at the transition to pore growth dominated by coalescence (Fig. 5-2), and so pore drag for the *rest* of swelling, and through it, via pore drag, long-term grain growth, and so pore coalescence rates. For reasonable values of materials parameters, the overall fit was much more sensitive to the boundary diffusion/pressure pair than to boundary mobility and surface diffusion.

We now discuss the materials and adjustable parameters in more detail.

A17-2 Individual parameters

M_B

The form of an expression for boundary mobility depends on the detail in data available (Yan et al., 1977; App. 9). We used a form suited to experimental grain growth data for the pore-free polycrystal. However, no grain growth data were available for AVCO's level of MgO doping, and, in Yan et al.'s (1977) Fig. 8 (see Fig. A15-1d), the boundary mobility data for systems most similar to AVCO included second phase drag. Bennison and Harmer (1985b) generated single phase grain growth data at 1600 C, for an MgO dopant concentration an order of magnitude lower than AVCO's. However, it is difficult to anticipate whether increasing the dopant concentration to AVCO's level would increase or decrease the mobility from their experimental value (Yan et al., 1977). For example, substitutional Mg should generate compensating point defects in the *oxygen* sublattice (Rasmunssen and Kingery, 1970), whereas *aluminum* ion diffusion should be rate-controlling for boundary and lattice diffusion (Frost and Ashby, 1982, p. 101). Consequently, we retained Bennison and Harmer's (1985b) 1600 C experimental rate constant, K_L, and their experimental grain growth exponent, m, of three, which was close to our experimental values.[2]

---

[2] Experimental m of between three and four were consistent with (a) at short times, a controlling boundary mobility, itself

Q_K

When boundary mobility is controlled by a segregated impurity atmosphere, its activation energy should be closer to that for lattice than for boundary diffusion (Yan et al., 1977). We generated fits for boundary activation energies between 420 kJ/mol (Q_B^{Al}) and 600 kJ/mol (high in the range of reported Q_L^{Al}: App. 15). As we did this, we compensated for changes in the boundary mobility parameters by small adjustments in surface diffusion parameters. Because unknown gases were trapped in pores, and the alumina was impure, these surface parameters were uncertain. In the results given here, we used a high reported lattice activation energy (577 kJ/mol; Fig. A15-1a,d) as the energy for boundary mobility, and a surface diffusion coefficient close to that of Dynys et al. (1980), but with a somewhat higher activation energy (650 kJ/mol; Fig. A15-1c). The results were rather *insensitive* to boundary mobility and surface diffusion parameters, but high activation energies were necessary for both, in order to fit grain growth data. (For lower values, the spread in numerical grain sizes, between 1350 and 1450 C temperature extremes, was somewhat less than in the experimental data.)

---

controlled by drag from a segregated impurity, giving an m of three, and (b) at long times, mixed pore drag/boundary mobility control, with relatively strong ωD_S-controlled pore drag, for which an m closer to four should hold (Brook, 1976).

δD_B; $(P_i V_v)_{ehp}$, T_{HP}

We fit the boundary diffusion parameters and the initial effective pressure simultaneously. In fitting P^o_{eff} (Ch.3's Eq. 18), the experimentally determined initial pore size and the global dihedral angle correction (App. 3) determined the initial capillarity component, P^o_{cap}. The applied pressure, P_{app} = 1 atm, was a known constant. Then, given the experimental as-received pore volume fraction, V^o_v, and assuming inert trapped gas only (i.e. P^G_{int} = 0), we adjusted the internal pore pressure/volume fraction porosity product at the end of hot-pressing, $(P_i V_v)_{ehp}$, to vary the initial effective pore pressure.

For pores closing at a relative density of 0.05 to 0.1, and a furnace atmosphere at 1 atm, then when no gas is lost from, or is generated in pores during final-stage sintering, $(P_i V_v)_{ehp}$ should have a value of 0.05 to 0.01 MPa at T_{HP} (App. 4).

We assumed a moderate hot-pressing temperature, T_{HP}, of 1500 C (Dorre and Hubner, 1984, p.204). The results were rather insensitive to this value, as it affected just the initial, inert trapped-gas component of internal pressure, P^I_{int} (Ch.3's Eq. 19), and, for the assumed T_{HP}, by only about five percent over the range of 100 degree C swelling temperatures. $(P_i V_v)_{ehp}$ was fit by bracketing experimental {V_v- and {pore size - grain size} data

points within the fan-shaped region bounded by constant-N and -f_3 numerical curves (Fig. 5-3,-4).[3]

In both figures, the numerical results, plotted *vs* grain size, were *in*sensitive to temperature, as were the experimental data. However, the *overall* fits of the fan-shaped regions between N and f_3 cases, to the experimental V_v and r data points, were quite sensitive to the assumed value for $(P_i V_v)_{ehp}$. The value used here, 0.02 MPa, is consistent with an applied hot-pressing pressure (P_{app}^{HP}) on the order of 20 MPa (App. 3-3), and was twice as high as the approximate *maximum* $(P_i V_v)_{ehp}$ of 0.01 MPa expected for purely inert, insoluble trapped gas. Some internal gas-generating chemical reactions apparently occurred during hot-pressing (App. 5).[4]

The fit value of $(P_i V_v)_{ehp}$ was rather *in*sensitive to variations in boundary mobility and surface diffusion parameters. However, it was quite sensitive to the boundary diffusion coefficient. The pressure-driven component of pore growth, $\dot{r}_p$, is linear in both

---

[3] The N/f_3 $\{r-\bar{L}_2\}$ fan rotated counterclockwise as P_{eff}^{o} increased (with $(P_i V_v)_{ehp}$). As P_{eff}^{o} increased, early pore growth rates and drag increased, which reduced grain growth rates throughout swelling.

[4] However, Fig. 5-9 shows that swelling could still be treated as due to inert gas, for the low P_{int}^{G} implied by $(P_i V_v)_{ehp}$ being close to 0.01 MPa.

P_{eff} and δD_B (Eq. 17 in the swelling model). So, as δD_B was reduced, $(P_i V_v)_{ehp}$ had to be increased, in order to maintain pore growth rates at short times. However, experimental {volume fraction - grain size} and {pore size - grain size} results were *linear* (Figs. 4-5,4-7), and this set upper limits to the boundary diffusion coefficient. For δD_B, then, we chose a pre-exponential and activation energy which converged to established data at high-temperature, and used as *low* an activation energy,[5] intermediate between Cannon et al. (1980) and Dynys et al. (1980), as still gave reasonably linear results (App. 15's Fig. A15-1b).

Dynys et al.'s (1980) δD_B, which was lower by at least an order of magnitude than the fit value, over the swelling temperature range, gave *linear* $\{\bar{L}_2 - V_v\}$ results, *even for constant-N_v runs*. For a $(P_i V_v)_{ehp}$ of 0.04 — twice the fit value — numerical and experimental swelling rates were similar for this case (and so the model can be fit to experimental results with reasonable values of all parameters *without* including coalescence. However, although δD_B were uncertain, the N_A results *cannot* be explained *without* coalescence.

---

[5] and so, as *high* a diffusion coefficient...

Appendix 18

Development of a uniaxial tensile test system

This section describes the uniaxial tensile test system which I designed, constructed and operated for creep fracture tests on HPA (Figs. 10-1,-2). The system was operated in dead load in the current work, but it also can be driven by an automated test frame — in tension, compression or bending — for which a common compressive/flexural load train and extensometer, but separate rigs, also were designed and built. If you wish further details of the system (e.g. mechanical drawings for the tunnel/shutter/window assembly) or comments on what should be changed, beyond those points noted in the text, please contact me. Section A18-4 lists full company names and locations of manufacturers whose products were used.

App. 19 discusses issues considered in designing the system. App. 20 describes improved tensile specimens and method of loading.

A18.1 Furnace

A cylindrical[1] clamshell furnace (Fig. 10-2) was built inside two rolled sheet steel shell halves, using insulating refractory board and cylinder (Zircar ALC, AL30, ZAL15, SALI).[2] the furnace's outside diameter was 300 mm; it was about 300 mm high. The hot zone was 150 ϕ by 150 mm high.[3,4] An insulating wall thickness of 75 mm proved to be satisfactory for tests to at least 1450 C. The 50 mm gap between the 25 mm thick wall of central cylinder, and the steel shell, was packed with bulk refractory fiber (Carborundum 'Fiberfrax').

A rectangular well, about 37w x 50h x 37d mm, was made in the rear insulating wall; opposite it, a rectangular, tapered

---

[1] A hexagonal or octagonal outer shell would be simpler to construct.

[2] All board machining was done with standard woodworker's router bits, on a drill press, using 12-20 thick mm plywood jigs (e.g. a simple turntable on which discs were milled). Before being machined, boards were submerged briefly in water, to prevent dust being generated during machining.

[3] Dimensioning abbreviations are: ϕ, diameter; w, width; h, height; d, depth; l, length.

[4] To minimize temperature gradients in specimens, near SiC pull rod ends, we would increase this hot zone height somewhat in the next furnace (say, to 150 ϕ x 250h mm).

sighting tunnel,[5] with an opening about 5w x 50h mm in cross section was made in the front half-cylinder. The well and tunnel were located so that a specimen would be between them during a creep test. To close the outside end of the sighting tunnel, an assembly was made to hold a plane, 80 ϕ x 10 mm thick crown glass disc (Spindler and Hoyer 39 0020) as a window, inside of which a 5 mm thick shutter of insulating board could be slid, to reduce radiative heat input to the glass disc.

Cross-shaped insulating inserts ('plugs'), 10 mm thick, were placed inside the well and tunnel, at the hot face end of each. Shaped to be complementary to the four flags to be sighted on a specimen (see Fig. 10-1a, and the insert at left of Fig. 10-2),[6] they served as radiative heat barriers. The rear plug kept the well cooler than the furnace's interior during a test, so passively generating the visual contrast by which a specimen's flags could be seen at high temperature.[7] The other reduced heat

---

[5] Carefully tapered to the minimum width profile that still permitted the swiveling telescope to sight a specimen's flags (i.e. narrower at the cold end). This taper, along with the plug insert at the hot end of the sight tunnel, minimized heat input to the window assembly.

[6] New inserts quickly can be made from scrap pieces of insulating board, to suit a new specimen design.

[7] Wiederhorn et al. (1988) show a very simple way to build a cool chamber inside an existing furnace, without modifying it.

input to the outer elements of the sight tunnel assembly. (This assembly was further protected by the insulating shutter, which was only opened to permit flag locations to be determined — say, every few hours during a creep run.)

The furnace was heated by six axial SiC elements (I^2R 'Starbar' Type RR, 3/8" ϕ x 6"HL x 17"OL),[8] driven by a PID control system (Eurotherm 810, 831, with variable transformer control of input voltage to the power controller: Powerstat 136BU).[9] A Type B control thermocouple, in a high-purity alumina insulator and sheath (Omega 'Omegatite 450'), ran radially and horizontally through a rear wall, between heating elements. Its hot junction was just beside the gauge length of a specimen during a creep test. In order to minimize temperature errors, the 0.010" diam. thermocouple wire was replaced frequently, and was repositioned carefully for each test (Bently, 1981; Froschauer and Schmidt, 1977).[10]

---

[8] In I^2R's literature, HL refers to heating length, and OL to overall length.

[9] Recently introduced control systems will drive SiC elements *without* requiring a variable transformer.

[10] See comment on thermocouple materials and maintenance in Ch.2, sectn 2.2. See also App. 21, which raises questions concerning temperature control in the overall flexural/tensile test series.

A18.2 Test machine and load train.

For the initial tests reported here, the tensile rig was adapted to a dead-load tensile creep tester (Satec, Model CE; 12000 lb capacity). Flat 'dogbone' creep specimens, 20w x 80l x 3d mm (Fig. 10-1a), were pinned with HP/SiC pins (6.4 ϕ x 25l mm) into 4.0 mm wide slots in the ends of cylindrical, 25 ϕ x 400 mm recrystallized SiC pull rods (Norton 'Crystar'; Fig. 10-1b). At their cold ends, about 120-150 mm from the outer faces of the furnace ends, the pull rods were again slotted, and were pinned, with steel pins, into standard universal joints (Boston Gear J125B), using machined steel adapters. The *lower* universal screwed onto the top end of a 20 ϕ mm steel rod,[11] whose lower end was threaded. This end ran through an oversize hole in a horizontal steel plate on the test frame, beneath which it was turned into a horizontally-split nut/washer with a greased, spherical mating surface.[12] This rod and nut served to adjust the

---

[11] Aluminum rod would be lighter, though, in the current tests, the weight of the lower load train imposed negligible stresses on a specimen, relative to the applied stress.

[12] When a specimen broke, a set collar, secured to the lower rod a short distance (5 mm) *above* the frame's lower steel plate, caught the lower load train, whose upper end — an incandescent pull rod end and broken half-specimen — then remained *inside* the furnace, held gently in the SiC rod's cutout in the furnace floor. As the lower load train fell, a rubber ring between the set collar and the steel plate cushioned the impact.

height of the specimen in the furnace. The *upper* universal joint fastened to the 20:1 load lever arm, via the Satec's existing pivoting adapter.

The furnace sat on a 6 mm thick steel shelf bolted to the tester machine's frame. Its rear half was held in position by a locking nut *set* on each of four studs on the front face of the frame. Each stud engaged a sheet metal tab screwed to one corner of the flat face of the rear furnace half. During a test, two spring-loaded steel clips held the furnace shut, like a suitcase. When these were released, the front half of the furnace was free to open. It was supported by the shelf while it was open.

The load pan, hung from the far end of the lever arm by a flexible length of sprocket chain, rested on a leadscrew-driven elevator. The fixed-speed, electric elevator drive was replaced with a reversible, variable-speed DC motor (Doerr Stedi-drive 059139, 1/4HP), which drove the leadscrew through the Satec's speed reduction gearbox.[13]

---

[13] For strain-gauged tests (which have not yet been performed) this should permit gently *un*loading a partially loaded, *mis*aligned specimen, in order to adjust its position. During loading, the multiple gauge signals should be logged, translated continuously into axial and bending strains, and displayed graphically by microcomputer. In the current work, it was used for unloading and reloading specimens in step-

A18.3 Optical extensometry.

Specimen creep elongation was measured by a 30 power telescope[14] (Spindler and Hoyer 45 0100, 03 8242, 44 9004) from outside the furnace. The telescope crosshairs sighted the knife-edge flag machined into each of four shoulders of a specimen (Fig. 10-1a) through the glass disc, down the sight tunnel (Fig. 10-2). With a bright specimen flag silhouetted in front of a plug *cutout* at the hot face of the cool well, visual contrast was quite adequate for extensometry at 1250 C. No green or blue optical filters (e.g. Spindler and Hoyer BG23, BG38) were necessary; for tests at 1250 C no eye protection was used.

The telescope was mounted, via custom clamp blocks, on an optical grade travelling stage (Micro-controle UT 100-50 MN). This stage had a 50 mm travel, and a micrometer-driven leadscrew with 1 mm pitch and a 10:1 gear reduction head. The micrometer's mechanical vernier scale had a resolution of 1 μm. The stage was mounted vertically on an extruded aluminum post (Micro-controle X95, CX 95 50), which was bolted to a micrometer-driven/quick release rotary base (Micro-controle TR 160). The combination of vertical stage and rotary base permitted specific target points on each

---

stress-change tests.

[14] A higher power — say, 50 X — would be preferable.

specimen flag to be located throughout a long creep test, with a typical precision of ±5 μm for the first generation of tests. The telescope's front lens was some 275 mm from a creeping specimen.

A18-4 Manufacturers

Duerr Electric; Cedarburg, Wisconsin.

Eurotherm Corp.; Reston, Virginia.

I Squared R Element Co.; Inc., Akron, New York.

Micro-controle; Evry, France.

Norton Co.; Worcester, Massachusetts

Omega Engineering; Stamford, Connecticut.

Satec Corp.; Grove City, Pennsylvania.

Spindler and Hoyer; Gottingen, West Germany.

Zircar Products, Inc.; Florida, New York.

Appendix 19

Uniaxial tensile creep test system design for high temperature structural ceramics

This section discusses factors in high temperature tensile test system design, in order to build a context for the current and proposed systems (Apps. 18,20). The discussion is oriented to research groups which may not have the resources to purchase the commercial test systems developed recently.

It is important to keep in mind the materials specificity of creep deformation and damage demonstrated by comparing flexural and tensile results for Si/SiC (Wiederhorn et al., 1986c,1988; Carroll and Tressler, 1988) with those reported here for HPA (Ch.12). Creep ductility is an important factor in designing inexpensive test systems, and Si/SiC is far less creep ductile than HPA. It should also be kept in mind that resources are seldom available for rapid, systematic trail and optimization of such systems; in different sections of this report, we present results on an initial system, and suggestions for an improved configuration.

A19.1 General

Specimen, load train and extensometer designs are closely linked. Ignoring here almost all questions related to the frame on which the tensile load train is mounted, and how the test trajectories are controlled (i.e. constant $\dot{\varepsilon}$, σ or load),[1] it is desirable to have:

1) the smallest specimen consistent with the stock supplied, the data sought (e.g. creep parameters, or damage and failure processes) in relation to extensometry, and with stress concentrations in relation to expressed material quality,

2) minimum total costs for both the load train and specimen (including flags); minimum hand finishing for the specimen; and both specimen dimensions and surface quality insensitive to machining and hand-finishing variations,

3) an inexpensive, durable load train, in which specimen/rig misalignment reliably can be held to tolerably low levels *for specific tests/materials*, and

---

[1] See constant-stress comments in App. 20, and Ch. 13.

4) robust, inexpensive extensometry, given the data sought, specimen design, material behavior under specific test conditions, and test machine control. (This includes flags, extensometer and data analysis.)

Machining contracts placed for high-T tensile research projects in ceramics are typically small, and only a few shops are capable of machining tensile specimens. For these reasons, when careful, nonstandard machining is sought (e.g. with post-machining metrology on each specimen) there is *no* substitute for close working relations with diamond machinists... Similarly, because damage accumulation studies are sensitive to materials quality, close contact with materials manufacturers is important.

A19.2 Specimen design

A19.2.1 Stock

Hot-pressed billet stock imposes constraints on specimen size which may not apply for sintered stock. Minimum specimen size, in relation to the specific billet stock supplied, *may* reduce data scatter, and should reduce materials and machining costs. Flare radius and head dimensions are more important factors than gauge length, in determining overall specimen size.

When stock permits, long specimens can extend on either side of a

mini-furnace, permitting cool grips to be used (Matsue et al., 1983; Fryer and Roberts, 1966). While, for tensile tests, the advantages of a compact specimen often will be more important, this principle could be used for the *multiaxial* tests required to determine damage mechanics parameters (Ch.9). Tubes could be machined from HP billets (with the tube axis normal to the HP direction) with a thinned gauge length and machined-in extensometer targets (Trampczynski et al., 1981). Such tubes could be tested in torsion and tension/torsion, with a miniature furnace and cold grips.

A19.2.2 Stress concentrations

We consider *elastic* stress concentrations only, as tentative specimen design guidelines. Creep stress redistribution, and materials and machining quality — expressed in damage processes specific to the material and test conditions — complicate using such predicted stress distributions as design criteria.

A19.2.2.1 Pin loading *through* the specimen head: Pin holes[2]

Flat 'dogbone' specimens, loaded by single pins, have been used by Govila (1982, HPSN; 1983, SiC), Wakai (1986), Wiederhorn et al. (1988; Si/SiC) and Carroll and Tressler (1988; Si/SiC).

---

[2] In App. 20, we recommend a specimen which is pin-loaded from beneath its flared shoulders.

Peterson (1953, p.81,99) summarizes *elastic* stress concentrations around a pin-loaded hole in a finite plate.[3] Frocht and Hill's (1940) strain gauge and photoelastic data suggest how other factors (such as the head height/width ratio and the pin/hole clearance) will affect the elastic stress concentration at such a pin-loaded hole in a finite plate.

Bevels on the pin hole *rims* aim to reduce parasitic bend stresses on one axis, and to eliminate machining damage, especially on the side on which the diamond drill emerges from the specimen. The flat bevels used in the current specimen were inexpensive to machine; however, the most effective bevels for bend stress reductions would be smooth, elliptical flares, with, say, the center third of a hole profile having a rather flat curve (personal communication, G.F. Lukas, MTS Systems Corp.).

If pin holes are not drilled with appropriate equipment and schedules, chipping and cracking will occur around the *exit* rims. In such a case, flat bevels sufficient to eliminate the chips — but not necessarily the associated sub-surface cracks — will have to be so large that the tendency for cracks to propagate from pin hole rims will be increased well beyond predictions for

---

[3] For pin/head ratios typical of ceramic tensile specimens, the K_{tb} curve of his Fig. 83 is appropriate.

flat plates. Minimizing exit rim damage is an issue that must be resolved with machinists.[4]

Offsetting this stress concentration is the small volume of material sampled by the extreme stresses. Material quality introduces a random factor: in the current flexural tests, cracks initiated from microstructural heterogeneities even at steady state tensile face stresses just over one half the transitional stress for rapid failures (100 *vs* ≈ 200 MPa: Ch. 11).

A19.2.2.2 Stress concentrations: flares

Peterson (1953, p.66,69) suggests that stress concentrations at flares are less important than those at pin holes. However, the current specimen dimensions fall far to the right of the data he presents. Wiederhorn et al. (1988) report Si/SiC specimens for *both* pin-and-clevis and 'clothespin' shoulder loading, which have very small flare radii. Materials-specific minimum flare radius is an unresolved design issue at this time.

A19.2.3 Specimen cross section

Specimens with *rectangular* cross-sections are potentially inexpensive to machine (Wiederhorn et al., 1986b), given hot-

---

[4] How serious it is in a given case may be materials/test condition dependent.

pressed billets of adequate thickness. Hand-lapping and -beveling such specimens calls for non-standard diamond tooling, is potentially unreproducible, and is tedious; beveling and lapping should be either done by the machinist or eliminated.[5] The machinist may be able to finish-lap the specimen. However, it may be more reasonable to eliminate lapping altogether, and so to sacrifice the surface damage data available from lapped specimens, in favor of data on damage processes at surfaces which have the rougher machined finishes anticipated for production parts.

In *longitudinally* grinding the narrow gauge length faces of rectangular specimens, in materials of moderate quality, chipping may occur along face edges.

It would be useful if specimen blanks which had been *sintered* as rectangular bars, could be machined to dogbone shape on narrow sides only, in order to compare creep damage processes on machined and as-sintered surfaces, in one specimen. However, specimens tend to warp in sintering, and this will limit the range of materials on which such comparative tests can be carried out.

---

[5] The hybrid axisymmetric design described in App. 19 eliminates such beveling by having an *axisymmetric* gauge length.

Fully axisymmetric specimens are potentially inexpensive to machine accurately. The cost and complications arise in making and maintaining suitable grips. Pears and Digesu (1965) described a buttonhead specimen system with metallic grips, for controlled atmospheres.

Axisymmetric specimens with *flared* heads and powder cushion grips have performed well (Lange et al., 1979; Lange and Diaz, 1978). The necessary hot grips will be more expensive, and will demand more design and operating skills than simple pin/slotted ceramic types.

Gruffel et al. (1988) report test results from a carefully designed tensile rig similar to Lange et al.'s (1979), but without powder cushions. The axisymmetric specimen is simple and compact. The axial extensometer's probes contact the pull rod assembly ends, and automatic data logging is routine, via the external LVDTs. Constant-stress tests therefore are possible. Given that ceramic materials for the rig are chosen well, and that clearances, materials sticking together at high temperatures, and machining are handled, this is a very attractive system.

A19.3 Extensometry

A19.3.1 Automation

For creep damage accumulation studies, automatic extensometers are better than manual for detecting and recording *abrupt* tertiary creep transients. However, if only creep deformation parameters need be determined, or if tertiaries develop gradually, this is less important, and manual extensometry — which is less costly — will serve. However, deformation feedback for test machine control will call for automated extensometry (contact or optical).

For high temperature studies on structural ceramics, any hot-zone extensometer parts will have to be machined from ceramic materials themselves. If they contact the specimen, provisions intended to prevent relative movement or chemical reactions at the contact points must not affect the specimen performance. For long-term, high-elongation damage studies, this requires care.

Lange et al.'s (1979) axial contact extensometer permits automatically recording strain data from LVDTs external to the furnace. In typical use, such a design need not bias damage processes in a specimen. However, designing, machining and maintaining such an extensometer is far more demanding than for *non-contact* types. The simpler axial contact extensometer reported by Gruffel et al. (1988) transfers most of these

concerns from the extensometer to the ceramic pull rod assembly, and is very attractive. (In App. 20, we discuss an alternative design which uses commercial contact extensometers which have simple ceramic parts.)

Among *non-contact* extensometers, an *automated* optical unit was described by Pears and Digesu (1965); they are available commercially at considerable cost (e.g. Zimmer). Components are available from which such systems could be assembled — such as stepper-motor driven, precision translation stages (e.g. Micro-controle), and microcomputer-based motor controllers.

A19.3.2 Optical extensometry: flags

When specimen size permits, and particularly when damage processes or large strains need be studied, machined-in ('integral') gauge length flares are attractive (Wakai, 1986). (Carroll and Tressler (1988) report using a similar specimen.)

In Wiederhorn et al.'s (1986b) flag system, indented, refractory wire flag extenders permit using a short-travel (e.g. 20 mm) translation stage (which is less expensive than a 50 mm unit, and minimizes the time required to take an elongation reading). If the ceramic parts of the flags do not slip or rotate[6] at high

[6] These flags will tend to rotate at large elongations, as gauge

elongations (HPA reaches creep strains an order of magnitude higher than Si/SiC; Wiederhorn et al., 1986c; Gruffel et al., 1988) gauge length strains can be calculated directly and accurately. Also, a small flare radius — and so, a compact specimen — should be possible, stress concentrations permitting. If such flags can be *re*used, they should give low total specimen/flag machining costs. For damage/failure studies, however, they must generate no fatal cracks from contact points. For these reasons, such flags will need to be tested for specific materials.

In contrast to the above flags, shoulder flags of the type used here cannot generate gauge length cracks. (Because they were fail-safe, they were chosen for our initial tensile tests on HPA.) However, calculating gauge length strains from specimen elongations measured at such flags is less direct than for either Wiederhorn et al.'s (1988) or integral flags (App. 20). At higher strains and cavitation levels, any such analysis is complicated by strain and cavitation gradients in flares. As important,

---

length cross-sectional dimensions decrease. Rotation magnitudes depend on several interrelated dimensions, as well as strain. Target points on upper and lower flag extender wires will rotate in *opposite* directions, relative to the gauge length, and, in most configurations, the magnitudes of the horizontal and vertical rotation components will differ between the two wire targets.

extensometry for shoulder flags is vulnerable to temperature gradients in the flares, particularly with small specimens and SiC pull rods. It is important to have a furnace hot zone tall enough to minimize temperature gradients at the specimen caused by heat loss down the pull rods, and by cold air leaks around the lower rod.

A19.3.3 Extensometry: visual contrast

A simple, passive cold 'well' gives good visual contrast for tests at 1200-1300 C. The type described in this report (Ch. 10; App. 18), was built into the wall of a furnace. Wiederhorn et al. (1988) show an alternative design that requires no modification to the furnace. They report using a high-intensity external light source and blue-green optical filter at 1300 C. For tests at 1250 C, we found filters unnecessary (e.g. Spindler and Hoyer BG38, BG23).

A19.4 Load train: alignment and materials

Christ and Swanson (1976) review alignment problems. Design considerations can be invalidated by inaccurate machining, low quality materials, careless test setup and poor system maintenance.

Alignment issues include provisions for sealing the furnace

against cold/hot air leaks around pull rods — without introducing stray bending stresses — which in turn relates to how the system design permits ready access to the specimen during loading, in order that initial alignment can be optimized.[7] This is a significant issue in a furnace designed to permit not just tensile, but also compressive *and* flexural tests (as was the current unit), because the lower tensile pull *rod* almost certainly will have a different diameter than the support *tube* for the other two tests. (Such a tube surrounds three extensometer probes (e.g. 3 ϕ mm alumina rods), which permit sensitive *differential* extensometry (by LVDT) of either compressive or flexural specimens.)

In the current tests, end-slotted, cylindric pull rods of commercial recrystallized SiC[8] performed satisfactorily (Fig. 10-1b). Materials and machining costs were relatively low. It is important that the hot pins and hot ends of the pull rods do not deform, either in controlled tests, or in accidental temperature excursions. Oversize (e.g. racetrack- or keyhole-shaped, Fig. 10-1a) pin holes will release deformed pins. Rod-end deformation

---

[7] A simple *cylindrical* furnace, constrained to slide vertically on guide rods, to clear the specimen, would be easier to build and seal than a clamshell design.

[8] Norton 'Crystar'.

which is not removed by remachining is likely to cause pins to break in subsequent tests, on or soon after loading. Large-diameter pull rods and hot-pins minimize these potential problems — for single-pin loading, at the cost of a larger specimen. For double-pin/shoulder loading (App. 20), this should be less important an issue.

Hot-pins must not fail by shear in long creep tests. For one-pin systems, the safest approach probably is to have large pin diameters and minimal clearance between the specimen head thickness and its rod-end slot, and to use a *fresh* pair of pins for each specimen. Pins are relatively *in*expensive; for the current specimen design, such a replacement schedule would add roughly 10% to the total specimen cost. Two-pin systems such as that proposed (App. 20) should be more forgiving.

In this work, hot-pin materials were not yet optimized; HP/SiC currently seems more durable than the recrystallized SiC from which the pull rods were machined.

It is desirable that hot pins not stick to the load rod holes in which they lie, or to the specimen. Many factors are involved (G.D. Quinn, personal communication). When pins stick, a targeted HF soak may be needed in cases where a moderate and carefully

considered blow does not release the parts following a test.[9]

Pin/slot loading is simple, but misalignment must be held reliably to low levels (in relation to damage tolerance) in each specimen. Stress analyses for eccentric loading are available (Christ and Swanson, 1976). When alignment must be guaranteed, each specimen likely will need to be strain-gauged. In such multiple-gauge tests, instrumentation must be considered carefully (Omega, 1987). For *lapped* specimen surfaces, gauge adhesives must be tested for the specific material and surface finish; little or no manufacturers' data apply to such surfaces. Leads must be soldered to gauges and bondable terminals *before* these foils are glued to a brittle specimen which is prone to damage by thermal shock. Purchasing gauges with *attached* leads will reduce the number of soldering operations. Wiederhorn et al. (1988), using LVDT-based measurements of curvature in crept Si/SiC specimens, report bending stresses of between 8 and 10% of the total tensile strain for their 'clothespin' rig, and of 6 to 8% for through-pin tests by Carroll and Tressler.

---

[9] In many cases, with a wood block held carefully between the steel tool and the ceramic target.

Appendix 20

Recommended uniaxial tensile creep test systems

This section describes several variations on an attractive uniaxial tensile, high temperature test system — specimen, extensometry and loading. First, the specimen form and loading are discussed. Specific recommendations then are made for specimens for optical, and then commercial contact extensometry. Finally, brief comments are made on using either type of extensometry in constant-stress, as opposed to dead-load tests.

A20.1 The specimen and loading

A hybrid specimen, with an axisymmetric gauge length, but flat, rectangular heads, was used by Ohji et al. (1987). It is similar to that drawn in Fig. A20-1, but does not have the flags on the gauge length. It offers many advantages, but demands a specific machine tool, in that it is machined longitudinally while being

rotated on centers.[1]

As sketched, Ohji et al. (1987) used double-pin loading under the flared specimen shoulders, instead on single pins through the specimen heads (as in our first specimen, Fig. 10-1). The heads then are quite short and narrow (giving a compact specimen), and there is no danger of cracks propagating from pin holes. (Such cracks caused problems in the first generation of tests, Ch.12.) While this is the loading geometry used in Wiederhorn et al.'s (1986b,1988) 'clothespin' rig, the pull-rod version described here should generate less misalignment *at high elongations* than such a rig, and no more than other simple pin-and-clevis rigs now in use (Wiederhorn et al., 1988). It is well suited to work in which 'some' misalignment can be tolerated, but in which very high elongations may be encountered — typical of HPA in creep fracture (Ch. 11; Dalgleish et al. (1985); Gruffel et al. (1988).

The axisymmetric gauge length will be ground *longitudinally*, and will be axially aligned.[2] Chipping while machining long faces of

---

[1] At least one such tool now is available in continental North America, and initial quotes indicate that specimen machining costs should be *lower* than for the first test specimen (Fig. 10-1a).

[2] For shoulder loading, the care required to align head through-holes with the gauge length in machining is replaced by the care needed to machine pin holes in pull rods accurately,

a rectangular gauge length will be eliminated, as well as beveling the long edges of the gauge length.[3]

Finish-grinding the entire central region of the specimen — flares, flags and gauge length (and the final gauge length lapping, if it is called for) — can potentially be done with a single, numerically-controlled tool path, while the specimen is rotated slowly, on centers, beneath a high-rpm, small-diameter diamond tool. Numerical control is not essential, but would make a wide range of flare profiles practical. Materials-specific flare design is currently an unresolved issue in creep fracture studies.

If specimen gauge lengths are to be *lapped*, it would be advantageous from the standpoint of the research group to have this operation carried out as the machinist's last operation, to eliminate hand-finishing in the lab. Alternatively, it may be as reasonable to eliminate lapping altogether, by working with *ground* finishes. Less-detailed surface damage data would be available than from lapped surfaces, however, data would be

---

and to set up the test accurately.

[3] Beveling still will be needed on flares at pin contact regions, for two-pin loading, as in Wiederhorn et al.'s (1986b) specimen for the 'clothespin' rig. It still will be needed on pin hole rims, for one-pin loading.

generated for damage processes at surfaces which have had standard industrial finishing schedules.

Such a hybrid design *could* have a through-hole head design similar to that of our first-generation specimen (Fig. 10-1a). If single-pin, through-head loading is chosen (instead of two-pin shoulder loading), the centering dimples needed in each end of the specimen for the axisymmetric grinding operation could serve to locate the specimen in a jig for drilling and finishing the through-holes accurately.

Ohji et al.'s (1987) load train was made of Mo, and was intended for high temperature tests in vacuum. For tests *in air*, similar hot universal joints probably could be machined in SiC, though machining costs, as well as clearances to recommend in mating parts (in relation to rig misalignment on the one hand, and materials sticking together after high temperature tests on the other) are currently uncertain. For rather ductile materials (such as HPA under the current test conditions), such double-pin loading probably could perhaps be used with simple, *one-piece* SiC pull rods similar to those in the current rig. In such a case, alignment would depend not on hot universals, but instead on metal universals at *cold* rod ends (as in the current load train), and on accurately machined hot-pin holes and specimen slots.

A20.2 Optical extensometry

If the hybrid specimen is machined with small flared flags at the ends of the gauge length, combining the designs of Wakai (1986) and Ohji et al. (1987), direct optical extensometry is possible, to high elongations (Fig. A20-1). Elongations are readily translatable into strains, whether or not significant creep cavitation occurs.[4]

There are no concerns connected with using separate, slotted flags placed on the gauge length (Wiederhorn et al., 1988: Si/SiC).[5] The high-elongation complications of the shoulder flags used in our first generation of tests are eliminated,[6] and the system is less sensitive to errors due to temperature gradients near pull rod ends.

There is no need that the specimen be thick enough that the flags are *completely* axisymmetric, as long as the specimen is tested so that its flat face is normal to the external extensometer

---

[4] Though constant-volume and dilational strain components cannot be separated during a test from such a single measurement (Raj, 1982b).

[5] Flags may slip or rotate at high elongations.

[6] One-dimensional deformation cannot be assumed, and cavitation gradients develop in flares.

telescope (as in the current tests). A specimen blank just over 3 mm thick should be adequate, depending on the amount of material to be removed in machining.

Fig. A20-1 is semi-schematic. Key dimensions are left unspecified, because no design so dependent on understanding diamond machining operations and tooling, and on specific machine tool capabilities, can be optimized without close consultation with experienced machine shop personnel.[7] On the other hand, the specimen probably is close to a reasonable final design, in that it uses several of Ohji et al.'s (1987) overall dimensions. It is somewhat more compact than the first-generation specimen used here (Fig. 10-1a).[8,9]

The specimen is drawn for a gauge length about 25 mm long; a more

---

[7] From our experience, some time should be spent *at* the machining facility.

[8] Largely because of the compact heads possible with shoulder loading.

[9] Also, as sketched, it should be machinable with only two sizes of rotary tool: one for the flares, and one for the flag root radius. Finally, the implied tool paths are simple. (These comments are tentative: the proposed design is not optimized for machining.) The small diameter tool which shapes the flags will need to run at very high speed in order to maintain *surface* speeds within recommended ranges.

compact specimen would result if the gauge length were shorter. No centering dimples are drawn in specimen ends, though they likely will be needed by the machinist.

For simplicity in a schematic diagram (Fig. A20-1), pin holes in the pull-rod ends are sketched with *circular* cross-sections. However, as for the first-generation design, some clearance should be left, against the possibility of pins deforming by creep during high temperature tests (Fig. 10-1b; App. 18). (This should be less of a problem with a smaller gauge cross sectional area, and with two pins per head, as opposed to one; however, the cost of a jammed pin is high.) Such clearance can be provided by axially-elongated holes (perhaps of keyhole shape, as used here: Fig. 10-1b). Accurate machining of pin holes in pull rods is critical, in order to minimize unwanted bending stresses.[10]

A20.3 Contact extensometry

Side-mount contact extensometers are available commercially (e.g. MTS Systems Corp., Series 632.xx), for measuring axial and diametral strains at high temperatures. These are either self-supporting, or are mounted on an external wall of the test furnace or on the test frame. They contact the specimen gauge

[10] As is careful test setup, for double-pin configurations.

length via pairs of horizontal probes (two and one pairs, respectively, for axial and diametral types). In each pair, one straight probe touches the specimen with a rounded end, and the other probe, slightly longer and hooked, curls around the opposite side of the specimen and holds it against the straight probe's tip.

For tests on HPA, such probes could be in flame-bent sapphire, rod stock for which is readily available. Such probes should not slip, initiate damage or bias damage processes in the specimen. Creep in the probes will have to be evaluated and handled.[11]

For *axial* extensometry, probe pairs could be placed close together at the start of the test, so that, even at high strains (e.g. $\varepsilon_f \approx 0.5$ in HPA at 1450 C: Gruffel et al., 1988), probe travel limits should not be a problem. *Diametral* extensometry may not measure generalized cavitation damage accurately, as this damage, depending on whether equiaxed or crack-like cavities dominate, will have a dominant *axial* strain component.[12]

---

[11] For tests on carbide or nitride systems, polycrystalline probes of similar materials likely could be fabricated by, e.g., extrusion and hot post-forming (given suitable binder systems), followed by sintering and possibly heat treatment (e.g. recrystallization).

[12] On the other hand, if constant-stress tests are based on the external load-bearing area, diametral extensometry may well

For such tests, a simpler specimen design than the previous one should be suitable — one similar to Ohji et al.'s (1987), with a plain axisymmetric gauge section and flat dogbone ends. (That is, similar to Fig. A20-1, but without the flags.) Either through-hole/single-pin loading (as in the current tests), or shoulder/double-pin loading could be used.

A20.4 Constant-stress tests

The high creep ductility of HPA makes constant-stress tests more attractive than dead-load for characterizing materials behavior (e.g. stress-strain rate relations).[13] Constant-stress tests require either a shaped loading cam on a dead-load machine, or continuous extensometry for feedback control of an automated test machine.[14]

---

serve.

[13] This is more an issue for HPA than for Si/SiC, which has failure strains an order of magnitude less.

[14] The axial contact extensometer described by Gruffel et al. (1988) is attractive, particularly if its designers were willing to share details of its design and materials choices. It represents an alternative to the systems described here, which build on the current rig.

If contact extensometry can be made to work, automated optical extensometry likely will be less attractive, because it will be more costly (even though the specimen sketched, Fig. A20-1, should be as well suited to manual as automatic to optical measurements.) A contact extensometer will make continuous strain data routinely available, and so could be used for feedback control of an automated test machine.

Constant-stress tests likely could be generated for *either* type of specimen/extensometry — flagged optical or contact — using a dead-load test machine with a logarithmically-shaped loading cam.

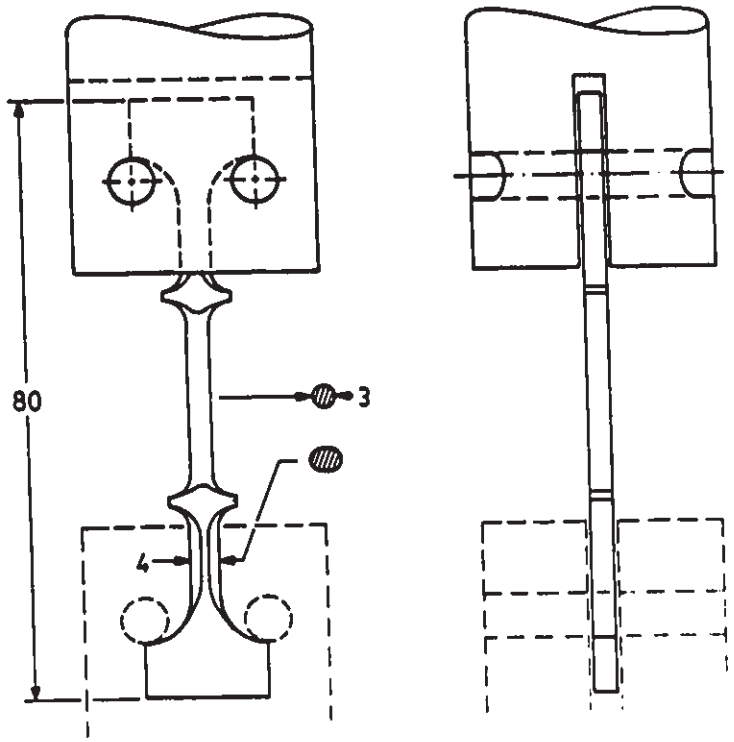

Fig. A20-1: Proposed, second-generation, uniaxial tensile test specimen (semi-schematic).

Appendix 21

Uniaxial tensile *vs* flexural strain rates

In this section, we use Chuang's (1986) results to derive an equation for the ratio of *calculated* strain rates for uniaxial tensile *vs* flexural creep tests — for a given material, at the same temperature and applied stress in each test. In terms of the initial elastic stress at the tensile face of the bend specimen, $\hat{\sigma}_{el}$, this ratio is:

$$\eta_{el} \equiv \left. \frac{\dot{\varepsilon}_T\{\sigma\}}{\dot{\varepsilon}_F\{\hat{\sigma}_{el}\}} \right|_{\sigma = \hat{\sigma}_{el}} \tag{1a}$$

In terms of the steady state stress at the tensile face, $\hat{\sigma}_s$, it is:

$$\eta_T \equiv \left. \frac{\dot{\varepsilon}_T\{\sigma\}}{\dot{\varepsilon}_F\{\hat{\sigma}_s\}} \right|_{\sigma = \hat{\sigma}_s} \tag{1b}$$

We modify his notation only slightly (e.g. to make normalized parameters more distinct). Variables are listed in section A21-3.

A21.1 Analysis

Chuang (1986) presents a general analysis of steady state flexural creep deformation, for tensile and compressive Norton creep laws having different pre-exponentials *and* stress exponents. Neglecting signs, the creep laws are:[1]

$$\dot{\varepsilon}_i = A_i \left(\frac{\sigma}{\sigma_o} \right)^{n_i}, \quad i = T, C \tag{2a}$$

$$A_T \neq A_C; \quad n_T \neq n_C \tag{2b}$$

The strain rate at the tensile face of a creeping bend bar, in Chuang's notation (Fig. A21-1a), is:

$$\dot{\hat{\varepsilon}}_F = \dot{K} H_T \tag{3}$$

Chuang writes the curvature rate of the neutral axis, $\dot{K}$, in terms of a normalized curvature rate:

$$\dot{K} \equiv \dot{\tilde{k}} (A_c/H) \tag{4}$$

Substituting both his ratio of Norton 'pre-exponent factors':

$$R \equiv \frac{A_T}{A_C} \tag{5}$$

and Eq. (4) into Eq. (3), we have:

---

[1] Chuang and Wiederhorn (1988) give the corresponding *transient* analysis.

$$\hat{\dot{\varepsilon}}_F = \dot{\tilde{k}} A_T \frac{\tilde{h}_T}{R} \tag{6}$$

Substituting Eqs. (2) and (6) into (1a) would give the general result for η_{el}. The corresponding equation for η_s could be generated using Chuang's Eq. (6):[2]

$$\frac{\hat{\sigma}_s}{\hat{\sigma}_{el}} = \frac{1}{6\tilde{m}} \left(\frac{\dot{\tilde{k}} \cdot \tilde{h}_T}{R} \right)^{1/n_T} \tag{7}$$

Chuang solves the problem numerically, but gives *no* general results for values of n and R applicable to HPA — two and approximately one, respectively (e.g. Porter et al., 1981; Ch.11 of this report; Gruffel et al., 1988: $1 < R < 3$). For this reason, general results for η_{el} are not given here. However, by assuming that the compressive and tensile stress exponents are equal ($n_T = n_C = n$), but leaving R arbitrary ($R \neq 1$), we can use his results for that special case.[3]

---

[2] But see Eq. (18)...

[3] We justify this assumption by Chuang's (1986) prediction of $\tilde{h}_C = 0.5$, when $n_T = n_C = n$ and $R \approx 1$ (Eq. 8, below, and Fig. A21-1b). This is consistent with earlier data that the neutral axis was stable at the centerline of an HPA test bar (at low ε; Robertson and Wilkinson, unpublished results), and with the uniaxial tensile and compressive data of Gruffel et al. (1988).

A21.2 Case: $n_T = n_C = n$, $R \neq 1$.

For this case, the neutral axis will be located at (Fig. A21-1a):

$$\tilde{h}_T \equiv \frac{H_T}{H} \quad , \quad 0 < \tilde{h}_T \; 1 \tag{8a}$$

From Chuang's Eq. (7), we can write this as:

$$\tilde{h}_T = R^{\frac{1}{n+1}} \left(1 + R^{\frac{1}{n+1}} \right)^{-1} \tag{8b}$$

Chuang gives the normalized curvature rate as a power law in the normalized bending moment:

$$\dot{\tilde{k}} = C \cdot \tilde{m}^{\,n} \tag{9}$$

in which he defines $\tilde{m}$ as:

$$\tilde{m} \equiv \frac{M}{BH^2\sigma_o} \tag{10}$$

For an applied moment written in terms of the initial elastic stress at the tensile face:

$$M = \hat{\sigma}_{el} \frac{BH^2}{6} \tag{11}$$

$\tilde{m}$ can be written as:

$$\tilde{m} = \frac{1}{6} \frac{\hat{\sigma}_{el}}{\sigma_o} \tag{12}$$

Chuang's constant C, in Eq. (9), is:[4]

---

[4] Correcting an error in the original paper, in which the R

$$C \equiv \left(\frac{\tilde{N}}{(1-\tilde{h}_T)^{\tilde{N}} + \tilde{h}_T^{\tilde{N}} \cdot R^{-1/n}} \right)^n \tag{13a}$$

where $$\tilde{N} \equiv \frac{2n+1}{n} \tag{13b}$$

We now assemble these results to give the equation for η_{el}. Substituting Eqs. (9) and (12) into (6):

$$\dot{\hat{\varepsilon}}_F = 6^{-n} \cdot C \cdot A_T \cdot \frac{\tilde{h}_T}{R} \left(\frac{\hat{\sigma}_{el}}{\sigma_o} \right)^n \tag{14}$$

Substituting Eqs. (14) and (2) into (1a):

$$\eta_{el} \equiv \left(\frac{A_T \cdot (\sigma/\sigma_o)^n}{6^{-n} \cdot C \cdot A_T \cdot \tilde{h}_T \cdot R^{-1} \cdot (\hat{\sigma}_{el}/\sigma_o)^n} \right)_{\sigma = \hat{\sigma}_{el}} \tag{15a}$$

$$= \frac{6^n \cdot R}{C \cdot \tilde{h}_T} \tag{15b}$$

where C and $\tilde{h}_T$ are functions of both R and n.

The ratio η_s can be generated from this result by substituting $n_T = n$ and Eq. (9) into (7), and the result into Eq. (15a):[5]

---

factor in the denominator of his Eq. (9) was raised to the *positive* $1/n$ power, and so was inconsistent with his Fig. 13.

[5] The calculated stress ratio, $(\hat{\sigma}_{el}/\hat{\sigma}_s) \approx 2$, is consistent with Cohrt et al.'s (1984b) Fig. 4, for $R \equiv S^n$, $S = 10$ and $n = 2$. This verifies the derivation.

$$\frac{\hat{\sigma}_s}{\tilde{\sigma}_{el}} = \frac{1}{6}\left(\frac{C\cdot\tilde{h}_T}{R}\right)^{1/n} \tag{16a}$$

$$= \eta_{el}^{-1/n} \tag{16b}$$

$$\dot{\hat{\varepsilon}}_F = A_T\cdot\left(\frac{\hat{\sigma}_s}{\sigma_o}\right)^n \tag{17}$$

and $$\eta_s = 1 \tag{18}$$

That is, when the redistributed, stationary stress at the tensile face is known, there should be *no* offset when uniaxial tensile and flexural results are plotted. *However,* the *uniaxial* creep rate parameters must be known in order to predict how the stress and strain will redistribute. Errors will occur when steady state $\hat{\sigma}_s$ and $\dot{\hat{\varepsilon}}$ are calculated from experimental measurements of the specimen's external curvature (as was done in this work), if the neutral axis position is not known.

A21-2.1 Results and discussion

For n = 2 and R values between 1 and 1000, the results are given in Fig. A21-1b. η_{el} increases monotonically from 1.4 to 4.8 with increasing R, the ratio of elastic to steady tensile face stresses increases from 1.2 to 2.2, and $\tilde{h}_T$ from 0.50 to 0.91. The results are rather insensitive to an uncertainty of ±0.2 in a

nominal n of 2. Even though $\tilde{h}_T$ seems rather insensitive to R for $n = 2$ (Fig. A21-1b), the change in creep pre-exponential is significant when plotted with the corresponding uniaxial tensile creep results (Fig. 11-5: flexural results for $R > 1$).[6]

In Fig. 11-5, tensile strain rates for ARCO HPA at 1250 C plotted an order of magnitude *above* its steady state flexural rates at the same temperature. For the two HPAs studied, stress exponents were close to two (Figs. 11-2,-5). Gruffel et al.'s (1988) results are $R \approx 1.3$ for Mg- and Mg-Y/HPA at 1450 C, and $R \approx 2$ to 3 for Mg-Ti/HPA at 1250 C.[7] ARCO's plotted flexural results assumed $R = 1$, and were for the experimentally-determined $n = 1.8$. Because calculated flexural strain rates are linear in the neutral axis location (i.e. $\hat{\dot{\epsilon}} \propto \tilde{h}_T$, Eq. 3), and $\tilde{h}_T$ depends on R (Eq. 8b), the calculated flexural $\dot{\epsilon}$ could be low by up to a factor of up to 1.2, for $1 \leq R \leq 3$ (Fig. A21-1b). This uncertainty is marked in Fig. 11-5 as *vertical* error bars on the triangular flexural data points. Similarly, $\hat{\sigma}_s$ could be

---

[6] In contrast to the systematic results of Carroll and Tressler (1988), Wiederhorn et al. (1988) and Chuang and Wiederhorn (1988), our internal damage data and creep results indicate no threshold stress for tensile cavitation, and so a one-, rather than a two-segment tensile creep law. The results given in Figs. A2-1b and 11-5 are for the simple case of only one creep law in tension and one in compression.

[7] 500 ppm(w) of MgO and Y_2O_3; 1 w/o Ti_2O_3. Chemical compositions of HPAs tested here are given in Table 2-1b.

overestimated by a factor of up to 1.2 (Eq. 16: (1.44/1.2)). This uncertainty is marked as *horizontal* error bars in Fig. 11-5. Taken together, these two effects for $R = 3$ shift the flexural results from a factor of 10 to a factor of 7.5 below the tensile results calculated for an assumed effective initial gauge length of 20 mm.

The uniaxial furnace was built to permit flexural, as well as uniaxial tensile and compressive tests. However, as the project developed, the flexural and uniaxial tensile tests were carried out in *different* furnaces. It is straightforward to estimate what fraction of Fig. 11-5's difference in flexural and tensile strain rates could be accounted for by plausible systematic errors in temperature between the two furnaces — say, up to 20 C. For a creep activation energy, Q, of about 400 and 500 kJ/mol (Ch. 10.1), such temperature differences, ΔT, would give the following ratios in strain rates at the same applied stress:

$\dot{\varepsilon}$ ratio [-]

Q [kJ/mol]	ΔT [C]		
	5	10	20
400	1.1	1.2	1.5
500	1.1	1.3	1.7

For a plausible ΔT of 10 C, these ratios are comparable to the uncertainties in $\hat{\dot{\varepsilon}}$ and $\hat{\sigma}_s$ arising from R's having possible values between one and three. However, they are far too small to explain the observed order of magnitude difference in calculated strain rates in Fig. 11-5. Thermocouples were carefully maintained (Ch.2), and rather improbable temperature differences of 120 and 95 C would be required for creep activation energies of 400 and 500 kJ/mol, respectively, to explain the entire factor of ten difference in strain rates.

For a combination of a larger effective gauge length than the 20 mm assumed (say, 25 mm), and flexural results shifted by an R of 10 rather than 3 (Fig. 11-5),[8] the vertical offset between uniaxial and flexural results would be reduced to a factor of 2.5 to 3. Systematic ΔT of 50 and 40 C still would be required to account for this difference, for activation energies of 400 and 500 kJ/mol, respectively. However, an R of 100 would move the flexural results to the lower limit of the band of tensile strain

---

[8] Which, with $\tilde{h}_T = 0.68$, could still be consistent with early experimental data that the neutral axis was stable. No uncertainties were calculated in the initial work (Robertson and Wilkinson, unpublished results), for the linear regressions used to calculate 'before' and 'after' positions of lines diamond- scribed on bar sides, from numerous travelling microscope data points. Porter et al. (1981) and Johnson et al. (1984) used such scribed lines to calculate flexural strains in HPA, but report no details of results.

rates (Fig. 11-5).

The cause of the offset between uniaxial and tensile strain rates in ARCO is not understood at this time, but likely combines an uncertain effective gauge length in the tensile specimens, a higher R than one, and a systematic temperature difference between the two test furnaces used.

The following action should be taken. First, the specimen recommended in App. 20 should be adopted for uniaxial tensile tests, as it eliminates gauge length uncertainties. Second, all tests should be done in one furnace (the clamshell unit described in App. 18). Finally, R should be determined for ARCO HPA, at creep test temperatures. The clamshell furnace should be used, with the existing tensile and compressive rigs (for compression, at least, tests will be run under computer control in the automated test system the equipment was designed to be compatible with). The R should be verified on a flexural specimen (the deeper the bar, the more accurate the results will be). In this, uncertainties in linear regressions should be included in the analysis, as data points from a travelling microscope are converted into scribed line positions on one specimen side.

A21.3 Variables

A_i, i=T,C pre-exponential in uniaxial tensile/compressive creep relations; [s^{-1}]

C dimensionless constant defined in Eq. (13a); [-]

$\dot{\varepsilon}$ uniaxial tensile strain rate; [s^{-1}]

$\dot{\hat{\varepsilon}}_F$ flexural strain rate; [s^{-1}]

$\dot{\varepsilon}_i$, i=T,C uniaxial tensile/compressive strain rates; [s^{-1}]

$\eta_{el,s}$ ratio of strain rates in tension to bending, for applied tensile stress equal to elastic/stationary tensile face stress; [-]

$\tilde{h}_T$ normalized neutral axis location in flexural specimen; [-]

H flexural specimen height; [m]

H_T distance of neutral axis from tensile face of flexural specimen; [m]

$\dot{\tilde{k}}$ normalized curvature rate of neutral axis of flexural specimen; [-]

$\dot{K}$ curvature rate of neutral axis of flexural specimen; [$m^{-1} \cdot s^{-1}$]

$\tilde{m}$ normalized applied bending moment; [-]

M applied bending moment; [N·m]

n, n_T, n_C creep stress exponents: common/tensile/compressive; [-]

$\tilde{N}$ parameter simplifying Eq. (13b); [-]

Q creep activation energy; [kJ/mol]

R ratio of uniaxial tensile to compressive pre-exponentials for creep relation; [-]

σ applied uniaxial tensile stress; [N/m^2]

$\hat{\sigma}_{el,s}$ applied elastic/stationary stress at tensile face of flexural specimen; [N/m^2]

σ_o reference stress for creep relation; [N/m^2]

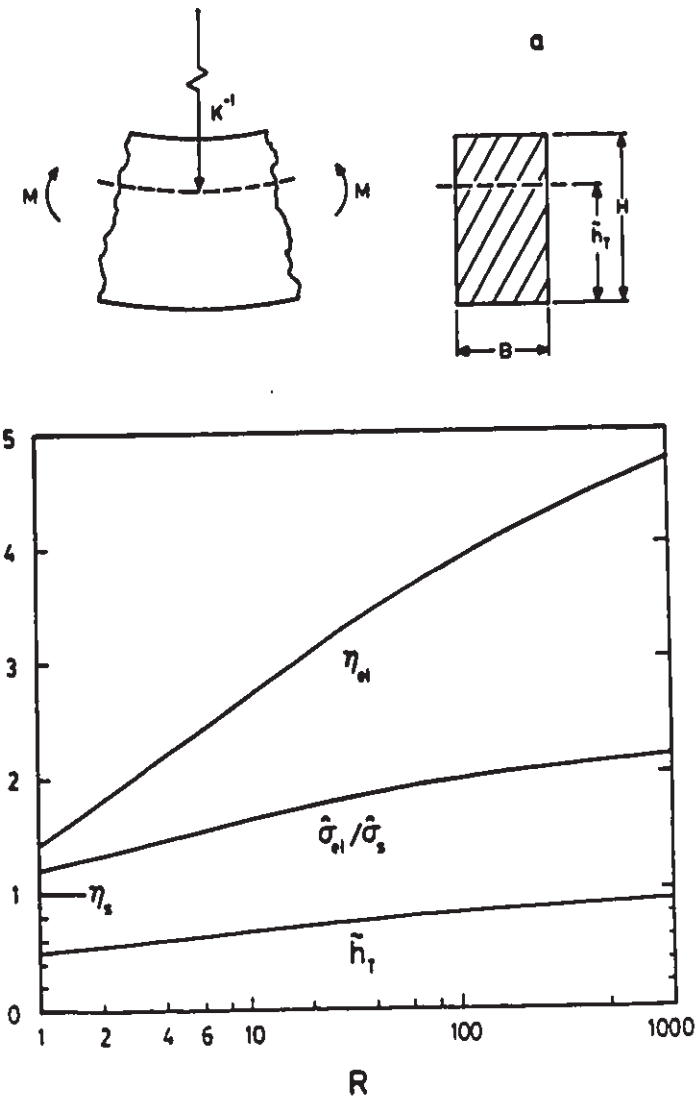

Fig. A21-1: Steady state flexural creep deformation, after Chuang (1986).

a) *General* flexural specimen at steady state ($n_T \neq n_C$; $A_T \neq A_C$). Neutral axis is dashed.

b) Case: $n_T = n_C = n = 2$, $1 \leq R \leq 1000$: $\eta_{el,s}$, uniaxial tensile *vs* steady state flexural strain rate ratios (re. elastic and stationary stresses at tensile face, respectively); elastic/stationary stress ratio at tensile face; and normalized neutral axis location, $\tilde{h}_C$.

15 References

Abbruzzese, G. and Lucke, K. (1986), A statistical theory of grain growth including texture and drag effects and its application to texture controlled grain growth, p. 1-14 in Hansen, N., Jensen, D.J., Leffers, T. and Ralph, B., Annealing processes - recovery, recrystallization and grain growth, Riso National Lab., Roskilde, Denmark.

Amato, I. and Columbo, R.L. (1964), The influence of organic additions on the solarization and grain growth of sintered UO_2, J. Nucl. Mater. 11 [3] 348-51.

Anderson, M.P. (1986), 'Simulation of grain growth in two and three dimensions, p. 15-24 in N. Hansen, D.J. Jensen, T. Leffers and B. Ralph, Eds., Annealing processes - recovery, recrystallization and grain growth', 7th RISO Intl. Symp. on Mater. Sci., RISO Natl. Lab, Roskilde, Denmark.

Arzt, E., Ashby, M.F., and Easterling, K.E. (1983), Practical applications of hot-isostatic pressing diagrams: four case studies, Met. Trans 14a, 211-221.

Ashby, M.F., (1980), The influence of particles on boundary mobility, p. 325-36 in A.R. Jones and T. Leffers, Eds., 1st RISO Intl. Symp. on Metall. and Mater. Sci., RISO Natl. Lab., Roskilde, Denmark.

Ashby, M.F. and Brown, L.M. (1983), Perspectives in creep

fracture, Pergamon, Oxford.

Ashby, M.F. and Dyson, B.F. (1984), Creep damage mechanics and mechanisms, NPL Rept. DMA(A)77, Teddington, England.

Bannister, M.J. (1980), Comment on "The role of MgO in the sintering of alumina", J. Am. Ceram. Soc. 63 [3-4] 229-30.

Barin, I. and Knacke, O. (1973), Thermochemical properties of inorganic substances, Springer-Verlag, Berlin.

Barnes, R.S. (1964), A theory of swelling and gas release for reactor materials, J. Nuc. Mater. 11 [2] 135-48.

Beeré, W. (1976), The intermediate stage of sintering, Metal Sci. 10, 294-6.

——— (1975a), A unifying theory of the stability of penetrating liquid phases and sintering pores, Acta metall. 23, 131-38

——— (1975b), The second stage sintering kinetics of powder compacts, Acta metall. 23, 139-45.

Bennison, S.J. and Harmer, M.P. (1983) Grain growth and cavity formation in MgO-doped Al_2O_3, p. 171-183 in M.F. Yan and A.H. Heuer, Eds., Character of grain boundaries, Adv. in Ceramics, V.6, Am. Ceram. Soc., Columbus OH.

Bennison, S.J. and Harmer, M.P. (1985a) Swelling of hot-pressed Al_2O_3, J. Am. Ceram. Soc. 68 [11] 591-97.

Bennison, S.J. and Harmer, M.P. (1985b) Grain-growth kinetics in the absence of a liquid phase, J. Am. Ceram. Soc. 68 [1] C-22 –

C-24.

Bently, R.E. (1982), The thermocouple: a modern view, Metals Austr=lasia 13 [9] 19-20,25.

Berry, K.A. and Harmer, M.P. (1986), Effect of MgO solute on microstructure development in Al_2O_3, J. Am. Ceram. Soc. 69 [2] 143-9.

Bevington, P.R. (1969), Data reduction and error analysis for the physical sciences, McGraw-Hill, New York.

Blumenthal, W. and Evans, A.G. (1984), High-temperature failure of polycrystalline alumina: II, Creep crack growth and blunting, J. Am. Ceram. Soc. 67 [11] 741-50.

Bogdamoff, J.L. and Kozin, F. (1985), Probabilistic models of cumulative damage, Wiley, New York.

Broek, D. (1982), Elementary engineering fracture mechanics, 3rd Edn., Martinus Nijhoff, Boston.

Brook, R.J. (1982), Fabrication principles for the production of ceramics with superior mechanical properties, Proc. Brit. Ceram. Soc. 32, 7-24.

_____ (1976), Controlled grain growth, p.331-64 in Wang, F.F., Ed., Treatise on mater. sci. and tech'y, V9, Ceramic fabrication processes, Academic, New York.

_____ (1969), Pore-grain boundary interactions and grain growth, J. Am. Ceram. Soc. 52 [1] 56-7.

Budworth, D.W. (1970), Theory of pore closure during sintering,

Trans. Brit. Ceram. Soc. 69 [1] 29-31.

Burke, K. and Cozzarelli, F.A. (1984), On the thermodynamic foundations of strain-dependent creep damage and rupture in three dimensions, Int. J. Solids Structures 20 [5] 487-97.

Cannon, R.M. and Coble, R.L. (1975), Review of diffusional creep of Al_{2-3}, pp. 81-100 in Bradt, R.C. and Tressler, R.E., Eds., Deformation of ceramic materials, Plenum, New York.

Cannon R.M., Rhodes W.H. and Heuer A.H. (1980), Plastic deformation of fine-grained alumina (Al_2O_3): I, Interface controlled diffusional creep, J. Am. Ceram. Soc. 63, 46-53.

Cao, H.C., Dalgleish, B.J., Hsueh, C.-H. and Evans, A.G. (1987), High-temperature stress corrosion cracking in ceramics, J. Am. Ceram. Soc. 70 [4] 257-64.

Carpay, F.M.A. (1977), The effect of pore drag on ceramic microstructures, p.261-75 in Fulrath, R.M. and Pask, J.A., Eds., Ceramic microstructures '76, Westview Press, Boulder CO.

Carroll, D.F. and Tressler, R.E. (1988), Accumulation of creep damage in a siliconized silicon carbide, J. Am. Ceram. Soc. 71 [6] 472-77.

———— (1985), Time-dependent strength of siliconized silicon carbide under stress at 1000° and 1100° C, J. Am. Ceram. Soc. 68 [3] 143-46.

Chokshi, A.H. and Porter, J.R. (1986), High temperature mechanical properties of single phase alumina, J. Mater. Sci. 21, 705-10.

Christ, B.W. and Swanson, S.R. (1976), Alignment problems in the tensile test, J. Testing and Eval. 4 [6] 405-17.

Chuang, T.-J. (1986), Estimation of power-law creep parameters from bend test data, J. Mater. Sci. 21 [1] 165-75.

Chuang, T.-J. and Wiederhorn, S.M. (1988), Damage-enhanced creep in a siliconized silicon carbide: Mechanics of deformation, J. Am. Ceram. Soc. 71 [7] 595-601.

Coble, R.L. (1970), Diffusion models for hot pressing with surface energy and pressure effects as driving forces, J. Appl. Phys. 41 [12] 4798-4807.

———— (1962), Sintering alumina: Effect of atmospheres, J. Am. Ceram. Soc. 45 [3] 123-7.

———— (1961), Sintering crystalline solids, I. Intermediate and final stage models, J. Appl. Phys. 32, 787-

Cocks, A.C.F. and Ashby, M.F. (1982), On creep fracture by void growth, Prog. in Mater. Sci. 27 189-244.

Cohen, E.R. and Taylor, B.N. (1986), The 1986 adjustment of the fundamental physical constants, CODATA Bull. 63.

Cohrt, H., Grathwohl, G. and Thummler, F. (1984a) Strengthening after creep of reaction-bonded siliconized silicon carbide, p.515-526 in Wilshire, B. and Owen, D.R.J., Creep and fracture of engineering materials and structures, Pt.1, Pineridge Press, Swansea, Wales.

———— (1984b), Non-stationary stress distribution in a ceramic bending beam during constant load creep, Res. mechanica 10 [1],

55-71.

Crouch A.G. and Pascoe, R.T. (1972), Density changes during the heat treatment of Fe_2O_3, Proc. Brit. Ceram. Soc. 20, 189-203.

Cwajna, J., Maciejny, A. and Malinski, M. (1986), Stereological criteria of grain size homogeneity, pp.273-78 in Hansen, N., Jensen, D.J., Leffers, T. and Ralph, B., Annealing processes - recovery, recrystallization and grain growth, Riso National Lab., Roskilde, Denmark.

Dalhleish, B.J. and Evans, A.G. (1985), Influence of shear bands on creep rupture in ceramics, J. Am. Ceram. Soc. 68 [1] 444-48.

Dalgleish, B.J., Slamovich, E.B. and Evans, A.G. (1985), Duality in the creep rupture of a polycrystalline alumina, J. Am. Ceram. Soc. 68 [11] 575-81.

Dalgleish, B.J., Johnson, S.M. and Evans, A.G. (1984), High-temperature failure of polycrystalline alumina: I, Crack nucleation, J. Am. Ceram. Soc. 67 [11] 741-50.

Davanas, K. and Solomon, A.A. (1986), Effect of capillarity and pore-size distributions on pore and cavity growth, pp. 139-153 in Hastings, I.J., Ed., Fission-product behavior in ceramic oxide fuel, Am. Ceram. Soc., Columbus, Ohio.

Davidge, R.W. (1979), Mechanical behavior of ceramics, Cambridge Univ. Press, Cambridge, England.

DeHoff, R.T. (1984), A cell model for microstructural evolution during sintering, p.23-34 in Kuczynski, G.C., Miller, A.E. and Sargent, G.A., Eds., Sintering and heterogeneous catalysis, Mater, Sci. Res. V.16, Plenum, New York.

DeHoff, R.T. and Aigeltinger, E.H. (1970), Experimental quantitative microscopy with special application to sintering, p.81-137 in Hirschorn, J.S. and Roll, K.H., Eds., Advanced experimantal techniques in powder metallurgy: fundamentals, methods and applications, Perspectives in Powder Metallurgy, V.5, Plenum, New York.

DeHoff, R.T. and Rhines, F.N. (1968), Quantitative microscopy, McGraw-Hill, New York.

Diggle, P.J. (1983), Statistical analysis of spatial point patterns, Academic, London.

Dorre, E. and Hubner, H. (1984), Alumina: processing, properties and applications, Springer-Verlag, Berlin.

Dynys, J.M., Coble, R.L., Coblenz, W.S. and Cannon, R.M. (1980), Mechanisms of atom transport during initial stage sintering of $Al_{2-3}O$, p. 391-404 in Kuczynski, G.C., Ed., Sintering processes, Mater. Sci. Res. V13, Plenum, New York.

Eadie, R.L. and Weatherly G.C. (1975), Solutions for the shrinkage rate in the intermediate stage of sintering, Scripta metall. 9, 285-94.

Evans, A.G. (1982a), Structural reliability: a processing-dependent phenomenon, J. Amer. Ceram. Soc. 65 [3] 127-37.

Evans, A.G. (1982b), The high temperature failure of ceramics, p. 53-134 in Wilshire,B. and Owen, D.R.J., Eds. Recent advances in creep and fracture of engineering materials and structures, Pineridge press, Swansea.

Evans, A.G. and Blumenthal, W. (1984), High temperature failure mechanisms in ceramic polycrystals, p.487-505 in Tressler, R.E. and Bradt, R.C., Eds., Deformation of ceramic materials II, Plenum, New York.

Evans, A.G. and Rana, A. (1980), High temperature failure mechanisms in ceramics, Acta metall. 28, 129-41.

Evans, H.E. (1984), Mechanisms of creep fracture, Elsevier Applied Science, New York.

Fairborz, S.J. Harlow, D.G. and Delph, T.J. (1985), The effects of nonperiodic void spacing upon intergranular creep cavitation, Acta metall. 33 [1], 1-9.

Francois, B. and Kingery, W.D. (1967), The sintering of crystalline oxides, II. Densification and microstructure development in UO_2, p. 499-525, in Kuczynski, G.C., Hooton, N.A. and Gibbon, C.F., Eds., Sintering and related processes, Gordon and Breach, New York.

Freund, F., King, B., Knobel, R. and Katherein, H. (1984), Low atomic number impurity atoms in magnesium oxide: hydrogen and carbon, p.119-138 in Kingery, W.D., Ed., Structure and properties of MgO and Al_2O_3 ceramics, Adv. in Ceram. V.10, Am. Ceram. Soc., Columbus OH.

Frocht, M.M. and Hill, H.N. (1940), Stress-concentration factors around a central circular hole in a plate loaded through pin in the hole [sic], Trans. ASME: J. Appl. Mech. 7 (A-5)-(A-9).

Froschauer, L. and Schmidt. D. (1977), Temperature measurement with Pt-Rh thermocouples - causes of errors and failure, Interceram 26 [2] 138-40.

Frost, H.J. and Ashby, M.F. (1982), Deformation-mechanism maps, Pergamon, Oxford.

Fryer, G.M. and Roberts, J.P. (1966), Tensile creep of porous polycrystalline alumina, Proc. Brit. Ceram. Soc. 6 [6] 225-32.

Fullman, R.L. (1953), Measurement of particle sizes in opaque bodies, Trans. AIME: J. Metals 197 [3] 477-52.

Gaskell, D.R. (1973), Introduction to metallurgical thermodynamics, McGraw-Hill, New York.

Gasson, P.C. (1983), Geometry of spatial forms, Ellis Horwood, Chichester, England.

Gifkins, R.C. (1970), Optical microscopy of metals, Pitman, London.

Govila, R.K., Herman, J.A. and Arnon, N. (1985), Stress rupture test rig designed for evaluation ceramic material specimens, ASME Rept. 85-GT-181, Gas turbine conf. and exhibit, Houston TX, March 1985.

Govila, R.K. (1983), High temperature uniaxial tensile stress rupture strength of sintered α-SiC, J. Mater. Sci. 18, 1967-76.

_____ (1982), Uniaxial tensile and flexural stress rupture strength of hot-pressed Si_3N_4, J. Am. Ceram. Soc. 65 [1] 15-21.

Grathwol, G. (1984) Creep and fracture of hot-pressed silicon nitride with natural and artificial flaws, pp.565-77 in Wilshire, B. and Owen, D.R.J., Creep and fracture of engineering materials and structures, Pt.1, Pineridge Press, Swansea, Wales.

——— (1983), Regimes of creep and slow crack growth in high-temperature rupture of hot-pressed silicon carbide, pp.573-86 in Tressler, R.C. and Bradt, R.C., Eds., Deformation of ceramic materials II, Plenum, New York.

Greenwood, G.W. and Boltax, A. (1962), The role of fission gas re-solution during post-irradiation heat treatment, J. Nuc. Mater. 5 [2] 234-40.

Gruber, E.E. (1986) Analysis of transient fission-gas release and swelling in oxide fuel, p.249-58 in Hastings, I.J., Ed., Fission-product behavior in ceramic oxide fuels, Am. Ceram. Soc., Columbus OH.

Gruber, E.E. (1967), Calculated size distributions for gas bubble migration and coalescence in solids, J. Appl. Phys. 38 [1] 243-50.

Gruffel, P., Carry, P. and Mocellin, A. (1988), Effect of testing conditions on superplastic creep of alumina doped with Ti and Y, Science of Ceramics 14, 587-92.

Gupta, T.K. (1978), Instability of cylindrical voids in alumina, J. Am. Ceram. Soc. 61 [5-6] 191-5.

——— (1971) Kinetics and mechanisms of pore growth in MgO, J. Mater. Sci. 6, 989-97.

Gupta, T.K. and Coble, R.L. (1968), Sintering of ZnO: II. Density decrease and pore growth during the final stage of the process, J. Am. Ceram. Soc. 51 [9] 525-8.

Handwerker, C.A., Cannon, R.M. and Coble, R.L. (1984),

Final-stage sintering of MgO, pp. 619-43 in Kingery, W.D., Ed., Adv. in Ceram. V.10, Structure and properties of MgO and Al_2O_3 ceramics, Am. Ceram. Soc., Columbus, Ohio.

Haroun, N.A. and El-Masry, M.A.A. (1981), Bloating of slip cast MgO, Ceramics Int. 7 [1] 38-40.

Helle, A.S., Easterling, K.E. and Ashby, M.F. (1985), Hot-isostatic pressing diagrams: new developments, Acta metall. 33 [12] 2163-2174.

Herring, C. (1950), Diffusional viscosity of a polycrystalline solid, J. Appl. Phys. 21, 437-45.

Heuer, A.H. (1979), The role of MgO in the sintering of alumina, J. Am. Ceram. Soc. 62 [5-6] 317-8.

Hillert, M. (1965), On the theory of normal and abnormal grain growth, Acta metall. 13, 227-38.

Hollenberg, G.W., Terwilliger, G.R. and Gordon, R.S. (1971), Calculation of stresses and strains in four-point bending creep tests, J. Am. Ceram. Soc. 54 [4] 196-99.

Howlett, S.P. and Brook, R.J. (1984), Density loss in sintered cobalt oxide, p.320-40 in J.D. Bolton and S. Hampshire, Eds., Mechanically, chemically and thermally induced failure in engineering materials, Proc. 2nd Irish Durability and Fracture Conf., N.I.H.E., Limerick, Ireland, March, 1984.

Hsu, F. and Solomon, A.A. (1983), Growth and inter-connection of pressurized pores in nickel and relation to stress rupture models, Acta. metall. 31 [3] 453-64.

Hsueh, C.H. and Evans, A.G. (1983), Microstructure evolution during sintering: the role of evaporation/ condensation, Acta metall. 31, 189-98.

——— (1981), Creep fracture in ceramic polycrystals — II. Effects of inhomogeneity on creep rupture, Acta metall. 29, 1907-17.

Hsueh, C.H., Evans, A.G. and Coble, R.L. (1982), Microstructure development during final/intermediate stage sintering — I. Pore/grain boundary separation, Acta. metall. 30, 1269-79.

Hull, F.C. and Houk, W.J. (1953), Statistical grain structure studies: plane distribution curves of regular polyhedrons, Trans. AIME: J. Metals 197 [4] 565-72.

Ikegami, T., and Moriyoshi, Y. (1984), Intermediate-stage sintering of a homogeneously packed compact, J.. Am. Ceram. Soc. 67 [3] 174-8.

Ikegami, T., Tsutsumi, M., Matsuda, S.-i., Shirasaki, S.-i., and Suzuki, H. (1978), A model of densification with simulatneous grain growth', J. Appl. Phys. 49 [7], 4238-41.

Jakus, K. and Wiederhorn, S.M. (1988), Creep deformation in four-point bending, J. Am. Ceram. Soc. 71 [10] 832-36.

JANAF thermochemical tables (1971; suppl. 1974, 1975, 1978), 2nd ed., Stull, D.R. and Prophet, H., Eds. (suppl. ed. by Chase et al.), U.S. Govt. Printing Office, National Bureau of Standards, Washington, DC.

Johnson, S.M. Dalgleish, B.J. and Evans, A.G. (1984), High-temperature failure of polycrystalline alumina: III, Failure

times, J. Am. Ceram. Soc. 67 [11] 741-50.

Johnson, D.L. (1970), A general model for the intermediate stage of sintering, J. Am. Ceram. Soc. 53 [10] 574-77.

Kachanov, L.M. (1986), Introduction to continuum damage mechanics, Martinus Niijhoff, Dordrecht.

Kapadia, C.M. and Leipold, M.H. (1973), Interrelation of pore size and grain size during grain growth of oxides, J. Am. Ceram. Soc. 56 [5] 289.

Kaspar, J.S. and Lonsdale, K. Eds,. (1959), Int'l. tables for X-ray crystallography, Vol. II, Mathematical tables, Kynoch press, Birmingham, England, p.46ff.

Kingery, W.D. and Francois, B. (1967), The sintering of crystalline oxides, I. Interactions between grain boundaries and pores, p. 471-99 in Kuczynski, G.C., Hooton, N.A. and Gibbon, C.F., Eds., Sintering and related phenomena, Gordon and Breach, New York.

Kossowsky, R., Millar, D.G. and Diaz, E.S. (1975), Tensile and creep strengths of hot-pressed Si_3N_4, J. Mater. Sci. 10 [6] 983-97.

Kuczynski, G.C. (1982), Statistical theory of sintering and microstructural evolution, p. 37-44 in Pejovnik, S. and Ristić, M.M., Eds., Sintering — Theory and practice, Mat. Sci. Monogr. V.14, Elsevier, Amsterdam.

Kumar, P. and Johnson, D.L. (1974), Sintering of CoO, II: Intermediate stage, J. Am. Ceram. Soc. 57 [2] 65-8.

Lange, F.F. (1980) Silicon nitride polyphase systems: fabrication, microstructure and properties, Intl. Metals Rev. 25 [1] 1-20.

Lange, F.F., Diaz, E.S. and Anderson, C.A. (1979), Tensile creep testing of improved Si_3N_4, Bull. Am. Ceram. Soc. 58 [9] 845-8.

Lange, F.F. and Diaz, E.S. (1978) Powder-cushion gripping to promote good alignment in tensile testing, J. Testing and Eval. 6 [5] 320-23.

Leckie, F.A. (1986), The micro- and macromechanics of creep rupture, Engng. Fract. Mech. 25 [5/6] 505-21.

———— (1978), The constitutive laws of continuum creep damage mechanics, Phil. Trans. Roy. Soc. Lond. A 288, 27-47.

Lemaitre, J. (1986), Local approach of fracture, Engng. Fract. Mech. 25 [5/6] 523-37.

———— (1984), How to use damage mechanics, Nuc. Engng. and Des. 80, 233-45.

Lou, V.L.K., Mitchell, T.E. and Heuer, A.H. (1985), REVIEW — Graphical displays of the thermodynamics of high-temperature gas-solid reactions and their application to oxidation of metals and evaporation of oxides, J. Am. Ceram. Soc. 68 [2] 49-58.

Lupis, C.P.H. (1983), Chemical thermodynamics of materials, North-Holland, New York.

Masuda, Y. and Watanabe, R. (1980), Ostwald ripening processes in the sintering of metal powders, pp.3-21 in Kuczynski, G.C., Ed., Mat. Sci. Res. V.13, Plenum, New York.

Matsusue, K., Fujisawa, Y. and Takahara, P. (1983) Tensile strength of pressureless-sintered silicon nitride at elevated temperature, Technical Rept No. NAL/TR-753, 18p, National Aerospace Lab., Tokyo (in Japanese).

Mocellin, A. and Kingery, W.D. (1973), Microstructural changes during heat treatment of sintered Al_2O_3, J. Am. Ceram. Soc. 56 [6] 309-314.

Murakami, S. and Sanomura, Y. (1985), Creep and creep damage of copper under multiaxial states of stress, pp.535-51 in Sawczuk, A. and Bianchi, G., Plasticity today: Modeling, methods and applications, Elsevier Applied Science, New York.

Morgan, C.S., McKorkle, K.H. and Powell, G.L. (1976), Pore growth in sintered thoria, J. Am. Ceram. Soc. 59 [3-4] 104-7.

Newman, J.C., Jr. and Raju, I.S. (1981) An empirical stress-intensity factor equation for the surface crack, Engng. Fract. Mech. 15 [1-2] 185-92.

Nichols, F.A. (1972a), On the diffusional mobilities of particles, pores and loops, Acta metall. 20, 207-214.

———— (1972b), Theory of grain growth in porous compacts, J. Appl. Phys. 37 [13] 4599-4602.

Occhionero, M.A. (1984), The influence of green density on sintering, M.Sc. Thesis, Case Western University, Cleveland, Ohio.

Occhionero, M.A. and Halloran, J.W. (1984), The influence of green density upon sintering, p. 89-102 in Kuczynski, G.C.,

Miller, A.E. and Sargent, G.A., Eds., Sintering and heterogeneous catalysis, Mat. Sci. Res., V16, Plenum, New York.

Ohji, T., Sakai, S., Ito, M., Yamauchi, Y. Kanematsu, W. and Ito, S. (1987), Yielding phenomena of hot-pressed Si_3N_4, High temperature technology 5 [3] 139-44.

Omega Engineering Inc. (1987), Practical strain guage measurements, p. E-36-62 and esp. E-44-45 in Pressure, strain and force measurement handbook and encyclopedia, Omega Engineering, Stamford CT.

Pasco, W.D. (1980), Vapor phase reactions in the aluminum-oxygen-carbon system, Ph.D. thesis, Rensselaer Polytechnic Inst.

Pearce, P . (1978), Structure in nature is a strategy for design, MIT Press, Cambridge MA.

Pears, C.D. and Digesu, F.J. (1965), Gas-bearing facilities for determining axial stress-strain and lateral strain of brittle materials, Proc. ASTM 65, 855-73.

Penny, R.K. and Marriott, D.L. (1971), Design for creep, McGraw-Hill, London.

Peterson, R.E. (1953), Stress concentration design factors, Wiley, New York.

Pilkington, R., Miller, D.A. and Worswick, D. (1981), Cavitation damage and creep crack growth, Met. Trans. 12A, 173-81.

Porter, J.R., Blumenthal, W. and Evans, A.G. (1981), Creep fracture in ceramic polycrystals-I. Creep cavitation effects in

polycrystalline alumina, Acta metall. 29, 1899-1906.

Press, W.H., Flannery, B.P. Teukolsky, S.A. and Vetterling, W.T. (1986), Numerical recipies, Cambridge University Press, New York.

Quinn, G.D. (1985), Static fatigue resistance of hot pressed silicon nitride, p.319-32 in Bradt, R.C., Hasselman, D.P.H. and Lange, F.F., Fracture mechanics of ceramics, V.8, Plenum, New York.

———— (1984), Properties testing and materials evaluation, p.298-311 in Ceramic Sci. and Engng. Proc., Proc. 12th Automotive Materials Conference, Am. Ceram. Soc., Columbus, OH.

———— (1983), Guide to the construction of a simple 1500° test furnace, Technical report TR83-1, US Army Materials and Mechanics Research Center, Watertown, MA.

Raj, R. (1982a), Intergranular creep in aggressive environments, Acta metall. 30 1259-68.

———— (1982b), Separation of cavitation-strain and creep strain during deformation, J. Am. Ceram. Soc. 65 [3] C-46.

Raj, R. and Ashby, M.F. (1975), Intergranular fracture at elevated temperatures, Acta metall. 23, 653-66.

Randle, V., Ralph, B. and Hansen, N. (1986), Grain growth in crystalline materials, p.123-142 in Hansen, N., Jensen, D.J., Leffers, T. and Ralph, B., Annealing processes - recovery, recrystallization and grain growth, Riso National Lab., Roskilde, Denmark.

Rasmunssen, J.J. and Kingery, W.D. (1970), Effect of dopants on

the defect structure of single-crystal aluminum oxide, J. Am. Ceram. Soc. 53 [8] 436-440.

Ratcliffe, R.T. (1965), The measurement of small density changes in solids, Br. J. Appl. Phys. 16, 1193-96.

Rest, J. (1986), Grain-boundary sweeping and liquifaction-induced fission-product behavior in nuclear fuel under severe-core-damage accident conditions, p. 223-48 in I.J., Hastings, Ed., Fission-product behavior in ceramic oxide fuels, Am. Ceram. Soc., Columbus OH.

Rhines, F.N. (1985), Microstructology; Part 3: Examples 1: Development and growth of grains and particles, Pract. Met. 22, 469-88.

Rhines, F.N. and Craig, K.R.; App. by DeHoff, R.T. (1974) Mechanism of steady-state grain growth in aluminum, Met. Trans. 5, 413-25.

Rhines, F.N. and DeHoff, R.T. (1984), Channel network decay in sintering, p. 49-61 in Kuczynski, G.C., Miller, A.E. and Sargent, G.A., Eds., Sintering and heterogeneous catalysis, Mater. Sci. Res. V.16, Plenum, New York.

Rice, R.W. (1969), The effect of gaseous impurities on the hot pressing and behavior on MgO, CaO, and Al_{2-3}, Proc. Brit. Ceram. Soc. 12, 99-123.

Riedel, H. (1987), Fracture at high temperatures, Springer-Verlag, Berlin.

Robertson, W.M. and Chang, R. (1966), The kinetics of grain-boundary groove growth on alumina surfaces, pp.49-60 in Kriegel,

W.W. and Palmour, H., III, Role of grain boundaries and surfaces in ceramics, Mater. Sci. Res. V.3, Plenum, New York.

Robertson, A.G. and Wilkinson, D.S. (1986), Damage accumulation in hot-pressed alumina during flexural creep and anneals in air, pp.311-26 in Bradt, R.C., Evans, A.G., Hasselman, D.P.H. and Lange, F.F., Fracture mechanics of ceramics, V.7, Plenum, New York.

Rosolowski, J.H. and Greskovich, C. (1975), Theory of the dependence on densification on grain growth during intermediate-stage sintering, J. Am. Ceram. Soc. 58 [5-6] 177-82.

Roy, S.K. and Coble, R.L. (1968), Solubilities of magnesia, titania and magnesium titanate in aluminum oxide, J. Am. Ceram. Soc. 51 [1] 1-6.

Saanouni, K., Chaboche, J.L. and Bathias, C. (1986), On the creep crack growth prediction by a local approach, Engng. Fract. Mech. 25 [5/6] 677-91.

Sata, T. and Sasamoto, T. (1984), Vaporization from magnesia and alumina materials, pp. 541-52 in Kingery, W.D., Ed., Advances in ceramics, V.10: Structure and properties of MgO and $Al_{2-3}O$ ceramics, Am. Ceram. Soc., Columbus OH.

Sawicka, B.D. and Palmer, B.J.F. (1988), Density gradients in ceramic pellets measured by computed tomography, Nuc. Insts. and Methods in Physics Res. A263, 525-28.

Shewmon, P.G., Lopez, H. and Parthasarathy, T.A. (1983), Chemically driven cavity growth, Scripta Met. 17, 39-43.

Solomon, A.A. and Hsu, F. (1980a), Swelling and gas release in

ZnO, J. Am. Ceram. Soc. 63 [7-8] 467-474.

———— (1980b), Analysis of hot-pressing, swelling and stress-rupture theories and comparison with experiment, p. 485-502 in G.C. Kuczynski, Ed., Sintering processes, Mtrls. Sci. Res. V.13, Plenum, NY.

Spears, M.A. and Evans, A.G. (1982), Microstructure development during final/intermediate stage sintering - II. Grain and pore coarsening, Acta metall. 30, 1281-9.

Speight, M.V. and Greenwood, G.W. (1964), Grain boundary mobility and its effects in materials containing inert gases, Phil. Mag. 9, 683-9.

Srolovitz, D.J., Anderson, M.P., Sahni, P.S. and Grest, G.S. (1984), Computer simulation of grain growth - II. Grain size distribution, topology, and local dynamics, Acta metall. 32 [5] 793-802.

Sundararajan, G. (1986), The effect of grain size on intergranular creep fracture, Res mechanica 17 [1] 59-70.

Trampczynski, W.A., Hayhurst, D.R. and Leckie, F.A. (1981), Creep rupture of copper and aluminum under non-proportional loading, J. Mech. Phys. Solids 29 [5/6] 353-74.

Tucker, M.O. (1981), The structure of interlinked grain boundary edge porosity, pp.59-87 in Gittus, J., Ed., Cavities and cracks in creep and fatigue, Appl. Sci. London.

Tuma, J.J. (1979), Engineering mathematics handbook, 2nd Ed., McGraw-Hill, New York.

Vieira, J.M. and Brook, R.J. (1984), Kinetics of hot- presssing: the semilogarithmic law, J. Am. Ceram. Soc. 67 [4] 245-49.

Wagman, D.D., Evans, W.H., Parker, V.B., Halow, I., Bailey, S.M. Schumm, R.H. and Churney, K.L. (1971), Selected values of chemical thermodynamic properties: Tables for elements 54 through 61 in the standard order of arrangement, NBS technical note 270-5, National Bureau of Standards, Gaithersburg MD.

Wakai, T. (1986), Superplastic processing in fine ceramics, J. Japan Soc. for Tech'y of Plasticity 27 [302], Special issue on superplastic materials and their working technologies, p. 374.

Wang, H.A. and Kroger, F.A. (1980), Pore formation during oxidative annealing of Al_2O_3: Fe and slowing of grain growth by precipitates and pores, J. Mater. Sci. 15, 1978-86.

Warman, M.O. and Budworth, D.W. (1967), Effects of residual gas on the sintering of alumina to theoretical density in vacuum, Trans. Brit. Ceram. Soc. 66 [6] 265-71.

Weast, R.C, Astle, M.J. and Beyer, W.H., Eds. (1985), CRC handbook of chemistry and physics, 66th Edn., CRC Press, Boca Raton, FA.

Wiederhorn, S.M., Roberts, D.E., Chuang, T.-J. and Chuck, L. (1988), Damage-enhanced creep in a siliconized silicon carbide: Phenomenology, J. Am. Ceram. Soc. 71 [7] 602-608.

Wiederhorn, S.M., Hockey, B.J., Krause, R.F., Jr., and Jakus, K. (1986a), Creep and fracture of a vitreous-bonded aluminum oxide, J. Mater. Sci. 21, 810-24.

Wiederhorn, S.M., Chuck, L., Chuang, T.-J. and Jakus,K. (1986b),

Standard tensile test development, 24th Automotive Technology Development Contractors' Coordinating Mtg., Oct. 29, 1986.

Wiederhorn, S.M., Chuck. L., Fuller, E.R. Jr. and Tighe, N.J. (1986c), Creep rupture of siliconized silicon carbide, p.755-73 in Tressler, R.E., Messing, G.L., Pantano, C.G. and Newnham, R.E., Eds. Tailoring multiphase and composite ceramics, Mater. Sci. Res. V.20, Plenum, New York.

Wiederhorn, S.M. and Fuller, E.R., Jr. (1985), Structural reliability of ceramic materials, Mater. Sci. and Engng. 71, 169-86.

Wiederhorn, S.M. (1983), A probabilistic framework for structural design, pp.197-226 in Bradt, R.C., Evans, A.G., Hasselman, D.P.H. and Lange, F.F., Eds., Fracture mechanics of ceramics, V.5, Plenum, New York.

Wilkinson, D.S. (1988), The effect of a non uniform void distribution on grain boundary void growth during creep, Acta metall. 36 [8] 2055-63.

Wilkinson, D.S. (1978), The mechanics of pressure sintering, Ph.D. Thesis, Cambridge University, Cambridge, England.

Wilkinson, D.S and Vitek, V. (1982), The propagation of cracks by cavitation: a general theory, Acta metall., 30, 1723-32.

Wong, B. and Pask, J.A. (1979), Models for kinetics of solid state sintering, J. Am. Ceram. Soc. 62 [3-4] 138-141.

Wurst, J.C. and Nelson, J.A. (1972), Lineal intercept technique for measuring grain size in two-phase polycrystal ceramics, J. Am. Ceram. Soc. 55 [2] 109.

Yan M.F. (1981), Microstructural control in the processing of electronic ceramics, Mater. Sci. and Engng. 48, 53-72

Yan, M.F., Cannon, R.M. and Bowen, H.K. (1977), Grain boundary migration in ceramics, p.276-307 in Fulrath, R.M. and Pask, J.A., Eds., Ceramic microstructures '76, Westview Press, Boulder CO.

Yan, M.F., Cannon, R.M. and Chowdry, U. (1980), Theory of grain growth during densification, Bell Labs internal report.

Yan, M.F., Cannon, R.M., Jr., Bowen, H.K. and Chowdry, U. (1983), Effect of grain size distribution on sintered density, Mater. Sci. and Engng. 60, 275-281.

Zhao, J. and Harmer, M.P. (1988a), Effect of pore distribution on microstructure development: I, Matrix pores, J. Am. Ceram. Soc. 71 [2] 113-20.

Zhao, J. and Harmer, M.P. (1988b), Effect of pore distribution on microstructure development: I, First- and second-generation pores, J. Am. Ceram. Soc. 71 [7] 530-39.